High-Temperature Superconductor Application to Undulators for Compact Free-Electron Lasers

—

Anwendung von Hochtemperatursupraleitern auf Undulatoren für kompakte Freie-Elektronen-Laser

Zur Erlangung des akademischen Grades eines

Doktors der Naturwissenschaften (Dr. rer. nat.)

von der KIT-Fakultät für Physik des
Karlsruher Instituts für Technologie (KIT)

genehmigte

Dissertation

von

M. Sc. Sebastian C. Richter

aus Tübingen

Tag der mündlichen Prüfung	:	05.05.2023
Referentin	:	Prof. Dr. Anke-Susanne Müller
Korreferent	:	Prof. Dr. Bernhard Holzapfel

Graduation Committee:

Chairman	:	Prof. Dr. Ulrich Husemann	Karlsruhe Institute of Technology
Ph.D. supervisor	:	Prof. Dr. Anke-Susanne Müller	Karlsruhe Institute of Technology
Members	:	Prof. Dr. Bernhard Holzapfel	Karlsruhe Institute of Technology
		Prof. Dr. Sebastian Kempf	Karlsruhe Institute of Technology
		Prof. Dr. Gudrun Heinrich	Karlsruhe Institute of Technology
Co-supervisors	:	Dr. Amalia Ballarino	CERN
		Dr. Axel Bernhard	Karlsruhe Institute of Technology
		Dr. Daniel Schörling	CERN

"The content of physics is the concern of physicists, its effect the concern of all men."
"Der Inhalt der Physik geht die Physiker an, die Auswirkungen alle Menschen."
- *The Physicists* (orig. German: *Die Physiker*), by Friedrich Dürrenmatt

Eidesstattliche Versicherung gemäß § 13 Absatz 2 Ziffer 3 der Promotionsordnung des Karlsruher Instituts für Technologie (KIT) für die KIT-Fakultät für Physik:

1. Bei der eingereichten Dissertation zu dem Thema
   "High-Temperature Superconductor Application to Undulators for Compact Free-Electron Lasers"/
   "Anwendung von Hochtemperatursupraleitern auf Undulatoren für kompakte Freie-Elektronen-Laser"
   handelt es sich um meine eigenständig erbrachte Leistung.

2. Ich habe nur die angegebenen Quellen und Hilfsmittel benutzt und mich keiner unzulässigen Hilfe Dritter bedient. Insbesondere habe ich wörtlich oder sinngemäß aus anderen Werken übernommene Inhalte als solche kenntlich gemacht.

3. Die Arbeit oder Teile davon habe ich bislang nicht an einer Hochschule des In- oder Auslands als Bestandteil einer Prüfungs- oder Qualifikationsleistung vorgelegt.

4. Die Richtigkeit der vorstehenden Erklärungen bestätige ich.

5. Die Bedeutung der eidesstattlichen Versicherung und die strafrechtlichen Folgen einer unrichtigen oder unvollständigen eidesstattlichen Versicherung sind mir bekannt.

Ich versichere an Eides statt, dass ich nach bestem Wissen die reine Wahrheit erklärt und nichts verschwiegen habe.

Karlsruhe, den

....
(**Sebastian C. Richter**)

Abstract

Short-period high-field undulators are essential components for the production of brilliant coherent light up to X-rays in compact light sources, e.g. synchrotrons or free-electron lasers (FELs). The compactness should come with a small footprint and thus lower costs, having to operate at lower energies. On the other side of the energy spectrum, future lepton colliders like CLIC or FCC-ee demand high-field damping wigglers for the production of low-emittance beams in order to increase the collision luminosity. The requirement of high magnetic fields for such insertion devices (IDs) already stimulated further development from permanent magnet wigglers and undulators to superconducting IDs. Here, the state-of-the-art technology Nb-Ti already reached its performance limits and is commonly operated at $4.2\,\mathrm{K}$ or lower, making its operation and cooling complex and expensive. Therefore, the above-described accelerators may benefit from the application of high-temperature superconductors (HTS), like ReBCO (rare-earth barium copper oxide): On the one hand, HTS makes magnetic field amplitudes in the range of $2\,\mathrm{T}$ or higher feasible for short undulator periods of $15\,\mathrm{mm}$ or smaller with magnetic gaps of $6\,\mathrm{mm}$ at $4.2\,\mathrm{K}$ or lower; this may also scale up to longer wiggler periods like $50\,\mathrm{mm}$. On the other hand, larger temperature margins will make operations at higher temperatures like $20\,\mathrm{K}$ or higher achievable, which may relax cryogenic requirements and thus reduce costs.

Within the scope of this thesis, the application of ReBCO in the form of coated superconducting tape to superconducting undulators for compact FELs was investigated for the three most common coil geometries (vertical and horizontal racetracks as well as a helical undulator). The parameter space in terms of the undulator period length λ_u, the magnetic flux density amplitude, and the magnetic gap was studied by means of electro-magnetic calculations. This revealed an operation range of $\lambda_\mathrm{u} \leq 20\,\mathrm{mm}$, where the application of ReBCO may be significantly superior to the current Nb-Ti technology. Consequently, modular coil models for all three geometries were designed with a λ_u of $13\,\mathrm{mm}$ and studied for their electro-magnetic performance and mechanical durability. To deal with the high engineering current densities of $2\,\mathrm{kA/mm^2}$ or more, a non-insulated (NI) winding approach was chosen. Subsequently, this thesis presents the technical design of a vertical racetrack (VR) coil and the very first design of a helical undulator wound with HTS tape, to the author's knowledge.

Important characteristics of coated ReBCO superconducting tapes for coil manufacturing were analyzed by bending and heating experiments as well as critical current measurements in self-field and external field at $77\,\mathrm{K}$. Furthermore, winding and splicing techniques were developed for coil manufacturing. Three VR prototype coils were manufactured and powered successfully at $77\,\mathrm{K}$ in liquid nitrogen, proving the feasibility and stability of the NI coil design, by operations with up to 300% of the critical current. Powering tests of two VR coils at $4.2\,\mathrm{K}$ showed safe operations at high engineering current densities of $2.3\,\mathrm{kA/mm^2}$ and generated magnetic fields of up to $1.5\,\mathrm{T}$ at $3.5\,\mathrm{mm}$ distance from the magnetic iron poles. The stability of the tested VR coils was once more demonstrated by operations beyond $3.6\,\mathrm{kA/mm^2}$ with produced magnetic fields in the region of $2\,\mathrm{T}$. Furthermore, the very first HTS helical undulator demonstrator was manufactured as a five-period short model wound with ReBCO superconducting tape. The first powering tests at $77\,\mathrm{K}$ suc-

cessfully proved the principle of this extremely compact and high-field undulator design. In summary, the potential of HTS for superconducting undulators has been demonstrated successfully as well as the feasibility to build and operate such designs with modular coils.

Kurzfassung (Abstract in German)

Kurzperiodische Undulatoren mit hohen Magnetfeldamplituden sind wesentliche Komponenten für die Erzeugung von brillantem kohärentem Licht mit Wellenlängen bis in den Röntgenbereich in kompakten Lichtquellen, wie beispielsweise in Synchrotrons oder Freie-Elektronen-Lasern (FELs). Die Kompaktheit sollte mit einer kleinen Stellfläche und damit relativ niedrigen Betriebsenergien einhergehen; beides hat geringere Investitions- und Betriebskosten zur Konsequenz. Auf der anderen Seite des Energiespektrums benötigen künftige Leptonen-Collider wie CLIC oder FCC-ee Dämpfungswiggler mit hohen Magnetfeldamplituden für die Erzeugung von Strahlen mit geringer Emittanz, um die Kollisionsluminosität zu erhöhen. Der Bedarf an hohen Magnetfeldern für solche Insertion Devices (IDs) hat bereits die Weiterentwicklung von Wigglern und Undulatoren basierend auf Permanentmagneten zu supraleitenden IDs angeregt. Hier stößt der Stand der Technik Nb-Ti schon an seine Leistungsgrenzen und wird üblicherweise bei 4.2 K oder darunter betrieben, was Betrieb und Kühlung komplex und teuer macht. Daher könnten die oben beschriebenen Beschleuniger von der Verwendung von Hochtemperatursupraleitern (HTS) wie ReBCO (Seltene Erden mit Barium-Kupferoxid) profitieren: Einerseits ermöglichen HTS Magnetfeldamplituden im Bereich von 2 T oder höher für kurze Undulatorperioden von 15 mm oder kleiner mit Magnetspalten von 6 mm bei 4.2 K oder niedriger; dies kann auch auf längere Wigglerperioden, wie z.B. 50 mm, skaliert werden. Andererseits wird durch größere Temperaturspannen der Betrieb bei höheren Temperaturen wie 20 K oder höher möglich, was die kryogenen Anforderungen lockern und somit die Kosten senken kann.

Im Rahmen dieser Dissertation wurde die Anwendung von ReBCO in Form von beschichteten bandförmigen Supraleitern für den Bau von supraleitenden Undulatoren für kompakte FELs für die drei gängigsten Spulengeometrien (vertikale und horizontale Rennbahnen, sowie ein helischer Undulator) untersucht. Der Parameterraum wurde in Bezug auf die Undulatorperiodenlänge λ_u, die Amplitude der magnetischen Flussdichte und den Undulatorspalt mittels elektromagnetischen Berechnungen untersucht. Dabei ergab sich ein Betriebsbereich von $\lambda_\mathrm{u} \leq 20$ mm, in welchem die Anwendung von ReBCO der derzeitigen Nb-Ti-Technologie signifikant überlegen sein kann. Infolgedessen wurden modulare Spulenmodelle für alle drei Geometrien mit einem λ_u von 13 mm entworfen und ihre elektromagnetische Leistung sowie mechanische Strapazierfähigkeit untersucht. Um die hohen technischen Stromdichten von 2 kA/mm^2 oder mehr zu handhaben, wurde der Ansatz einer nicht isolierten (NI) Wicklung gewählt. In der Folge wird in dieser Dissertation das technische Design einer vertikalen Rennbahn-(VR-)spule und das nach Wissensstand des Autors allererste Design eines mit HTS Band gewickelten helischen Undulators präsentiert. Wichtige Eigenschaften von beschichteten ReBCO-Supraleiterbänder für die Spulenherstellung wurden durch Biege- und Heizexperimente sowie Messungen von kritischen Strömen in Eigenfeldern und externen Feldern bei 77 K analysiert. Darüber hinaus wurden Wickel- und Verbindungstechniken für die Spulenherstellung entwickelt. Drei VR-Prototypspulen wurden gefertigt und erfolgreich bei 77 K in Flüssigstickstoff bestromt, wobei die Machbarkeit und Stabilität des NI-Spulendesigns durch den Betrieb mit bis zu 300% des kritischen Stroms nachgewiesen wurde. Bestromungstests von zwei VR-Spulen bei 4.2 K zeigten

IV

einen sicheren Betrieb bei hohen technischen Stromdichten von $2.3\,\mathrm{kA/mm^2}$ und erzeugten Magnetfelder von bis zu $1.5\,\mathrm{T}$ in $3.5\,\mathrm{mm}$ Distanz zu den magnetischen Eisenpolen. Die Stabilität der getesteten VR-Spulen wurde nochmals durch den Betrieb bei und jenseits von $3.6\,\mathrm{kA/mm^2}$ mit erzeugten Magnetfeldern im Bereich von $2\,\mathrm{T}$ aufgezeigt. Darüber hinaus wurde der allererste helische HTS Undulator-Demonstrator basierend auf Wicklungen mit beschichteten ReBCO-Supraleiterbändern in Form eines Kurzmodells mit fünf Perioden gefertigt. Die ersten Bestromungstests bei $77\,\mathrm{K}$ haben das Prinzip und die Machbarkeit dieses extrem kompakten und hochfeldfähigen Undulators erfolgreich bewiesen.

Zusammenfassend wurde das Potential von HTS für supraleitende Undulatoren erfolgreich demonstriert, ebenso wie die Machbarkeit, solche Designs mit modularen Spulen zu bauen und zu betreiben.

Contents

Contents

List of abbreviations

ANL   Argonne National Laboratory

APS   Advanced Photon Light Source

CERN   European Organization for Nuclear Research

CLIC   Compact Linear Collider

DESY   German Electron Synchrotron (Deutsches Elektronen-Synchrotron)

DPG   German Physical Society (Deutsche Physikalische Gesellschaft)

FCC-ee   Future Circular Collider, as electron-positron collider

FEL   Free-electron laser

HR   Horizontal racetrack

HTS   High-temperature superconductor

ID   Insertion device

KARA   Karlsruhe Research Accelerator (former name: ANKA)

KIT   Karlsruhe Institute of Technology

LHC   Large Hadron Collider

LHe   Liquid helium

linac   linear accelerator

LN_2   Liquid nitrogen (also LN2)

LTS   Low-temperature superconductor

MQE   Minimum quench energy

Nb-Ti   Niobium-titanium

Nb_3Sn   Niobium-tin

PMU   Permanent magnet undulator

***Re*BCO**   *Rare-earth* Barium Copper Oxide

SCU   Superconducting undulator

STFC   Science and Technology Facilities Council

VR   Vertical racetrack

XLS   CompactLight Project

1. Introduction

Over the last decades, the application of synchrotron light has become more and more valuable not only in various natural sciences like physics, chemistry, and biology, but also in the fields of archaeological science, paleontology, and cultural heritage [1, 2, 3, 4]. New scientific approaches are possible in order to study matter, chemical reactions, and biological processes due to the X-rays' high time and spatial resolution. Additionally, non-destructive and non-invasive processes are a great help to examine fragile items of a wide range like microscopic paint fragments, fossils, historical musical instruments, or ceramics [5]. All thanks to synchrotron radiation and its diverse use such as infrared spectroscopy, X-ray absorbance spectroscopy, X-ray diffraction, X-ray fluorescence, or X-ray computed tomography. There is a high worldwide demand for synchrotron light, especially in the hard X-ray spectrum with photon wavelengths below 1 nm, as a consequence of its multipurpose. However, synchrotron light sources like a free-electron laser (FEL) are complex and thus expensive machines with a rather large footprint, which only major accelerator laboratories are capable of realizing. As the demand further grows, this current well-defined spread around the globe needs to be changed. One approach was made by the so-called CompactLight design study (XLS), which the European Union funded as an international collaboration with the goal "to facilitate the widespread development of X-ray FEL facilities across Europe and beyond, by making them more affordable to construct and operate, through an optimum combination of emerging and innovative accelerator technologies." [6]. While compactness is truly a desirable goal, more compact designs commonly imply lower energy particle beams and consequently lead to a crucial need for high-field short-period undulators for keeping the light production up to X-rays. However, the state-of-the-art superconducting undulator technology has reached its performance limits and cannot provide magnetic flux density amplitudes in the range of 2 T for short periods smaller than 15 mm. Consequently, new solutions must be found to realize this challenging goal.

One promising approach was investigated in the scope of this thesis, namely the application of high-temperature superconductors (HTS), such as ReBCO to superconducting undulators. $Rare\text{-}earth$ barium copper oxide (ReBCO) makes magnetic flux density amplitudes in the range of 2 T or higher feasible for short undulator periods at 4.2 K and can make operations at higher temperatures such as 20 K or higher achievable, which may relax cryogenic requirements, and thus reduce costs. Additionally, it is commercially available as coated superconducting tapes, ready for use, unlike other superconductors, e.g. Nb_3Sn. The designs of the three most common undulator coil geometries (vertical and horizontal racetracks as well as a helical undulator) were investigated, followed by the manufacturing of 13 mm period coils and a helical undulator demonstrator with a non-insulated (NI) winding approach to ensure safe operations for high engineering current densities in the order of $2\,\mathrm{kA/mm^2}$. The outcome of this thesis hence includes the technical design of a vertical racetrack (VR) coil and the very first design to the author's knowledge of a helical undulator wound with HTS tape. The VR coils were powered successfully at 77 K and
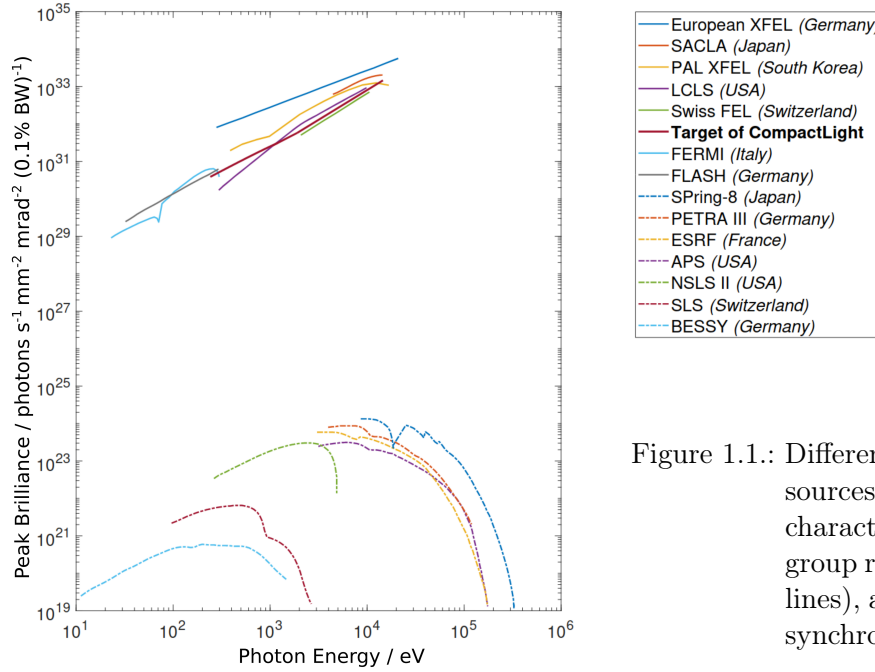
Figure 1.1.: Different synchrotron light sources and their photon characteristics [6]. The top group represents FELs (solid lines), and the bottom group synchrotrons (dashed lines).

4.2 K, proving the feasibility, safety, and stability of the NI coil design, by impressive operations beyond the critical current. Further, safe operations at 4.2 K generated magnetic fields up to the region of 2 T. Therefore, the potential of HTS, more specifically ReBCO, for superconducting undulators has been demonstrated successfully as well as the feasibility to build and operate such no-insulation designs safely with modular coils.

The research work was carried out at the European Organization for Nuclear Research (CERN, former "Conseil européen pour la recherche nucléaire") as well as at the Karlsruhe Institute of Technology (KIT). Additionally, the work of this thesis and its achievements were performed in the frameworks of CompactLight, CLIC, and FCC-ee, providing a valuable contribution to the research communities by investigating short-period high-field undulators and their implementation.

1.1. Insertion devices for synchrotron light sources and future lepton colliders: undulators and wigglers

After Alfred-Marie Liénard first predicted in 1898 that charged particles emit radiation when being accelerated, an electron beam's first optical synchrotron radiation was seen in 1947 at a General Electric research laboratory's synchrotron [7, 8]. The production of synchrotron radiation and its brilliance has been further studied and optimized over the last century, which enabled the exploitation of the entire available spectrum from hard X-rays down to the infrared for diverse applications as stated in the introduction above. The photon's peak brilliance of synchrotron radiation facilities for short wavelengths to the present day is presented in Figure 1.1 with the addition of the projected CompactLight parameters. Modern synchrotron radiation sources utilize so-called insertion devices (IDs) for radiation production, implemented in straight sections of the accelerator, which are called insertions. A common characteristic of IDs is a magnet structure that generates an alternating magnetic field, i.e. multiple dipoles in series. Incoming accelerated charged particles are therefore forced by the Lorentz force onto an undulating trajectory. However, these structures must be invisible along their length for the beam, meaning a field integral equal to zero, not introducing a total beam deflection or offset that might harm the beam's
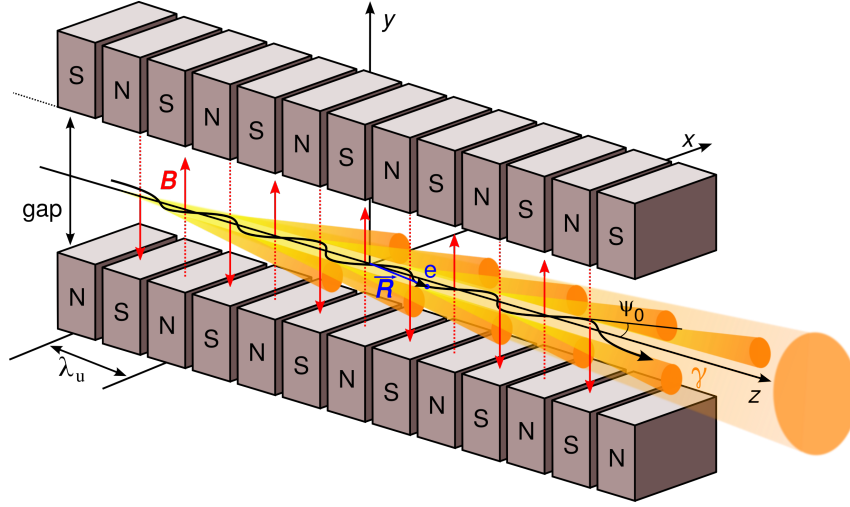
Figure 1.2.: The functional principle of a plane undulator and its radiation cones. The path of a charged particle, e.g. an electron e, with the energy γ is given by the vector $\vec{R}$. Graphic modified from [9].

stability. Undulators are a kind of such alternating magnets which fulfill this criterion. Their working principle is introduced in more detail in the following chapter's section 2.2. Magnetic field calculation methods for undulators are presented in multiple sections of chapter 2.

The plane undulator is illustrated in Figure 1.2 with its important parameters:

- the undulator period length λ_u, defining the length of a single undulator period,

- the magnetic gap g, defining the distance between the dipoles,

- the magnetic field B with oscillating amplitude B_0,

- the maximum angle regarding the z-axis Ψ_0, and

- the particles' energy γ.

Further parameters of interest are the number of periods N_u which defines the undulator length $L_{ID} = N_u \lambda_u$.

As the particle beam is deflected transversely in undulators, a possible interference of the radiated photons may result in a higher photon brilliance as compared to bending magnets, where the particle beam's trajectory is curved, which can be seen in a line spectrum with sharp peaks. Therefore, to accomplish the next generation of highly brilliant but also compact light sources, undulator magnets are essential components for the production of coherent light, especially up to hard X-rays in synchrotrons and free-electron lasers [10]. As described simultaneously with the above-introduced CompactLight project, the compactness should come with a small footprint and thus lower costs, having to operate at lower energies, which makes short-period and high-field undulators of high interest for such machines.

In Figure 1.1 the difference in brilliance between synchrotrons as storage rings and FELs can be well seen by about five orders of magnitude. The brilliance $\mathcal{B}$, also known as spectral brightness, is described for a given wavelength as the number of emitted photons $N_{photons}$ per second, per unit area, and per unit solid angle of the source, and per photon energy bandwidth which gives the respective units as [10, 11]

$$[\text{Brilliance}] = [\mathcal{B}] = \frac{N_{photons}}{\text{s} \cdot \text{mm}^2 \cdot \text{mrad}^2 \cdot (0.1\% \, \text{BW})} \ . \tag{1.1}$$

Figure 1.1 also shows how the characteristic spectrum from synchrotrons drops rapidly after it has reached a certain critical energy, characterized by the critical frequency $\omega_c \propto B_0 \gamma^2$, with the magnetic field amplitude B_0 and the beam energy γ.

Therefore, the emitted photon energy can directly be influenced via the beam energy and the applied magnetic field, thus tuning the undulator range. Higher beam energies in storage rings are only possible by means of stronger bending magnets or a larger radius and stronger radio frequency (RF) cavities for particle acceleration. Yet, the energy is somewhat limited by the overall synchrotron radiation power loss $P_{\text{sync}} \propto \gamma^4/\rho^2$, which is given here for a storage ring's bending magnet with radius ρ. Many undulator harmonics are used for radiation production, in which the intensity drops with the underlying synchrotron radiation spectrum with its critical frequency. In FELs, in contrast, commonly only the fundamental wavelength of the undulator is used and tuning uses both, beam energy and undulator tuning. Therefore, the critical frequency is not really an issue. The radiation losses are not a limiting factor in FELs, however, the beam energy obviously determines the saturation power. Anyway, high beam energies in FELs as in every linear accelerator imply high acceleration gradients and/or long structures. Consequently, large-footprint accelerators are required, scaling linearly with energy.

Briefly summarized, all endeavors to increase the beam energy would imply significantly higher costs and complex reorganization. Consequently, creating higher magnetic fields by the use of the alternating fields of undulators or wigglers is the more beneficial and economic solution, e.g. when aiming for the production of hard X-rays.

In the following the wavelength of the radiated synchrotron light from an undulator λ_γ is anticipated, having multiple harmonics numbered by k, as further explained in detail in the next chapter 2. However, the harmonic condition cannot be met for even integers k.

$$\lambda_\gamma = \frac{\lambda_u}{2k\gamma^2} \left(1 + \frac{K^2}{2}\right) \ . \tag{1.2}$$

Here, the undulator strength parameter K is defined with the undulator period λ_u, the undulator magnetic field amplitude B_0, the speed of light c, and the electron charge and rest mass e and $m_{e,0}$ as

$$K = \frac{e\lambda_u B_0}{2\pi m_{e,0}c} \approx 93.37 \cdot B_0 \bigg|_{\text{in T}} \cdot \lambda_u \bigg|_{\text{in m}} \ , \tag{1.3}$$

and therefore defines the motion of the particles in the magnet.

The aimed region for the XLS design study is displayed as an example of a compact synchrotron radiation facility with relatively low beam energies in Figure 1.3. Here, a contour plot displays the achievable peak brilliance as a function of λ_u and K at $5.5\,\text{GeV}$ within the boundaries of the desired photon wavelength range. A high peak brilliance favors high K values, however, then requires short periods. Consequently, high magnetic flux densities are actually needed. In this given scenario, values of $K \in [0.5, 2.5]$ are necessary to produce the desired hard X-rays with high brilliance. For a given period, on the other hand, the K range is always determined by the boundaries of the desired photon energy range.

Within the scope of this thesis, the term "undulator" will cover magnets with $K \leq 4$. Here, $K \leq 1$ defines weak undulators with a rather weak deflection and $K > 1$ defines strong undulators, which are more commonly utilized. A magnet with a $K \gg 1$ represents the limit case of the strong undulator and is called a wiggler. The brilliance spectra of different insertion devices are displayed in Figure 1.4. Undulators with sharp harmonics are easy to distinguish from wiggler and bending magnets, having a continuous spectrum with the critical photon frequency at the top.
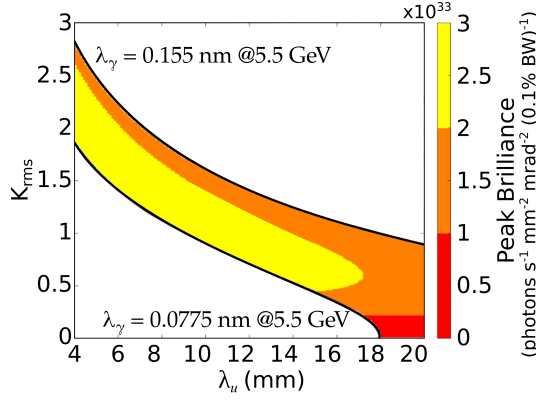
Figure 1.3.: Aimed peak brilliance of the XLS project and emitted photon wavelength λ_γ at an energy of 5.5 GeV. Adapted from [12].
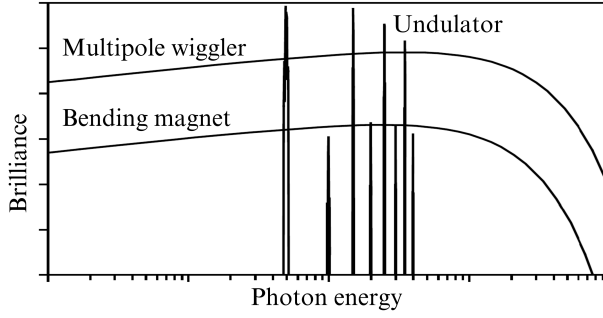

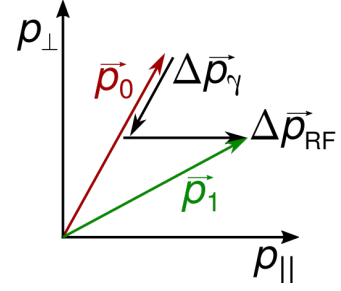Figure 1.4.: Sketched brilliances of different insertion devices [13].

Figure 1.5.: The functional principle of radiation damping.

As discussed, brilliance is an important figure of merit when comparing synchrotron light sources. Likewise, alternating magnetic fields are critical for the particle beams of even larger machines. The next generation of high-energy particle accelerators, i.e. future lepton colliders like CLIC or FCC-ee, demand high-field damping wigglers for the production of low-emittance beams in order to reduce the collision cross-section. However, the design of an optimized undulator magnet for a particular synchrotron radiation production may differ from a wiggler, as seen above.

Figure 1.5 shows the principle of radiation damping in storage rings' wigglers, where photons are emitted by a relativistic charged particle, e.g. an electron, due to a magnetic field deflection. Before the deflection, the particle has a momentum $\vec{p}_0$. Due to the emitted synchrotron radiation, the momentum decreases by $\Delta\vec{p}_\gamma$. Accelerating structures, like RF cavities, re-accelerate the particle in the storage ring within each turn in the desired direction, thus increasing the momentum parallel to the beam trajectory $\Delta\vec{p}_{RF}$. Before and after this process, the absolute momenta $\vec{p}_0$ and $\vec{p}_1$ are of the same value, but consist of different components. After the radiation damping, $\vec{p}_1$ has a larger momentum in beam trajectory direction, here $\vec{p}_\parallel$, which results in a smaller beam emittance.

Summarized, undulators mainly serve as radiation sources in synchrotrons and FELs, whereas wigglers are commonly used for damping oscillating particle bunches in colliders reducing the beam emittance, and thus the beam size. Yet, wigglers are likewise employed in light sources for the production of intense hard radiation, i.e. with energies well above the critical energy of the bending magnets, and favor shorter period lengths for increasing the number of poles and thereby the photon flux. All scenarios have a particular interest in using high-field insertion devices, which makes the undulator magnets investigated in this thesis equally relevant for both, the particle accelerator and the synchrotron radiation community.

Permanent magnet, normal- and superconducting undulators

Since a charged particle beam passed through an undulator for the first time in 1952 at the Stanford linear accelerator (SLAC) [14], undulators became a constant in the production of synchrotron radiation and wigglers for damping the beam size. Permanent magnets were used for this very first undulator magnet supported by soft iron poles to guide the magnetic flux. Interestingly, normal- and superconducting undulators were developed almost simultaneously, with the first superconducting helical undulator magnet installed in 1975 at Stanford University and operated in the first FEL [15]. This was shortly followed by the installation of a normal conducting planar electromagnet in 1979 at SPEAR [16]. In 1980, the first superconducting undulator magnet was installed in a synchrotron: the VEPP-3 storage ring at the Budker Institute of Nuclear Physics. However, permanent magnet undulators (PMUs) were so successful that it was not until the late 1990s at KIT that superconducting undulators were again further developed and optimized [17]. Still, the vast majority of undulators and wigglers today are built with permanent magnets as they are low-maintenance devices thanks to being able to operate at room temperature. Normal conducting electromagnetic undulators are an absolute exception and not competitive. The development from permanent magnet wigglers and undulators to superconducting IDs was mainly stimulated by the requirement of high magnetic field amplitudes.

Nowadays, the achievement of higher magnetic flux densities on the beam axis resulted in an improvement of the emitted photon brilliance of high energy x-rays, which made Nb-Ti the state-of-the-art technology in superconducting IDs. Synchrotron light sources like the Karlsruhe Research Accelerator (KARA) at KIT and the Advanced Photon Light Source (APS) at Argonne National Laboratory (ANL) are only two successful examples where optimized Nb-Ti planar undulators currently operate reliably with high performance [18, 19, 20], whereas helical Nb-Ti undulators were further investigated e.g. at the STFC Daresbury Laboratory and at ANL [21, 22]. The German Electron Synchrotron (DESY) operates permanent magnet wigglers in Petra III to reduce the beam emittance, while a superconducting damping wiggler prototype for CLIC was successfully tested in operation at KARA, KIT [23]. The performance of Nb-Ti is maxed out with the CLIC wiggler's parameters of $B_0 = 3\,\mathrm{T}$, $\lambda_\mathrm{u} = 50\,\mathrm{mm}$, and a $12\,\mathrm{mm}$ magnetic gap. Having reached its performance limits and being commonly operated at $4.2\,\mathrm{K}$ or lower, Nb-Ti makes its operation and cooling relatively complex and expensive.

Consequently, when aiming for still higher fields or equally high fields at smaller periods other materials have to be explored. The same applies when a more sustainable and cheaper operation is desired, without conceding degradation in the performance. One group of materials might be high-temperature superconductors (HTS), which are introduced in detail in the next chapter's section 2.3. Another could be the superconductors Nb_3Sn or MgB_2, which have to undergo several complex production treatments after winding to become superconducting. Nevertheless, a $50\,\mathrm{cm}$ long prototype wound with Nb_3Sn wire was studied at ANL as well as a $25\,\mathrm{cm}$ long prototype wound from MgB_2 wire at the Ohio State University [24, 25]. Compared to Nb_3Sn and MgB_2, the ready-to-use HTS wires, commonly produced as tapes, may make their application to the major geometries for undulators easier, as displayed in Figure 1.6. An HTS version of the CLIC damping wiggler was investigated as an example and might be able to deliver around $4\,\mathrm{T}$ peak fields according to calculations [26].
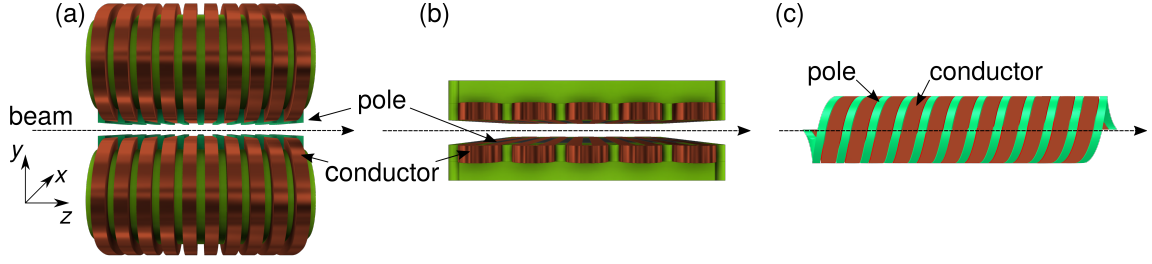
Figure 1.6.: Models of different undulator and wiggler geometries, wound from tape-shaped conductors and investigated within the scope of this thesis. (a) vertical race-track (VR) coils, (b) horizontal racetrack (HR) coils, (c) a helical undulator coil.

Experimental applications of HTS as tape-shaped superconductor wire to superconducting undulators started around 2012 with an insulated vertical racetrack (VR) approach [27]. The first proof of principle for non-insulated and partially insulated VR windings with a jointless HTS tape winding scheme for $\lambda_{\mathrm{u}} \geq 16\,\mathrm{mm}$ was demonstrated in 2017 with achieved engineering current densities J_{e} of $2.1\,\mathrm{kA/mm^2}$ at $4.2\,\mathrm{K}$ [28]. This was 40% higher compared to similar Nb-Ti devices. Also in 2017, a compact undulator concept was presented based on laser-structured HTS tapes, first as non-insulated winding, later in 2021 as soldered tape stack [29, 30]. This design achieved J_e around $2.2\,\mathrm{kA/mm^2}$ with B_0 of around $1\,\mathrm{T}$ for $\lambda_{\mathrm{u}} = 8\,\mathrm{mm}$ in a $4\,\mathrm{mm}$ magnetic gap. Further recent approaches of applying HTS to undulators featured bulk staggered arrays [31, 32]. As this material is rather difficult to purchase, stacked HTS tapes may be also an option here.

However, the achievement of high current densities brings not only advantages, like higher peak fields. The high currents make quench protection a major concern in these operating regions besides the new challenges for the winding procedures that need to be tackled due to the superconductor's tape geometry. As quench protection for HTS magnets has not been fully mastered, yet, the above-mentioned undulator studies based on HTS tape had to carefully power their devices well below the critical current.

Within this thesis, a non-insulated dry-wound approach is studied to prevent hotspots and thus quenches. Compared to other designs, the superconductor is always supported by enough normal conducting material, which allows the current to always bypass the superconducting path and stabilizes the coil. The here-designed VR coil includes also an iron core and poles to boost the field and reduce radial forces on the conductor. Furthermore, a very compact and novel helical design was developed for the application of coated *Re*BCO superconducting tapes to undulators.

1.2. Scope and research question

Within the scope of this thesis, the application of ReBCO in the form of coated superconducting tape to superconducting undulators for compact FELs is investigated for the three most common coil geometries (vertical and horizontal racetracks as well as a helical undulator). This should include simulation studies as well as the manufacturing of prototype coils for experimental studies and therefore poses the following research questions:

- What is the ideal optimized parameter space for the application of ReBCO, thus where may the application of ReBCO be significantly superior to the current Nb-Ti technology?

- How can common undulator coil designs be realized with coated ReBCO superconducting tapes? What are the technical challenges, constraints, and which characteristics of coated ReBCO tapes are the most critical for coil manufacturing?

- Consequently, what manufacturing techniques and processes need to be developed when applying coated ReBCO superconducting tapes to undulator coils?

- As ReBCO enables very high current densities above $2\,\mathrm{kA/mm}^2$ at $4.2\,\mathrm{K}$, how can such coils be powered and protected? How stable are operations and performances at different cryogenic temperatures?

In summary, this thesis evaluates the questions of the HTS' potential for superconducting undulators as well as the feasibility to build and operate such designed magnets. Provided that a successful operation is feasible, the question of the real HTS undulator coil performance will follow up next.

1.3. Outline

The structure of this thesis is organized starting with fundamentals to prepare the basis for calculations and the magnet design, followed by the presentation of the experimental results and their discussion. A final conclusion with an overview of the achievements closes this thesis.

After a general introduction in chapter 1, chapter 2 gives an overview of the theory and application in FELs of superconducting undulators as well as of the investigated superconducting materials, therefore sets up the background of the following work. In chapter 3, a parameter space study is performed within the framework of the EU-funded design study CompactLight (XLS), comparing low-temperature superconductors to the investigated high-temperature superconductor ReBCO. As a result of further presented electromagnetic and mechanical investigations, the designs of a vertical racetrack coil and a helical undulator are presented.

For proof of principle, VR coils were manufactured and tested at two different operating temperatures: $77\,\mathrm{K}$ and $4.2\,\mathrm{K}$. Furthermore, the very first HTS helical undulator demonstrator[1] with a short-model length of five periods was wound from ReBCO superconducting tape and tested at $77\,\mathrm{K}$. Preceding experimental studies concerning ReBCO tape superconductors and the developed coil manufacturing process are presented and discussed in chapter 4. This is followed by chapter 5, covering all built coils' powering test results and analyses at the two tested cryogenic temperatures.
In the end, the achievements of this thesis are summarized and conclusions are drawn as well as prospects are given.

---

[1]To the author's knowledge.

2. Fundamentals of superconducting undulator magnets and FELs

The fundamental principles that find application in this thesis and define its close background can be found in this chapter. First of all, the magnetic field in undulators is derived from Maxwell's equations, followed by a description of implemented methods of the utilized finite-element software, such as Opera [33], to calculate the field distributions in electromagnets. Next, the fundamentals of free-electron lasers are introduced with a focus on undulator radiation, providing the higher frame of reference of this thesis. This chapter is completed with an overview of applied superconductivity and superconducting magnets including important parameters. This directly prepares the basis for the following magnet design chapter 3.1.

2.1. Field calculation methods for undulators

In the previous chapter, undulators and wigglers were introduced as insertion devices in synchrotron light sources with an alternating magnetic field. The magnetic field description of the investigated geometries has to differentiate between planar undulators, such as VR and HR coils, and helical undulators. Both geometries are essential parts of this thesis and were designed electro-magnetically as well as measured experimentally in the following chapters. The following two subsections present derivations and give an introduction to the calculation methods of such devices, applied in the electro-magnetic design process. This introduction does not claim complete integrity. Full detailed backgrounds can be found in the relevant literature [34, 35, 36, 37], which was used as the basis to perform the following recapitulation.

2.1.1. Analytical field calculation methods

In the following, the magnetic flux density is considered in the undulator's magnetic gap g between the magnetic poles, which is assumed to be free of sources. Figure 1.2 already introduced a planar undulator's conventional coordinate system with the beam going in $\hat{z}$-direction and the field amplitude in $\hat{y}$-direction. Assuming an infinitely long periodic undulator, this magneto-static derivation starts from two basic Maxwell's equations, valid in a vacuum environment:

$$\nabla \cdot \vec{B} = 0 \ , \tag{2.1}$$

$$\nabla \times \vec{H} = \vec{J} \ , \tag{2.2}$$

where $\vec{B}$ is the magnetic field, or magnetic flux density, $\vec{H}$ is the field intensity, and $\vec{J}$ is the current density. Here, $\vec{B}$ and $\vec{J}$ are integrated over a surface, with $[B] = 1 \, \mathrm{Vs/m^2}$ and

$[\vec{J}] = 1\,\mathrm{A/m^2}$. $\vec{H}$ is unlike integrated along a line with $[\vec{H}] = 1\,\mathrm{A/m}$.
The magnetic field and field intensity in the magnetic aperture are connected via the vacuum permeability μ_0 as

$$\vec{B} = \mu_0 \vec{H} \,, \tag{2.3}$$

with $\mu_0 = 1.25663706212(19) \times 10^{-6}\,\mathrm{N/A^2} \approx 4\pi \times 10^{-7}\,\mathrm{H/m}$ as redefined in 2019 [38]. Additionally when in a vacuum, the current density consequently becomes $\vec{J} = 0$. The total magnetic scalar potential Ψ ($[\Psi] = 1\,\mathrm{A}$) is then defined for $\nabla \times \vec{H} = 0$:

$$\vec{H} = -\nabla \Psi \,, \quad \text{with } \nabla \times (\nabla \Psi) = 0 \,. \tag{2.4}$$

Next, the Laplace-Equation is created by inserting equations (2.4) and (2.3) into equation (2.1):

$$\nabla \cdot \vec{B} = -\nabla \cdot \mu_0 \nabla \Psi = -\mu_0 \nabla^2 \Psi = 0 \,. \tag{2.5}$$

The potential along the assumed infinite undulator can be described by a sum over all separable functions in the 3-dimensional space:

$$\Psi(x,y,z) = \sum_{m=1}^{\infty} \mathcal{X}_m \mathcal{Y}_m \mathcal{Z}_m \,. \tag{2.6}$$

With the undulator period λ_{u} defining the periodicity via the fundamental wave number $k_0 = 2\pi/\lambda_{\mathrm{u}}$, the flux along the z-axis can be developed with constants a_m and b_m as:

$$\mathcal{Z}_m = a_m \cos(mk_0 z) + b_m \sin(mk_0 z) \,. \tag{2.7}$$

This can be inserted into the Laplace-equation (2.5) followed by an execution of ∇^2:

$$\left(\mathcal{Y}_m \frac{\partial^2 \mathcal{X}_m}{\partial x^2} + \mathcal{X}_m \frac{\partial^2 \mathcal{Y}_m}{\partial y^2} \right) - m^2 k_0^2 \mathcal{X}_m \mathcal{Y}_m = 0 \,. \tag{2.8}$$

The considered undulator is now assumed not only of infinite length but also of infinite width along the x-axis, defining it as a planar undulator from here on. The x-component can then be seen as

$$\frac{\partial \mathcal{X}_m}{\partial x} = 0 = \frac{\mathrm{d}\mathcal{X}_m}{\mathrm{d}x} \,, \tag{2.9}$$

which reduces equation (2.8) assuming an equal partial to total deviation:

$$\frac{\mathrm{d}\mathcal{Y}_m}{\mathrm{d}y^2} = m^2 k_0^2 \mathcal{Y}_m \,, \tag{2.10}$$

for which the known solution exists generally with constants c_m and d_m as

$$\mathcal{Y}_m = c_m \sinh(mk_0 y) + d_m \cosh(mk_0 y) \overset{\text{sym.}}{=} c_m \sinh(mk_0 y) \,. \tag{2.11}$$

Here, the symmetric condition (sym.) of the undulator $B_y(y) = B_y(-y)$ lets the term with the hyperbolic cosine disappear. This leads to the solution of equations (2.3) and (2.4) for each component:

$$B_x = 0 \,, \tag{2.12}$$

$$B_y = \sum_{m=1}^{\infty} \Big(A_m \cos(mk_0 z) + B_m \sin(mk_0 z) \Big) \cdot \cosh(mk_0 y) \,, \tag{2.13}$$

$$B_z = \sum_{m=1}^{\infty} \Big(-A_m \sin(mk_0 z) + B_m \cos(mk_0 z) \Big) \cdot \sinh(mk_0 y) \,, \tag{2.14}$$
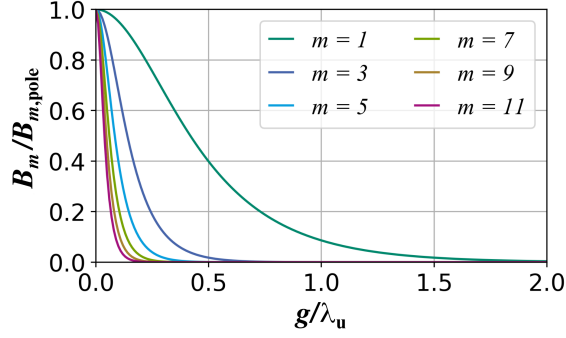
Figure 2.1.: Ratio of the central B_m and pole $B_{m,\text{pole}}$ field amplitude for several odd harmonics m, evaluated at $y = 0$ and $y = g/2$, respectively

with the constants A_m and B_m, to be defined by the boundary conditions. Assuming a perfect undulator, an odd function is required here, implying that all even harmonics B_m and skew harmonics A_m disappear. For considering only the central field on the center of the beam axis, $y = 0$ has to be applied. Consequently, the ratio between B_m and the field at the pole tip $B_{m,\text{pole}}$ at $y = g/2$ can be written as

$$\frac{B_m}{B_{m,\text{pole}}} = \frac{1}{\cosh(m\pi \frac{g}{\lambda_\text{u}})} \;.\tag{2.15}$$

Evaluating equation (2.15) for odd harmonics as seen in Figure 2.1 shows a steep decay of the ratio already from $m \geq 3$, implying a decrease of the magnetic field amplitude B_m. Additionally, a decrease of B_m can be noticed when increasing the gap, especially for shorter undulator periods. With the higher harmonics being relatively small, executing the summation or integrating the field leads to a valid approximation for a **planar undulator**:

$$B_x = 0 \;,\tag{2.16}$$
$$B_y = B_{y,0} \sin(k_0 z) \cdot \cosh(k_0 y) \;,\tag{2.17}$$
$$B_z = B_{z,0} \cos(k_0 z) \cdot \sinh(k_0 y) \;,\tag{2.18}$$

with the magnetic field amplitude $B_{v,0} \equiv B_1$ for $v \in \{x, y\}$. On the beam axis is $y = 0$, which lets B_z vanish and makes B_y only a function of sine.

When considering now the magnetic field on the beam axis of an ideal **helical undulator** as displayed in Figure 2.2, fields on both transverse axes, x- and y-axis, are present with a variable phase difference φ (generally $\varphi = \pi/2$):

$$B_x = B_{x,0} \sin(k_0 z) \;,\tag{2.19}$$
$$B_y = B_{y,0} \sin(k_0 z + \varphi) \;,\tag{2.20}$$
$$B_z = 0 \;.\tag{2.21}$$

A more detailed matter concerning field derivations and end field descriptions of helical undulators can be found in the literature [39, 40, 41, 42].

Termination and field integrals As undulators are insertion devices, they must be transparent for the beam, meaning not introducing a total beam deflection or a displacement in the trajectory that might harm the beam's stability. Essentially, the beam entrance must match the beam exit in both vertical and horizontal positions, which also applies to the beam entrance and exit angles. This is done by setting the first and second field integrals, FI_1 and FI_2, equal to zero. Here, FI_1 integrates the magnetic flux along the
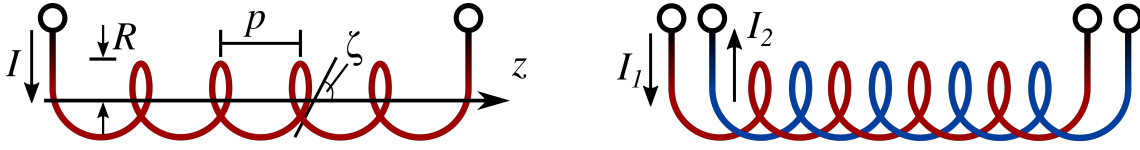
Figure 2.2.: Schematic sketches of a single helical (left) and a bifilar helical coil (right)
along the z-axis with pitch $p = \lambda_\mathrm{u}$ and radius R. The escaping arc ζ describes
the angle between the helical slope and the z-axis. In the case of the bifilar
coil, both helices may also be powered in series ($I_1 = I_2$).

undulator length L_ID, whereas FI_2 integrates additionally over the variation in z:

$$FI_1 = \int^{L_\mathrm{ID}} B_y(z) \, \mathrm{d}z \quad \text{and} \quad FI_2 = \int^{L_\mathrm{ID}} \int^z B_y(z') \, \mathrm{d}z' \, \mathrm{d}z \ . \tag{2.22}$$

As $B_x = B_z = 0$ in the center of the gap, the vertical position and angle are unmodified
and only By must be considered. The first field integral FI_1 can be treated by either
a symmetric or an antisymmetric design, which have an odd or even number of poles,
respectively. A common technique to realize the second field integral FI_2 is the adding of
extra poles, so-called matching periods, with $1/4\, B_{y,0}$ and $-3/4\, B_{y,0}$ at each end.

2.1.2. Calculation methods for magnetic field amplitudes

Once again, the magnetic flux density is considered in the undulator's magnetic gap g
between the magnetic poles, which is assumed to be free of sources. Figure 1.2 already
introduced a planar undulator's conventional coordinate system with the beam going in
$\hat{z}$-direction and the field amplitude in $\hat{y}$-direction. Here, it will be shown that the planar
undulator can be described as a limit case of calculations done for a helical undulator.
Consequently, a helical undulator electromagnet wound in a bifilar scheme is considered in
the beginning. Both geometries are essential parts of this thesis and are designed electro-
magnetically as well as measured experimentally in the following chapters.
Figure 2.2 displays schematically the shape of a helical and a bifilar helical coil and the
characteristic parameters. Assuming an infinitely long periodic undulator, this magneto-
static derivation starts from two basic Maxwell's equations, introduced in equations (2.1)
and (2.2). The field of a bifilar helical undulator is defined by the helical geometry of
its conductor. From equation (2.1), the magnetic vector potential $\vec{A}$, $[\vec{A}] = \mathrm{Tm}$, can be
defined as

$$\nabla \times \vec{A} = \vec{B} \ . \tag{2.23}$$

With equations (2.3) and (2.2) this leads to

$$\nabla \times \vec{A} = \mu_0 \vec{H} \ , \tag{2.24}$$

$$\frac{1}{\mu_0} \nabla \times (\nabla \times \vec{A}) = \vec{J} \ . \tag{2.25}$$

As $\nabla \times \vec{A} = \nabla \times (\vec{A} + \nabla\phi)$, where ϕ is a smooth scalar field, the divergence of a curl is
zero, but not unique, and may be treated as gauge invariance. The Coulomb gauge fixes
this by setting $\nabla \cdot \vec{A} = 0$. Here, suitable boundary conditions have to be chosen to show a
unique solution of this problem [36]. With this equation (2.25) becomes

$$\frac{1}{\mu_0} \left(-\nabla^2 \vec{A} + \nabla(\nabla \cdot \vec{A}) \right) = \vec{J} \ , \tag{2.26}$$

$$\nabla^2 \vec{A} = -\mu_0 \vec{J} \ . \tag{2.27}$$

The vector potential does not permit any current to escape, which makes it source-free and given for a line current within a closed loop $\mathcal{L}$. With the position vector of the field point $\vec{r}$ on this loop and the position vector of the source point $\vec{r}'$, the vector potential can be rewritten as

$$\vec{A}(\vec{r}) = \frac{\mu_0 I}{4\pi} \oint^{\mathcal{L}} \frac{\mathrm{d}\vec{r}'}{|\vec{r} - \vec{r}'|} \; . \tag{2.28}$$

Inserting this finding in equation (2.23) yields the Biot-Savart law:

$$\vec{B}(\vec{r}) = \frac{\mu_0 I}{4\pi} \oint^{\mathcal{L}} \frac{\mathrm{d}\vec{r}' \times (\vec{r} - \vec{r}')}{|\vec{r} - \vec{r}'|^3} \; , \tag{2.29}$$

where the acronym $\vec{s} \equiv \vec{r} - \vec{r}'$ is often used. The Biot-Savart law is commonly used to calculate the magnetic field amplitude in electro-magnets besides other methods that are introduced later. Here, a clear field dependence on the current I can be seen, such that $B \propto I$, which makes conductors with a higher current carrying ability directly interesting for higher magnetic fields.

First, only one indefinite helix is considered for the determination of a bifilar helical undulator's magnetic field. Here, the so-called escaping arc ζ of the helix can be found as

$$\zeta = \arctan\left(\frac{p}{2\pi \cdot R}\right) \; , \tag{2.30}$$

with the helical pitch $p \equiv \lambda_{\mathrm{u}}$ and radius R as presented in Figure 2.2. In the following $\zeta > 0$ is assumed for a considered helical coil with a finite magnetic field on its central axis. **The helix in a 3-dimensional Cartesian coordinate system** can then be described in $\hat{z}$-direction by

$$x = R \cdot \cos(\phi) \; , \quad y = R \cdot \sin(\phi) \; , \quad z = R \cdot \phi \tan(\zeta), \tag{2.31}$$

where z steps up by $2\pi R \tan(\zeta) = p$ for $\phi = 2\pi$. As the on-axis magnetic field is in focus, points on the z-axis are congruently found as follows:

$$s_x = -R \cdot \cos(\phi) \; , \quad s_y = -R \cdot \sin(\phi) \; , \quad s_z = -R\phi \tan(\zeta) + \Phi, \tag{2.32}$$

$$\mathrm{d}r_x' = -R \cdot \sin(\phi)\,\mathrm{d}\phi \; , \quad \mathrm{d}r_y' = R \cdot \cos(\phi)\,\mathrm{d}\phi \; , \quad \mathrm{d}r_z' = R\tan(\zeta)\,\mathrm{d}\phi. \tag{2.33}$$

First, the focus is on the B_z-component for $R > 0$. Applying the Biot-Savart law from eqation (2.29) with the acronym $\vec{s} \equiv \vec{r} - \vec{r}'$ then yields

$$B_{z,0} = \frac{\mu_0 I}{4\pi} \oint \frac{(\mathrm{d}\vec{r}' \times \vec{s})|_z}{s^3} = \frac{\mu_0 I}{4\pi} \oint \frac{s_y \mathrm{d}r_x' - s_x \mathrm{d}r_y'}{s^3} \; . \tag{2.34}$$

Now the origin is set to the point where $B_{z,0}$ is determined by $s = (s_x^2 + s_y^2 + s_z^2)^{\frac{1}{2}} = R\sqrt{1 + \phi^2 \tan^2(\zeta)}$ and limits are chosen accordingly for the integration with a potential distance b from the coil's center and a total number of turns N as

$$\phi_1 = -N\pi + \frac{b}{R\tan(\zeta)} \; , \tag{2.35}$$

$$\phi_2 = N\pi + \frac{b}{R\tan(\zeta)} \; . \tag{2.36}$$

This together with taking the infinite periodic geometry into account, the closed line can be dropped which forms equation (2.34) further into a shape that can be solved [43]:

$$B_{z,0} = \frac{\mu_0 I}{4\pi R} \int_{\phi_1}^{\phi_2} \frac{\mathrm{d}\phi}{\left[1 + \phi^2 \tan^2(\zeta)\right]^{\frac{3}{2}}} \tag{2.37}$$

$$= \frac{\mu_0 I}{4\pi R \tan(\zeta)} \left(\frac{\pi R N \tan(\zeta) + b}{\sqrt{R^2 + \left(\pi R N \tan(\zeta) + b\right)^2}} + \frac{\pi R N \tan(\zeta) - b}{\sqrt{R^2 + \left(\pi R N \tan(\zeta) - b\right)^2}} \right) \; . \tag{2.38}$$

Now, a point P is assumed, which lies within the helical coil in the defined distance b from the z-axis with $b < R$. Then β_1 and β_2 describe the angles between the z-axis and the vectors connecting P with the outermost ends of the helical coil. Consequently, one of β_i has to be greater than $\pi/2$. With this equation (2.38) can be rewritten as

$$B_{z,0} = \frac{\mu_0 I}{4\pi R \tan(\zeta)} \cdot (\cos(\beta_2) - \cos(\beta_1)) \ . \tag{2.39}$$

The length of a coil l commonly describes the distance between the outermost ends of a coil, with n turns per unit length:

$$l = 2\pi R N \tan(\zeta) \, , \quad \text{with } N = n \cdot l \ . \tag{2.40}$$

This reforms the last equation to

$$B_{z,0} = \frac{\mu_0 n I}{2} \cdot (\cos(\beta_2) - \cos(\beta_1)) \ . \tag{2.41}$$

Assuming now an infinite helical coil implies an infinite number of turns N:

$$\lim_{N \to \infty} B_{z,0} = \frac{\mu_0 I}{2\pi R \tan(\zeta)} = \mu_0 n I \ . \tag{2.42}$$

The components $B_{x,0}$ and $B_{y,0}$ can be treated consistently with equation (2.34) and are listed in appendix A.1 in their integral formula. In general, these integrals are not equal to zero, which implies a spiral. Assuming now again an infinite helical coil lets B_x disappear due to its odd functions under the integral. However, the y-component becomes

$$B_{y,0} = -2\pi R n^2 \mu_0 I \int_0^\infty \frac{\cos(\phi) + \phi \sin(\phi)}{[(2\pi R n)^2 + \phi^2]^{\frac{3}{2}}} \mathrm{d}\phi \ . \tag{2.43}$$

By integrating term by term, it can be shown that the solution of this integral is given with the modified Bessel functions of the second kind K_j yielding [43]

$$B_{y,0} = -n\mu_0 I \cdot [2\pi R n \cdot K_0(2\pi R n) + K_1(2\pi R n)] \ . \tag{2.44}$$

For a bifilar helix, this description can simply be summed up for the two currents I_1 and I_2 as the fields superimpose [44, 45]. An additional rearrangement of the presented parameters leads to the following:

$$B_{y,0} = -\frac{\mu_0(I_1 + I_2)}{\lambda_{\mathrm{u}}} (k_0 R \cdot K_0(k_0 R) + \cdot K_1(k_0 R)) \tag{2.45}$$

A limit case can now be examined to determine the field amplitude of a straight wire parallel to $\hat{z}$ and at distance R from the z-axis, which may be used for a planar undulator. Setting $\zeta = \frac{\pi}{2}$ or $n = 0$ implies the consequence of $B_z = 0$. This yields

$$\lim_{n \to 0} B_{y,0} = -\frac{\mu_0 I}{2\pi R} \ . \tag{2.46}$$

2.1.3. Numerical field calculation methods

The previous sections derived the magnetic field in an undulator's aperture for the magneto-static scenario from Maxwell's equations. Besides the conductor, ferromagnetic materials, like iron, are commonly utilized to boost the pole fields by roughly 15 to 20%, to modify appearing forces, and to guide the magnetic flux in electromagnets. This also applies to the designed modular prototype coils in this thesis. The Biot-Savart law is not able to calculate the complete magnetic field in an electromagnetic undulator including ferromagnetic materials but needs to be supported by separate vector and scalar potential methods. The magnetic field distribution has to be described accordingly as a boundary value problem, which these numerical methods are able to solve. How this is treated mathematically and implemented in software would go beyond the scope of this thesis and can be found in detail in particular articles and books [35, 36]. What follows is a rough overview of the principles.

The magnetization M needs to be introduced with $[M] = \text{A/m}$ when doing calculations with ferromagnetic materials and transforms equation (2.2) with $\vec{B} = \nabla\vec{A} = \mu_0(\vec{H} + \vec{M})$ to

$$\frac{1}{\mu_0}\nabla \times (\nabla \times \vec{A}) = \vec{J} + \nabla \times \vec{M} \ , \tag{2.47}$$

which is one option to calculate the magnetic field. Again applying the Coulomb gauge gives the vector Poisson equation

$$\nabla^2 \vec{A} = -\mu_0(\vec{J} + \nabla \times \vec{M}) \ . \tag{2.48}$$

As a two-case scenario is considered: one with an in-vacuum field and one with an iron domain, the magnetic vector potential is split accordingly with the two parts defined as the impressed vector potential $\vec{A}_\text{s}$ caused by source currents in space and the reduced vector potential $\vec{A}_\text{r}$ caused by the iron magnetization. With the linearity of the nabla operator, this gives

$$\nabla\vec{A} = \nabla \times (\vec{A}_\text{r} + \vec{A}_\text{s}) = \nabla \times \vec{A}_\text{r} + \nabla \times \vec{A}_\text{s} \ . \tag{2.49}$$

Consequently, the magnetic field can also be described by the reduced vector potential:

$$\vec{B} = \mu_0\vec{H}_\text{s} + \nabla\vec{A}_\text{r} \ . \tag{2.50}$$

Ampère's law can be used to calculate the magnetic field, which leads to the so-called curl-curl vector potential method. Here, $\vec{B} = \nabla \times \vec{A}$ is valid and equation (2.2) is used as

$$\nabla \times \frac{1}{\mu}(\nabla \times \vec{A}) = \vec{J} \ , \tag{2.51}$$

with $\mu = \mu_r\mu_0$, where the relative permeability μ_r can be found besides the vacuum permeability μ_0. Here, the magnetic permeability μ describes the permeability of a specific (ferromagnetic) material and can also be described as $\mu = \mu_0(1 + \chi_\text{V})$, with the volume magnetic susceptibility χ_V, defined by $\vec{M} = \chi_\text{V}\vec{H}$.

A similar approach for magneto-static problems as presented in equation (2.49) can be done when by splitting up $\vec{H}$:

$$\vec{H} = \vec{H}_\text{r} + \vec{H}_\text{s} \ , \tag{2.52}$$

where the source field is found as $\nabla \times \vec{H}_\text{s} = \vec{J}$ and $\nabla \times \vec{H}_\text{r} = 0$ is defined. Likewise, a reduced magnetic scalar potential Ψ_r can be introduced, for which the following is valid:

$$\nabla \times (\nabla\Psi_\text{r}) = 0 \ , \tag{2.53}$$

Consequently, equation (2.52) results in

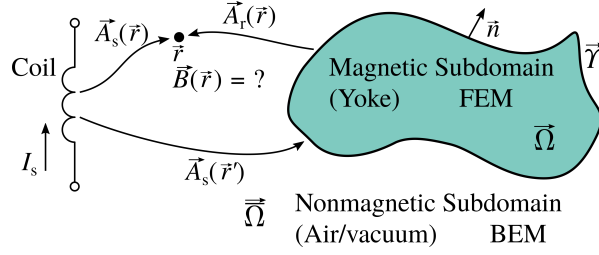$$\vec{H} - \vec{H}_\text{s} = -\nabla\Psi_\text{r} \ , \tag{2.54}$$

Figure 2.3.: Visualized BEM-FEM coupling. To determine the magnetic field at a point $\vec{r}$, a superposition of the vector potentials $\vec{A}(\vec{r})_\text{s}$ and $\vec{A}(\vec{r})_\text{r}$ is applied. The source vector potential $\vec{A}(\vec{r}')_\text{s}$ affects $\vec{r}$ directly as well as the magnetic subdomain $\vec{\Omega}$, representing a yoke. The yoke then creates $\vec{A}(\vec{r})_\text{s}$ acting also on $\vec{r}$ [46].

Applying equation (2.1) gives further

$$\nabla \cdot (\mu \nabla \Psi_\text{r}) = \nabla \cdot \mu \vec{H}_\text{s} \ , \tag{2.55}$$

where the Biot-Savart law can be used to find $\vec{H}_\text{s}$. Similar absolute values but opposite directions can be found for $\vec{H}_\text{r}$ and $\vec{H}_\text{s}$ in highly permeable regions, which may lead to errors that add up when the cancellation calculation is performed [35]. This can be avoided by going back to the total magnetic scalar potential Ψ in regions without induced current, thus $\nabla \vec{H} = 0$:

$$\vec{H} = -\nabla \Psi \ . \tag{2.56}$$

Applying once more equation (2.1) gives

$$\nabla \cdot (\mu \nabla \Psi) = 0 \ . \tag{2.57}$$

The following interface conditions couple the current-free domain with Ψ to the current-carrying domain's Ψ_r:

$$-\mu \nabla \Psi \cdot \vec{n} = \mu_0 (\vec{n} \cdot \vec{H}_\text{s} - \nabla \Psi_\text{r} \cdot \vec{n}) \ , \tag{2.58}$$

$$\vec{n} \times \nabla \Psi = \vec{n} \times \vec{H}_\text{s} - \vec{n} \times \nabla \Psi_\text{r} \ , \tag{2.59}$$

with the outward unit normal vector $\vec{n}$ of the interface or boundary, pointing from the ferromagnetic to the vacuum or air domain, as displayed in Figure 2.3.

With the made derivations it was shown that only the ferromagnetic domain must be treated as a boundary value problem due to its non-linearity. One option to deal with this is utilizing the so-called "boundary-element method finite-element method" (BEM-FEM) [47, 46], which has the advantage of not needing an all-embracing mesh for the entire problem as sketched in Figure 2.3. Although this theory was in the end not applied in the following calculations, it provides a very comprehensive understanding of treating a boundary value problem given by the application of ferromagnetic materials in the magnet design and is therefore worth the excursion. To handle the non-linear magnetic permeability μ, solely the magnetic sub-domain $\vec{\Omega}$ has to be meshed with a focus on the elements along its border. The field at the distant boundaries is typically insignificant and thus assumed to be zero in order to define boundary conditions $\vec{\Upsilon}$ for the numerical calculation of $\vec{A}_\text{r}$. Iterative solving steps for a non-linear equation system demonstrated that the following continuity requirements are satisfied in boundary elements [47]:

$$\vec{n} \cdot \vec{B} = 0 \ , \tag{2.60}$$

$$\vec{n} \times \vec{H} = \vec{k} \ , \tag{2.61}$$

where $\vec{k}$ represents a possible surface current density. Finding the solution determines the values of all nodes or elements in the magnetic sub-domain. As a result, $\vec{A}_\text{r}$ can be calculated and subsequently superimposed on $\vec{A}_\text{s}$, which follows the Biot-Savart law.

Within this thesis, most of the electro-magnetic calculation work was done by using the software Opera [33]. The here implemented and applied methods are summarized in the following:

- Vector potential (3D): $\frac{1}{\mu_0} \nabla \times (\nabla \times \vec{A}) = \vec{J}$.
  Applied in the definition of so-called "circuit element conductor" and can calculate the current's skin effect. The entire model has to be meshed with a particularly fine mesh strongly necessary for the conductors.

- Reduced vector potential (3D): $\vec{B} = \mu_0 \vec{H}_{\mathrm{s}} + \nabla \times \vec{A}_{\mathrm{r}}$.
  Applied in the definition of so-called "Biot-Savart conductors" and works with the Biot-Savart law to calculations of source fields.

- Two scalar potentials (3D): A combination of the below-described potentials.
  The combination makes magneto-static calculations stable and very accurate.

  - Reduced magnetic scalar potential: $\nabla \cdot (\mu \nabla \Psi_{\mathrm{r}}) = \nabla \mu \vec{H}_{\mathrm{s}}$.
    Potential errors due to cancellation calculations in non-linear magnetic materials may increase numerical errors.

  - Total magnetic scalar potential: $\nabla \cdot (\mu \nabla \Psi) = 0$.
    No induced currents must exist.

- Vector potential (2D): $\nabla^2 \vec{A} = \mu_0 (\vec{J} + \nabla \times \vec{M})$.
  Applied in the definition of conductor areas, primarily in 2D. The entire model has to be meshed with a particular fine mesh necessary for the conductors.

2.2. Free-electron lasers

Similar to the commonly known laser, standing for light amplification by stimulated emission of radiation, a free-electron laser (FEL) generates coherent radiation based on the interaction between the emitted photons from undulators and their source particles. A relativistic charged particle beam (usually electrons) is accelerated by a linear accelerator (linac). The source of the coherence is the so-called microbunching effect of the particle beam on the scale of the radiation wavelength, caused by the transmission of energy between the particles and the emitted photons. Consequently, comparing spontaneously emitted light from a particle beam traveling through an undulator to that emitted by an FEL one can see a significant enhancement. Short pulse lengths, high intensity, and brilliance combined with coherent photons make it a very attractive light source.

In the following, an FEL's working principle is briefly introduced. As undulators are key components for light production in FELS, this application provides the higher frame of reference for the undulator coils and their parameters investigated in this thesis. This introduction does not claim complete integrity. Full detailed backgrounds can be found in common literature, from where most of the derivations were performed [48, 13, 49, 50, 37].

2.2.1. Undulator trajectories

In the following, trajectories of relativistic charged particles and their synchrotron radiation emitted in planar and helical undulators are reviewed. The magnetic field, or magnetic flux density, of a planar undulator along the z-axis was introduced by equation (2.17) as

$$\vec{B}_{\mathrm{planar}}(z) = (B_x,\ B_y,\ B_z) = \left(0,\ B_{y,0} \sin(k_0 z),\ 0\right) , \quad \text{where } k_0 = \frac{2\pi}{\lambda_{\mathrm{u}}} . \qquad (2.62)$$

The magnetic field of a helical undulator along the z-axis is known from equations (2.19) and (2.20) and for this approach given with a phase difference of $\varphi = \pi/2$ as

$$\vec{B}_{\text{helical}}(z) = (B_x,\ B_y,\ B_z) = \big(-B_{x,0}\sin(k_0 z),\ B_{y,0}\cos(k_0 z),\ 0\big)\ . \tag{2.63}$$

When a charged particle with charge e moves with velocity $\vec{v}_{\text{e}}$ through an undulator, it is influenced by the Lorentz force $\vec{F}_{\text{L}}$ given as

$$\vec{F}_{\text{L}} = e\vec{v}_{\text{e}} \times \vec{B}\ . \tag{2.64}$$

Since the moving particle is commonly ultra-relativistic, relativistic factors with the speed of light c become

$$\beta = \frac{v_{\text{e}}}{c} \approx 1 \quad \text{and} \quad \gamma = \sqrt{\frac{1}{1-\beta^2}} \gg 1\ . \tag{2.65}$$

A planar undulator is considered to demonstrate the approach. With the above-shown relations, the relativistic equations of motion can be directly given as a pair of differential equations with the particle's rest mass $m_{\text{e},0}$ and the particle's energy γ, assuming an initial particle position at $x = y = 0$:

$$m_{\text{e},0}\gamma\ddot{x} = m_{\text{e},0}\gamma\frac{\mathrm{d}^2 x}{\mathrm{d}t^2} = -eB_{y,0}\sin(k_0 z)\dot{z}\ , \tag{2.66}$$

$$m_{\text{e},0}\gamma\ddot{z} = m_{\text{e},0}\gamma\frac{\mathrm{d}^2 z}{\mathrm{d}t^2} = eB_{y,0}\sin(k_0 z)\dot{x}\ . \tag{2.67}$$

Integrating equation (2.66) yields

$$\dot{x} = \frac{eB_{y,0}}{m_{\text{e},0}\gamma k_0}\cos(k_0 z)\ . \tag{2.68}$$

By means of equation (2.65), the constant particle velocity is given as

$$\beta^2 c^2 = \dot{x}^2 + \dot{z}^2 \tag{2.69}$$

$$\Rightarrow \dot{z} = \beta c\sqrt{1 - \frac{\dot{x}}{\beta^2 c^2}}\ . \tag{2.70}$$

Two scenarios are now considered: First, a trajectory with a rather small maximum deflection angle Ψ_0 is assumed for the transverse velocity $\dot{x}$, which can then be neglected as in equation (2.70) (weak undulator approximation). The general deflection angle is described by ξ. Therefore, the approximation $\dot{z} \approx \beta c$ can be made, yielding for the derivative of x with respect to z:

$$x'(z) = \xi = \frac{\mathrm{d}x(z)}{\mathrm{d}z}\bigg|_{K\ll 1} \approx \frac{eB_{y,0}}{\beta c m_{\text{e},0}\gamma k_0}\cos(k_0 z) = \frac{K}{\beta\gamma}\cos(k_0 z)\ . \tag{2.71}$$

Here, the undulator strength parameter K from the introduction chapter 1 recurs and is defined as

$$K = \frac{eB_{y,0}}{cm_{\text{e},0}k_0} = \frac{eB_{y,0}\lambda_{\text{u}}}{2\pi c m_{\text{e},0}}\ . \tag{2.72}$$

As already stated in the introduction, undulators with $K \leq 1$ are so-called weak undulators. This results in a Ψ_0 that is smaller than the opening angle of the synchrotron radiation cone, given by $1/\gamma$.

In the second scenario, $K > 1$ is assumed, thus a so-called strong undulator, and therefore a rather large maximum deflection angle Ψ_0 for the transverse velocity $\dot{x}$. Consequently,

the just neglected term in equation (2.70) becomes larger, thus more powerful, and yields then

$$x'(z) = \xi = \left.\frac{\mathrm{d}x(z)}{\mathrm{d}z}\right|_{K>1} = \frac{K\cos(k_0 z)}{\beta\gamma\sqrt{1 - \frac{K}{\beta^2\gamma^2}}} \ . \tag{2.73}$$

It can be shown, that for the strong undulator, the particle velocity is derived by a transformation of the longitudinal coordinates [49]. Here, the transformation goes back to the time t' in the co-moving system with the electron having the following longitudinal velocity:

$$\beta^* c = \beta c\left(1 - \frac{K^2}{4\beta^2\gamma^2}\right) \ . \tag{2.74}$$

The transformation then results in

$$\dot{x}(t') = \frac{cK}{\gamma}\cos(\Omega_\mathrm{p} t') \ , \tag{2.75}$$

$$\dot{z}(t') = \beta^* c - \frac{cK^2}{4\beta^2\gamma^2}\sin(2\Omega_\mathrm{p} t') \ , \tag{2.76}$$

with the oscillation frequency $\Omega_\mathrm{p} = \beta^* k_0 c$. This system of coupled differential equations can now be integrated and yields the **particle trajectory in a planar undulator**[1]:

$$\vec{R}_\mathrm{planar}(t') = \begin{pmatrix} \frac{K}{\beta\gamma k_0}\sin(\Omega_\mathrm{p} t') \\ 0 \\ \beta^* c t' + \frac{K^2}{8\beta^2\gamma^2 k_0}\cos(2\Omega_\mathrm{p} t') \end{pmatrix} \ . \tag{2.77}$$

This trajectory is seen as a figure-of-eight diagram in the co-moving frame due to the fact that the transverse oscillation in R_x has half the frequency compared to the longitudinal oscillation in R_z. Therefore, also terms of a higher order than the linear ones should be considered when calculating the radiation spectrum.

When considering now the magnetic field on the beam axis of an ideal bifilar helical undulator according to equation (2.63), an analog derivation as above can be performed finding the frequency $\Omega_\mathrm{h,v} = \beta_\mathrm{h}^* k_0 c = k_0 \beta c\sqrt{1 - K_v/(\beta^2\gamma^2)}$ with $v \in \{x, y\}$, and yields the **particle trajectory in a helical undulator** with :

$$\vec{R}_\mathrm{helical}(t') = \begin{pmatrix} \frac{K_x}{\beta_\mathrm{h}^*\gamma k_0}\cos(\Omega_\mathrm{h,x} t') \\ \frac{K_y}{\beta_\mathrm{h}^*\gamma k_0}\sin(\Omega_\mathrm{h,y} t') \\ \beta^* c t' \end{pmatrix} \ . \tag{2.78}$$

Note that this elliptical trajectory becomes circular for the specific case of $B_{x,0} = B_{y,0}$.

2.2.2. Undulator radiation

The derived particle trajectory inside an undulator together with general calculation approaches for synchrotron radiation, including the Liénard-Wiechert potentials, lead to the radiation field and can be found in common literature [44, 13, 49, 37]. A short overview of the main characteristics is given in the following.

Accelerating charged particles forces them to emit synchrotron radiation, which can be described as any electromagnetic radiation. Starting from Maxwell's equations it can be shown that a coupling of the electric field $\vec{E}$ and the magnetic field $\vec{B}$ exists:

$$\vec{B} = \frac{1}{c}(\vec{E} \times \vec{n}) \ , \tag{2.79}$$

---

[1]Terms of higher orders than $\left(\frac{K}{\beta\gamma k_0}\right)^2$ were neglected.

where $\vec{n}$ is the normalized vector in the direction of the observer. Consequently, energy can be transported through space, which is described via the Poynting vector $\vec{S}$, again for the observer, as

$$\vec{S} = \frac{1}{\mu c}(\vec{E} \times \vec{B}) = \frac{E^2 \cdot \vec{n}}{\mu c} = \frac{1}{R^2}\frac{\mathrm{d}^2 W}{\mathrm{d}\Omega \mathrm{d}t}\vec{n} \ , \tag{2.80}$$

with R being the distance between the point of emittance and the point of observation. The Poynting vector, therefore, describes the energy flux per time and per unit area, with the unit solid angle Ω.

The characteristics of undulator radiation can be calculated from the radiation term of the Liénard-Wiechert potentials

$$\vec{E}(t) = \frac{e}{4\pi c \epsilon_0} \left[\frac{\vec{n} \times \left((\vec{n} - \vec{\beta}) \times \dot{\vec{\beta}} \right)}{R \left(1 - \vec{n} \cdot \vec{\beta} \right)^3} \right]_{\mathrm{ret}} \ . \tag{2.81}$$

Inserting the derived equations from the previous subsection 2.2.1 leads to the radiation field which is proportional to the undulator flux density amplitude B_y, explaining the motivation for optimizing this parameter. Note that for the weak undulator, this is rather straightforward in contrast to the strong undulator. For the latter, the complex periodic motion cannot be described by a pure sinus, which makes the expansion of the radiation field $E(t)$ into a Fourier series necessary. Yet, the Fourier integrals after inserting the equations of motion would go beyond the scope of this chapter and can be found in the literature [49].

Taking the above-made derivations into account, the power P per solid angle can be found as

$$\frac{\mathrm{d}P}{\mathrm{d}\Omega} = \frac{R^2 |\vec{E}|^2}{\mu_0 c}(1 - \vec{n} \cdot \vec{\beta}) \ , \tag{2.82}$$

whereas the average angular power distribution over the undulator length L_{ID} is given as

$$\frac{\mathrm{d}^2 P}{\mathrm{d}\Omega \mathrm{d}\omega} = \frac{2R^2 |\vec{E}|^2}{\mu_0 L_{\mathrm{ID}}} \ . \tag{2.83}$$

Further, a summation of all harmonics and angles yields the total power of the strong undulator radiation in a vacuum, emitted by a single particle:

$$P_{\mathrm{tot,rad}} = \frac{2 r_0 c^3 e^2 \langle B \rangle^2 W_e^2}{3(m_{e,0} c^2)^3} \ , \tag{2.84}$$

with the classical electron radius $r_0 = e^2/(4\pi \epsilon_0 m_{e,0} c^2)$, where ϵ_0 is the vacuum permittivity and the particles Energy $W_e = m_{e,0} c^2 \gamma$. It is well visible that the power scales with $(m_{e,0} c^2)^{-4}$ for a given particle energy, which makes particles of greater rest mass m_0 not as efficient for the production of synchrotron light as lighter ones, such as electrons.

2.2.2.1. Photon wavelength

To generate coherent light, the conditions for interference have to be fulfilled. As shown in Figure 2.4, light interference of the same particle over one period is possible when the particle is one or more whole emitted wavelengths λ_γ behind. Here, the angle of photon emittance is θ for the trajectory derived in equation (2.71). As the wavefront moves with the speed of light c, it will have moved by $\lambda_\mathrm{u}/\beta_z^*$ while the particle needs a time of $\lambda_\mathrm{u}/(c\beta_z^*)$ for one period. Then the distance between the two wavefronts can be given as

$$d = \frac{\lambda_\mathrm{u}}{\beta_z^*} - \lambda_\mathrm{u} \cos(\theta) \ = m\lambda_\gamma \ , \qquad \text{with } m \in \mathbb{N}. \tag{2.85}$$
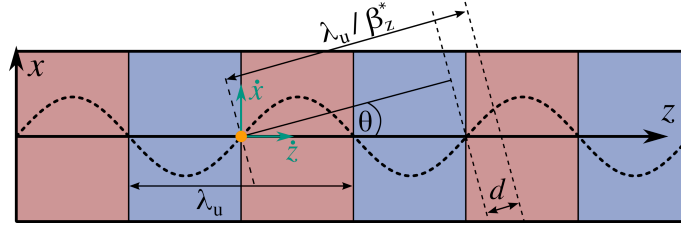
Figure 2.4.: Sketched trajectory of a charged particle within the field of an undulator with period length λ_u. The transverse and longitudinal velocities are marked with $\dot{x}$ and $\dot{z}$, respectively.

This can now be further approximated and expanded [13], leading to the **undulator equation for planar undulators**:

$$m\lambda_\gamma \approx \lambda_\mathrm{u}\left(1 + \frac{1}{2\gamma^2} + \frac{\lambda_\mathrm{u}K^2}{4\beta\gamma^2}\right) - \lambda_\mathrm{u}\cos(\theta) \ , \tag{2.86}$$

$$\Leftrightarrow$$

$$\lambda_\gamma = \frac{\lambda_\mathrm{u}}{2\gamma^2 \cdot m}\left(1 + \frac{K^2}{2} + \theta^2\gamma^2\right) \ , \tag{2.87}$$

Since all used approximations are very well fitting for small angles θ, the approximation is generally recognized as an equation.

When considering now the magnetic field on the beam axis of an ideal helical undulator according to equation (2.63), an analog derivation as above can be performed for small angles θ by defining $K_x(B_x)$ and $K_y(B_y)$ for each field component. This yields the **undulator equation for helical undulators**:

$$\lambda_\gamma = \frac{\lambda_\mathrm{u}}{2\gamma^2 \cdot m}\left(1 + \frac{K_x^2}{2} + \frac{K_y^2}{2} + \theta^2\gamma^2\right) \ . \tag{2.88}$$

Here, it is worth noticing that phase variation φ does not influence the emitted wavelength.

2.2.2.2. Photon flux distribution and brilliance

Generally, planar undulators produce linearly polarized radiation, whereas helical undulators produce circularly or elliptically polarized photons. The angular spectral power density as the basis for the photon flux can be further calculated from equation (2.83):

$$\frac{\mathrm{d}^2 P_m}{\mathrm{d}\Omega\mathrm{d}\omega} = \frac{3P_\mathrm{tot,rad}N_\mathrm{u}}{2\pi c k_0} \cdot A_m(K) \ , \tag{2.89}$$

where the central frequency was chosen to be $\Delta\omega = 0$. The function $A_m(K)$ is given with the Bessel functions J_i and for odd integers m as

$$A_m(K) = \frac{m^2 K^2}{\left(1 + \frac{1}{2}K^2\right)^2} \cdot \underbrace{\left[J_{\frac{m-1}{2}}\left(\frac{mK^2}{4 + 2K^2}\right) - J_{\frac{m+1}{2}}\left(\frac{mK^2}{4 + 2K^2}\right)\right]^2}_{:=JJ_m(\Xi)} \ . \tag{2.90}$$

Here and for a planar undulator is $\Xi = mK^2/(4 + 2K^2)$. Equation (2.90) is plotted in Figure 2.5, where saturation and accumulation of peaks can be seen for larger K parameters.

So far, only a single particle was considered. The more practical interest is the photon flux for a beam current I_b, representing I_b/e particles. Having derived the above equation, another conversion yields the **angular flux distribution of a planar undulator** by dividing by the energy of each photon, thus $\frac{h\omega}{2\pi}$ with the Planck constant h. The result can be given given by the number of photons N_photons per the unit solid angle Ω and in terms of a relative bandwidth $\mathrm{d}\omega/\omega$ as

$$\left.\frac{\mathrm{d}N_\mathrm{photons,planar}}{\mathrm{d}\Omega\,\mathrm{d}\omega/\omega}\right|_{\theta=0} = \frac{eN_\mathrm{u}^2\gamma^2}{2\epsilon_0 ch}\cdot I_\mathrm{b}\cdot\Lambda\left(\frac{N_\mathrm{u}\Delta\omega}{\omega_1}\right)\cdot A_m(K)\ ,\tag{2.91}$$

with the numbers of periods N_u, the Planck constant h, the beam current I_b. The function Λ, based on the so-called "lineshape function" $\omega = k\omega_1 + \Delta\omega$. Here, frequencies next to the harmonics are considered with

$$\Lambda\left(\frac{N_\mathrm{u}\Delta\omega}{\omega_1}\right) = \frac{\sin^2\left(\frac{N_\mathrm{u}\pi\Delta\omega}{\omega_1}\right)}{N^2\sin^2\left(\frac{N_\mathrm{u}\pi\Delta\omega}{\omega_1}\right)}\ .\tag{2.92}$$

From equation (2.91) one can derive the integrated flux of photons in the central cone with the fine structure constant $\alpha = \frac{e^2}{2ch\epsilon_0}$:

$$\dot{N}_\mathrm{photons,planar} = \alpha\pi N_\mathrm{u}\frac{I_\mathrm{b}}{e}\frac{\Delta\omega}{\omega}\left(\frac{1+\frac{K^2}{2}}{m}\right)A_m(K)\tag{2.93}$$

$$= 1.43\times10^{14}\ N_\mathrm{u}I_\mathrm{b}\left(\frac{1+\frac{K^2}{2}}{m}\right)A_m(K)\ .\tag{2.94}$$

The last line includes further simplifications and conversion in practical units of photons per second and per 0.1% bandwidth.

Similar as above, the **angular flux distribution of a helical undulator** with $\varphi = \pi/2$ can be given as

$$\left.\frac{\mathrm{d}N_\mathrm{photons,helical}}{\mathrm{d}\Omega\,\mathrm{d}\omega/\omega}\right|_{\theta=0} = \frac{eN_\mathrm{u}^2\gamma^2}{2\epsilon_0 ch}\cdot I_\mathrm{b}\cdot\Lambda\left(\frac{N_\mathrm{u}\Delta\omega}{\omega_1}\right)\cdot A_m(K_x,K_y)\ ,\tag{2.95}$$

Likewise, from equation (2.95) one can derive the integrated flux of photons in the central cone with the fine structure constant α as

$$\dot{N}_\mathrm{photons,helical} = \alpha\pi N_\mathrm{u}\frac{I_\mathrm{b}}{e}\frac{\Delta\omega}{\omega}\left(\frac{1+\frac{K_x^2}{2}+\frac{K_y^2}{2}}{m}\right)A_m(K_x,K_y)\ .\tag{2.96}$$

As stated earlier, the elliptical particle trajectory turns into a circular one for the common case of $B_{x,0} = B_{y,0}$. The arguments of the Bessel functions become zero as a result of $K_x = K_y = K$, which spares only J_0 in $A_m(K_x,K_y)$. J_0 can only be reached for $m = 1$, thus only the first harmonic exists in this case with a pure circular polarization.
With this note, equation (2.96) can be rewritten as

$$\dot{N}_\mathrm{photons,helical} = \alpha\pi N_\mathrm{u}\frac{I_\mathrm{b}}{e}\frac{\Delta\omega}{\omega}\left(\frac{1+K^2}{m}\right)A_m(K,K)\tag{2.97}$$

$$= 2.86\times10^{14}\ N_\mathrm{u}I_\mathrm{b}\left(\frac{K^2}{1+K^2}\right)\ .\tag{2.98}$$

The last line as above includes further simplifications and conversion in practical units of photons per second and per 0.1% bandwidth.
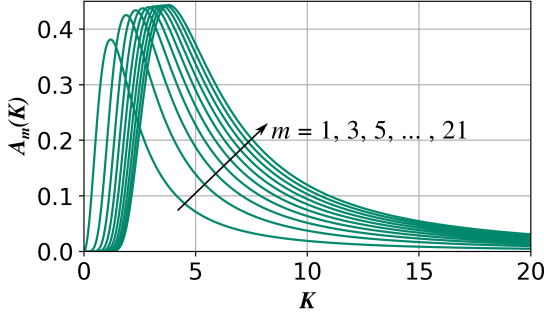
Figure 2.5.: Amplitude of the central brilliance function considering $\mathcal{B} \propto A_m(K)$ for typical K and m parameters.
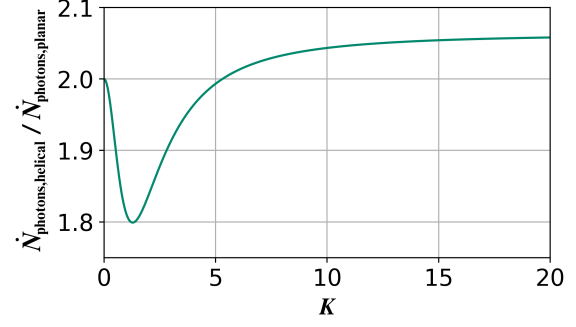
Figure 2.6.: Ratio between the produced photon flux of a planar and helical undulator $\dot{N}$ for typical K parameters ($m = 1$).

Here, it is worth noticing the similarities and differences between the planar and the helical case. An absolute variation can be detected when considering the first harmonic:

$$\left.\frac{\dot{N}_{\text{photons,helical}}}{\dot{N}_{\text{photons,planar}}}\right|_{m=1} = \frac{\left(1 + K^2\right) A_1(K, K)}{\left(1 + \frac{K^2}{2}\right) A_1(K)} \tag{2.99}$$

$$= \frac{2.86}{1.43} \frac{\left(\frac{K^2}{1+K^2}\right)}{\left(1 + \frac{K^2}{2}\right) A_1(K)} \quad > 1 \ . \tag{2.100}$$

Equation (2.99) is plotted in Figure 2.6 and demonstrates the superior efficiency of a helical undulator compared to a planar undulator in terms of photon production by a minimum factor of around 1.8.

Brilliance Earlier in the introduction, the brilliance was presented and already briefly described by equation (2.101). For an undulator in a known accelerator, the central brilliance $\mathcal{B}$ at angle $\theta = 0$ can be described via the photon flux $\dot{N}$ and the effective source sizes Σ_v and divergences $\Sigma_{v'}$ as follows [51, 13]:

$$\mathcal{B} = \frac{\dot{N}}{4\pi^2 \Sigma_x \Sigma_y \Sigma_{x'} \Sigma_{y'}} \ , \tag{2.101}$$

where $\Sigma_v = \sqrt{\sigma_v^2 + \sigma_r^2}$ and $\Sigma_{v'} = \sqrt{\sigma_v'^2 + \sigma_r'^2}$, with $v \in \{x, y\}$ and the source sizes and divergences of the beam σ_v and σ_v', plus the spatial source size σ_r with its divergence σ_r'. With the pulse duration σ_τ and the repetition frequency ν, the peak brilliance $\hat{\mathcal{B}}$ then equals

$$\hat{\mathcal{B}} = \frac{\mathcal{B}}{\sigma_\tau \nu} \ . \tag{2.102}$$

(a) Low-Gain FEL.   (b) High-Gain FEL.
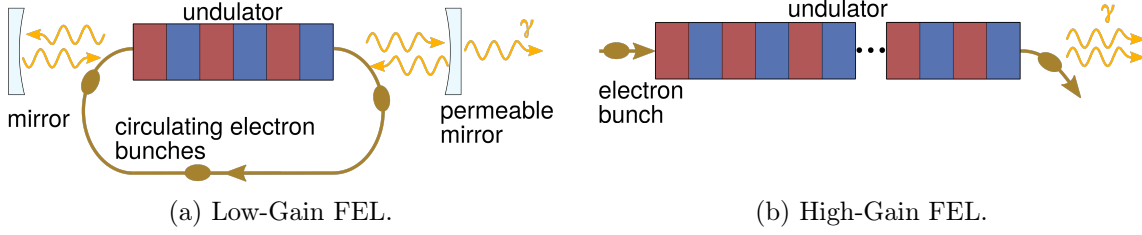
Figure 2.7.: Theory of operation sketched for a Low-Gain and a High-Gain FEL [50].

2.2.3. FEL radiation

Undulators are the key element for the production of free-electron laser (FEL) radiation. Figure 2.7 displays two different systems:

(a) The Low-Gain FEL produces radiation that can be collected by means of optical resonators, e.g. mirrors. This covers the infrared up to the visible spectrum. Multiple circulations of electron bunches produce the radiation, which undergoes only minor amplification.

(b) The High-Gain or SASE FEL produces radiation beyond the operation of optical resonators with a π-deflection. Therefore one passage through the undulator line must be sufficient, using Self-Amplified Spontaneous Emission (SASE). Here, the amplification is achieved by means of so-called microbunching, and photons of the ultraviolet (UV) up to the hard X-ray spectrum are emitted.

2.2.3.1. The Low-Gain FEL

The oscillating movement of electrons inside the undulator with its periodic transverse velocity component v_x enables the coupling to the electrical field of the photons. Therefore the particle is now considered to have the electron charge $-e$. The electro-magnetic wave is given with its electric field E

$$E_x(z,t) = E_0 \cos(k_\gamma z - \omega\gamma t + \varphi_0) \ , \quad \text{with } k_\gamma = \frac{\omega_\gamma}{c} = \frac{2\pi}{\lambda_\gamma} \ . \tag{2.103}$$

The energy change of an electron with respect to this E-field is given as

$$\frac{\mathrm{d}W}{\mathrm{d}t} = \frac{\mathrm{d}\,\gamma m_{\mathrm{e}} c^2}{\mathrm{d}t} = -e v_x(t) E_x(t) \ . \tag{2.104}$$

With the above-derived velocity in equation (2.75), this can be written for an electron as

$$\frac{\mathrm{d}W}{\mathrm{d}t} = -e \frac{cK}{\gamma} \cos(k_0 z) \cdot E_0 \cos(k_\gamma z - \omega_\gamma t + \varphi_0) \tag{2.105}$$

$$= \frac{cKeE_0}{2\gamma} \left[\cos(\mathcal{P}) + \cos(\chi)\right] \ , \tag{2.106}$$

with the ponderomotive phase $\mathcal{P}(t) \equiv (k_\gamma + k_0)z(t) - \omega_\gamma t + \varphi_0$
and $\chi(t) \equiv (k_\gamma - k_0)z(t) - \omega_\gamma t + \varphi_0$. Note that a constant $\mathcal{P}$, i.e. $\mathrm{d}\mathcal{P}(t)/\mathrm{d}t = 0$, leads to a continuous energy transfer, featuring the undulator equation (2.87). From here, the resonance electron energy $W_{\mathrm{r}} = \gamma_{\mathrm{r}} m_{\mathrm{e}} c^2$ can be defined further by rearranging the undulator equation:

$$\gamma_{\mathrm{r}} = \sqrt{\frac{\lambda_{\mathrm{u}}}{2\lambda_\gamma} \left(1 + \frac{K^2}{2}\right)} \ . \tag{2.107}$$

Electrons with this energy emit photons with λ_γ and have a constant ponderomotive phase. Assuming now a particle energy W gives the relative energy deviation:

$$\eta = \frac{W - W_{\rm r}}{W_{\rm r}} = \frac{\gamma - \gamma_{\rm r}}{\gamma_{\rm r}} \quad \text{for } |\eta| \ll 1 \ . \tag{2.108}$$

For the Low-Gain case, the coupling between the ponderomotive phase and the relative energy deviation can now be described as

$$\frac{\mathrm{d}\mathcal{P}}{\mathrm{d}t} = 2k_0 c\eta \ , \quad \text{with } \frac{\mathrm{d}\eta}{\mathrm{d}t} = -\frac{eE_0 K}{2m_{\rm e} c\gamma_{\rm r}^2} \cos(\mathcal{P}) \ , \tag{2.109}$$

which are known as the FEL pendulum equations. As the intensity in the Low-Gain FEL increases over time, it is generally considered that the light wave's field amplitudes gets larger linearly with time as $I_\gamma(t) \approx I_{0,\gamma}(1 + 2\delta \cdot t_{\rm u})$, where δ is a small quantity ($\delta t_{\rm u} \ll 1$, with an electron's travel time through the undulator $t_{\rm u}$). Therefore, the FEL gain function G in the Low-Gain regime is given as the E-field's relative energy growth per passage of the undulator, known as the Madey theorem:

$$G_{\rm LG}(\eta) = \frac{\Delta W_\gamma}{W_\gamma} = -\frac{\pi e^2 \hat{K}^2 N_{\rm u}^2 \lambda_{\rm u}^2 n_{\rm e}}{4\eta_0 m_{\rm e} c^2 \gamma_{\rm r}^3} \frac{\mathrm{d}}{\mathrm{d}\xi}\left(\frac{\sin^2(\xi)}{\xi^2}\right) \ , \tag{2.110}$$

with the particle density $n_{\rm e}$, the number of undulator periods $N_{\rm u}$, the dimensionless variable $\xi = 2\pi N_{\rm u}\eta$, and the modified undulator parameter $\hat{K}$ with the Bessel functions J_i as

$$\hat{K} = K \cdot JJ_1\left(\frac{K^2}{4 + 2K^2}\right) \ . \tag{2.111}$$

For a helical undulator, K can be utilized for both gain cases as there is no longitudinal oscillation. Note that the function $JJ_m(\frac{K^2}{4+2K^2})$ already appeared in equation (2.90), the amplitude function A_m above, which shows the common origin of a planar undulator.

2.2.3.2. The High-Gain FEL

The commonly considered 1D-High-Gain theory is briefly summarized in the following. Therefore, the E-field from equation (2.103) is now written in its complex and marked with a tilde for simplifying the mathematics with respect to complex quantities:

$$\tilde{E}_x(z,t) = \tilde{E}_x(z)\mathrm{e}^{i(k_\gamma z - \omega_\gamma t)} \ , \tag{2.112}$$

where now also the field amplitude is considered to be a function of z (cf. low-gain FEL). Additionally, an electric charge density ρ and the consequential current density j are assumed for the bunch with an infinite spread:

$$\rho(\mathcal{P}, z) = \rho_0 + \tilde{\rho}_1(z)\mathrm{e}^{i\mathcal{P}} \ , \tag{2.113}$$

$$j(\mathcal{P}, z) = j_0 + \tilde{j}_1(z)\mathrm{e}^{i\mathcal{P}} \ , \tag{2.114}$$

where the real part defines the real charge density and the modulation of the charge density $\tilde{\rho}_1(z)\mathrm{e}^{i\mathcal{P}}$ is assumed to be initially small. Further, the oscillation in the longitudinal direction is neglected here and the motion in the longitudinal direction is therefore described as a uniform movement with average drift velocity $\bar{\beta}$,

$$z(t) = \bar{v}_z t = \bar{\beta}ct = \left[1 - \frac{1}{2\gamma^2}\left(1 + \frac{K^2}{2}\right)\right] \ , \tag{2.115}$$

ignoring higher harmonics, but using the modified undulator parameter $\hat{K}$ from equation (2.111) when needed. The coupling between the E-field and the charge density can be described by the inhomogeneous wave equation

$$\left[\nabla^2 - \frac{1}{c^2} \frac{\partial^2}{\partial t^2} \right] \vec{E} = \mu_0 \frac{\partial \vec{j}}{\partial t} + \frac{1}{\epsilon_0} \nabla \rho \; , \tag{2.116}$$

where ∇ becomes $\partial/\partial x$ in this case. As the last derivative of $\nabla \rho$ is much smaller than the first term, it is insignificant in the 3D theory and vanishes in the 1D theory [50]. The z-dependent amplitude of the E-field is used to apply the so-called "slowly varying amplitude" approximation to receive the coupling between E-field and the charge density

$$\frac{\mathrm{d}\tilde{E}_x}{\mathrm{d}z} = -\frac{\mu_0 c \hat{K}}{4\gamma} \cdot \tilde{j}_1 \; , \tag{2.117}$$

which can be seen as laser amplification. The modulation of the charge distribution caused by the interaction with the electromagnetic field of the radiation induces a modulated longitudinal electrical field, which counteracts the microbunching (see the below paragraph) and has the amplitude of

$$\tilde{E}_z(z) \approx \frac{i}{\epsilon_0 k_\gamma \tilde{\rho}_1(z)} \; . \tag{2.118}$$

The last two equations can now be combined in order to find the longitudinal field in relation to the derivative of the transverse field:

$$\tilde{E}_z = i \frac{4\gamma c}{\omega_\gamma K} \cdot \frac{\mathrm{d}\tilde{E}_x}{\mathrm{d}z} \; . \tag{2.119}$$

The coupling further reforms the energy-transfer to $\frac{\mathrm{d}\eta}{\mathrm{d}t} = \frac{-e E_0 \hat{K}}{2m_\mathrm{e} c \gamma_\mathrm{r}^2} \cos(\mathcal{P})$. Now a reformulation of the pendulum equations, known from the low-gain FEL in equation (2.109), is possible by replacing the time t by the longitudinal coordinate z according to $z(t) = \bar{\beta} ct$, with $\bar{\beta} \approx 1$:

$$\frac{\mathrm{d}\mathcal{P}}{\mathrm{d}z} = 2k_0 \eta \; , \quad \text{with } \frac{\mathrm{d}\eta}{\mathrm{d}z} = -\frac{e E_0 \hat{K}}{2m_\mathrm{e} c^2 \gamma_\mathrm{r}^2} \cos(\mathcal{P}) \; . \tag{2.120}$$

For the second pendulum equation, the electric field amplitude of the light wave has now to be treated with the z-dependence. Furthermore, the energy change due to the interaction between the electron and the space charge field has to be taken into account. To further treat these two counteracting behaviors, it is now required to take the real part of this equation as the relative energy deviation is always a real quantity:

$$\frac{\mathrm{d}\eta}{\mathrm{d}z} = -\frac{e}{m_\mathrm{e} c^2 \gamma_\mathrm{r}} \mathrm{Re}\left[\left(\frac{\hat{K}\tilde{E}_x}{2\gamma_r} + \tilde{E}_z \right) \right] e^{i\mathcal{P}} \; . \tag{2.121}$$

In summary, it was shown that the amplification process in an FEL is clearly a many-particle effect. Assuming a monoenergetic particle beam with energy W, this can all be summarized in the Third-Order Equation of the high-gain FEL as:

$$\frac{\hat{E}_x'''}{\Gamma^2} + 2i \frac{\eta}{\rho_\mathrm{FEL}} \frac{\hat{E}_x''}{\Gamma^2} + \left[\frac{k_\mathrm{p}^2}{\Gamma^2} - \left(\frac{\eta}{\rho_\mathrm{FEL}} \right)^2 \right] \frac{\hat{E}_x'}{\Gamma} - i\tilde{E}_x = 0 \; . \tag{2.122}$$

Here, the important FEL measures are the gain parameter $\Gamma = \sqrt[3]{\frac{\mu_0 \hat{K}^2 e^2 k_0^2 n_\mathrm{e}}{4\gamma_\mathrm{r} m_\mathrm{e}}}$,

the FEL or Pierce parameter $\rho_\mathrm{FEL} = \frac{\Gamma}{2k_0}$, and

the space charge parameter $k_\mathrm{p} = \frac{\omega_\mathrm{p}^*}{c} \sqrt{\frac{2\lambda_\gamma}{\lambda_\mathrm{u}}}$ with the plasma frequency $\omega_\mathrm{p}^* = \sqrt{\frac{n_\mathrm{e} e^2}{\gamma_\mathrm{r} \epsilon_0 m_\mathrm{e}}}$.
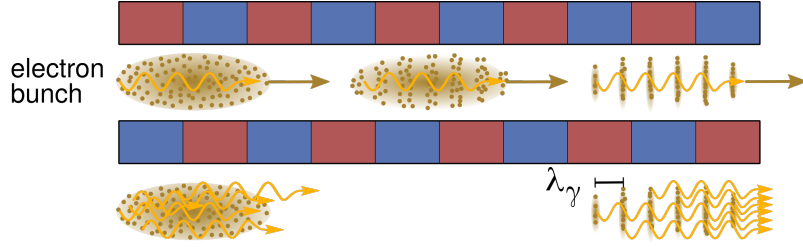
Figure 2.8.: The principle of microbunching. Interaction and exchange of energy, depending on the particle's longitudinal position modulate the bunch density into multiple microbunches, located at a distance of the emitted radiation wavelength λ_γ.

Equation (2.122) can be solved with the approach $\tilde{E}_x(z) = Ae^{\alpha z}$. If the particles' energy is equal to the resonance energy, thus $\eta = 0$, and the space charge density $k_{\mathrm{p}} = 0$ is neglected, the following solution can be found:

$$\tilde{E}_x \propto \mathrm{e}^{\frac{z}{L_g}} \;, \quad \text{with the gain length } L_{\mathrm{g}} \equiv \frac{1}{\sqrt{3}\Gamma} \approx \frac{\lambda_{\mathrm{u}}}{4\pi\sqrt{3}\rho_{\mathrm{FEL}}} \left(1 + \frac{\sigma_\delta^2}{\rho_{\mathrm{FEL}}^2}\right) \;. \qquad (2.123)$$

As noted, the relative rms energy spread σ_δ allows a more practical description of an FEL with respect to the undulator design parameters, with the Alfvén current $I_{\mathrm{A}} \approx 17\,\mathrm{kA}$ and the beam peak current I_{b} [52]:

$$\sigma_\delta = \frac{\sigma_\gamma}{\gamma_0} \ll \rho_{\mathrm{FEL}} = \sqrt[3]{\frac{I_{\mathrm{b}} K^2 J J_1 \left(\frac{K^2}{4+2K^2}\right)^2}{16 I_{\mathrm{A}} \gamma_0^3 \sigma_x^2 k_0^2}} \qquad (2.124)$$

Finally, the FEL gain function G in the High-Gain regime is given as for the relative energy deviation and the position in the undulator (cf. equation (2.110)):

$$G_{\mathrm{HG}}(\eta) = \left(\frac{\tilde{E}_x(\eta, z)}{E_{\mathrm{in}}}\right)^2 - 1 \;, \quad \text{with } E_{\mathrm{in}} = \tilde{E}_x(0) \;. \qquad (2.125)$$

Microbunching   In an FEL, the linac provides the acceleration of particle bunches, which are guided through the undulator lines. The particles' trajectory inside the undulators was already introduced and derived from the provided magnetic field. As a consequence of deflective acceleration, the particles start to radiate synchrotron radiation but also interact with the emitted photons as it was shown in the preceding paragraph. The entire principle is sketched in Figure 2.8. This complex interaction and exchange of energy can briefly be summarized as processes of energy gain or loss depending on their longitudinal position. Studying the phase space in this background, taking the growth of the field amplitude of the light wave $\tilde{E}_x$ as well as the evolution of the space charge field $\tilde{E}_z$ particularly into account as in equation (2.121), leads to the following observation: as a result, the particle bunch density is modulated into multiple periodic disks, the so-called microbunches, located at a distance of the emitted radiation wavelength λ_γ. These microbunches have a smaller longitudinal spread than λ_γ and particles in these microbunches emit coherent radiation. The fixed phase relation of the microbunches causes a coherent and maximum amplification of the microbunches' emitted radiation with λ_γ. Consequently, the energy amplification increases until a saturation limit is reached for fully established microbunching. This saturation can be approximated with the beam power $P_{\mathrm{beam}} = (\gamma_{\mathrm{r}} m_{\mathrm{e},0} c^2 I_0)/e$ as

$$P_{\mathrm{sat}} \approx \frac{4}{3}\rho_{\mathrm{FEL}} P_{\mathrm{beam}} \;. \qquad (2.126)$$

Table 2.1.: Selected superconductors and important properties. [54, 55, 56, 57, 58, 59, 60].

Material	Critical Temperature T_c / K	Critical B-Field B_i / T		
		Type-I		
Ga	1.1	$B_c =$	0.006	
In	3.4	$B_c =$	0.03	
Sn	3.7	$B_c =$	0.03	
		Type-II		
Nb-Ti	9.6	$B_{c2} =$	14.5	
Nb_3Sn	18.1	$B_{c2} =$	25	
MgB_2	39	$B_{c2} =$	74	
		High-temperature superconductors		
$Bi_2Sr_2CaCu_2O_8$ (BSCCO-2212)	90	$B_{c2\parallel} > 250,$		$B_{c2\perp} > 60$
$YBa_2Cu_3O_7$ (YBCO)	92	$B_{c2\parallel} > 240,$		$B_{c2\perp} = 110$

2.3. Applied superconductivity

In 1911, a group around H. Kamerlingh Onnes discovered at the University of Leiden that mercury suddenly had a non-measurably small resistivity below 4.2 K, thus the phenomenon of superconductivity was revealed [53]. Since then, many other materials across metals, compounds, and metallic alloys showed the same superconducting characteristic of having a zero resistivity below an individual critical temperature T_c. A few important superconductors are listed in Table 2.1. The theory of superconductivity and its application can be found in detail in the literature [61, 62, 55, 63]. This subsection will give a brief introduction to the most relevant aspects for this work.

All superconductors have in common to conduct high current densities without any resistance. Nevertheless, the superconducting materials may be split into type-I and type-II superconductors. The group of type-I superconductors generally covers elements like mercury, gallium, indium, and tin. In their superconducting state, the magnetic field is expelled up to their critical field B_c, with leaving only a thin layer of surface shielding currents. This effect is called the Meissner-Ochsenfeld effect [64], and the superconducting state of type-I superconductors is named the Meissner phase. Above B_c, type-I superconductors become normal conducting as displayed in Figure 2.9a for the magnetization M, which is the magnetic moment per unit volume.

Compounds and alloys such as Niobium-Titanium (Nb-Ti), Niobium-Tin (Nb_3Sn), and rare-earth barium copper oxides (*rare-earth* $Ba_2Cu_3O_{7-\delta}$, short: *Re*BCO) are commonly found in the group of type-II superconductors. This group, including the named examples, is widely used for building superconducting magnets and features two critical fields: B_{c1} and B_{c2}, with typically $B_{c1} < B_{c2}$. For fields below B_{c1}, superconductors of type-II have an identical behavior as those of type-I (see Figure 2.9b). However, above B_{c1} the so-called Shubnikov phase starts for low-temperature superconductors, where the field penetrates the superconductor through quantized vortices, so-called fluxoids, each causing screening currents in its direct environment. Vortices may be (actively) fixed on well-defined structures such as micro-structural defects in the superconductor, which is known as flux pinning. Likewise, high-temperature superconductors are penetrated by fluxoids above B_{c1}, where the so-called vortex glass or lattice starts as sketched in Figure 2.9d. Here, thermal fluctuations may directly enhance vortex density fluctuations while pinning disorders tend to minimize such fluctuations, yet, keeping the material in a superconducting-mixed state

[65]. With increasing operating temperature, thermal fluctuations prevail and cause a flux-liquid. This limit is described by the so-called "irreversibility line".

The Lorentz force will also finally act on the vortices, as soon as a current is applied to the superconductor within a perpendicular magnetic field to the direction of the current. The location of the vortices next to the micro-structural defects is yet energetically favorable as they are held in place with a pinning force. The state where the pinning force compensates the Lorentz force exactly in value represents the state of the critical current density J_c. However, the vortices are forced to move when the Lorentz force exceeds the pinning force. As a result, resistance is caused for the current flow which usually ends the superconducting state. For ideal type-II superconductors, this happens as soon as $B > B_{c1}$ as no pinning forces exist.

By means of the three introduced parameters T_c, B_c, and J_c, a critical surface in the (T, B, J) parameter space can be described for each superconductor. The superconducting state of a material can be found on or below this surface. Figure 2.10 sketches the critical surfaces of Nb-Ti, Nb_3Sn, and YBCO. These surfaces can be described by semi-empiric scaling laws, stored in appendix B. Furthermore, the superconductive characteristics depend on external operating conditions such as radiation load, strain, and magnetic field orientation (for ReBCO) [66, 67].

2.3.1. LTS and HTS

When considering type-II superconductors, a general classification into low-temperature superconductors (LTS) and high-temperature superconductors (HTS) can be found. Here, the boiling temperature of liquid nitrogen (LN_2, $T_{LN_2} = 77\,K$) is used to divide the materials into the two groups with respect to their T_c (see also Table 2.1). Figure 2.11 gives an overview of state-of-the-art superconductors and their parameters. This thesis focuses on HTS, more specifically on coated ReBCO tapes. However, comparisons to the state-of-the-art LTS technology for superconducting undulators, Nb-Ti, are done.

Low-temperature superconductors Nb-Ti is a ductile material that is commonly implemented in the form of multifilamentary twisted wires, forming strands. The length of these strands can be produced in the order of several kilometers. One of the well-known applications of Nb-Ti is its utilization for the LHC main bending dipole magnets. Here, fully-transposed cables, so-called Rutherford cables, were used to reduce losses due to eddy currents and increase mechanical stability. As the practical critical limit of Nb-Ti is reached between 9 and 10 T at 1.9 K, other materials have to proceed to tackle the challenges of the next high-energy accelerators. Today, Nb_3Sn is the most promising candidate to reach maturity for its application in accelerator magnets. However, this brittle material needs a relatively complex treatment, called wind-and-react, when being applied to superconducting magnets. Different filaments of Nb and Sn have to be separated in an initial step during winding before a reaction at up to over 900 K and over multiple hours is needed to produce finally the superconductor Nb_3Sn [71]. Afterward, the brittle superconductor has to be protected, e.g. by an epoxy resin impregnation. Nevertheless, for the next generation of accelerator magnets at CERN, bending dipole magnets based on Nb_3Sn are foreseen to be implemented in the FCC, with a target field of up to 16 T [72].

High-temperature superconductors High-temperature superconductors are crucial when aiming for magnetic fields of 20 T and beyond, as well as for high fields in short-period undulators. HTS not only show a relatively high $T_c > T_{LN_2}$, but also superconducting states in rather high fields and for high currents at low temperatures. The latter is especially
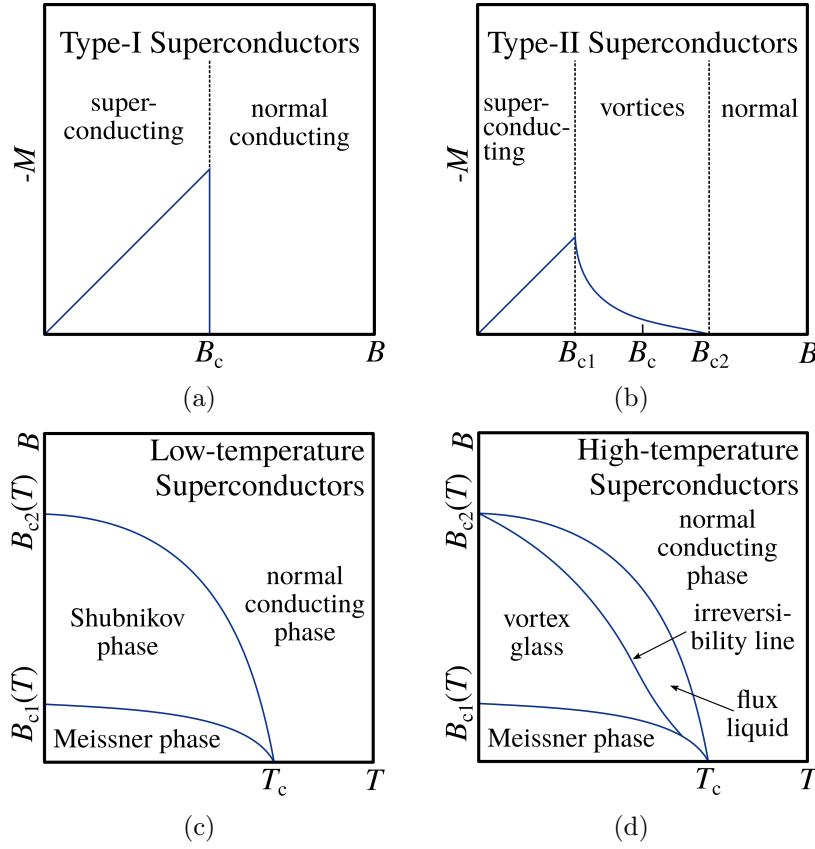
Figure 2.9.: Superconductors of type-I and II. The upper graphs show the magnetization M over the magnetic field B. Lower graphs show B over the temperature T. (a) Type-I superconductors' M drops to zero after the critical field B_c is reached. Below B_c, the Meissner phase excludes the magnetic flux from the superconductor. (b) Type-II superconductors' M decreases steadily to zero after having reached B_{c1}. Below B_{c1}, the Meissner phase is present. Between B_{c1} and B_{c2}, vortices penetrate the material on fixed positions but keep the superconducting state. After B_{c2} the vortices will move and thus transition the material to the normal phase. (c) Magnetic field over temperature for low-temperature superconductors. (d) Magnetic field over temperature for high-temperature superconductors as described in section 2.3. Graphs adapted from [65, 55].
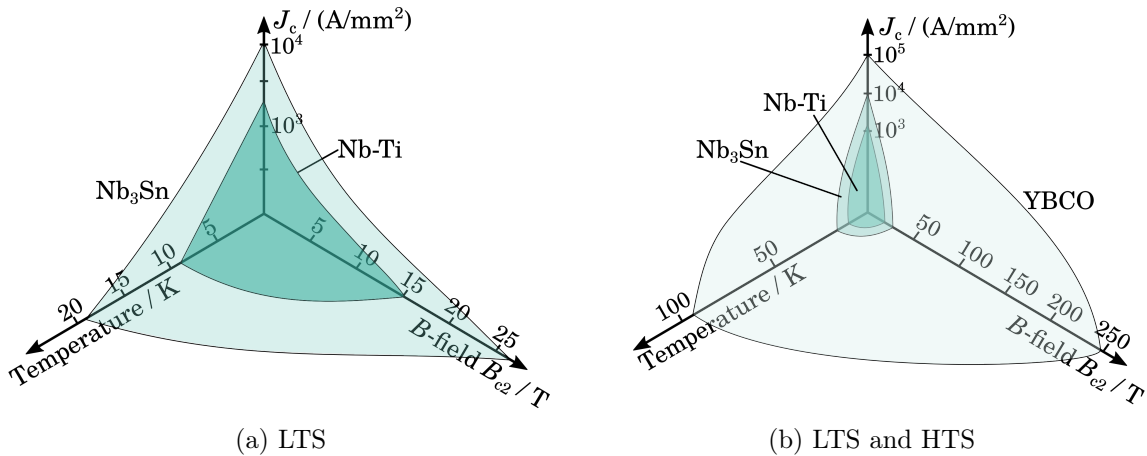
Figure 2.10.: Critical current density surfaces of different superconductors: Nb-Ti, Nb$_3$Sn, and YBCO, as example of *Re*BCO. Plots inspired by [68, 69].
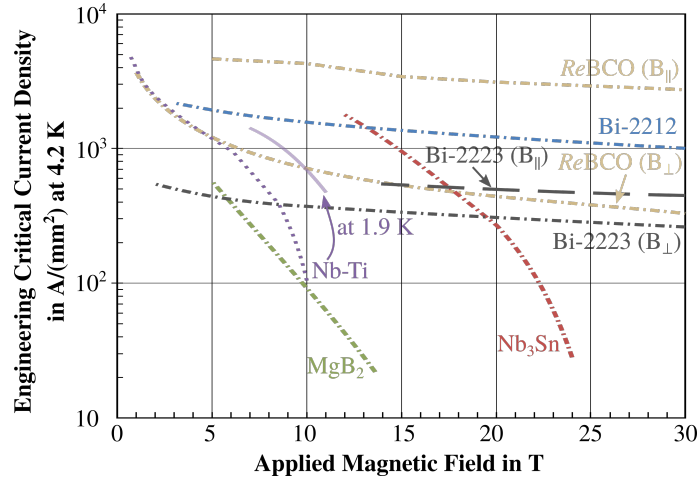
Figure 2.11.: Different state-of-the-art superconductors and their critical engineering current density. Plot adapted from [70].

crucial for short periodic structures as high field gradients are common over the conductor pack. Therefore, this thesis investigated their application to undulators. As Figure 2.9d displays, HTS have so-called irreversible fields, smaller than critical fields, for which the vortices with their fluxoids are moving due to the Lorentz force. A voltage is introduced over the conductor as a result and therefore limits the material at this point for its application to superconducting magnets. Further constraints in HTS are given by the presence of grain boundaries. Only very small misalignment is tolerated when producing high-current carrying films, which limits the feasible conductor lengths [55].

Nevertheless, for the application in superconducting magnets, there are currently two HTS materials sufficiently mature [73]: Bismuth strontium calcium copper oxide (BSCCO) and rare-earth barium copper oxide (*Re*BCO). Both have critical temperatures above $90\,\mathrm{K}$ and critical fields B_{c2} well above $100\,\mathrm{T}$ [74]. BSCCO-2212 is nowadays available as round wires, whereas *Re*BCO is commercially sold as coated tape superconductor. However, to achieve a consistently high critical current density, BSCCO-2212 requires a quite complex various-stage heat treatment, comparable to $\mathrm{Nb_3Sn}$ [75]. Another drawback is the silver-made matrix to hold the filaments, which is necessary for the treatment but also keeps the conductor cost at a stable high level due to the price of silver. Therefore, *Re*BCO was chosen to be investigated within the scope of this thesis with the focus on solving the challenges related to its application as coated superconducting tape to short-period undulator coils in order to achieve magnetic field amplitudes in the order of $1.5\,\mathrm{T}$ and beyond.

2.3.2. Coated *Re*BCO superconductors

Superconducting compounds from rare-earth elements combined with barium copper oxides were first discovered in 1987 with the element yttrium as $\mathrm{YBa_2Cu_3O_{7-\delta}}$ (YBCO), having a critical temperature of $T_c = 93\,\mathrm{K}$ and an upper critical field limit of $B_{c2} = 168 \pm 26\,\mathrm{T}$ [76, 74]. Nowadays, gadolinium is also widely used, but other rare-earth elements are possible as well without influencing the superconducting properties significantly, creating the generic term "*Re*BCO".

*Re*BCO superconductors are commercially available as so-called coated conductors, where a thin superconducting film is deposited on a carrier inside a tape. Figure 2.12 shows a sketch of a coated *Re*BCO superconducting tape. Besides *Re*BCO, the multilayered tape consists of a substrate, Hastelloy (C-276) or stainless steel, which acts as thin film growth and pro-
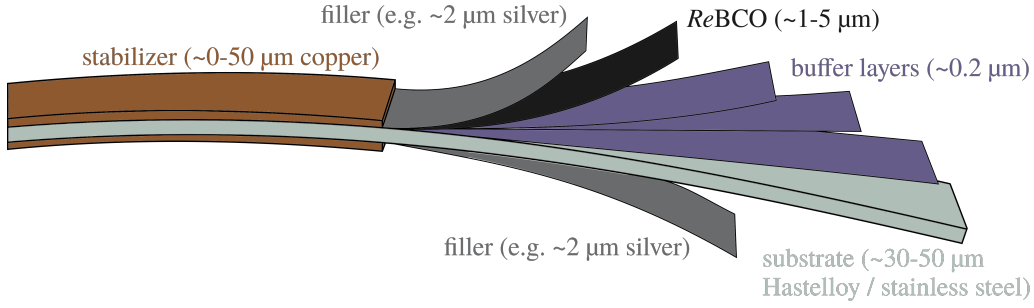
Figure 2.12.: Cut through a coated *Re*BCO superconductor tape with several layers and
their typical order of thickness. Hastelloy (or stainless steel) serves as the
substrate for mechanical stability. Copper is used as the main stabilizer for
thermal and conductive stability, but can be reduced down to 0 μm. Copper
and silver are commonly coated around the other layers. Adapted sketch [69].
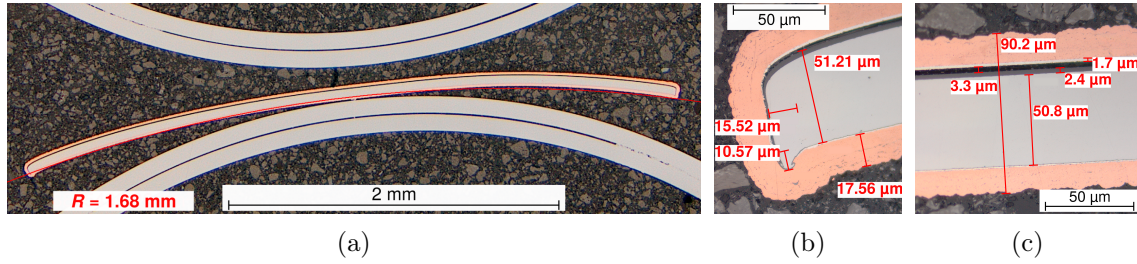
Figure 2.13.: Polished cross-sections of a coated *Re*BCO superconducting tape from Bruker
with several layers under the optical microscope. (a) Due to the production
process, the tape may be bent along its width. (b) Mechanical cutting and
electroplating of copper may result in a so-called dog bone, where the tape
edges are thicker than the center. (c) Different layers and their measured
thicknesses.

vides mechanical robustness. Extremely fine buffer layers are used to support the epitaxial
growth of the few micrometers thick *Re*BCO crystallites on top of the substrate. This stack
is covered in a thin silver sleeve to prevent the *Re*BCO layer to undergo chemical reactions
with the copper, which is coated around it. Compared to other materials such as Nb_3Sn
or BSCCO-2212, no further complex treatments are necessary. Superconducting *Re*BCO
tapes are typically ready-for-use and provide extremely high current densities as displayed
in Figures 2.11 and 2.10. Additionally, *Re*BCO as a material is not the cost-driving factor
leaving the potential to bring the prices down due to mass production. Currently, mainly
the fusion research, for example, the International Thermonuclear Experimental Reactor
(ITER) and power applications drive the market to lower prices with their high need for
HTS.

Due to the tape manufacturing process, the tapes may have so-called dog boning effects
or have a transverse curvature as seen in Figure 2.13. The dog boning effect describes the
fact that the tape edges are thicker than its center and is usually caused by mechanical
cutting and/or electroplating of copper, as it is common for tape manufacturers to produce
tapes with a width of 12 mm and further cut it down to smaller widths. To counteract
this misalignment in the geometries, optical tape slitting by means of laser cutting was
introduced to limit this and potential mechanical damage. The transverse curvature is a
result of Bruker's manufacturing technique and was only seen here.
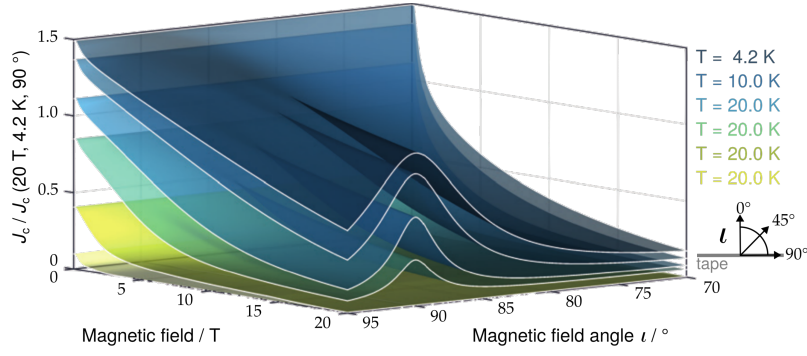
Figure 2.14.: *Re*BCO coated conductor J_c surfaces. Normalized critical current density over the magnetic field and field angle (sketched on the right) for different temperatures. Plot adapted from [69].

2.3.2.1. The critical surface of *Re*BCO

The critical surface of *Re*BCO was already introduced above. It clearly differs from any LTS material, especially in terms of the in-field behavior. Additionally to the boundary conditions temperature, current, and B-field dependencies, one can observe that the magnetic field angle ι with respect to the *Re*BCO tape's plane has a significant influence, as presented in Figures 2.14 and 2.15 for multiple temperatures. Therefore, the critical current density is described by three parameters as $J_c(B, T, \iota)$. The critical current drops rapidly for other configurations than the parallel orientation, coming to a minimum around the perpendicular arrangement and becoming even more distinct when higher magnetic fields are applied. Then, the discrepancy in critical current measured in parallel or perpendicular magnetic field directions may vary by more than 50% [77].

The reason for this anisotropic behavior can be found in *Re*BCO's crystalline structure. The unit cell of YBCO is shown in Figure 2.16. In epitaxial growth, the highlighted crystallographic planes are aligned parallel to the band surface. The yellow sketched barium (Ba) atoms sit in the center of the planes as well as the magenta yttrium (Y). Copper (Cu) and oxygen (O) are drawn in brown and blue, respectively. Here, the CuO_2 planes contribute the most to the superconducting state. When a magnetic field is applied with a perpendicular direction through these planes, thus parallel to the planes' normal vector, the induced screening currents circulate within each plane resulting in a relatively weak flux pinning as no current is forced through the crystallographic planes' boundaries [78]. This differs for magnetic fields with parallel orientation to the *Re*BCO's plane, where the field penetrates in between the CuO_2 planes with a vortex size much larger than the plane's distance, thus not harming the superconducting state. Consequently, *Re*BCO superconducting tapes can tolerate parallel fields well whereas perpendicular magnetic fields have a heavy impact.

Lately, flux pinning techniques advanced more and more making this anisotropy less relevant. Engineering current densities of over $2\,\mathrm{kA/mm^2}$ were reached at $4.2\,\mathrm{K}$ and $20\,\mathrm{T}$ and also for higher temperatures such as $20\,\mathrm{K}$ and $20\,\mathrm{T}$ promising values above $1\,\mathrm{kA/mm^2}$ showed the great potential of coated *Re*BCO tapes [79].

2.3.2.2. Types of *Re*BCO cables: Roeble, CORC, (twisted) stack

High operating currents are preferred to be transported by a compact conductor cable alignment in superconducting magnets. This allows for keeping the current density high as well as the magnet's inductance smaller and thus makes faster ramping rates for driving the current feasible. Keeping the inductance small is particularly important for ramping
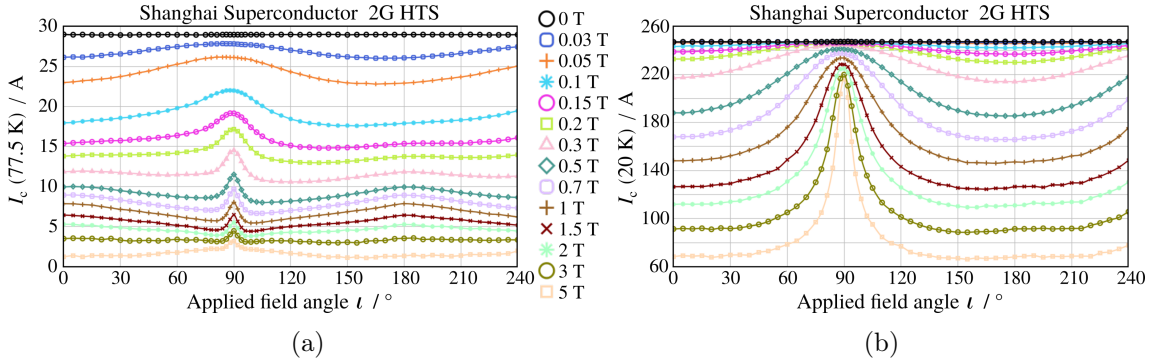
Figure 2.15.: Angular anisotropy and B-field dependency of a state-of-the-art coated ReBCO superconductor at (a) 77.5 K and (b) 20 K. Data and plots reproduced from [80].
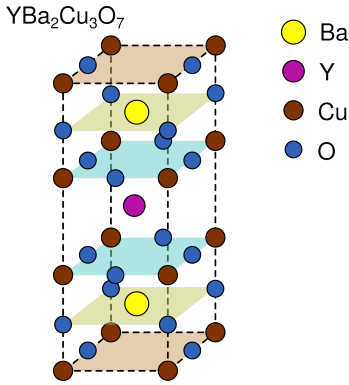
Figure 2.16.: Unit cell of YBCO - a ReBCO crystal structure. Different atoms are displayed by individual color and size. Planes are indicated by rectangles and represent the universal crystalline structure of a ReBCO, e.g. top and bottom CuO chains and the two center CuO_2 planes.

the field up as well as ramping the magnet down in cases of malfunction, e.g. a quench (see section 2.4.1). This is commonly achieved by combining multiple superconductors into a cable. As the commonly used, fully transposed Rutherford cables are not suitable for tape-shaped conductors, new geometries had to be developed. Figure 2.17 gives an overview of possible geometries of ReBCO cables based on coated tapes: Stacks of tapes, or a twisted stack, Roebel, and CORC are the most prominent examples.

The most straightforward approaches are stacks or twisted stacks of tapes, providing also the basis for more complex cable types [81, 82]. The high packing fraction, thus a high filling factor, and relatively simple construction without harming the superconductor make it an attractive and cost-efficient choice. Further, a twisted stack can provide transposition in order to reduce losses. However, a cable of stacked tapes can preferably bend in the soft-way direction, meaning around the transverse axis, whereas hard-way bending along the tape's longitudinal axis is problematic.

A variation of the tape stack is the so-called Roebel cable, providing a slightly smaller filling factor. This design dates back to 1913 when it was created to reduce AC losses in copper power bus-bars and was transferred to tape superconductors almost 100 years later at KIT in Germany [83, 84]. The Roebel cable consists of a stack of punched tapes orientated and folded together in a meandering way. With this technique, a full tape transposition is possible, however, the superconductor gets mechanically harmed and a lot of material is wasted. Nevertheless, their potential was demonstrated by transporting currents over 10 kA in 10 T magnetic fields at 4.5 K [85]. Consequently, Roebel cables were used to manufacture the full HTS Feather-M2 magnet at CERN [69].

A popular third option is the so-called CORC (Cable On Round Core) cables, which are based on a round copper core, providing bending as for round LTS cables [86, 87, 88]. The superconducting tapes are wound around the core in several layers, providing partial transposition but reducing the filling factor significantly. Still, transport current densities
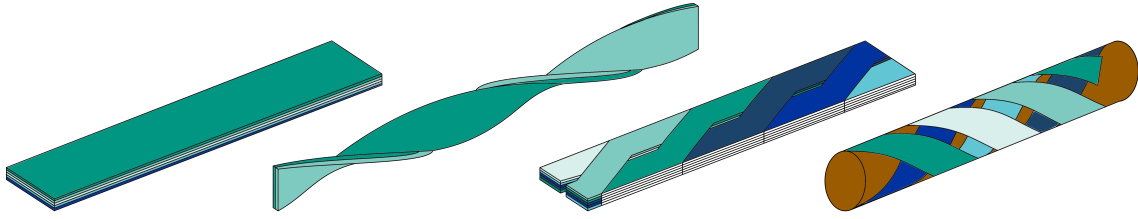
Figure 2.17.: Different cable types from coated *Re*BCO tape superconductors. Left: Stack of multiple tapes with no transposition. Center-left: Twisted stack of tapes with no transposition. Center-right: Roebel cable consisting of a stack of punched tapes that are fully transposed. Right: CORC® (Cable on Round Core) configuration, which is partially transposed with a copper core.

of around $650\,\mathrm{A/mm^2}$ were demonstrated at $12\,\mathrm{T}$ and $4.2\,\mathrm{K}$.

For undulators, a high packing fraction is of high relevance, as especially short-period magnets have only a very limited space for conductors. Further, Roebel cables have currently rather large physical dimensions with a width of around $12\,\mathrm{mm}$, which disqualifies them for applications to short-period undulators. Therefore, a stack of tape was chosen for the magnet design with one or two tapes as cable layout.

2.4. Superconducting magnets

As the demand for high-field magnets rises with future accelerator projects such as FCC or CLIC, fusion power plants, and undulators, the application of superconductors to electromagnets becomes crucial. It was shown above, that high current densities are feasible without any resistances inside a superconducting coil allowing it to achieve way higher magnetic fields than normal conducting magnets, e.g. wound from copper, or permanent magnets could ever achieve. Prominent examples in accelerator physics are the LHC main dipoles with a nominal operating field of $8.33\,\mathrm{T}$ for a $7\,\mathrm{TeV}$ beam energy [89]. The operating temperature for this field is $1.9\,\mathrm{K}$, roughly leaving a 14% margin to the magnet's short sample limit of $9.65\,\mathrm{T}$. When operating a superconducting magnet, such margins are essential for a safe operation. The superconducting magnet needs to be operated at a certain distance from T_c, which establishes an enthalpy margin against thermal perturbations. For similar reasons, a margin of the operating current density to J_c is necessary to guarantee thermal stability and also avoid so-called training effects, that may appear in superconducting magnets. Here, the conductor might move due to electromagnetic forces or material changes during the cool-down. As a consequence, motion, even on microscopic levels, sets free energy and thus causes the magnet to heat up. The short sample determines an absolute limit in terms of operation, as the operating current equals the critical current locally at some point in the coil. Therefore, a superconducting magnet is operated on its so-called load line, which shows the peak magnetic field on the superconductor for a defined operating current density as shown in Figure 2.18. Here, the short sample limit is located at the intersection of the critical current surface and the load line for a chosen operating temperature. The load line is calculated based on the entire magnet geometry, including the coil-winding, support, and iron poles. Common margins vary between 10% and 20%.
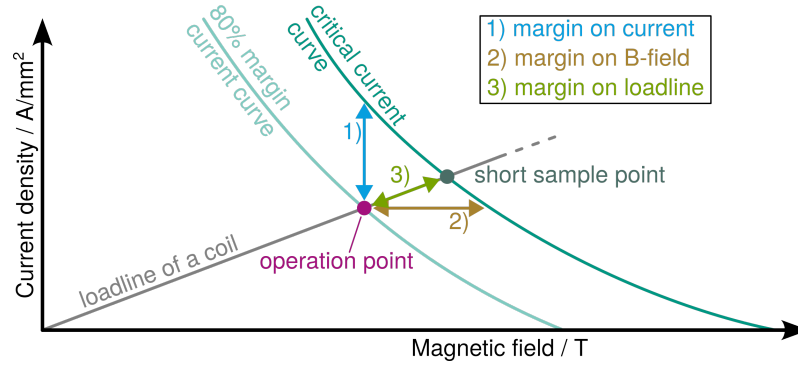
Figure 2.18.: Principle of a load line and a commonly used margin illustrated by intersection points of the load line with the critical current surface of a superconductor. Short sample and operation points are marked.

Down to the present day, there is no HTS accelerator magnet in use. However, stand-alone solenoids manufactured with ReBCO superconducting tape created magnetic fields in the conductor of 16.5 T at 23 K [90]. At lower temperatures, high fields of up to 45.5 T were reached using ReBCO-based solenoids in a 31.1 T background field [91]. This clearly demonstrated ReBCO's potential for superconducting magnets with high engineering current densities. However, operations in such regimes are critical and push the superconductor close to its limits. The risk of a transition to the normal conducting state, called quench, is omnipresent and protection is still challenging to achieve.

2.4.1. Quench

Superconducting magnets, especially HTS magnets, can carry current densities well above the limit for normal conductors. However, they have to be operated within the above-described margins, on or below their critical surface. The most likely cause of failure is a local thermal runaway, which strikes through the critical surface causing a transition to the normal conducting state, commonly referred to as quench. Here, thermal instabilities drive the temperature locally above the current-sharing temperature $T_{cs} < T_c$, allowing the superconductor to carry less current. Consequently, the current flows partly in the stabilizing copper matrix, causing a low-resistance zone. The resulting ohmic heating $P = RI^2$ depends on the electrical resistance R and current I in the conductor. It has to be cooled, otherwise, further heating may cause a growth of this normal conducting zone and finally lead to a quench. The energy which is needed to trigger such a normal conducting zone is known as the Minimum Quench Energy (MQE) and gives a description of the conductor stability. To increase the MQE, copper or silver are used as stabilizers in the conductor's cross-section. With a lot of energy stored in a superconducting magnet, a quench can have serious and even irreversible harmful consequences for the superconductor. To prevent such incidents, the thermal runaway must be detected early to allow a ramp-down of the magnet and/or switching off the magnet's power supply.

However, the protection against a quench in HTS as well as its detection is still challenging and not completely accomplished. This challenge has high priority in order to mature HTS technology and receives high attention [92]. Consequently, there are multiple approaches how to detect and subsequently dissipate the magnet's stored energy internally or externally. Examples of detection methods span over optic fibers [93], acoustic detectors [94, 95], pick-up antennas [96], LTS quench detectors [97], and coupling secondary coils [98]. Measuring the voltage over the conductor is one more common method [99], as the presence of a voltage features a reliable parameter for an existing normal conducting zone. Its sim-
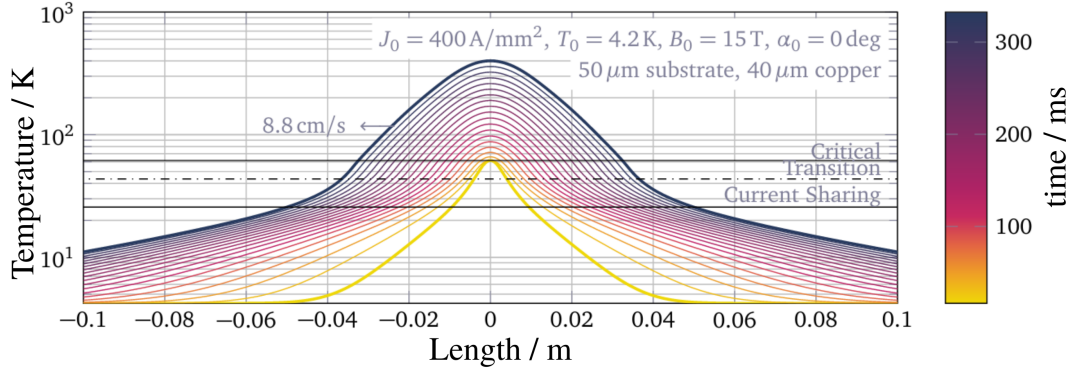
Figure 2.19.: Graph of quench propagation speed in one dimension for a coated $ReBCO$ superconductor, being in the order of $9\,\mathrm{cm/s}$, whereas for LTS, such as $\mathrm{Nb_3Sn}$, the propagation speed would be around $8\,\mathrm{m/s}$. Plot adapted from [69].

plicity makes it applicable to the vast majority of the superconducting magnets and thus got steadily improved to a kind of state-of-the-art method [100].

Quench detection is one step ahead of triggering a protection scheme. Depending on the stored energy, the power supply may be simply switched off. Small coils and cables can generally deal with this approach. Magnets with higher stored energies certainly need active protection. Here, a very common method is to heat up the superconductor in a controlled way, using so-called quench heaters to distribute the energy in a greater volume, thus mass [101]. The principle of this method got further developed, e.g. by Coupling Loss Induced Quench (CLIQ) systems [102], quench absorption coils [103], inductively coupled energy dissipaters [104], and energy extraction units (E³SPreSSO) [105]. Another different strategy is contained by no-insulation coils [106, 107]. Here, coils are wound in a non-insulated (NI) way providing a current redistribution to bypass potential hotspots within the coil in case of a normal conducting zone formation. As a result, the peak temperature of the hotspot gets limited. However, as a tradeoff, one has to deal with an increased ramp-up time, induced eddy currents, as well as potential unbalanced Lorentz forces [108].

Additional to all methods, it is advantageous to separate a quenching coil when multiple magnets are connected in series. This was done for example for the LHC beam diagnostics undulator, where each half period may be monitored and protected individually using parallel connected resistors [109]. An NI winding was chosen to be applied to the undulator coils, designed and manufactured within the work of this thesis because of its simple but effective approach. Additionally, the relatively low stored energy in the hereinafter presented prototype coils makes them ideal test material, also for investigating the limits of charging times.

As HTS, such as coated $ReBCO$ superconductors, are characterized by a relatively high T_{c}, they provide the opportunity to be operated stably at various temperatures with regard to a thermal runaway. In addition, the heat capacity grows rapidly with temperature in a cryogenic environment, which may result in a more than three magnitudes higher MQE for HTS compared to LTS. However, a relatively slow propagation velocity of the normal conducting zone in HTS is the result, being approximately two orders of magnitude smaller than compared to LTS [110, 111]. Figure 2.19 gives an idea of the quench propagation speed for a coated $ReBCO$ superconductor. This becomes crucial when observing the voltage for detecting and preventing a potential quench. More time will be needed until the voltage hits defined thresholds, thus providing a relatively late warning.

2.4.2. Magnet parameters

Electromagnets have the advantage of field tuning by changing the operating current. This may be generally easier than for permanent magnets, for instance, where the field tuning has to be done by mechanically changing the aperture of the magnet, implying a complex mechanic. The following subsection briefly introduces parameters that play an important role in the electromagnet's operation conditions and therefore in the following design considerations, namely appearing forces, stored energy, and inductance [112].

Forces   The Lorentz force was already introduced in equation (2.64) and is used here to describe the force $\vec{F}_{\text{cond}}$ on a conductor with current density $\vec{J}$ and volume $\mathcal{V}$ within a magnetic field $\vec{B}$:

$$\vec{F}_{\text{cond}} = \int^{\mathcal{V}} \vec{J} \times \vec{B}\,\mathrm{d}V\ . \tag{2.127}$$

Further forces appear between the different poles of a periodic undulator magnet, consisting of an upper and a lower part. When considering a planar undulator with a length $L_{\text{ID}} = N_{\text{u}}\lambda_{\text{u}}$, a width w of constant peak field in x-direction, and a sinusoidal magnetic field as introduced above $B_y = B_{\text{y},0}\sin(k_0 z)$ yields [13]

$$F = \frac{1}{2\mu_0} \int_{-\frac{w}{2}}^{\frac{w}{2}} \int_{-\frac{L_{\text{ID}}}{2}}^{\frac{L_{\text{ID}}}{2}} B_y^2\,\mathrm{d}z\,\mathrm{d}x = \frac{B_{\text{y},0}^2 L_{\text{ID}} w}{4\mu_0}\ . \tag{2.128}$$

A consequence of this force is that the aperture needs to be supported in order to counteract the attracting magnetic poles.

Energy   The energy also has an influence on the occurring forces. Assuming a homogeneous B-field in $\mathcal{V}$ and $\vec{B} = \mu\vec{H}$ is valid with a constant μ, then the magnet's stored energy W can be given as

$$W = \int^{\mathcal{V}} \left(\int_0^B \vec{H}(\vec{B}) \cdot \mathrm{d}\vec{B} \right) \mathrm{d}V = \frac{B^2 V}{2\mu}\ . \tag{2.129}$$

This can also be measured when powering, thus charging, an electromagnet until time point τ while keeping track of the voltage U and the applied current I:

$$W = \int_0^\tau U(t)I(t)\,\mathrm{d}t\ . \tag{2.130}$$

Inductance   The magnetic flux $\Phi_B = LI$ is used to determine the inductance L via the current I. For this purpose, the following differential equation has to be solved:

$$U(t) = \frac{\mathrm{d}\Phi_B}{t} = \frac{\mathrm{d}LI}{\mathrm{d}t} = \underbrace{\left(\frac{\partial L}{\partial I}I + L \right)}_{:=\bar{L}} \frac{\mathrm{d}I}{\mathrm{d}t} + \underbrace{\frac{\partial L}{\partial t}I}_{\substack{\to 0 \text{ for} \\ \text{stationary operation}}} = \bar{L}\frac{\mathrm{d}I}{\mathrm{d}t}\ , \tag{2.131}$$

where the term $\frac{\partial L}{\partial I}I$ becomes insignificant for non or highly saturated magnets. When current and the inductance are constant, the stored energy can be given by the inductance:

$$W = \frac{1}{2}LI^2\ . \tag{2.132}$$

3. Design of superconducting undulator magnets

This chapter covers the design studies performed in order to optimize and mature the planned coils as well as their manufacturing and operation. The three most common undulator coil geometries were investigated in this work, i.e. horizontal racetrack (HR) and vertical racetrack (VR) coils as well as a helical undulator coil geometry. To find the most advantageous working parameters of a high-temperature superconducting (HTS) undulator magnet, the design work started with analytical 2D electro-magnetic parameter space investigations, to be further investigated in 3D for modular coils and short models. The two investigated modular planar coil designs with coated ReBCO tape superconductors are displayed in Figure 3.1. The designs were further enhanced by mechanical analyses and field quality studies which defined boundary conditions. Finally, a complete vertical racetrack coil design is presented in detail as it was chosen to be applied to the modular prototype HTS undulator coils. Furthermore, two options for a helical undulator to be wound from coated ReBCO tape superconductor - the first presented designs for an HTS tape wound helical undulator to the author's knowledge.

Substantial parts of the following sub-chapters 3.1 and 3.2 have already been presented at international conferences and/or have been published [12, 113, 114].

3.1. Electro-magnetic design

All investigative electro-magnetic simulations were performed using the commercial software Opera [33]. Critical current density J_c fits of the investigated superconductors, e.g.
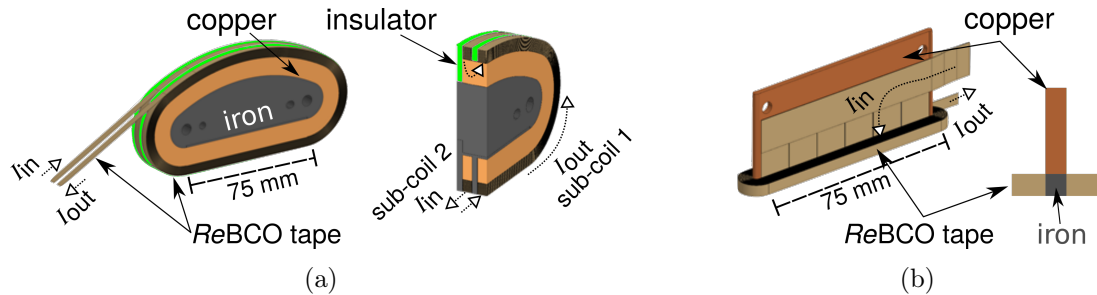
Figure 3.1.: Visualization of the designed and investigated planar undulator coils. (a) A vertical racetrack (VR) coil that covers one undulator period with two sub-coils including iron poles, sharing a copper winding body. (b) A horizontal racetrack (HR) coil with a central copper body housing a 50 mm long iron pole.

ReBCO, were used to describe the performance as a function of operating temperature and the magnetic flux density B on the conductor for all, plus the field angle for ReBCO (see section 2.3). The J_c fits were defined for single tape superconductors, based on CERN internal reports and can be found at full length in appendix B [115, 116, 117]. Due to this definition, there may be minor deviations to the measured critical current values described in the following chapter 5. Whereas J_c is commonly used to solely refer to the superconducting material's critical current density, the engineering current density J_e can be derived from J_c to describe the (critical) current density across the whole wire cross-section, e.g. the ReBCO tape. Utilization of the latter is in most design cases more concrete when designing superconducting magnets, thus will be employed in the following. Consequently, both notations of the current densities imply the critical engineering current density $J_{c,e}$, directly connected to J_c by a volumetric filling factor of the wire. A perpendicular orientation of the magnetic flux density (B-field) on the ReBCO layer was considered for all investigated geometries, to assume a worst-case scenario. Therefore, the perpendicular component of the absolute field was monitored in particular and utilized to define the respective J_c.

Anisotropy of the ReBCO's critical field

As introduced in the previous chapter's section 2.3, the investigated HTS ReBCO holds an anisotropy of its critical B-field, which features a significant addition, thus difference compared to low-temperature superconductors (LTS). The critical current of LTS such as niobium-titanium (Nb-Ti) and niobium-tin (Nb$_3$Sn) does not depend on the field angle, only on the absolute field value and its operating temperature. Figure 3.2 shows a sector of an infinite 2D undulator design with iron poles and a period length of $\lambda_u = 13\,\text{mm}$ having a 6 mm gap. The B-field strength on the conductor cross-section can be seen as a contour plot, and the implied tape orientation for an HR or VR undulator geometry is sketched on the side. Tapes closer to the poles or the beam pipe see varied B-field lines, especially relative to the tape's ReBCO plane orientation. Consequently, the tape orientation defines the absolute B-field that can be tolerated by the material, without losing its superconducting characteristic. As seen earlier, higher currents in coated ReBCO tape superconductors are generally attained when the magnetic flux density lines are positioned parallel to the tape's plane. This comes into play when further investigating and designing an HTS undulator magnet based on ReBCO, but also has to be taken into account when discussing the following calculated results by noting different on-axis magnetic flux densities for different superconductor orientations in the coils.

3.1.1. 2D electro-magnetic simulations

Opera 2D was used to investigate the parameter space of planar undulators in two dimensions for undulator periods λ_u between 5 and 15 mm, gap size g between 3 and 9 mm, and the resulting magnetic flux density (B-field) amplitude $B_y \equiv B_0$ on the beam axis. A helical undulator may also be represented approximately by the VR coil's tape alignment, having a comparable 2D geometry along its beam axis. All investigated models included iron poles with iron yokes as displayed in Figure 3.2. The width and height of the superconductor cross-section were varied for every configuration to find the optimized shape. The plotted values are given for 80% of the given critical engineering current density at 4.2 K on the respective undulator magnet's load line, respecting commonly agreed safety margins of LTS magnets (see section 2.3). However, the fact that a 2D geometry was used here to represent simply the B-field around the beam pipe but not for other parts of the conductor led to this choice of a rather conservative margin of 20% when investigating the
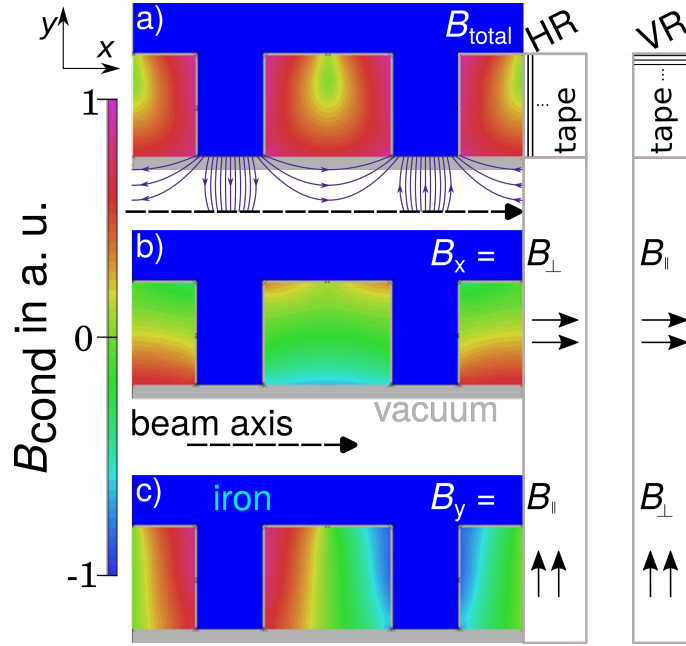
Figure 3.2.: 2D electro-magnetic mirror-models of an undulator with flux density lines in the vacuum and sketched most obvious tape orientations for VR and HR geometries on the side. The total B-field and its components are given as a contour on the conductor cross-section in arbitrary units in (a), (b), and (c), respectively.

potential of ReBCO in the first order. The discussed anisotropy of the ReBCO's critical field may lead to further boundary conditions in the 3D coil design and may reduce the margin further to commonly applied margins around 10%, as presented later in subsection 3.1.2.

The focus of the graphs was narrowed down to $g \leq 6\,\text{mm}$, as it is the high B-field region with particular interest for FELs. However, K parameters were plotted in the full range with the attractive zone between 1 and 2 marked for better orientation. No further optimization of the geometry was performed regarding the anisotropy of the ReBCO's critical field, e.g. varying the tapes angle other than for the HR and VR common orientation.

Nb-Ti The state-of-the-art technology for superconducting undulators, Nb-Ti, was investigated as a comparison for the corresponding undulator parameters and the achievable B_y as shown in Figure 3.3a. For reaching B-fields higher than $1.5\,\text{T}$, gap sizes around or smaller than $5\,\text{mm}$ are needed as well as $\lambda_u > 10\,\text{mm}$. The calculated engineering current densities are around $1\,\text{kA/mm}^2$. Period lengths from $9\,\text{mm}$ with gaps of $4\,\text{mm}$ make desired K parameter values above one feasible. Nb-Ti is a mature and reliable technology for superconducting undulators and wigglers, which has proven stable operation under the demanding conditions of several storage rings worldwide. However, it has reached its performance limits, and significantly higher fields for shorter periods will not be feasible with this technology.

Nb$_3$Sn Additionally, Nb$_3$Sn-based superconducting undulators were investigated, as this superconductor is currently the first candidate for the next generation of high-field accelerator magnets [118]. Its performance is displayed in Figure 3.3b where a shift of the contour towards a higher B-field amplitude can be observed. Here, B-fields up to $2\,\text{T}$ may be feasible for $g < 6\,\text{mm}$ and $\lambda_u \geq 10\,\text{mm}$. Appropriate K parameter values above one are

Table 3.1.: B-field values optimized for the materials ReBCO and Nb-Ti with a gap of 6 mm and operational engineering current densities of 80% $J_{c,e}$ at 4.2 K in 2D.

λ_{u} in mm	ReBCO HR B_{y} in T	ReBCO VR B_{y} in T	Nb-Ti B_{y} in T
13	2.3	1.7	1.2
14	2.7	2.0	1.4
15	3.0	2.3	1.5

feasible for $\lambda_{\mathrm{u}} \geq 9$ mm with gaps of 3.5 mm. The calculated engineering current densities are between 1 and 1.5 kA/mm^2. However, the performance of Nb$_3$Sn in superconducting undulators has to be considered with care. Besides the complex treatment of Nb$_3$Sn strands (c.f. section 2.3), operation at higher current densities would create larger eddy currents that cannot be sufficiently fixed in place by the pinning forces, thus may result in an unstable operation caused by flux jumps. Further developments might resolve this issue in the future.

ReBCO The calculations for coated ReBCO tape superconductors in the VR and HR geometry are shown in Figure 3.4. A significant shift of the contour towards a higher B-field amplitude with respect to Nb-Ti and Nb$_3$Sn can be seen for both cases. Both geometries make favored K parameter values above one feasible already for period lengths from roughly 7 mm with gaps of 3 mm. For B-fields higher than 2 T in the VR geometry, gap sizes around or smaller than 5 mm are needed or $\lambda_{\mathrm{u}} > 12$ mm. The HR geometry enables B-fields greater than 2 T already for $g \leq 6$ mm. In general, superior performance can be observed in 2D for the HR geometry down to an undulator period length of 7 mm. This is a clear consequence of the different B-field orientations relative to the superconductor's plane: especially high fields are less tolerated in perpendicular orientation, as seen earlier. Here, the calculated engineering current densities are in the range between 2 and 3 kA/mm^2, with the VR geometry being at the lower and the HR geometry at the upper limit.

A practical comparison between the HTS ReBCO performance and that of the LTS state-of-the-art material Nb-Ti for a gap of 6 mm results in the values stated in Table 3.1. When regarding the average performance of the HR and VR ReBCO geometry, a peak enhancement of up to 77% for the on-axis B-field amplitude may be feasible compared to the Nb-Ti design, demonstrating the ReBCO's potential.

A region where ReBCO clearly outperforms the LTS technology and simultaneously is within reach of a K around 2 narrowed the parameter space down to $\lambda_{\mathrm{u}} \in [11, 13]$. With a convenient magnetic gap size of 5 or 6 mm and the ambitious goal of 2 T B-fields, an undulator period length of 13 mm was chosen to be further investigated for both geometries. The optimized 2D period consists of two 2.5 mm wide iron poles and two 4×5 mm^2 superconductor blocks. This decision was supported by the fact that a width of 4 mm is the most common value after 12 mm among all commercially available coated ReBCO conductors on the market.
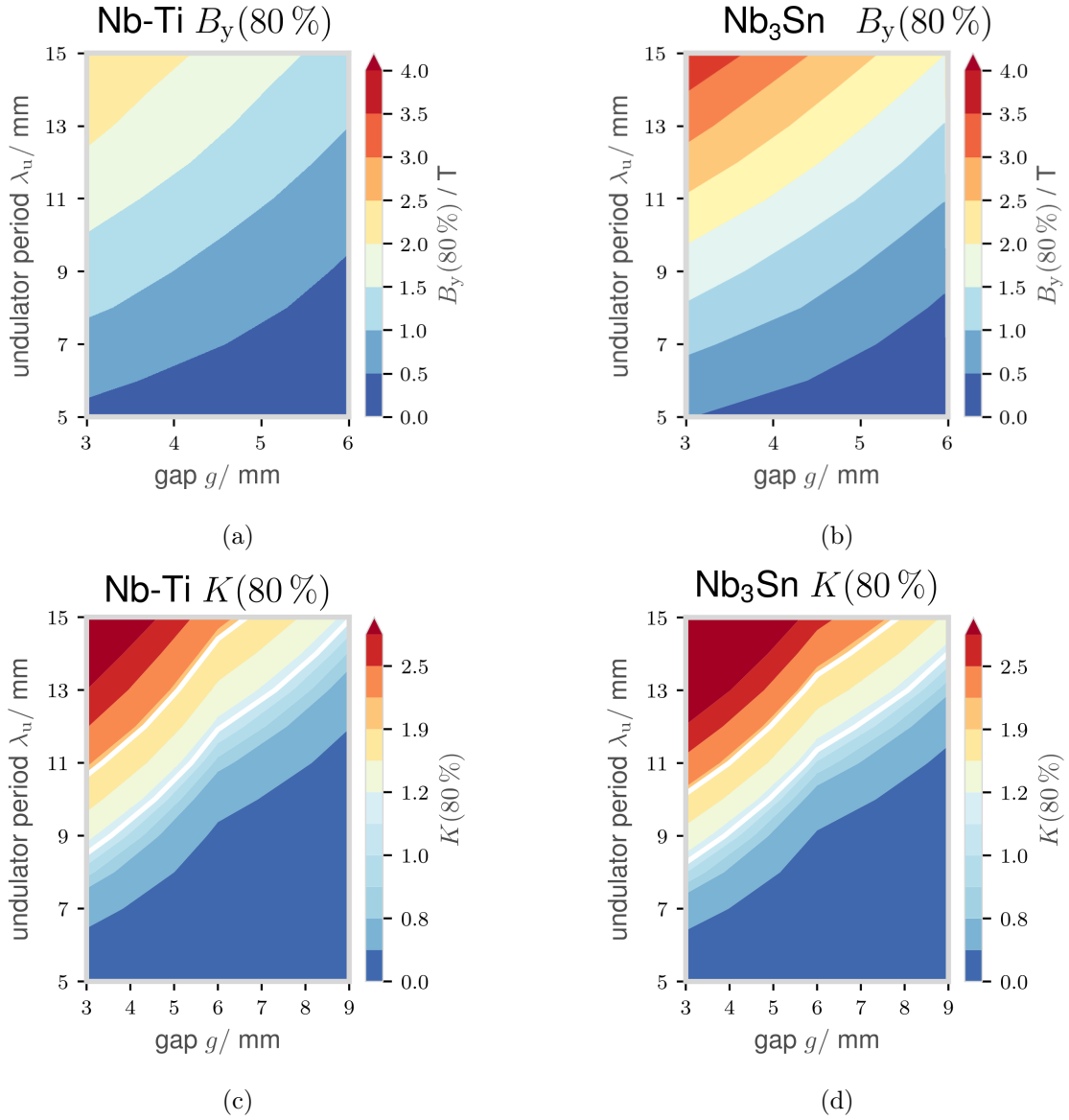
Figure 3.3.: Parameter space graphs for 2D electro-magnetic simulations of a supercon-
ducting undulator wound with Nb-Ti in (a) and (c) and Nb$_3$Sn wires in (b)
and (d). The magnetic field B_y and the respective K were calculated with
80% of the critical current at $4.2\,\mathrm{K}$ for the gap g and undulator period length
λ_u. K of 1 and 2 are marked with white lines. Plots reproduced from [12].

(a)

(b)

(c)

(d)
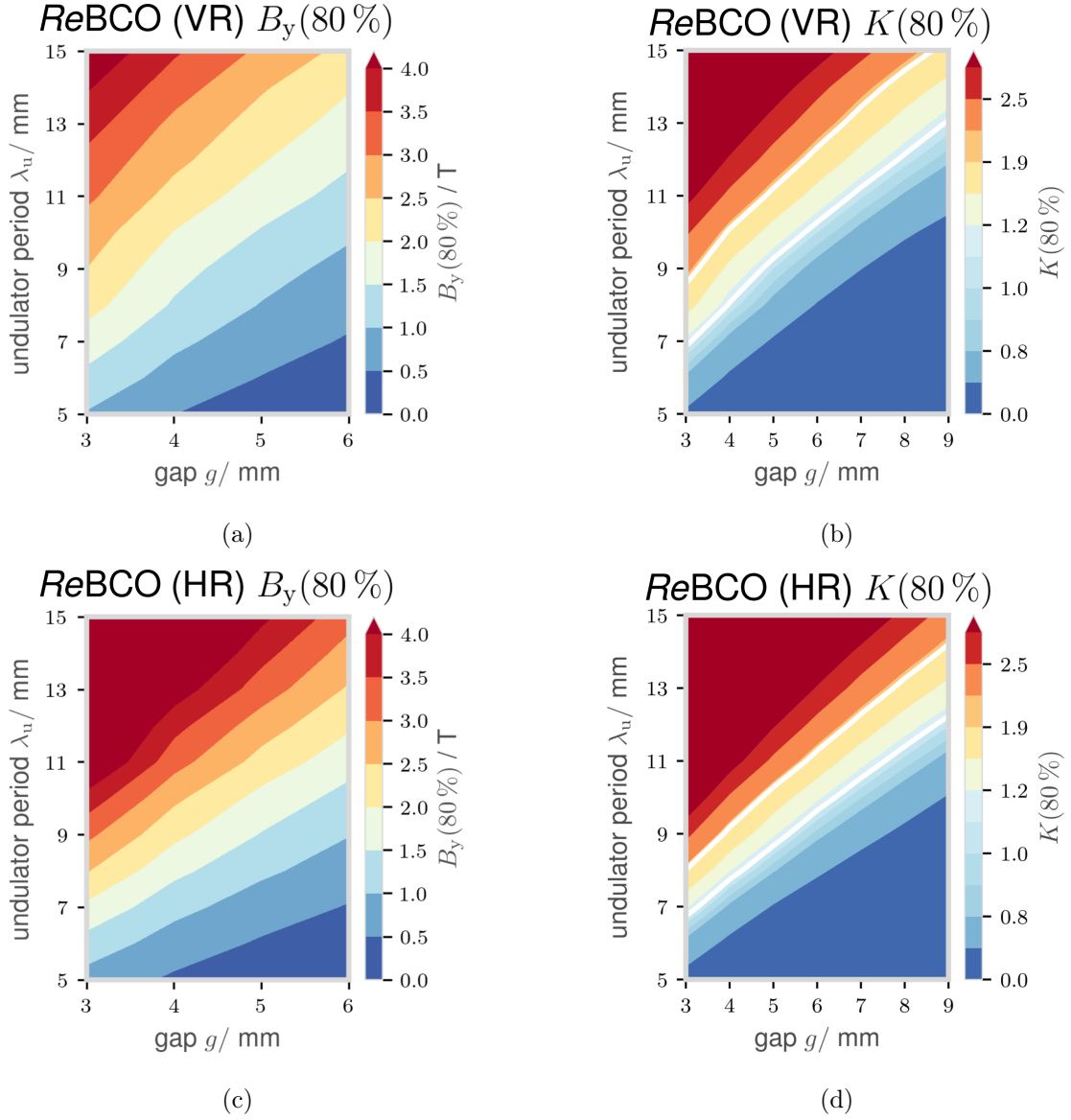
Figure 3.4.: Parameter space graphs for 2D electro-magnetic simulations of a supercon-
ducting undulator wound with coated *Re*BCO superconductor tape: (a) and
(b) Vertical racetrack (VR) geometry. (c) and (d) Horizontal racetrack (HR)
geometry. The magnetic field B_y and the respective K were calculated with
80% of the critical current at 4.2 K for the gap g and undulator period length
λ_u. K of 1 and 2 are marked with white lines. Plots reproduced from [12].

(a) VR coil at 4.2 K.   (b) VR coil at 77 K.
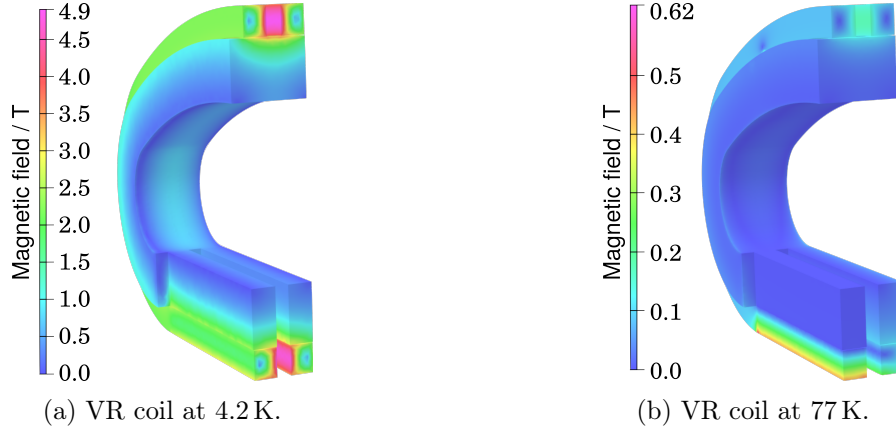
Figure 3.5.: 3D electro-magnetic simulations of a one-period VR coil geometry. The absolute magnetic field B_{cond} is shown as a color contour on the conductor and copper body for two temperature zones: (a) $J_{\mathrm{e}}(4.2\,\mathrm{K}) = 2071\,\mathrm{A/mm^2}$, (b) $J_{\mathrm{e}}(77\,\mathrm{K}) = 75\,\mathrm{A/mm^2}$. Graphics are reproduced from [113].

3.1.2. 3D electro-magnetic simulations

To investigate load lines and forces, full three-dimensional magnetic designs were elaborated and analyzed for the cases of interest identified in the 2D study. This supported the so-far acquired results and further brought investigations of the resulting magnetic field on the conductor B_{cond} at 4.2 K and 77 K into focus. Opera 3D [33] was used to investigate single undulator coil modules in three dimensions further, including the observation of the magnetic flux density on-axis and on the coils' entire superconductor volume. Further calculations included the resulting Lorentz forces caused by the operating current densities at the respective operating temperature. The investigations of these single modules prepare the basis for the experimental investigations in chapter 5 and are therefore analyzed in more detail. All investigations were performed for a defined undulator period λ_{u} of 13 mm and gap sizes g between 5 and 7 mm. In the following step, short undulator models of HR and VR coils as well as a helical undulator were studied. All investigated planar HR and VR models included iron poles with iron yokes if not specified differently. The optimized superconductor cross-section had the dimensions of $4 \times 4\,\mathrm{mm^2}$ for the HR geometry, $4 \times 5\,\mathrm{mm^2}$ for the VR geometry, and $4 \times 6\,\mathrm{mm^2}$ for the helical short model. Conductors solely described by the Biot-Savart law were used to describe the superconducting coils with respective current densities. Therefore, the utilized software Opera calls them simply "Biot-Savart conductors" and applies a constant current density J to the defined volume's cross-section.

Vertical racetrack geometry   Figure 3.5 displays the absolute magnetic field on the conductor stack B_{cond} as well as on the copper winding body for a VR coil at 4.2 K and 77 K. The plotted values are given for 80% of the critical engineering current density at 4.2 K and for $J_{\mathrm{c,e}}$ at 77 K on the coil's load line, respecting a safety margin compared to LTS magnets at low temperatures. The iron poles and core with the highest magnetic fields are hidden for a better scale.

Comparing both performances, one can see a clear asymmetric B-field distribution for the applied current at 77 K on the straight conductor close to the beam pipe. This is a direct consequence of the VR coil's asymmetric geometry, having a central and a lateral iron pole. At 77 K, the generated B-field with a maximum of 0.62 T is well below the iron saturation and therefore heavily guided by the yoke. The generated B-field increases significantly to a maximum B-field of 4.9 T for higher operating currents at lower temperatures down

(a) HR coil at 4.2 K.   (b) HR coil at 77 K.
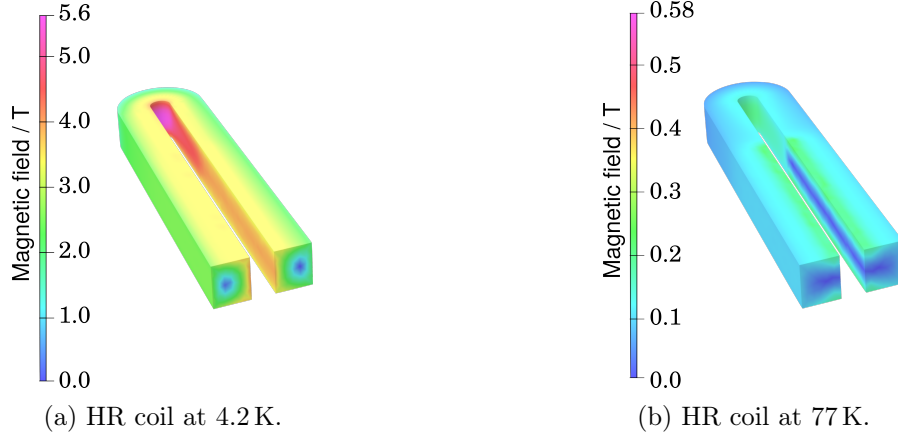
Figure 3.6.: 3D electro-magnetic simulations of an HR coil geometry. The absolute magnetic field B_{cond} is shown as a color contour on the conductor for two temperature zones: (a) $J_{\mathrm{e}}(4.2\,\mathrm{K}) = 2071\,\mathrm{A/mm^2}$, (b) $J_{\mathrm{e}}(77\,\mathrm{K}) = 75\,\mathrm{A/mm^2}$.

to 4.2 K. Reducing the margin on the load line by 10% to 10%, a current density of $2.3\,\mathrm{kA/mm^2}$ would become feasible, generating a 5.5 T field on the conductor. Here, the influence of the iron on B_{cond} is smaller. This can also be noted when observing the location of the maximum B-field on the conductor pack: for the performance with currents at 77 K, the maximum is located close to the iron pole tip, whereas for currents at 4.2 K there is a uniformly high zone on the edges of the opposed sub-coils, not only in the region of the iron poles. Additionally, $B_{\perp}$ is onbserved to be 99.95% B_{cond} for the VR coil at 4.2 K, supporting the assumption of investigating the perpendicular component.

Although investigating a single one-period VR coil, an on-axis B_{y} of 1.38 T was calculated for $J_{\mathrm{op}} = 2071\,\mathrm{A/mm^2}$ at 3.5 mm distance below the central iron pole at 4.2 K, showing the ReBCO's potential.

Horizontal racetrack geometry   Figure 3.6 shows the absolute magnetic field on the conductor stack B_{cond} for an HR coil at 4.2 K and 77 K. As seen earlier, the HR geometry has a preferred coated ReBCO tape orientation regarding the B-field lines. To allow a better direct comparison with the VR coil, however, the plotted values are given for the same current densities as for the VR coil at the respective temperatures, namely $J_{\mathrm{e}}(4.2\,\mathrm{K}) = 2071\,\mathrm{A/mm^2}$ and $J_{\mathrm{e}}(77\,\mathrm{K}) = 75\,\mathrm{A/mm^2}$. Here, the iron pole with the highest magnetic fields is hidden for a better scale as well as the copper body. Both performances show a rather symmetric B-field distribution on the conductor as a consequence of a symmetric HR coil geometry around one central pole. The generated absolute B_{cond} had maxima of 0.58 T and 5.6 T for operating currents at 77 K and 4.2 K, respectively. A 20% load line margin at 4.2 K would allow a potential operating current density of $2.58\,\mathrm{kA/mm^2}$ with a resulting absolute field on the conductor of 6.9 T. For lower temperatures, the location of the maximum B_{cond} can be found on the inner curved side of the conductor pack whereas it was located on the conductor edges next to the iron pole at 77 K due to the iron's influence. Here, $B_{\perp}$ can be found as 57.14% B_{cond} for the HR coil for operating currents at 4.2 K, showing the significantly different alignment of magnetic density flux lines compared to the above presented VR coil and the HR's potential. A B_{y} of 1.26 T is calculated at 3.5 mm distance below the central iron pole for $J_{\mathrm{e}}(4.2\,\mathrm{K})$.
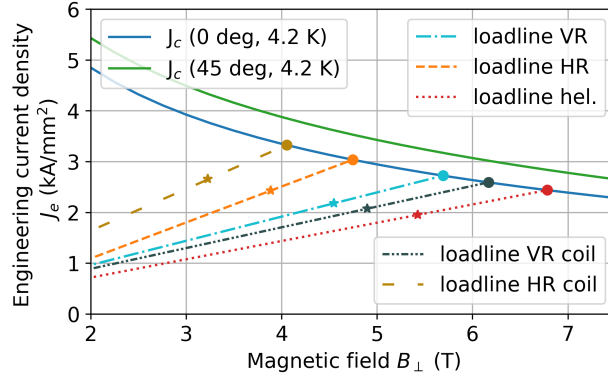
Figure 3.7.: Load lines of five-periods undulator short-models and of single VR and HR coils for comparison. The maximum perpendicular magnetic field component on the conductor is plotted with respect to the applied J_e. The individual $J_{c,e}$ for Bruker HTS with a 20% margin are marked with dots and stars, respectively.

Table 3.2.: Engineering critical current densities $J_{c,e}$ and investigated operating values $J_{e,op}$ ($\gtrsim 20\%$ margin) of the analyzed HR, VR, and helical short models plus respective modular coils. Iron was replaced by holmium (Ho) in the short models for further analyses. All for $\lambda_u = 13\,\text{mm}$, a 5 mm gap and at 4.2 K.

	HR	VR	helical	HR coil	VR coil	HR (Ho)	VR (Ho)
$J_{c,e}$ (A/mm^2)	3038	2724	2440	3326	2592	2973	2704
$J_{e,op}$ (A/mm^2)	2500	2000	2000	2071	2071	2500	2000

3.1.2.1. Short model undulators

Short models of HR and VR with iron poles, as well as an iron-free helical undulator with five undulator periods, were investigated for $\lambda_u = 13\,\text{mm}$ and a gap $g = 5\,\text{mm}$. As short models represent the full-size undulator magnet, it is crucial to demonstrate the feasibility of their design based on the above-presented modular coils. In the following, three-dimensional electro-magnetic simulations of the investigated undulator geometries are presented and discussed in the form of five period-long short models. Their load lines are displayed in Figure 3.7 together with the modular coil's load lines, all constrained by the perpendicular magnetic field component.

A deviation between the single VR and HR coils and their respective short models was expected due to the significantly different overall geometries, therefore needed further investigations in terms of applied forces and field distribution, both on-axis and on the superconductor. All calculated engineering critical current densities $J_{c,e}$ and the investigated operating values $J_{e,op}$, having an approximate safety margin of 20%, are noted in Table 3.2. However, the $J_{c,e}$ of the HR geometries have to be considered with some care, as they seem relatively high in value. Consequently, the HR coils were further investigated with a rather large safety margin. The worst-case scenario would be to take the absolute magnetic field as a reference parameter rather than its perpendicular component on the conductor. In this case, HR and VR geometries would fall comparable on the current VR load lines, making the VR coil an attractive representative candidate for further experimental investigations. The on-axis B-fields B_y of all short models are plotted in Figure 3.8 for their respectively selected $J_{e,op}(4.2\,\text{K})$. The HR and VR short models show a drift of the B-field along the beam axis due to missing corrector coils (or matching periods) at the beginning and end of the rather limited geometries, where the field fades back to zero.
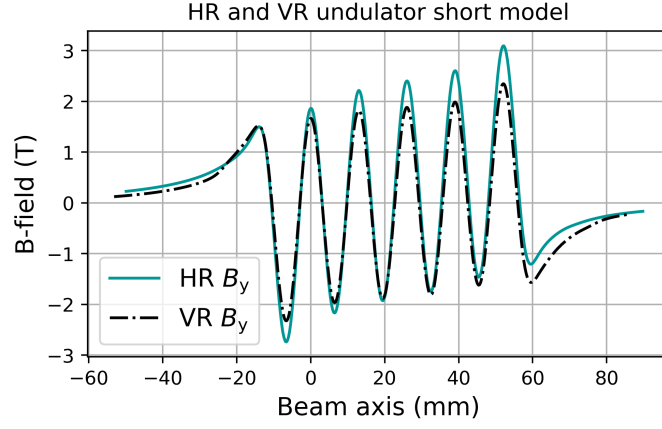
(a)
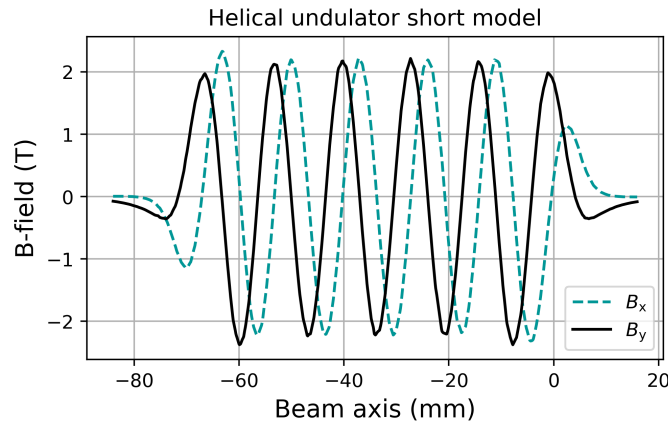
(b)

Figure 3.8.: Graph of the magnetic field B_{y} along the beam axis of each short undulator model for $\lambda_{\mathrm{u}} = 13\,\mathrm{mm}$ and a gap of $5\,\mathrm{mm}$. All short models were investigated for their respective $J_{\mathrm{e,op}}(4.2\,\mathrm{K})$: (a) HR $2500\,\mathrm{A/mm^2}$, VR $2000\,\mathrm{A/mm^2}$, and (b) helical undulator $2000\,\mathrm{A/mm^2}$ for option 1 (cf. section 3.5).
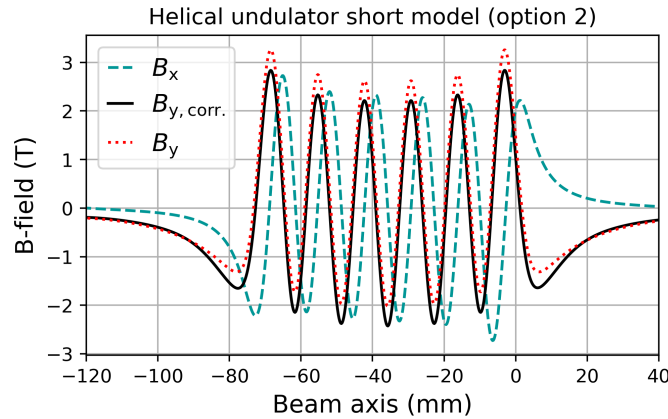
Figure 3.9.: Graph of the magnetic field B_{y} along the beam axis of the helical undulator, design option 2 (cf. section 3.5), for $\lambda_{\mathrm{u}} = 13\,\mathrm{mm}$, a $5\,\mathrm{mm}$ gap, and $J_{\mathrm{e,op}}(4.2\,\mathrm{K}) = 2000\,\mathrm{A/mm^2}$. The correction for $B_{y,\mathrm{corr}}$ was realized by a $0.38\,\mathrm{T}$ background field along the helical structure.

Figure 3.8b shows the B-field behavior of the helical undulator by displaying both B-field components perpendicular to the beam axis. Here, B_x and B_y construct a helical magnetic flux density vector. The designed tape return path options may be compensated and are presented in section 3.5. However, an opposing tape stack ending (option 2) results in an asymmetric shape of the field amplitudes B_x and By, shown in Figure 3.9, and makes field corrections necessary. Applying a $0.38\,\mathrm{T}$ background field along the bifilar helix, as an example, already improves the field significantly ($B_{y,\mathrm{corr}}$).

Vertical racetrack geometry   Figure 3.10 shows the absolute magnetic field on the conductor B_cond for the VR short model's critical engineering current density $J_\mathrm{c,e}$ and engineering current density for operation $J_\mathrm{e,op}$ with iron poles and core side by side. As already seen for the single VR coil, the highest B-field can be observed on the opposing coil sides of the superconducting stack. This applies especially to the outermost coils of the presented VR short model where the peak fields can be detected due to the ending geometry. Corrector coils with $1/4$ and $3/4$ of the original coil width could be used to reduce these end fields further.

Horizontal racetrack geometry B_cond for the HR short model with iron poles is presented in Figure 3.11a for a $J_\mathrm{e,op}$. The maximum B-field is observed in the region of the inner curved sides of the conductor stack. Therefore, changing the coil end of the horizontal racetrack may significantly reduce the field on the conductor, thus allowing higher currents and on-axis fields. This was briefly investigated by splitting one HR coil up into two with different lengths as seen in Figure 3.11b. With this simple approach, the maximum B_cond can already be reduced by about 10% moving the location of the maximum on-conductor field towards the central iron pole of each coil. Another approach to reduce the field on the coil ends and to get rid of the rather tight bending radii when going to small periods like $13\,\mathrm{mm}$, might be the application of so-called cloverleaf coils with alternating varying straight lengths [119, 120, 121]. However, further investigation and resources beyond the scope of this work would have been necessary.

Helical geometry   Figure 3.12 displays B_cond for the helical undulator short model's engineering operating current density $J_\mathrm{e,op}$ without iron poles. Both coil-end design options are taken into consideration (cf. section 3.5). The maximum B-field can be observed on the opposing coil sides of the superconducting stack as well as on the innermost turns next to the central beam pipe. Cross-sections along the beam pipe show the B-field distribution inside the tape stacks in Figure 3.13. Here, Figure 3.13b shows the planned demonstrator short model of the helical undulator and the field on its superconductor for $J_\mathrm{c,e}(77\,\mathrm{K}) = 350\,\mathrm{A/mm^2}$. Having only 12 turns, the demonstrator is planned to be tested only at $77\,\mathrm{K}$, for which this simulation serves as a reference. Here, the pattern of B_cond is comparable to the full-size short model with 120 turns. For both helical cases, possible tape return paths are neglected, yet, their design can be found later in section 3.5.
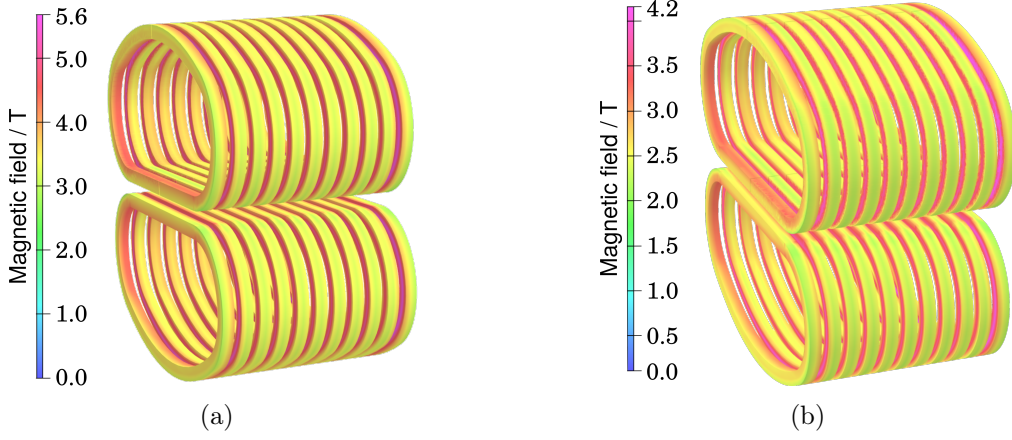
Figure 3.10.: 3D electro-magnetic simulations of a five-periods VR short model. The absolute magnetic field B_{cond} is shown as a color contour on the conductor for (a) $J_{c,e}(4.2\,K) = 2724\,A/mm^2$ and (b) $J_{e,op}(4.2\,K) = 2000\,A/mm^2$. Iron and copper are hidden for an enhanced view.
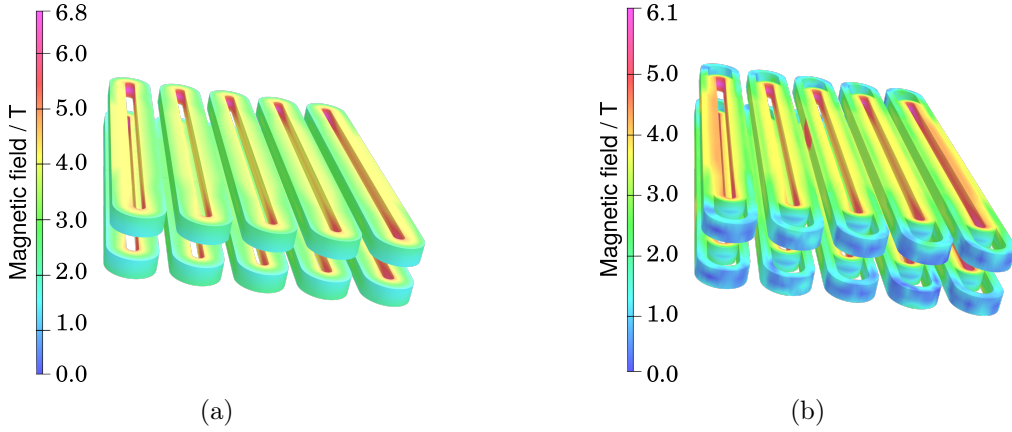
Figure 3.11.: 3D electro-magnetic simulations of two five-periods HR short models: (a) A simple HR design, (b) a double HR design. The absolute magnetic field B_{cond} is shown as a color contour on the conductor for $J_{e,op}(4.2\,K) = 2500\,A/mm^2$. Iron and copper are hidden for an enhanced view.
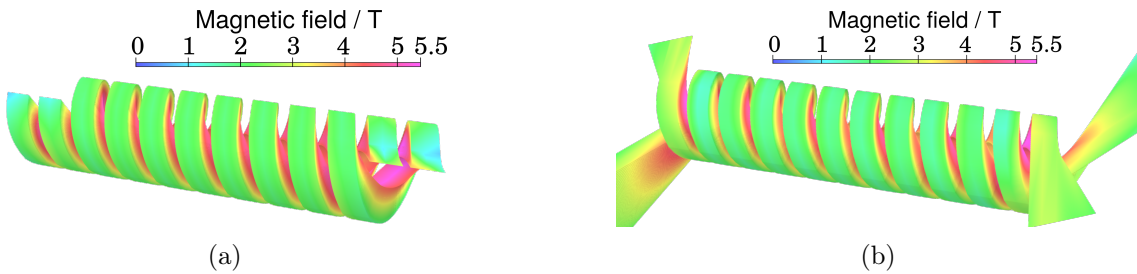
Figure 3.12.: 3D electro-magnetic simulation of a five-period helical undulator short model. The absolute magnetic field B_{cond} is shown as a color contour on the conductor for $J_{e,op}(4.2\,K) = 2000\,A/mm^2$, approximately 80% $J_{c,e}(4.2\,K)$. (a) The design with a parallel tape stack ending (option 1, cf. section 3.5). (b) The design with an opposing tape stack ending (option 2, cf. section 3.5). Winding bodies are hidden for an enhanced view.

(a)   (b)
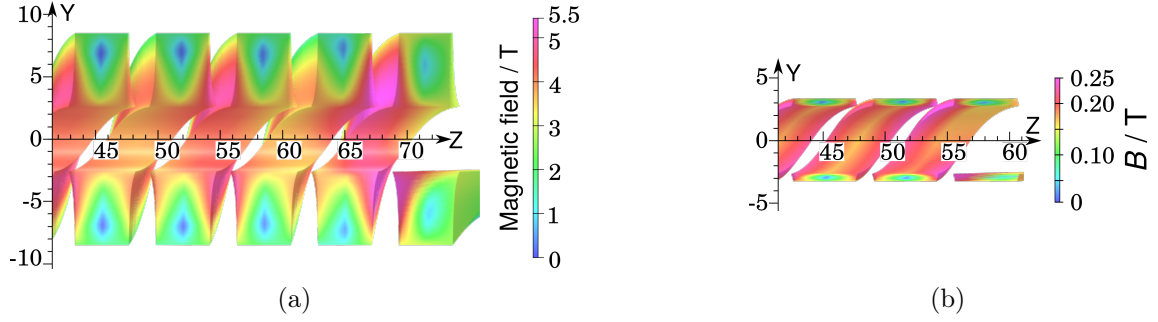
Figure 3.13.: 3D electro-magnetic simulations of a helical undulator short model (left) and demonstrator (right) with five periods and an opposing tape stack ending (option 2, cf. section 3.5). The absolute magnetic field B_{cond} is shown as a color contour along the beam pipe on the conductor's cross-section for (a) $J_{e,op}(4.2\,K) = 2000\,A/mm^2$, approximately 80% $J_{c,e}(4.2\,K)$, and (b) $J_{c,e}(77\,K) = 350\,A/mm^2$. Scale in mm.

3.1.3. Ferromagnetic materials

Superconducting as well as normal conducting magnets use poles made of ferromagnetic material to increase the magnetic flux density in certain regions or to prevent fringe fields that may influence the magnet's performance. In these investigations, iron was implemented in the coil's design not only to improve the peak field performance but also as core material in the vertical racetracks to adjust the direction of the forces, such that the main stress becomes compression (cf. section 3.2). This made the calculation methods more complex as explained above in subsection 2.1.3.

The most prominent materials to be used are pure iron or steel with saturation values around 2.1 T. However, there are further attempts to push the saturation to higher values, e.g. Vacuumschmelze's Vacuflux® and Vacodur® with saturations of 2.3 T. Another example is the application of the rare earth metal holmium in magnetic poles which is only ferromagnetic below 20 K with a saturation of roughly 2.5 T [122, 123]. Holmium may also be anti-ferromagnetic (between 20 and 133 K) or paramagnetic (above 133 K), which makes its usage challenging. The *B*-*H*-curves of holmium, iron, and AISI 1010 low-carbon steel at 4.2 K are plotted in Figure 3.14.

As holmium provides the highest saturation among the presented ferromagnetic materials, its application to the designed HTS undulator short models was investigated within this work and compared to iron and air for their individual $J_{e,op}(4.2\,K)$ (cf. Table 3.2). Iron as the pole and core material provides an increased *B*-field of about 8% for VR and HR compared to air. Here, a massive iron winding body for the helical undulator short model may improve the *B*-field by 13%. Utilizing holmium, further *B*-field enhancements for the VR and HR short models of up to approximately 13% and 12% can be calculated respectively, making it a very attractive choice for boosting the magnet's performance at 4.2 K. Also, the helical undulator short model would benefit from an additional 8% *B*-field increase. All changes apply for the same $J_{e,op}(4.2\,K)$ as without the ferromagnetic material, thus implying a change of the load line. In the end, iron was chosen for coil manufacturing due to its availability and straightforward application.
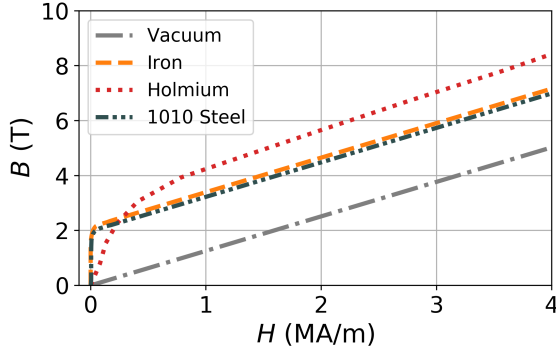
Figure 3.14.: Simplified *B-H* curves of iron, holmium, steel 1010, and vacuum/air at 4.2 K.

3.2. Mechanical design

All investigative mechanical simulations were performed utilizing the software ANSYS Workbench [124]. The von-Mises stress and strain were mainly calculated for two processes concerning the modular coils and undulator short models: First, the material shrinking due to the uniform cool-down from a room temperature of 300 K to a possible operating temperature of 4.2 K. Second, the caused Lorentz forces by powering the coils.

Note, that von-Mises analyses are commonly used for maximum stress and strain evaluations in isotropic ductile materials, such as steel. It may be debatable to use von-Mises here as the investigated coils are not isotropic and the high-temperature superconductor *Re*BCO is a brittle material. However, *Re*BCO's volumetric percentage in the overall coil is rather small and large pieces of the coil are made of metals. Additionally, the *Re*BCO tape superconductor stacks were modeled as a homogeneous material as described below. The Lorentz forces were calculated from the 3D electro-magnetic calculations, presented in the preceding sections, and transferred to the mechanical models as element force densities. In the mechanical models, all solid surface contacts were defined as so-called bonded contact regions, which prevented sliding and therefore may overestimate the caused stress. All materials' properties were taken into account respectively. However, the 4 mm wide coated *Re*BCO tape superconductor stacks were modeled as a homogeneous material as the layered structure makes the below-presented properties challenging to measure. Consequently, the different materials were treated according to their volume percentage with considered layer thicknesses of 3 μm thick YBCO, 7 μm silver, 40 μm copper, and 100 μm stainless steel, Besides the thermal contraction, the following properties for solid materials were defined for the temperature range between 4.2 K and 300 K [125, 126]:

- Poission's ratio, measuring a material's deformation in directions perpendicular to the direction of the applied loading.

- Young's modulus, describing a material's compressive or tensile stiffness for a lengthwise applied loading in the linear elastic region in GPa.

- Shear modulus, measuring a material's elastic shear stiffness in GPa.

Note that apart from measuring these three properties, it is also possible to calculate the missing parameter, as long as the other two are known.
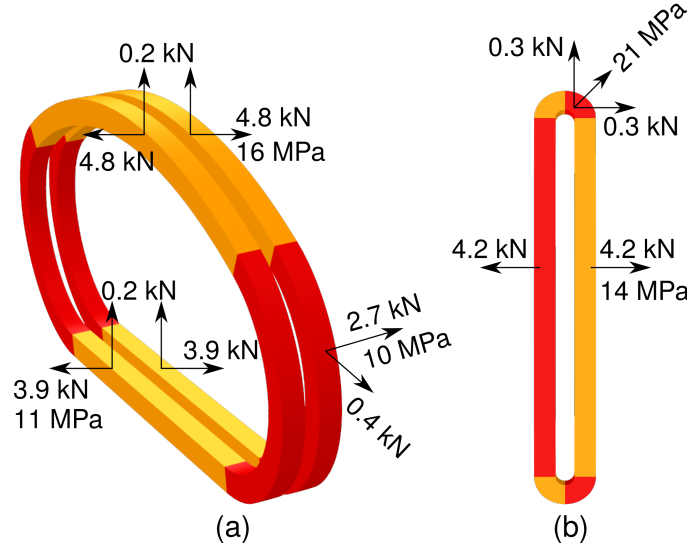
Figure 3.15.: Lorentz forces on modular vertical and horizontal racetrack (VR and HR) undulator coils, all calculated at 4.2 K. (a) One-period VR coil ($J_{\mathrm{e,op}} = 2071 \, \mathrm{A/mm^2}$), (b) HR ($J_{\mathrm{e,op}} = 2800 \, \mathrm{A/mm^2}$).

3.2.1. Modular undulator coils

Figure 3.15 displays the Lorentz forces on the investigated modular undulator coils (VR and HR) for their respective $J_{\mathrm{e,op}}$ at 4.2 K. Stacked together, these modular geometries can be used to assemble a short model or a full-size undulator magnet. All coils are split into segments to showcase the direction of the forces.

Vertical racetrack geometry The modular VR coil, which consists of two sub-coils, shows the strongest forces in opposing coil directions with 4.8 kN and an equivalent of 16 MPa. Here, the relatively small iron core also helps to reduce the expanding forces of the superconductor stack by about 6%. The stress due to the cool-down and powering at 4.2 K of the designed VR coil is shown in Figure 3.16a. The resulting allocation of the stress can be once more seen as a cause of the asymmetric geometry. Maximum values of about 64 MPa can be detected on the edges of the superconducting tape stack.

Horizontal racetrack geometry As expected, the two parallel sides of the HR coil want to expand with a maximum force of 4.2 kN, seeing 14 MPa. However, the ends of the coil are even more stressed in the radial direction by 21 MPa. The analysis concerning the stress due to the cool-down and powering at 4.2 K for the designed single HR coil is presented in Figure 3.16b. A relatively high $J_{\mathrm{e,op}}$ was chosen to test the limits of this rather small coil. Maximum values of about 42 MPa are monitored on the edges of the superconductor stack next to the iron pole in the coil's center.

For both investigated modular VR and HR coils, the stress is shown to stay well below tolerable thresholds of 600 MPa that might harm the superconducting properties of coated ReBCO tape superconductor [67, 127]. Stresses on the other materials can be neglected due to low values. To prevent any movement of the coated ReBCO tapes, a stainless steel supporting structure was designed to fix the superconductors and keep the coils compressed starting from the cool-down.

3.2.2. Short model undulators

Vertical and horizontal racetrack   Figure 3.17 displays the stress on the superconducting tape stacks of the designed VR and HR undulator short models as a consequence of the cool-down and powering at 4.2 K. The VR short model was investigated for its $J_{\mathrm{c,e}}$ to demonstrate the manageable stress up to the electro-magnetic limits. As the relatively high $J_{\mathrm{c,e}}$ of the HR geometry has to be regarded with some caution, the HR short model was investigated for its $J_{\mathrm{e,op}}$. Both racetrack geometries have their maxima of stress on the superconductors close to their iron pole location with around 360 MPa for the VR and 488 MPa for the HR. Furthermore, the VR and HR short models show rather thin regions of high stress, which may be overcome by increasing the manufacturing margins. Yet, this should be experimentally validated by manufacturing short undulator models and e.g. applying pressure measurement films to regions of interest. Although the investigated short models show higher absolute stress values than the modular coils, the revealed stresses are below tolerable thresholds and in expected regions, not showing a showstopper for the two racetrack designs.

Helical geometry   Contrary to the two racetrack geometries, the helical undulator module presents itself with a well-balanced set of forces during operation with values around 200 N or rather 4 MPa, caused by its symmetric geometry displayed in Figure 3.18a. Further investigation of the designed coil ends, presented in section 3.5, will most likely show similar values as compared to the VR and HR geometries. Due to their relatively simple shapes (solenoid and half racetrack), both proposed helical coil end options should be well to handle, especially since they stand out of the magnet's structure. A quarter of the helical short model is shown with its stress caused by the cool-down and powering at 4.2 Kin Figure 3.18b. Here, the cool-down has a significant influence and caused scattered high-stress regions of up to 552 MPa, also on the winding body made of stainless steel. However, the connections between surfaces may be difficult to model in a helical structure when preventing any edge movement with nearly no flat surfaces. Therefore this result has to be met with care and is probably exaggerated by the boundary condition of bonded surface contacts. Nevertheless, the revealed stresses in the helical module are below tolerable thresholds, not showing a showstopper for the helical undulator designs.
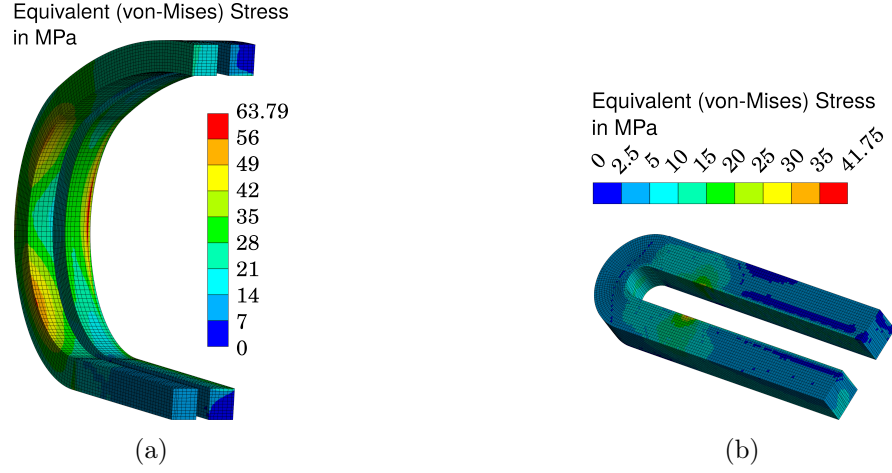
Figure 3.16.: Equivalent stress on the modular coils due to a uniform cool-down from $300\,\mathrm{K}$ to $4.2\,\mathrm{K}$ and powering. (a) VR with $2071\,\mathrm{A/mm^2}$. (b) HR with $2800\,\mathrm{A/mm^2}$.
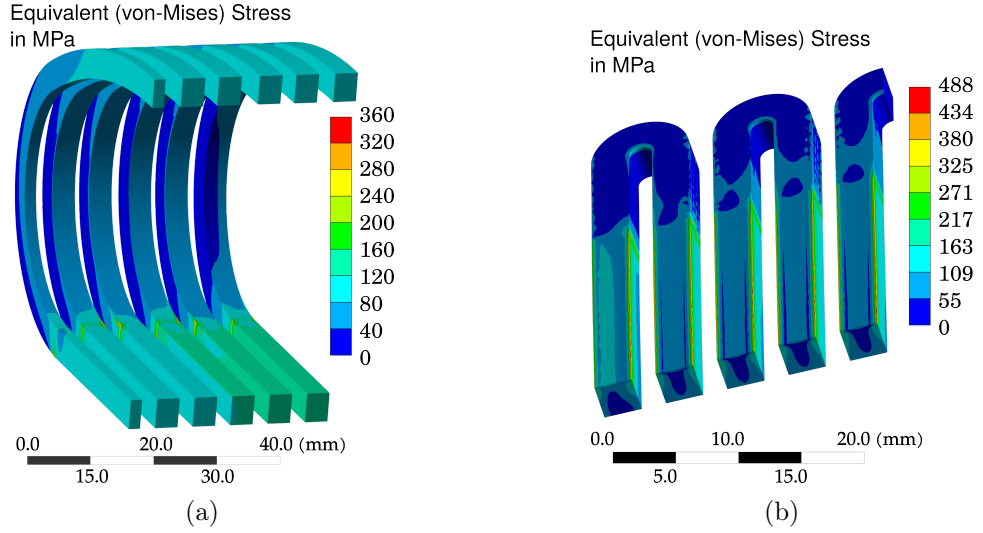
Figure 3.17.: Equivalent stress on undulator short models due to a cool-down from $300\,\mathrm{K}$ to $4.2\,\mathrm{K}$ and powering. (a) VR with $2724\,\mathrm{A/mm^2}$. (b) HR with $2500\,\mathrm{A/mm^2}$.
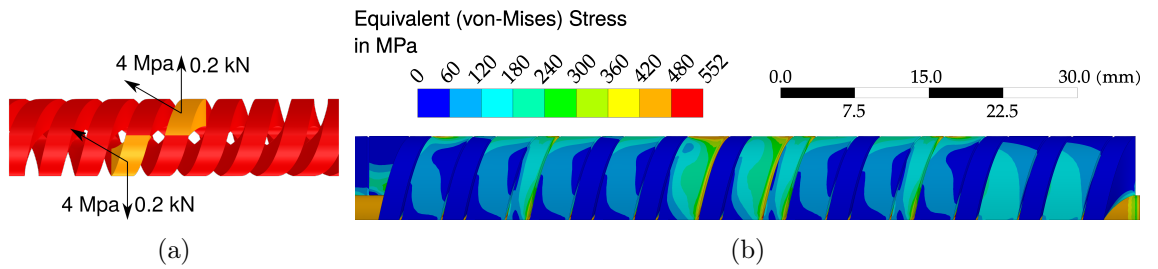
Figure 3.18.: Mechanical investigations of the helical undulator module calculated for $J_{\mathrm{e,op}} = 2000\,\mathrm{A/mm^2}$ at $4.2\,\mathrm{K}$. (a) Lorentz forces, (b) Equivalent stress due to a cool-down from $300\,\mathrm{K}$ to $4.2\,\mathrm{K}$ and powering.

3.3. Field quality studies

For the application in synchrotrons and FELs, the performance of undulators must be well controlled in steady operation and during the charging and discharging process. On the one hand, a non-zero field integral may have devastating consequences for the beam and could even harm the machine when particles get dumped in an uncontrolled way. On the other hand, the phase error acts as a limiting factor for the emitted radiation (cf. subsection 3.3.3). Both may be additionally influenced by current sharing in a non-insulated coil. However, also the application of an undulator in a synchrotron, a ring accelerator, or an FEL plays a role when reviewing potential sources of malfunction. Transient field effects, for example, may have a larger impact on undulators in synchrotrons which depend on a stable beam compared to run-through-once undulators in FELs. In the following, eddy currents were investigated during the ramping process of the designed VR and HR undulator geometries, as the used ReBCO superconductor was copper-coated and the undulator design includes large copper and iron bodies. The generated eddy currents in these metals are finite but may have the potential to influence the field on the beam axis in a disturbing way. Consequently, their current density and decay time need to be investigated. Further research should also focus on eddy currents inside the superconducting layers, as they may cause a hysteresis loop for the on-axis field based on eddy currents, as recently described for an HTS undulator bulk structure [128].

Furthermore, the mechanical margins of the winding, thus finite errors, constitute a potential source of field errors. Variations in the winding position were therefore analyzed with respect to a change in the field amplitude.

Another potential error source in static conditions may be the current distribution in non-insulated windings, as planned and exercised in the following chapters. However, this is not straightforward to investigate by means of calculations and would go beyond the scope of this thesis. Here, experimental field studies in HTS undulator short models may also be a well-feasible approach. Other future investigations may cover particle tracking and potential beam emittance growth due to mechanical errors in a known storage ring configuration.

3.3.1. Dynamic electro-magnetic: current ramping

2D Opera [33] simulations were utilized to investigate eddy currents in normal conducting metals around the superconducting coils during the current ramping process of the designed VR and HR undulators, wound with copper-coated ReBCO superconducting tape. Therefore, the copper winding body, the iron poles, as well as the copper layers of the superconducting tape were monitored. Both geometries were analyzed for a 13 mm period length and a 6 mm gap, having a conductor cross-section of 4×5 mm (VR) and 4×4 mm (HR). The 100 µm thick superconducting tapes were split up into two parts: the copper coating of 40 µm and the 60 µm thick rest, mainly consisting of stainless steel and the ReBCO layer. For the latter, the current density was driven over 900 s up to a plateau of 2 kA/mm^2 where it remained steady for another 300 s. This corresponded to a maximum J_e of 1.2 kA/mm^2 in the overall undulator groove. Eddy currents were observed during this process in all conductive materials of the model. Iron and copper were described with their electrical conductivity at 4.2 K, being approximately 1×10^8 S/m and 3.268×10^9 S/m, respectively. For copper, a RRR of around 40 was assumed.

Figure 3.19 shows the magnetic field build-up for different time steps as an example of a VR undulator geometry. The B-field amplitude B_0 at the beam axis increases over time and shows clearly the two absolute maxima below the iron poles within the undulator period. After the current density reaches its plateau value of 2 kA/mm^2, a change in B_0
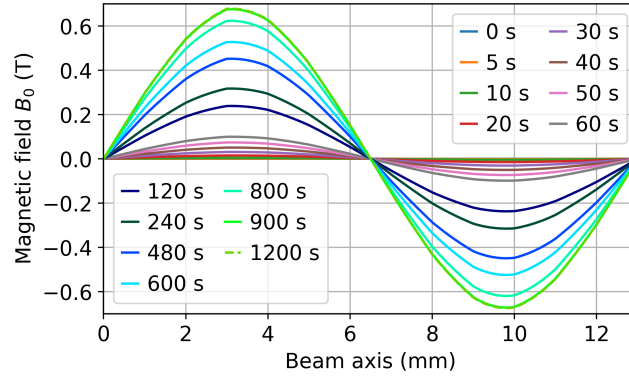
Figure 3.19.: *B*-field buildup for various time steps in a 2D 13 mm period, 6 mm gap VR undulator during 900 s current ramping with the influence of eddy currents.

of $\Delta B_0 \approx 0.38\%$ can be observed for both geometries over 300 s. The current density distribution, including the induced eddy currents, can be seen for different time steps in Figure 3.20. Here, subfigures 3.20a to 3.20d display the investigated HR geometry, whereas subfigures 3.20e to 3.20f show the VR geometry as an example. Due to the start of the current ramp, relatively large eddy currents of $47\,\mathrm{A/mm^2}$ and $27\,\mathrm{A/mm^2}$ are seen after the first 120 s. They stabilize around $15\,\mathrm{A/mm^2}$ while the current is constantly driven up and become insignificant 300 s after the plateau is reached. However, directly after the current ramping has finished, they are already more than a factor of 100 smaller than the applied current. Consequently, they influence the overall current density by about $<0.5\%$ and thus are insignificant already directly after the current ramping for the given ramp rate of $2.2\,\mathrm{A/s}$.

3.3.2. Mechanical margins

For a precise undulator adjustment, all modular coils have to be placed to meet the target values. Otherwise, *B*-field components of higher order may be introduced due to deviations in the pitch, shearing, or roll angles. To avoid this, pin holes and rods are mainly designated to align the VR coils to a full-size undulator. However, deviations in the superconductor stack height might appear, e.g. due to the acting Lorentz forces of the coated *Re*BCO tapes. A direct influence on the magnetic field amplitude B_0 would be the consequence. Investigations of different stack heights were performed for modular VR coils by means of 3D electro-magnetic simulations. All models were operated with $J_{\mathrm{op}}(4.2\,\mathrm{K}) = 2071\,\mathrm{kA/mm^2}$ for their designed 5 mm superconductor stack height. A relatively large height reduction of 8% (here 0.4 mm) corresponds to a relative change in B_0 of -9%, whereas smaller variations of 2% (here $\pm 0.1\,\mathrm{mm}$) show a relative change in B_0 of approximately $\pm 2\%$. Consequently, the coils need precise coil winding techniques as well as strong support during powering to avoid any tape stack movement that may cause variation.

3.3.3. Phase errors and their effects on undulator radiation

As introduced earlier, undulators are mainly used as light sources. Having seen different sources of malfunction implies the question of tolerable field deviations for the undulator radiation. Here, unfortunately, no straightforward answer can be deduced. It is not only a matter of relative amplitude deviations but also of their distribution and is best to be evaluated in a short model magnet. A comprehensive description concerning undulators can be found in [129], which is briefly summarized in the following.
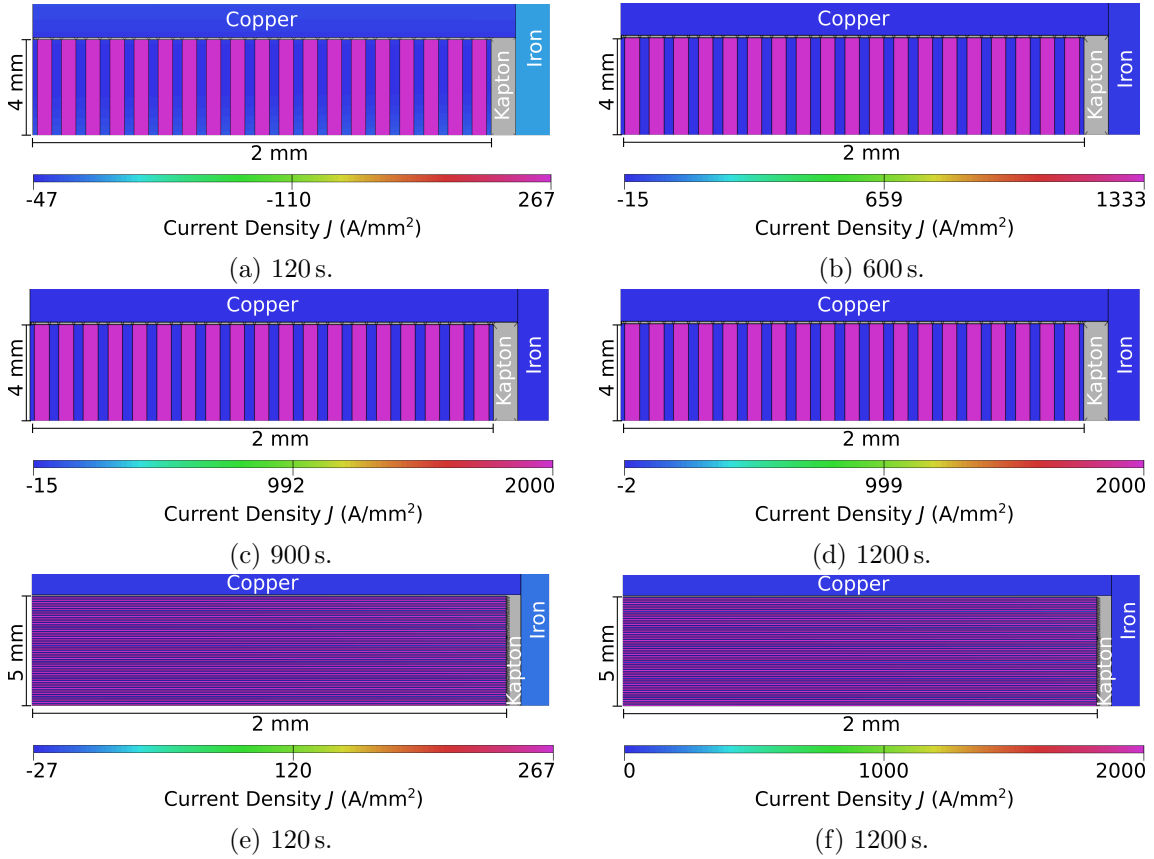
Figure 3.20.: Close-ups of current density rampings with caused eddy currents in 2D 13 mm period, 6 mm gap undulator geometries at 4.2 K. Each graph shows about half an undulator groove. (a) to (d) HR geometry, (e) and (f) VR geometry.

Three main types of phase errors can be found. First, smooth variations along the undulator length L_{ID} caused by steady varying field amplitude errors are defined as systematic errors (σ_{sm}). They originate most likely from a variation in the magnetic gap, but can also arise from another parameter variation such as periodicity. Second, local magnetic field errors may generate random phase errors (σ_{Ψ}), thus can be described by a random-walk process, which can further introduce errors in the electron trajectory as well as angular errors. The latter causes phase oscillation (σ_{Δ}) between negative and positive poles as the third error type. However, phase oscillations are rather small, having relatively less influence on the radiation's spectral properties. Random and systematic malfunctions, in contrast, both typically reduce the peak brilliance, whereas the systematic component may additionally broaden the brilliance spectrum, causing a deteriorated integrated flux, yet not to the same amount.

In general, phase errors are built up cumulatively from all three types. A good figure of merit to describe the potential peak brilliance reduction, independently of the number of magnet poles, is the overall rms phase error σ_{ϕ}, which can sum all three error types as

$$\sigma_{\phi} \simeq \sqrt{\sigma_{\mathrm{sm}}^2 + \sigma_{\psi}^2 + \sigma_{\Delta}^2} \ . \tag{3.1}$$

It was shown that the on-axis peak brightness due to phase errors is reduced by a factor $R_{\hat{\mathcal{B}}} = \mathrm{e}^{-m^2 \sigma_{\phi}^2}$ [130]. However, the rms local phase error as in the reduction factor $R_{\hat{\mathcal{B}}} = \mathrm{e}^{-a \cdot m^2 \sigma_{\psi} n_p}$ may be the better or rather additional choice to the rms phase error for describing the integrated flux reduction, though being dependent on the number of magnetic poles n_p and a constant a.
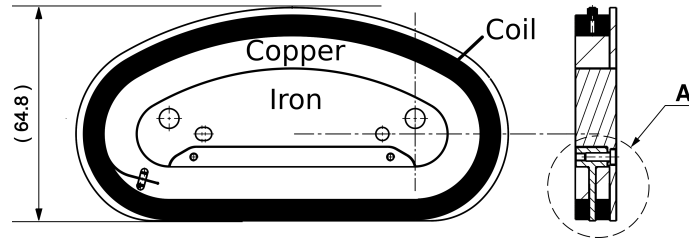
Figure 3.21.: Technical drawings of the VR coil. Front view (left) and cross-section (right). Zone A is displayed in Figure 3.29 in more detail. Measures in millimeters.
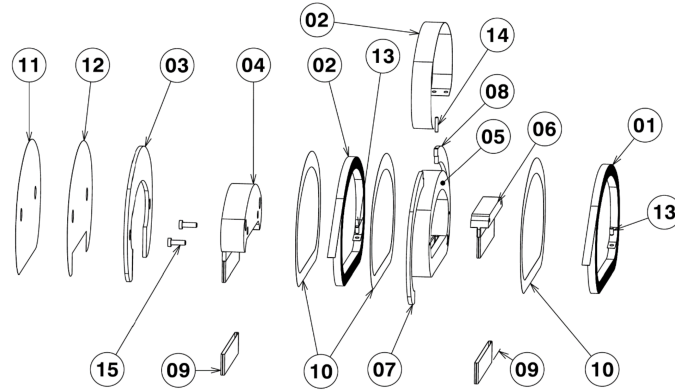
Figure 3.22.: Exploded view of the VR coil. (1) VR sub-coil 1, (2) VR sub-coil 2 with 10 mm wide HTS connection tape, (3) G11 insulation, (4) iron body with lateral pole, (5) copper winding body, (6) iron body with center pole, (7) and (8) central G11 insulation, (9) Kapton$^{®}$ insulation sleeves, (10), (11), (12) Kapton$^{®}$ insulation sheets, (13) pin to fix the tape, (14) G11 dowel, (15) hex socket low head screws, for fixing the iron parts.

3.4. A coated *Re*BCO tape-based vertical racetrack design

The above-presented investigations of electro-magnetic and mechanical performances led to the technical design of a vertical racetrack undulator prototype coil: the VR coil. Design parameters for the three planned prototype coils can be found in Table 3.3. As presented earlier and already displayed in Figure 3.1a, the VR coil spans over an undulator period of 13 mm housing two VR sub-coils Both sub-coils are wound on the same winding body, which consists of a 10.5 mm wide and 9.9 mm thick copper ring including an iron core and poles for B-field enhancement.

The period consists of two 4 mm wide superconducting tape stacks with 5 mm of height and two 2.2 mm wide iron poles, leaving some margin e.g. for insulation. This modular construction should allow easy replacement of single periods within a long undulator magnet, in case of need. The central iron body includes pinholes and voids for aligning the coils by means of rods and pins when being stacked to a full-size undulator. Figure 3.21 presents a technical drawing with a side and cross-section view. Here, the iron core is split into two parts: the central iron pole and the iron core connected to the lateral iron pole, which allows an assembly by sliding them one after another into the copper winding body and clamping them together with two screws (c.f. also Figure 3.29). All parts needed for the VR coil manufacturing are presented in Figure 3.22 in form of an exploded component view.

Table 3.3.: Design parameters of the VR undulator coils

$\lambda_\mathrm{u} = 13\,\mathrm{mm}$	**VR coil #1, #2**	**VR coil #3**
Sub-coil cross-section	$4 \times 5\,\mathrm{mm}^2$	$4 \times 4.6\,\mathrm{mm}^2$
HTS tape manufacturer	Bruker HTS	SuperPower
HTS tape dimension	$4\,\mathrm{mm} \times 100\,\mathrm{\mu m}$	$4\,\mathrm{mm} \times 45\,\mathrm{\mu m}$
∟ substrate thickness	$50\,\mathrm{\mu m}$	$30\,\mathrm{\mu m}$
Number of turns	51	102
∟ cable type	single HTS tape	single HTS tape
$J_\mathrm{c,e}$ in self-field at $77\,\mathrm{K}$ (LN$_2$)		
$J_\mathrm{c,e}(0.6\,\mathrm{T}, 77\,\mathrm{K})$	$75\,\mathrm{A/mm}^2$	$222\,\mathrm{A/mm}^2$
$I_\mathrm{c,sim}(0.6\,\mathrm{T}, 77\,\mathrm{K})$	$30\,\mathrm{A}$	$40\,\mathrm{A}$
$B_0(I_\mathrm{c}, 3.5\,\mathrm{mm})$	$0.14\,\mathrm{T}$	$0.28\,\mathrm{T}$
$80\%\ J_\mathrm{c,e}$ in self-field at $4.2\,\mathrm{K}$ (LHe)		
$J_\mathrm{e}(4.9\,\mathrm{T}, 4.2\,\mathrm{K})$	$2071\,\mathrm{A/mm}^2$	$2222\,\mathrm{A/mm}^2$
$I_\mathrm{sim}(4.9\,\mathrm{T}, 4.2\,\mathrm{K})$	$828\,\mathrm{A}$	$400\,\mathrm{A}$
$B_0(I_\mathrm{sim}, 3.5\,\mathrm{mm})$	$1.38\,\mathrm{T}$	$1.24\,\mathrm{T}$
Stored energy	$130.4\,\mathrm{J}$	$130.5\,\mathrm{J}$
Inductance	$380.4\,\mathrm{\mu H}$	$380.7\,\mathrm{\mu H}$
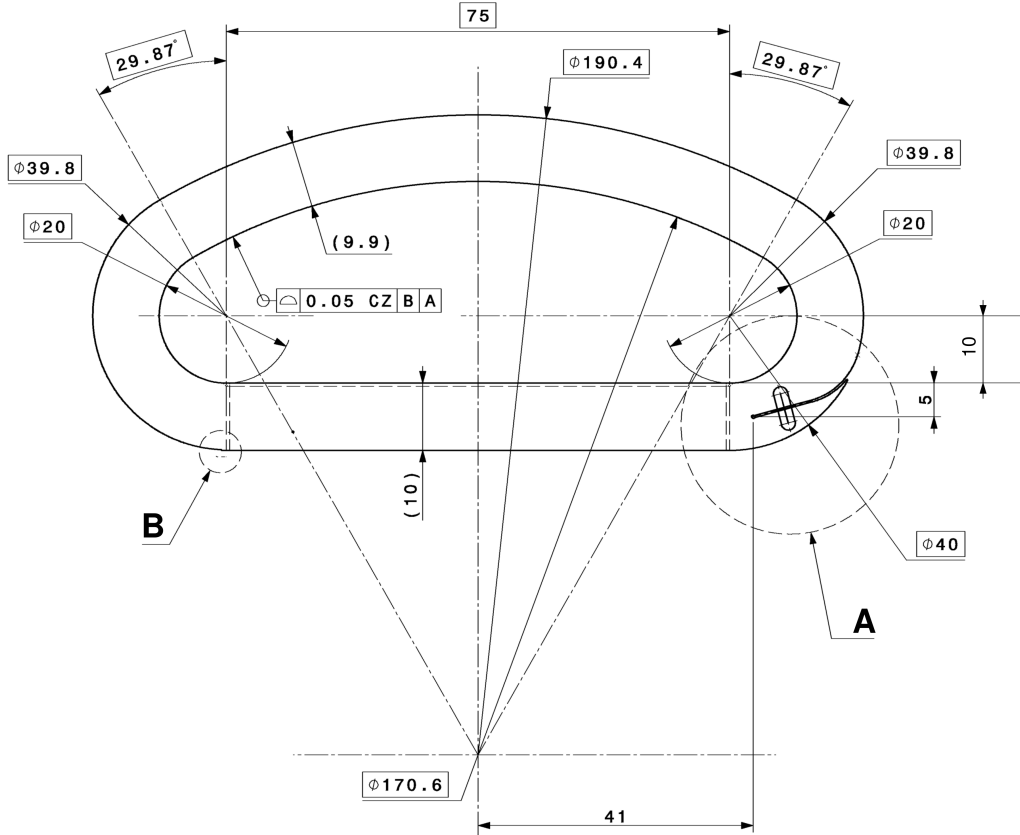
Figure 3.23.: Technical drawings of the VR coil's copper body. (A) Slit and pinhole to fix the HTS tapes, including the 10 mm wide and 100 µm thick connection HTS tape, and start the coil winding. (B) Endpoint of the connection HTS tape. All dimensions and measures are given in millimeters.

The three VR coils were manufactured from two different coated *Re*BCO superconducting tapes, both having a width of $w_{\text{tape}} = 4 \pm 0.2$ mm:

- Two coils wound from Bruker HTS tape, with a thickness of $t_{\text{tape}} = 100$ μm.

  - Designed to withstand mechanical stress and for operations at low temperatures (≤ 20 K),

  - Experimentally determined $I_{\text{c}}(77\,\text{K}, \text{s.f.}^{[1]}) \approx 92$ A and $I_{\text{c}}(4.2\,\text{K}, 5\,\text{T}) \approx 735$ A.

- One coil wound from SuperPower HTS tape (SCS4030-AP), with a thickness of $t_{\text{tape}} = 45$ μm.

  - Designed for high current densities and small bending radii,

  - Experimentally determined $I_{\text{c}}(77\,\text{K}, \text{s.f.}^{[1]}) \approx 178$ A and $I_{\text{c}}(4.2\,\text{K}, 5\,\text{T}) \approx 650$ A; $I_{\text{c}}(4.2\,\text{K}, 7\,\text{T}) \approx 550$ A

As a consequence of the different tape thicknesses t_{tape}, the designated conductor cross-section of 4×5 mm² has to be filled with a different amount of turns $n_{\text{turns}} = 5\,\text{mm}/t_{\text{tape}}$. The two VR coils wound from Bruker HTS tape, therefore, have 50 turns, plus 1 turn as a safety margin.

As shown in Figure 3.23, the straight section and the two different arc types then define the total length of tape l_{tape} needed for one VR sub-coil with n being the layer number wound:

$$l_{\text{SideArc}} = \frac{150.13°}{360°} \cdot 2\pi \cdot (20\,\text{mm} + n \cdot t_{\text{tape}})\,\text{mm} \ , \tag{3.2}$$

$$l_{\text{CenterArc}} = \frac{59.74°}{360°} \cdot 2\pi \cdot (95.3\,\text{mm} + n \cdot t_{\text{tape}})\,\text{mm} \ , \tag{3.3}$$

$$l_{\text{Tape,Bruker}} = \int_0^{51} 75\,\text{mm} + 2l_{\text{SideArc}} + l_{\text{CenterArc}}\,\mathrm{d}n \approx 15\,\text{m} \ . \tag{3.4}$$

Equation (3.4) shows that a total length of approximately $2 \times 15\,\text{m} = 30\,\text{m}$ of Bruker HTS tape is needed for a VR coil. For the thinner SuperPower HTS tape, the amount would increase to 2×33 m. However, for a better direct comparison in terms of magnet charging times, the coil wound with the SuperPower HTS tape was decided to have exactly double the turns compared to the other two (102 vs. 51). This results in a reduced tape stack height of 4.6 mm instead of 5 mm and requires $l_{\text{Tape,SuperPower}} \approx 2 \times 30$ m.

A non-insulated (NI) coil winding procedure is chosen for all to deal with the relatively high current densities with respect to the quench protection (see subsection 3.4.5). Further details concerning the ideal VR coil design, directly linked to the operation of the coils, are presented in the following part of this section. Final technical drawings with applied margins are attached in appendix C.

3.4.1. Support structure

As mentioned earlier, a structure has to prevent any movement of the coated *Re*BCO tapes during the powering tests and keep the coils compressed during cool-down and operation. The support structure was designed to consist of non-magnetic stainless steel (here 316LN) and insulation plates (G10), supporting the coil and the copper leads. An exploded view of the VR coil sitting in the center is shown in Figure 3.24. From its flat sides, the VR coil is supported by G10 plates bolted together by means of stainless steel plates. The flat bottom and side arcs of the VR coil sit in two Kapton®-insulated stainless steel bodies, while copper leads clamp the coil from the top and provide the electrical connection to

---

[1]self-field
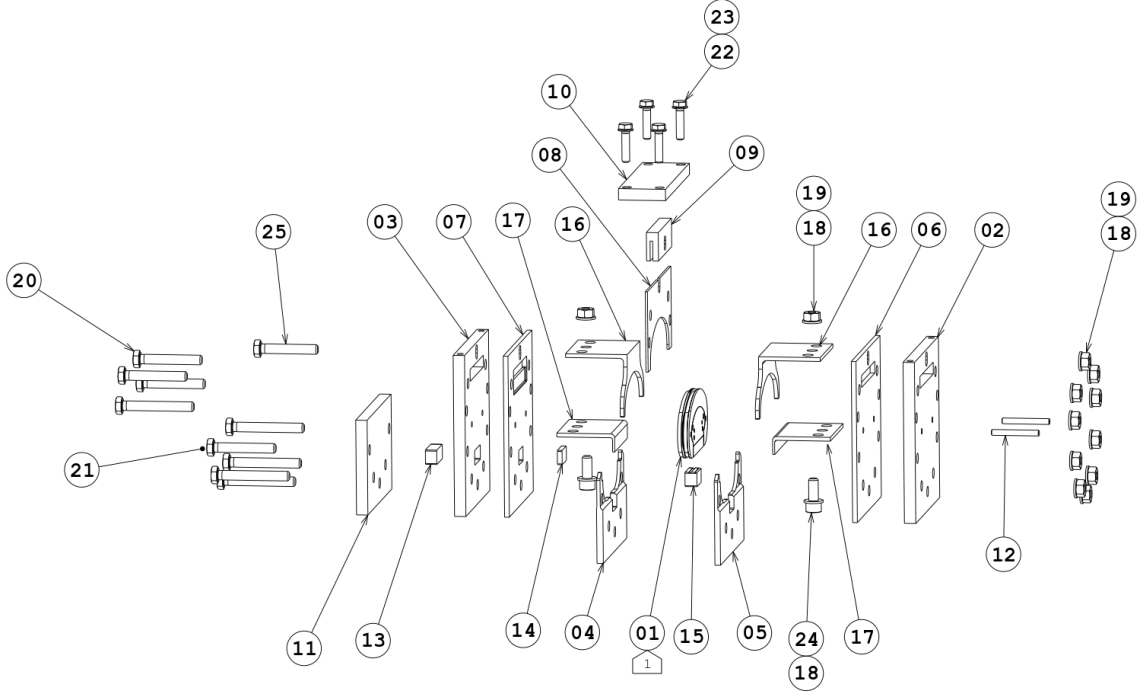
Figure 3.24.: Exploded view of the support structure based on stainless steel (ss). (1) VR coil, (2) and (3) ss plates, (4) and (5) lower ss support, (6) and (7) G10 plates, (8) central G10 divider, (9) upper G-10 stamp, (10) top ss plate, (11) ss cover plate, (12) G10 dowels, (13), (14), (15) filler blocks for sensors (ss and G11), (16) copper leads, (17) G10 leads support, (18) and (19) M10 ss washer and nut, (20) M10x65 ss screws, (21) M10x75 ss screws, (22) M8x35 ss screw, (23) M8 bronze washer, (24) M10x25 ss screw, (25) M10x65 ss screw.

the power supply. Therefore, a good electrical connection must be established between the copper leads and the outermost turns of the VR coil, achieved by an estimated contact pressure of around 5 MPa. The pressure can be enforced by torquing down the four M8 bolts on the top plate. Spring washers were placed on the bolts to keep the clamping pressure during cool-down.

The stress area (threaded part) of an M8 bolt is $36.6\,\mathrm{mm}^2$. The load should not exceed 75% of the maximum capacity load. Taking the yield stress of an A4-50 stainless steel bolt with 500 MPa, the maximum allowed load for one bolt is then

$$F_{\mathrm{max}} = 500\,\mathrm{MPa} \cdot 36.6\,\mathrm{mm}^2 \cdot 0.75 = 13.725\,\mathrm{kN} \ . \tag{3.5}$$

The area A of the 4 mm wide copper leads on the VR coil is given with values in equations (3.2) and (3.3) for $n = 51$. The force needs to create a pressure of 5 MPa on both copper leads:

$$F_{\mathrm{CuLeads}} = 2A \cdot 5\,\mathrm{MPa} \approx 6.3\,\mathrm{kN} \ . \tag{3.6}$$

With four screws, this force can equally be distributed via the top plate. However, during the cool down to 4.2 K there is a variation in the material shrinkage between copper and steel. The total linear contraction of a length L from room temperature (RT) to a temperature T is defined as the following fraction, thus given in %:

$$\frac{\Delta L}{L} = \frac{L_{\mathrm{RT}} - L_{\mathrm{T}}}{L_{\mathrm{RT}}} \ . \tag{3.7}$$

When cooling down from room temperature to 4.2 K, copper shrinks 0.327%, stainless steel 0.296%, and G10 0.241% [68]. With the given dimensions in the order of 13 mm

this results in a maximum shrinkage of 40 µm, which can easily be covered by the applied clamping pressure. Spring washers on each screw respectively need to compensate for this and maintain the pressure. For full compression, 885 N is the maximum force an M8 spring washer can take, according to its manufacturer. With equation (3.6), the four M8 bolts need to provide 6.3 kN, which leads to

$$6.3\,\text{kN}/4 = 1.575\,\text{kN} \ . \tag{3.8}$$

Consequently, two spring washers per bolt should be sufficient. On both sides, the stainless steel plates are bolted together by ten M10 bolts. From the electro-magnetic calculations, a maximum of combined forces on the side plates plus margin can be estimated to 36 kN at 4.2 K. Taking a maximum allowed load of around 20 kN per M10 bolt, this can easily be handled by the provided configuration.

3.4.2. Temperature margin

Superconducting magnets have to operate in a cryogenic environment. As cryostats have a significant energy consumption, minimizing the heat dissipation during the operation is always crucial when designing superconducting magnets, e.g. a full-size undulator. In the case of the investigated modular superconducting undulators in this work, electrical joints are most likely the main heat contribution. Further heat sources may be eddy currents or the impact of synchrotron radiation on the magnet, which should be further investigated.

3.4.2.1. Resistive joints

Based on the operating experience at KARA, KIT, an absolute cooling power of 2 W/m is estimated to be well feasible at 4.2 K [19]. The designed undulator period length of 13 mm then defines the heat load threshold per undulator period as

$$2\,\text{W/m} \cdot 13\,\text{mm} = 26\,\text{mW} \ . \tag{3.9}$$

A full undulator model requires two VR coils, consequently, 13 mW for a single modular VR coil should be met. In an early design stage, both sub-coils were soldered directly to the shared copper winding body as it would connect them electrically. However, to reduce the heat load and enhance the electrical connection between the two sub-coils, a 10 mm wide coated *Re*BCO tape was included in the design as a superconducting connection, the so-called "c-tape". The innermost turns of both sub-coils should be soldered face-to-face with their superconducting sides to this c-tape, thus aiming for the lowest possible resistance between the superconductors. For this orientation, a joint area resistance of $R_{\text{joint,f2f}} = 36\,\text{n}\Omega\,\text{cm}^2$ at 4.2 K was derived from earlier CERN internal investigations [131]. Potential low-temperature solders to protect the superconducting properties are presented in Table 3.4. As the straight section of the coils face the beam pipe, this is designed to be along the curved side of the D-shaped winding body (c.f. Figure 3.23).

In view of the entire design, the straight length is chosen to be 75 mm long, providing a large enough good B-field region but also supplying a joint surface of $A_{\text{jointC}} = 9.53\,\text{cm}^2$ for a single sub-coil. Assuming an operational current of $I_{\text{op}}(4.2\,\text{K}) = 828\,\text{A}$, this gives a power dissipation for the outgoing current of

$$P_{\text{sub−coil,out}} = I_{\text{op}}(4.2\,\text{K})^2 \cdot \frac{R_{\text{joint,f2f}}}{A_{\text{jointC}}} \approx 2.6\,\text{mW} \ . \tag{3.10}$$

The same may be feasible for the in-going current, doubling $P_{\text{sub−coil,out}}$. Therefore, including the connections to the neighboring VR coils when being stacked to a full-length

Table 3.4.: Potential solders for coated ReBCO superconducting tape with melting temperatures below $200\,°C$ and their tensile strength at room temperature [68]. Solders marked with ^{A} and $^\Omega$ were chosen for the VR coil's first and last turn.

Solder	Melting temperature in $°C$	Tensile strength in MPa
63Sn-37Pb	183	52
62Sn-36.65Pb-0.35Sb	183	-
62Sn-36Pb-2Ag (Sirius 1DI) ^{A}	179	44
In	157	1.9
97In-3Ag $^\Omega$	143	5.5
52In-48Sn	118	11.8
66.3In-33.7Bi	72	-
50Bi-25Pb-12.5Sn-12.5Cd (Wood's metal)	70	31

undulator with many periods, one VR coil may emit a total power of

$$P_{\text{VRcoil,total}} = 4 \cdot P_{\text{sub-coil,out}} = 10.4\,\text{mW} \ , \tag{3.11}$$

leaving some margin to the threshold value. Copper terminals for in- and out-going current of the full undulator magnet will also include HTS current leads and most likely have extra cooling supplies, e.g. by boiling helium.

3.4.2.2. Eddy currents

Caused by a change in the magnetic field, eddy currents arise during the ramping of the undulator magnet. This is investigated in the previous subsection 3.3.1 with respect to the field quality. A second possible cause of a rapid magnetic field change would be a quench of the superconducting undulator magnet. For both scenarios, 2D electro-magnetic simulations show rather small eddy currents in the stabilizing copper and iron parts of the coil, rather fast decaying. Consequently, these eddy currents would not contribute significantly to the heat load and thus can be neglected.

However, persistent eddy currents in the superconducting tapes may be an issue for the field quality and should be further investigated. One possible countermeasure might be to power the VR coils close to their critical current, leaving less room in the superconductor for eddy currents. Another approach might be to power the NI coils first above their critical current if possible when having stabilized them with enough normal conducting material. After driving the current down slowly to the operational value, the magnetic field may change less, thus inducing less persistent eddy currents.

3.4.3. Magnetic measurement

Together with the VR coil design, a supporting structure based on non-magnetic stainless steel is framed as earlier described in detail. A pocket for measurement instrumentation is provided in this structure, right below the center of the straight coil section, where the beam pipe would be located.

Two Hall sensors from the company AREPOC were utilized to measure the magnetic field amplitude B_0 below the two iron poles of the VR coil. Both sensors had dimensions of $5 \times 7 \times 1\,\text{mm}^3$ and were operated with $100\,\text{mA}$. To ensure a mechanically stable operation between room temperature and $1.5\,\text{K}$, the Hall sensors were glued on a ceramic plate, which
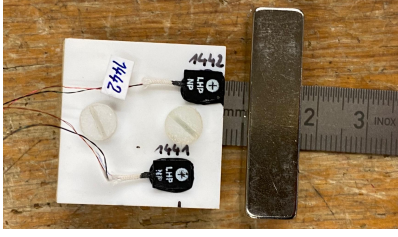
Figure 3.25.: Picture of the two used Hall sensors (No. 1441 and 1442) glued to a ceramic plate in front of a bar magnet for signal tests at 300 K. Scale in cm.

(a) Charging. (b) Steady state powering. (c) Discharging.
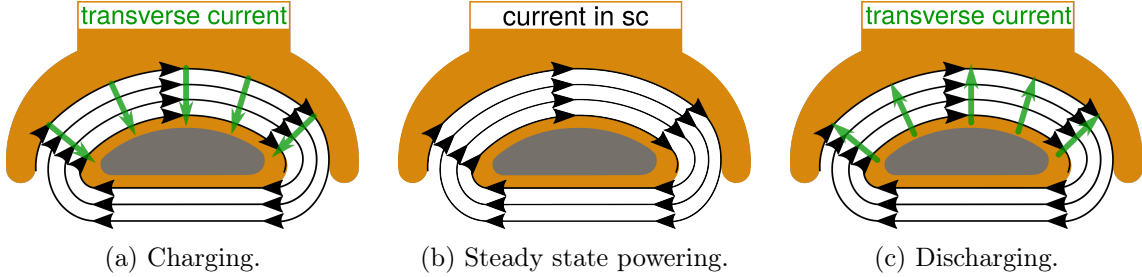
Figure 3.26.: Illustration of current paths in a non-insulated VR coil. The superconductor and its current are shown as a spiral with a current direction. A transverse current flow during (dis-)charging skips this spiral as shown in (a) and (c). Copper and iron bodies are sketched in solid colors and are not to scale.

was screwed to a G10 block. The prepared block with Hall sensors No. 1441 and 1442 can be seen in Figure 3.25, with a permanent bar magnet in front of the sensors to test their setup. The entire set-up is inserted in the supporting structure and fixed with a screw from the outside, as seen in the next chapter's Figure 5.1b. When in place, the Hall sensors' active areas were at distance $d = 3.5$ mm below the iron poles.

3.4.4. Insulation

The VR coil is targeted to be a non-insulated (NI) coil, as already stated earlier. Consequently, no insulating material is located in between the coils' turns, allowing the current to freely distribute in transverse directions. Therefore, the voltage signals across the coils may appear other than for an insulated coil. This should be especially true during the charging and discharging process, for which the current flow is displayed in Figure 3.26. A simplified version of the VR coil's circuit diagram can be found in Figure 3.27. During charging the superconducting VR coil, the current can choose between the transverse path with resistance $R_{\mathrm{tr},i}$ or the superconductive but inductive path with $R_{\mathrm{SC},i}$ and $L_{\mathrm{SC},i}$ of each sub-coil i. In the beginning, the current is most likely pushed in both routes, causing a voltage increase across the coil before slowly flowing completely into the superconducting spiral, resulting in a voltage decay. For a steady-state operation, the current flows in the superconducting path. When driving down the current in the VR coil, a transverse current flow may again appear, enabling a faster discharge and a negative voltage across the coil. In order to separate the NI sub-coils from each other, two 2.3 mm thick and 7.3 mm high quadrant G11 plates cover the round sides of the VR coil. A schematic cross-section view can be seen in Figure 3.28. Only the innermost turns of each sub-coil are connected, being both soldered to the 10 mm wide superconducting connection tape.

In the straight part of the D-shaped VR coil, the two iron poles replace the G11 separator. They are wrapped in a double layer of 50 µm thick Kapton® foil, to insulate the superconducting tape stacks from each other as shown in Figure 3.29. One 2 mm thick semicircular G11 plate covers the back side of the VR coil together with two Kapton® foils. There is no insulation planned between the copper and the iron bodies, nor between the copper winding body and the coated ReBCO tapes.

Figure 3.27.: A simplified circuit diagram for one turn sub-coils of the VR coil. The two main potential current paths (transverse and circular) in the NI sub-coils are shown. Both inductances $L_{\mathrm{sc},i}$ may interact because of the small physical distance which can be described by a mutual inductance L_{M} in an electrical circuit model as shown in [132]. Graphic adapted from [114].

Figure 3.28.: Schematic cross-section of the two sub-coils of the VR coil. Current can always flow along the superconductor or transverse. Both sub-coils are separated by a G11 insulation and only connected by a 10 mm wide connecting coated ReBCO tape conductor.

Figure 3.29.: Ideal technical close-up from Figure 3.21 of the 13 mm period VR coil with its iron poles and sub-coils. Materials are given by number: (1) iron body with pole 2, (2) iron pole 1, (3) copper body, and (4) ReBCO tape layers. Applying mechanical margins changes the numbers slightly. All measures are in millimeters.

(a) Transverse current.

(b) Hotspot with heating.

Figure 3.30.: Illustration of current paths in the dry wound, non-insulated VR coil for an existing hotspot. The superconductor and its current are shown as a spiral with a current direction. A transverse current flow skips this spiral, can redistribute, and therefore cause local heating. Copper and iron bodies are sketched in solid colors and are not so scale.

3.4.5. Quench detection and coil protection

With the application of high-temperature superconductors like *Re*BCO, magnets may be operated by engineering current densities of $J_{\mathrm{op}} \geq 2 \, \mathrm{kA/mm^2}$. For these high current density regions, the protection of a magnet is still challenging, especially in a quench event (see section 2.4.1). The here presented VR coil utilizes a non-insulated (NI) winding approach, allowing the current to redistribute to the neighboring turns within the coil to bypass normal conducting zones or to enlarge them, causing a reduction in the hotspot temperature.

Figure 3.30a illustrates a transverse current flow, e.g. if the coil becomes completely normal conductive, whereas Figure 3.30b shows schematically the current paths in case of a local hotspot, where the current may skip one or more turns. However, if the hotspot exceeds the critical temperature of the superconductor, a transition to the normal conducting state is triggered, which is referred to as quench. This irreversible transition forces all the current to flow through the stabilizing material of the conductor, thus the copper coating, generating resistive heating. For high current densities, the heating will enforce a steep increase in temperature of the entire coil or magnet which may cause severe damage to the materials, including the superconductor. Therefore, the magnet has to be switched off. To detect a potential quench that would be seen in a rise in voltage, the voltage will be monitored across both sub-coils by means of voltage taps on the inner- and outermost turns. The presented NI-designed VR coil allows a fully transversal current flow, with the copper winding body ring acting as additional stabilizing material. This may gain some time for driving down the current or even allow the complete energy to be dumped into the VR coil itself, depending on the available cooling power. Another protection is the modular VR coil design. The LHC beam diagnostics undulator demonstrated that each half period may be monitored and protected individually using parallel connected resistors [109]. The energy will be extracted into the resistor and the current can bypass the affected undulator coil in case of a quench. As seen in Table 3.3, the stored energy in the VR coil is rather small ($\ll 1 \, \mathrm{kJ}$).

However, the high J_{op} has to be extracted in case of a quench to avoid burning the VR coil. As mentioned in the previous chapter, the characteristics of the HTS materials make it quite challenging to model a quench in detail. For this reason, adiabatic conditions were assumed using an estimation of the quench load at a homogeneous B-field to get a conservative approximation for the hotspot temperature over time.
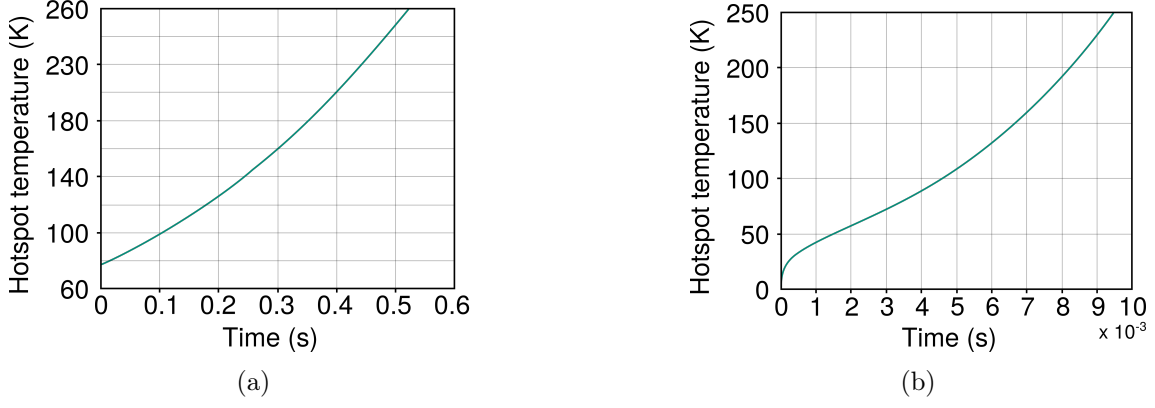
Figure 3.31.: Hotspot temperatures over time for an operating VR coil with a copper RRR of 100. (a) $I_{\mathrm{op}}(77\,\mathrm{K}) = 112\,\mathrm{A}$ and (b) $I_{\mathrm{op}}(T_0 = 4.2\,\mathrm{K}) = 900\,\mathrm{A}$.

Defined operating currents $I_{\mathrm{op}}(T_0 = 4.2\,\mathrm{K}) = 900\,\mathrm{A}$ and $I_{\mathrm{op}}(77\,\mathrm{K}) = 112\,\mathrm{A}$ lead to the following equation [36, 62]:

$$\int_{t_0}^{t} I_{\mathrm{op}}(t)^2 \mathrm{d}t = \eta A^2 \cdot \int_{T_0}^{T_{\mathrm{max}}} \frac{c_{\mathrm{v}}(T)}{\rho_{\mathrm{e}}(T, RRR)} \mathrm{d}T \,, \tag{3.12}$$

with t_0 being the starting time of an occurring quench, the cross-section of the tape A, the volumetric filling factor of copper η, and the operating and hotspot temperature T_0 and T_{max}. The temperature-depended parameters are the volumetric heat capacity c_{v} and the electrical resistivity ρ_{e}. The latter also depends on the applied magnetic field as well as the RRR. Here, a constant B-field of $B(4.2\,\mathrm{K}) = 6\,\mathrm{T}$ and $B(77\,\mathrm{K}) = 0.6\,\mathrm{T}$ as well as a RRR of 100 are assumed. c_{v} and ρ_{e} are calculated as the mean of $50\,\mu\mathrm{m}$ copper and $50\,\mu\mathrm{m}$ stainless steel, being stabilizer and substrate of the coated ReBCO superconducting tape. The quench detection can be triggered within Milliseconds. Figure 3.31 shows the hotspot temperature rise over time for the two investigated operating temperatures. The superconducting properties of ReBCO begin to degrade around $200\,^{\circ}\mathrm{C}$, thus $473\,\mathrm{K}$. With reaction times until reaching $250\,\mathrm{K}$ of more than $0.5\,\mathrm{s}$ at $77\,\mathrm{K}$ and $9\,\mathrm{ms}$ at $4.2\,\mathrm{K}$, the system should have enough time to dump the energy and the current. This analysis shows that the protection of a high-current density operation of the VR coil is feasible within the given time constraints.

(a) First design with close-ups.   (b) Elaborated design with tape.
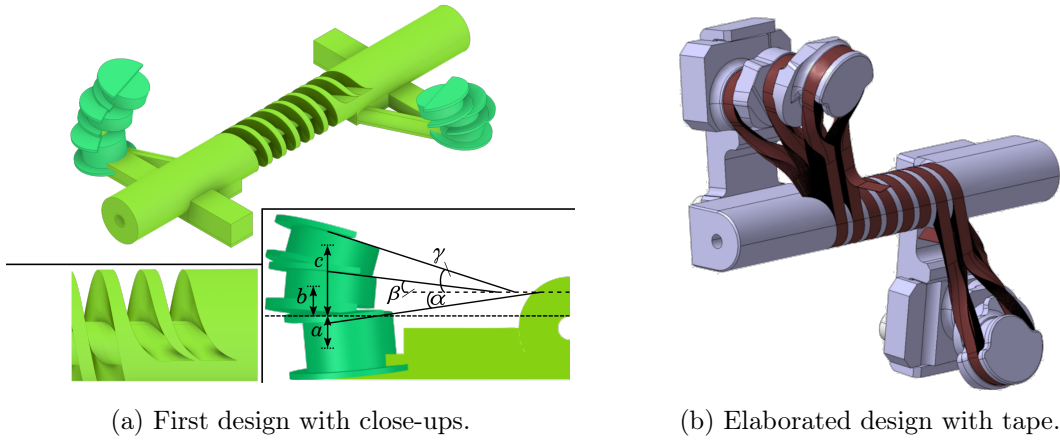
Figure 3.32.: Option 1 for a helical undulator based on a bifilar helix, wound from coated
ReBCO tape superconductor. The tape is returned via three spools along the
side of the undulator. Both tape stacks exit parallel on the same height level.

3.5. Coated ReBCO tape-based helical undulator designs

The research of this work included the design of helical undulators, wound from coated
ReBCO tape superconductor. So far, helical undulators already exist in the form of per-
manent magnet structures as well as superconducting undulators, wound from Nb-Ti wires
[21, 133, 22]. Especially superconducting helical undulators have proven to be very com-
pact with a small footprint and efficient in terms of light production by surrounding the
beam pipe producing circularly polarized photons. Therefore, and in contrast to e.g. a
VR coil geometry, almost the entire length of the superconductor may contribute to the
magnetic field amplitude on the beam axis, making it an attractive choice for the use of still
rather expensive HTS materials concerning the superconductor length. In the following,
the very first designs up to date of an HTS tape wound helical undulator to the author's
knowledge are presented.

The major part of the helical undulator consists of a bifilar helix with winding pitches of
13 mm, which correspond to λ_u. A helix in a 3-dimensional Cartesian coordinate system
can be described in $\hat{z}$-direction, which is equivalent to the beam direction, as stated in the
previous chapter's section 2.1.2. The winding body is suggested to be 3D printed from
titanium to ensure rigidity and should be anodized for electrical isolation. To cover and
support the helical structure from the outside, a tube may be installed. The superconductor
stack cross-section was optimized to 4×6 mm, making it convenient to utilize 4 mm wide
coated ReBCO tape superconductor. The presented helical undulator is designed with a
magnetic gap of 5 mm, implying a minimum bending radius of 2.5 mm for the innermost
and a maximum bending radius of 8.5 mm for the outermost turn. The very first turn may
also be wound with a copper tape of $\leq 100\,\mu m$ thickness to prepare the best possible wind-
ing surface for the tape superconductor. The challenge of the tape winding is the tape's
limited degrees of freedom when it comes to bending directions compared to a round wire
as well as the changing winding angle with increasing radius (see also Figure 4.17 in the
following chapter). This is taken into account when designing the two different coil ends.
Table 3.5 presents the main design parameters of the helical undulator short model and
its planned demonstrator. Both helical magnets are to be manufactured using 4 ± 0.2 mm
wide superconducting ReBCO tape from the supplier SuperPower (SCS4030-AP), hav-
ing the currently thinnest available stabilizer thickness of only $30\,\mu m$, which is crucial for
realizing small bending radii down to 2.5 mm.

Table 3.5.: Design parameters of the helical undulator short model (SM) and its demonstrator (Demo), based on design option 2. Both have a 5 mm magnetic gap.

$\lambda_\mathrm{u} = 13\,\mathrm{mm}$	Helical undulator SM	Helical undulator Demo
Sub-coil cross-section	$4 \times 6\,\mathrm{mm}^2$	$4 \times 0.6\,\mathrm{mm}^2$
HTS tape manufacturer	SuperPower HTS	SuperPower
HTS tape dimension	$4\,\mathrm{mm} \times 50\,\mathrm{\mu m}$	$4\,\mathrm{mm} \times 50\,\mathrm{\mu m}$
∟ substrate thickness	$30\,\mathrm{\mu m}$	$30\,\mathrm{\mu m}$
Number of turns	120	12
∟ cable type	2 HTS tapes stack (f2b*)	2 HTS tapes stack (f2b*)
$J_\mathrm{c,e}$ in self-field at 77 K (LN$_2$)		
$J_\mathrm{c,e}(0.25\,\mathrm{T}, 77\,\mathrm{K})$	$88\,\mathrm{A/mm}^2$	$350\,\mathrm{A/mm}^2$
$I_\mathrm{c,sim}(0.25\,\mathrm{T}, 77\,\mathrm{K})$	$35\,\mathrm{A}$	$140\,\mathrm{A}$
$B_0(I_\mathrm{c}, 3.5\,\mathrm{mm})$	$0.14\,\mathrm{T}$	$0.1\,\mathrm{T}$
80% $J_\mathrm{c,e}$ in self-field at 4.2 K (LHe)		
$J_\mathrm{e}(5.6\,\mathrm{T}, 4.2\,\mathrm{K})$	$2000\,\mathrm{A/mm}^2$	$1985\,\mathrm{A/mm}^2$
$I_\mathrm{sim}(5.6\,\mathrm{T}, 4.2\,\mathrm{K})$	$800\,\mathrm{A}$	$794\,\mathrm{A}$
$B_0(I_\mathrm{sim}, 3.5\,\mathrm{mm})$	$2.0\,\mathrm{T}$	$0.6\,\mathrm{T}$

* *Re*BCO layers face-to-back (f2b), both facing the winding body.

Option 1   For option 1, the tape is returned via three spools along each side of the undulator body as displayed in Figure 3.32. This option was motivated by locating the return points away from the beam pipe, not influencing the beam. All coils are positioned with a different angle and height to accommodate the parallel in-going and out-coming tapes on the same level in the best possible average: The tilt angles are $\alpha = $ -6.5°, $\beta = 5.8$°, and $\gamma = 16.0$° for the ascending coils, respectively. The centers of the return spools are shifted in height with $a = -6\,\mathrm{mm}$, $b = 4\,\mathrm{mm}$, and $c = 9\,\mathrm{mm}$ with respect to the innermost turn. Acting on the assumption of a 50 μm thick tape superconductor, the first, lowest spool takes the first 20 turns, after which the next 30 turns are returned via the center spool before the last, top spool should take the remaining 70 turns. As the winding force will add up, the return spools with a diameter of 15 mm should be additionally supported by an external structure. They are located at a safe distance greater than 30 mm to the beam pipe, far enough not to influence the beam. However, there is no fixed support, yet, between the helix and the return spools which may accommodate the tape stack height and tape angle. To fill this gap and support the superconductor stack, a ductile material, e.g. wax or a precise 3D printed body might be used. Likewise, copper could be used as a 3D print to act as a terminal for powering the magnet. A possible disadvantage of this option 1 design may be the limited space for normal conducting current leads which most likely have to be applied via the return spool and/or in the space between the spools and the undulator structure. Another solution to overcome the lack of space might be to wind the HTS helical undulator turn-by-turn from multiple shorter single-piece lengths of superconductors which are solder-connected at the respective ends, rather than winding the magnet from one long single piece of superconductor. Especially when considering undulator lengths of several tens of meters for FELs, this might be an attractive choice. The needed further developments would have gone beyond the scope of this thesis. Nevertheless, this helical design option 1 is worth undergoing future investigations and improvements as it provides a very advantageous superconductor geometry for its return paths with respect to the magnetic flux density quality on the beam axis.
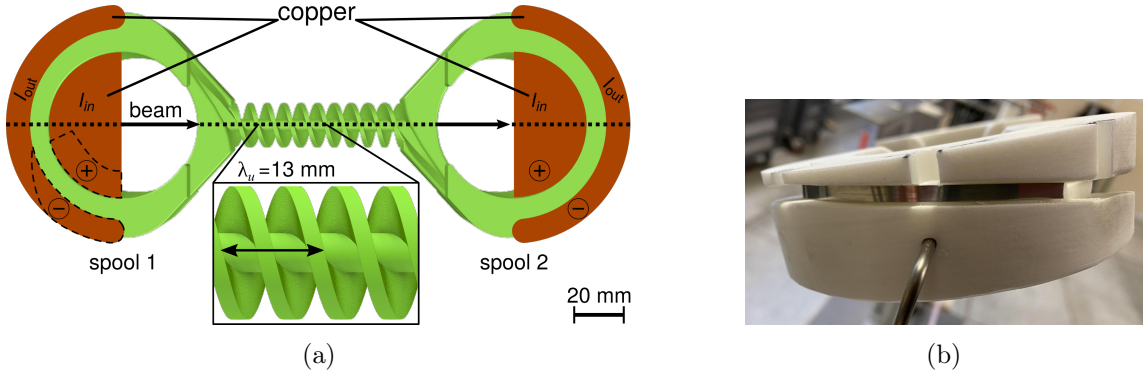
Figure 3.33.: Option 2 for a helical undulator based on a bifilar helix, wound from coated
            ReBCO tape superconductor. (a) The tape is returned via two big spools in
            line with the undulator. For the demonstrator, solely the dashed encircled
            areas were realized as terminals. Two tape stacks exit v-shaped on the oppo-
            site sides and height levels, conjoined by half a spiral on each spool as shown
            in (b).

Option 2   Design option 2 is presented in Figure 3.33 and allows all 120 turns of the
superconducting tape always to be wound on the same rigid structure, thus being mechan-
ically well supported. This design option was chosen for the manufacturing of the first
helical undulator demonstrator short model due to its simplicity and stability (see subsec-
tion 4.4.3 in the following chapter). Consequently, it is described in more detail than the
first design option.
Two bigger spools with an inner radius of 35 mm at the end of the helical structure and
in line with the undulator are used to return the tape. Therefore, the tape has to enter
and exit the undulator body v-shaped on opposite sides. The different height levels force
the tape to follow half a spiral around each return spool. Normal conducting current leads
can be placed as half circles in the region of the return spools, allowing the current to flow
radially in case of any higher resistance in the helical path, e.g. due to hotspots of normal
zones. Here, the spools' given inner radius defines an overall soldered joint area of

$$A_{\text{joint,Hel}} = 4\,\text{mm} \cdot 2\pi \cdot 35\,\text{mm} \approx 8.8\,\text{cm}^2 \ . \tag{3.13}$$

The above-presented VR coil design provides a joint area in the same order of magnitude
(cf. equation (3.10)) for a similar operating current value $I_{\text{op}}(4.2\,\text{K})$. However, a face-to-
back (f2b) superconductor configuration is applied due to the approach of using a two-tape
stack cable. As a result, the current will face a direct soldered connection from the copper
terminal to the first tape, followed by an f2b configuration for the second tape. From
earlier investigations at CERN [131], a joint area resistance $R_{\text{joint,f2b}} = 290\,\text{n}\Omega\,\text{cm}^2$ was
experimentally determined for this configuration. An approximation of the total power
dissipation of the in-going and out-going joint with $I_{\text{op}}(4.2\,\text{K}) = 800\,\text{A}$ yields:

$$\begin{aligned}
P_{\text{Hel,in-out}} &= 2\left(P_{\text{tape1}} + P_{\text{tape2}}\right) \\
&= 2\left(I_{\text{op}}(4.2\,\text{K})^2 \cdot \frac{R_{\text{joint,f2f}}}{A_{\text{joint,Hel}}} + \left(\frac{I_{\text{op}}(4.2\,\text{K})}{2}\right)^2 \cdot \frac{R_{\text{joint,f2b}}}{A_{\text{joint,Hel}}}\right) \approx 15.8\,\text{mW} \ .
\end{aligned} \tag{3.14}$$

The here provided area satisfies the constraint of 2 W/m (or rather 26 mW per 13 mm
period) easily as this power is dissipated per five periods in the designed short model.
A longer full-size HTS helical undulator magnet may further lower the average power
dissipation per meter, as the terminals may stay the same size.
The most challenging region in this design option is the transition from the helical path to
the return spool where the tapes have to be twisted and aligned although having different

escaping arcs ζ at the helix's exit and entry. Spacers may be needed to further optimize this region for a full tape stack of 120 turns. Field corrections are necessary to generate a circular helical field, as the two tape stacks which exit in a v-shape on the opposite sides and height levels create an asymmetry between the absolute values of the two field components B_x and B_y. Twisting the return spools by an angle around the $\hat{z}$-axis may counter this effect to some extent. Yet, both field options have their application with the light production of circularly or elliptically polarized photons, respectively. Besides these considerations, two (half) solenoids are needed to counterbalance the stray fields of the return spools.

Helical undulator demonstrator   Design option 2 is further simplified for the demonstrator magnet, which only consists of 10% of the aimed turns (cf. Table 3.5). The copper terminals are therefore realized at one return spool only and reduced in size with joint areas of roughly $125\,\text{mm}^2$, as demonstrator tests are exclusively foreseen at $77\,\text{K}$ with operating currents not higher than $200\,\text{A}$. This is sketched by dashed lines in Figure 3.33a. In a second optimization step, for a helical undulator demonstrator to be tested at $4.2\,\text{K}$, the complete current in- and outlets have to be realized in copper to manage the high current densities in regions of $2\,\text{kA/mm}^2$ and, if possible, above.

4. Experimental studies of coated *Re*BCO tape superconductor

This chapter presents the more fundamental experimental research covering the in-field conducting performance, the minimum bending radius, and temperature tolerances of coated *Re*BCO tape superconductors. The characterization of the high-temperature superconductor *Re*BCO in the form of tapes prepared the basis for the superconducting undulator coil manufacturing by validating and further optimizing the design and powering tests in cryogenic environments. All experiments were performed at CERN and/or KIT. Substantial parts of the following sub-chapters 4.2 and 4.4 have already been published [134, 113, 114].

4.1. In-field I_c measurements

First powering tests of the undulator prototype coils are performed at $77\,\mathrm{K}$ in a liquid nitrogen ($\mathrm{LN_2}$) bath. To experimentally determine the critical current I_c of the foreseen superconductor inside a magnetic field (B-field) beforehand, an experiment was set up with permanent bar magnets and tape samples of Bruker HTS tape as seen in Figure 4.1. The used fit (see appendix B) was known to be critical for field regions smaller than $0.5\,\mathrm{T}$ and therefore had to be validated and if needed to be adapted, especially for perpendicular field directions. As presented in the previous chapter, electro-magnetic simulations predicted a maximum B-field on the superconductor of approximately $0.6\,\mathrm{T}$ at $77\,\mathrm{K}$ for the vertical racetrack undulator coils. Consequently, two permanent bar magnets with $0.6\,\mathrm{T}$ and $0.4\,\mathrm{T}$ were chosen to be placed directly and with perpendicular field orientation on the surface of the tape for respective tests. The current was ramped-up while the voltage over the tape sample was monitored by means of soldered voltage taps and a nanovoltmeter. As for the bending experiments in the next section, I_c of a tape was derived from a non-linear voltage fit:

$$U = \underbrace{U_0}_{\text{Offset}} + \underbrace{\mathrm{r} \cdot I}_{\text{Resistive slope}} + \underbrace{U_c \left(\frac{I}{I_c}\right)^n}_{\text{Powerlaw}}, \tag{4.1}$$

with constants r and n. Figure 4.2a shows the measured voltage as a function of the applied current as well as the solid line representing the I_c threshold of $4.5\,\mathrm{\mu V}$, derived from the electric field criterion of $1\,\mathrm{\mu V/cm}$. Critical currents $I_c(77\,\mathrm{K})$ of $34\,\mathrm{A}$ and $39\,\mathrm{A}$ are found for $0.6\,\mathrm{T}$ and $0.4\,\mathrm{T}$ at the superconductor, respectively. The measured values helped to adjust the existing I_c fitting functions for $77\,\mathrm{K}$ [116] as seen in Figure 4.2b, thus giving confidence for the VR undulator coils' first powering tests in liquid nitrogen.
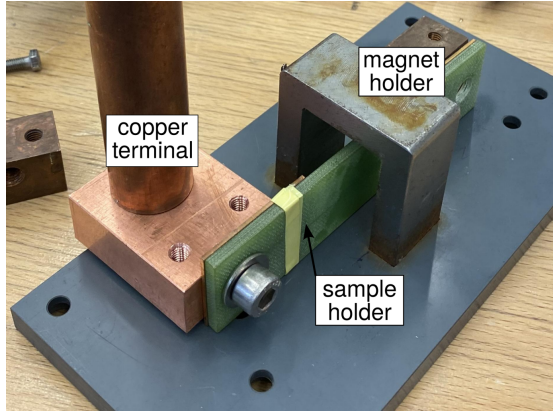
(a) Overview.
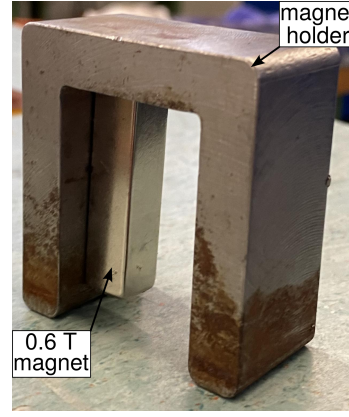
(b) Support with permanent magnet.

Figure 4.1.: I_c measurement setup for superconducting tapes under a constant B-field at 77 K in liquid nitrogen. A 0.6 T and a 0.4 T bar magnet were used with perpendicular field direction to the superconducting plane.

(a)

(b)
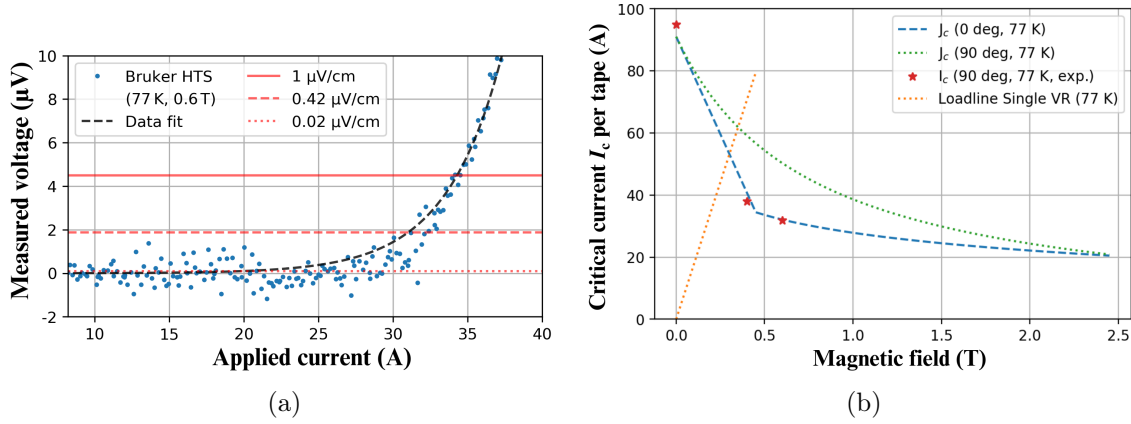
Figure 4.2.: Results of the in-field I_c measurement at 77 K in LN$_2$. (a) An I_c measurement curve of a Bruker HTS ReBCO tape wit 0.6 T applied perpendicular B-field. The solid red line represents the electrical field criterion of 1 μV/cm, whereas the dashed and dotted red lines show more conservative criteria. The data fit was done with the formula (4.1). (b) Measurement points on the calculated vertical racetrack (VR) coil's load line for Bruker HTS ReBCO tape. The solid blue and dashed green curves represent critical current fits for respective B-field orientations.

4.2. Bending limits

Compact undulator geometries with short periods like 15 mm and below most likely imply conductor bending radii smaller than 10 mm, which is the minimum approved bending radius from most of the coated ReBCO tape superconductor manufacturers. However, the investigated horizontal racetrack (HR) and helical undulator coil geometries demand bending radii of 1.25 mm and 2.5 mm, respectively, for an undulator period length λ_u of 13 mm and a magnetic gap of 5 mm. As a consequence of the induced strain on the superconducting material when moving to smaller bending radii, the superconducting characteristics may be harmed.

Earlier studies showed that compressing the ReBCO layer leads to the advantage of smaller bending radii without critical current (I_c) degradation rather than pull strain [135]. To the author's knowledge, there existed only one data source for (helical) bending radii smaller than 5 mm including two specific tapes at the point of this experiment [87]. This lack of data motivated the following bending experiment including the design of two new bending rigs, presented in the following.

4.2.1. Experimental methods and setup

The I_c performance of various coated ReBCO tape superconductors was investigated for multiple bending radii from 10 mm down to 1.25 mm. The tape specimens were bent at room temperature to simulate the coil winding, then cooled down to 77 K in liquid nitrogen (LN$_2$) for powering tests. The electric field criterion of 100 µV/m was employed to identify I_c of a tape specimen from V-I measurements. The voltage was measured with soldered voltage taps and a nanovoltmeter around the bent region while the current was driven up. Three different bending rigs at KIT and CERN were used to bend a tape specimen down to a I_c degradation of 70 % or more.
From the bending radius R, one can derive the approximate strain ϵ on the superconducting layer as

$$\epsilon = \frac{-t_{\mathrm{sub}}}{2R + t_{\mathrm{sub}} + 2t_{\mathrm{stab}}} \approx \frac{-t_{\mathrm{sub}}}{2R + t_{\mathrm{sub}}} \ , \tag{4.2}$$

with the substrate and stabilizer thickness t_{sub} and t_{stab}. Compression of the ReBCO layer will be seen as negative bending strain. The smallest radius for which the measured I_c showed degradation of less than 5 % was defined as the minimum bending radius R_{min} of a tape specimen.
Figure 4.3 shows the used bending rigs at KIT. With the already existing so-called "Goldacker" bending rig at KIT's Institute for Technical Physics (ITEP), tape specimens can be investigated down to a bending radius of 5 mm continuously [136, 135]. By using gear wheels the Goldacker bending rig is capable of bending tapes in a liquid nitrogen bath by moving the clamped tape ends on a circular shaped path (see Figure 4.3a). The caused uncertainty of the exact bending shape was shown to be around 2 % [137].
The mechanic of the Goldacker bending rig allows one to measure reversible I_c degradation (measurements after bending at $R = \infty$) and to confirm the results of the newly designed bending rig, presented in the following. A second bending rig was designed for fast cooldowns and manufactured to study bending radii smaller than 5 mm: the so-called "U-bend" rig uses replaceable bending bodies and is shown in Figure 4.3b and c. The bending bodies were 3D-printed to investigate bending radii $R \in \{10, 8, 7, 6, 5, 4, 3, 2.5, 1.25\}$ mm. In addition to normal bending, half helical twist bends with different angles are as well feasible with the U-bend rig, as demonstrated in Figure 4.3d. D-shaped frames with fixation holes allow 5° steps for the diagonal alignment. For both configurations, the tape specimen is supported from the copper terminals down to the bending body. Two sleeves cover the tape right after the copper terminals to reduce the strain in the s-shaped region. Pressure is applied by means of springs and nuts to press the bending body onto the tape, ensuring a tight fit.

To further investigate helical bending and to confirm the results for random samples once more, a helical bending rig with exchangeable bodies was designed and manufactured at CERN. Here, the 3D-printed bending bodies have the same variation of radii R as above. The helical pitch of the bending bodies, displayed in Figure 4.4, measured 13 mm, as the setup aims to investigate the winding feasibility of a helical undulator with such a period length.
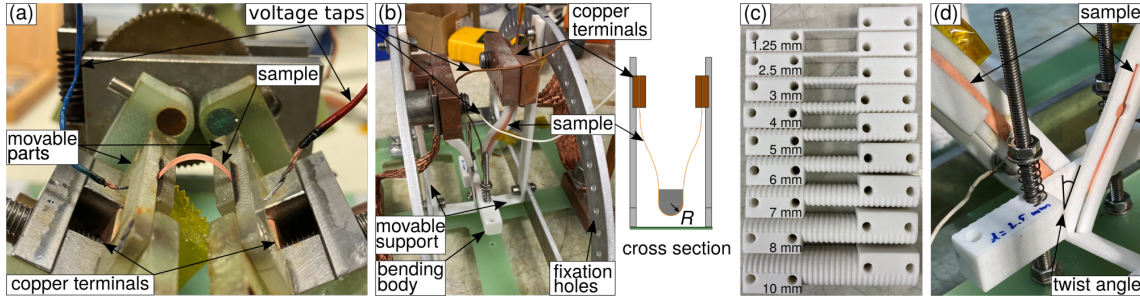
Figure 4.3.: Bending configurations utilized for the *Re*BCO tape bending experiment at KIT. (a) The Goldacker bending rig which can be used down to a 5 mm bending radius. (b) The newly designed U-Bend rig which uses bending bodies and a cross-section sketch. The movable support can also be used for twist bending by means of different fixation holes. (c) 3D-printed bending bodies to be used in the U-bend rig. (d) Detailed view of The U-bend rig's twist-bend setup with a 30° configuration. Pressure was applied by springs and nuts ensuring an optimal fit of the superconducting tapes around the bending bodies. Graphic reproduced from [134].
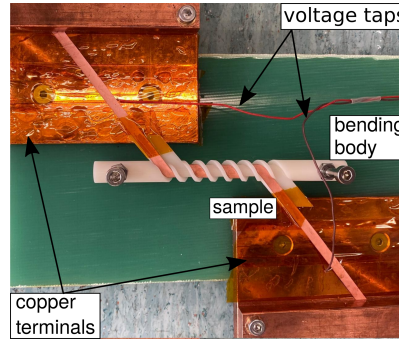
Figure 4.4.: *Re*BCO helical bending rig utilized at CERN. Helical winding bodies were 3D-printed with the same radii as shown in Figure 4.3. The superconducting tape was wound three times around the body with a winding pitch of 13 mm.

4.2.2. Results

The relative I_c degradation over the bending radius is drawn in Figure 4.5. All tested tape specimens and results are summed up in Table 4.1.

Reversible degradation can be observed for all tested specimens but ShanghaiSCT's ST1911-78, down to the tested 5 mm. Besides Bruker's tape, all specimens show similar behavior of an abrupt I_c decay after their R_{min} is reached. Bruker's tape decays continuously from $R = 10$ mm to smaller bending radii. A possible explanation could be the use of stainless steel as substrate material, whereas all other manufacturers use Hastelloy®. SuperPower's SF12050-AP and SCS4050-AP as well as THEVA's TPL4120 tape show a similar bending performance with an R_{min} of 4 mm, having all the same substrate thickness of 50 µm. Their measurements are plotted in Figure 4.5b, where the bending strain is calculated additionally according to equation (4.2) and marked on a second x-axis for further analyses. Although having almost the same material parameters, the two tested ShanghaiSCT tape specimens show a different performance with R_{min} of 7 mm and 2.5 mm, for the 4 mm wide ST1910-19 and the 10 mm wide ST1911-78, respectively. This behavior is not understood yet and may need further investigation, e.g. more samples. The smallest measured R_{min} of 2 mm in this study is reached by the tapes with the thinnest substrates of 30 µm and 25 µm from SuperPower as seen in Figure 4.5c. A thin substrate generates less stress and

(a) 50 μm thick substrate tapes.

(b) 50 μm thick substrate tapes.

(c) Tapes of various substrate thicknesses.

(d) Half helical twist bending.
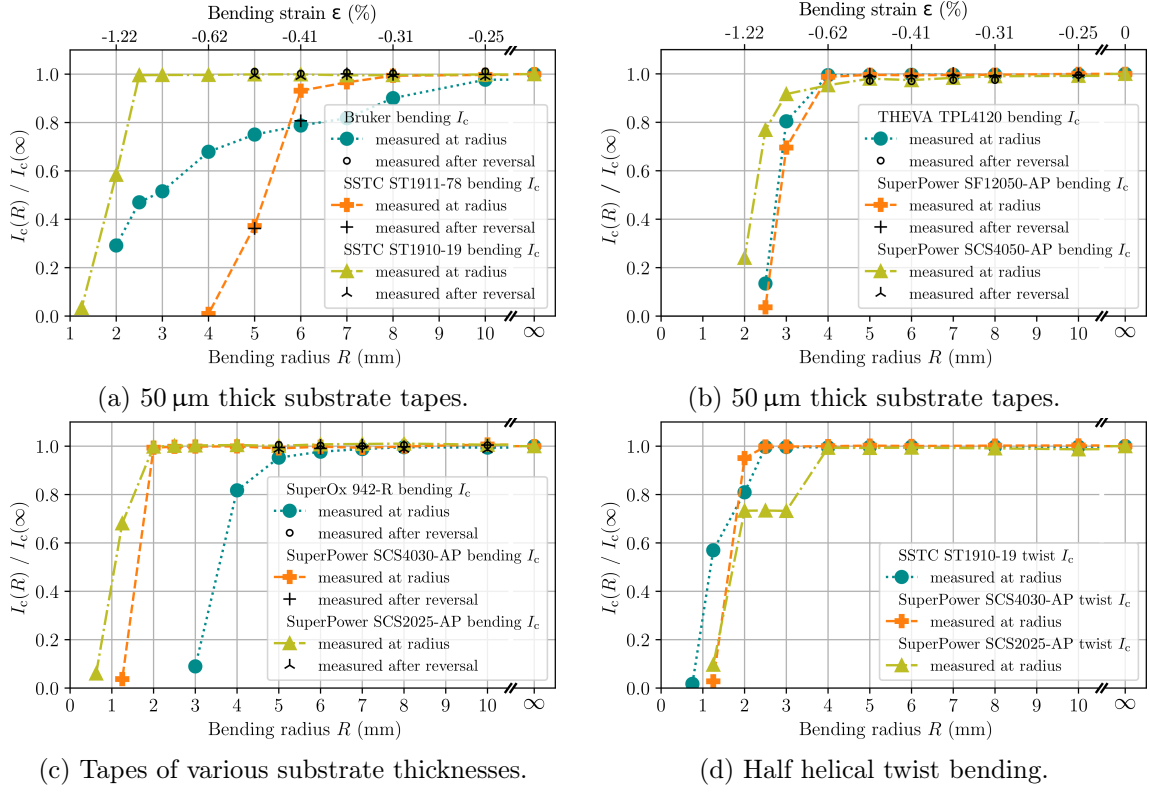
Figure 4.5.: Relative critical current over the bending radius R. Specimens in (a) and (b) have a substrate thickness of 50 μm, (c) SuperOx 942-R with 60 μm, SuperPower SCS4030-AP with 30 μm and SCS2025-AP with 25 μm thick substrate. (d) Various specimens for half helical twist bending. Plots reproduced and adapted from [134].

strain on the superconducting layer, making thinner substrates favorable for smaller bending radii on the one hand, but degrading the mechanical strength of the superconductor tape on the other hand.

Half-twist and helical bending

For the half twist and helical bending, no tests regarding reversible degradation were safely possible, without risking damaging the tape specimens mechanically. The three tapes with the smallest bending radii were tested again in the half-twist bending setup. Their performance can be seen in Figure 4.5d. As expected, Superpower SCS4050-AP and ShanghaiSCT ST-1910-19 show similar performance as for normal bending. Superpower SCS2025-AP showed an earlier degradation this time ($R_{min} = 4$ mm compared to 2 mm for normal bending). However, the constant I_c values between $R = 4$ mm and 2 mm after a first abrupt degradation hint at external mechanical damage, e.g. during the exchange of the bending bodies and may need further investigations. Unfortunately, there was no more spare tape to redo the test.

With the helical bending rig at CERN, specimens of the two coated ReBCO tape superconductors which are planned to be used for the undulator prototype coil manufacturing were tested. The measurements could confirm the previously obtained results and are displayed in Figure 4.6. Bruker's tape degrades even less severely compared to normal bending whereas Superpower SCS4030-AP shows the same bending performance of $R_{min} = 2$ mm, thus supporting its use for the helical undulator demonstrator aiming at a minimum bending radius of 2.5 mm.

Table 4.1.: Tape specimens and parameters (tape width w_{tape} and thickness t_{tape}, stabilizer thickness t_{stab} and substrate thickness t_{sub}), measured critical current I_{c} at 77 K and minimum bending radius R_{min}, for which the critical current degraded less than 5%. Table reproduced and adapted from [134].

Manufacturer	Reference	w_{tape}	t_{tape}	t_{stab}	t_{sub}	$I_{\text{c}}(77\,\text{K})$	R_{min}
Bruker	-	4 mm	105 µm	50 µm	50 µm	91 A	10 mm
THEVA	TPL4120	4 mm	80 µm	20 µm	50 µm	167 A	4 mm
ShanghaiSCT	ST1911-78	10 mm	95 µm	40 µm	50 µm	360 A	7 mm
ShanghaiSCT	ST1910-19	4 mm	95 µm	30 µm	50 µm	159 A	2.5 mm
SuperOx	942-R	4 mm	76 µm	10 µm	60 µm	127 A	5 mm
SuperPower	SF12050-AP	12 mm	55 µm	Ag only	50 µm	428 A	4 mm
SuperPower	SCS4050-AP	4 mm	100 µm	40 µm	50 µm	135 A	4 mm
SuperPower	SCS4030-AP	4 mm	42 µm	10 µm	30 µm	130 A	2 mm
SuperPower	SCS4025-AP	2 mm	36 µm	10 µm	25 µm	65 A	2 mm
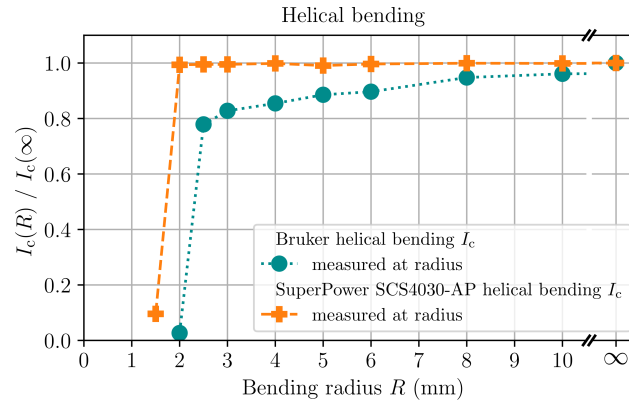
Figure 4.6.: Relative critical current over bending radius R. The two superconducting tapes to be used for undulator prototype coil winding were tested for helical bending.

(a) Samples #1, #2, #3.

(d) Samples #7, #8, #9 after 12 h at 200 °C.

(b) Samples #4, #5, #6 after 12 h at 150 °C.

(e) Samples #10, #11, #12 after 3 h at 250 °C.

(c) Samples #7, #8, #9 after 3 h at 200 °C.

(f) Samples #10, #11, #12 after 12 h at 250 °C.
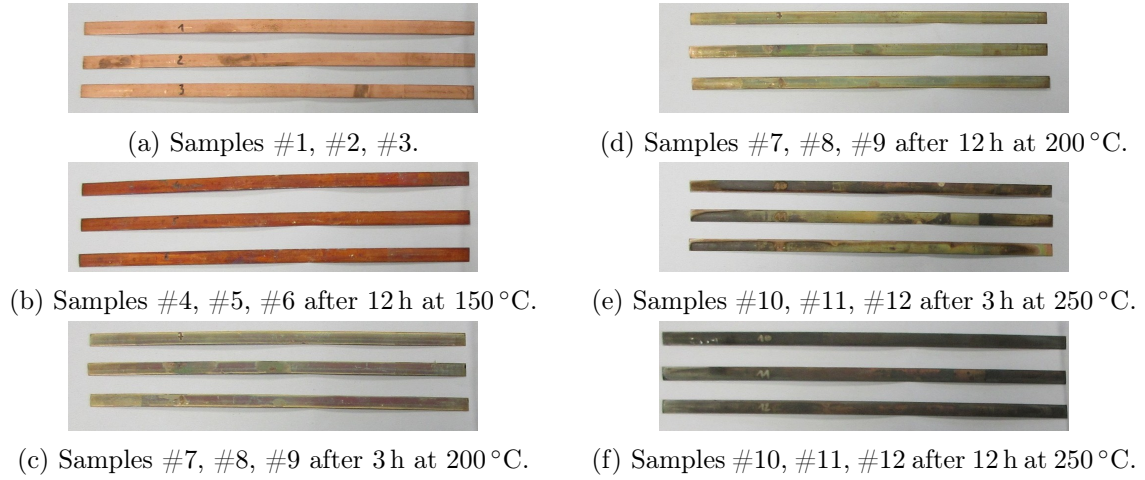
Figure 4.7.: Heat treatment of coated ReBCO tapes. 120 mm long samples from Bruker HTS coated ReBCO tapes were heated for 3 h, 6 h and 12 h, respectively.

4.3. Temperature tolerance and splicing

Splices of coated ReBCO superconducting tapes are inevitable when designing a modular undulator magnet. Likewise, connections between superconductors and normal conductors like copper require soldered connections for the best possible electrical contacts. Previous studies have already shown a reduction of the superconducting tape's critical current when undergoing heat treatment, yet different samples may behave differently [67]. Especially temperatures well above 200 °C are critical for the ReBCO layer.

For a better understanding of the Bruker HTS tape batch, to be used for the VR undulator coils, several 120 mm long specimens were tested in various heat treatments. Three specimens without treatment are taken as reference and stored at room temperature. The influence of four temperatures T on the tape specimens was investigated by storing them in an oven: $T \in \{150, 190, 200, 250\}$ °C. For each temperature, three specimens were tested for their I_c in self-field at 77 K in liquid nitrogen before the heat treatment cycles and subsequently after the first cycle of 3 h, second after additional 3 h, and third after another 6 h more of heating. As earlier, the used electrical field criterion was always 1 µV/cm. Due to this heat cycling process, copper clamps were used instead of soldered voltage taps to measure the voltage over the specimens for the ramping current [138]. Figure 4.7 gives a visual impression of the specimens after their respective heat treatment. Oxide layers slowly transformed the shiny copper into a dark green appearance.

The $I_c(77\,\text{K})$ of Bruker HTS tape in self-field without any heat treatment was in agreement with the above-measured value of 91 A. All measurement results are plotted in Figure 4.8. The first light degradation effects greater than 2% are observed after 6 h at 190 °C. Degradation of more than 5% can be seen after 6 h at 200 °C. A clear decline of I_c of about 20% is detected for 250 °C, already after the shortest heating cycle of 3 h. For all investigated specimens, the observed I_c degradation is not linear with time nor with temperature.

As a consequence of the observed critical current degradation, a fixed upper temperature limit of 200 °C as short as possible is defined for all soldering and splicing processes in the further experimental work.
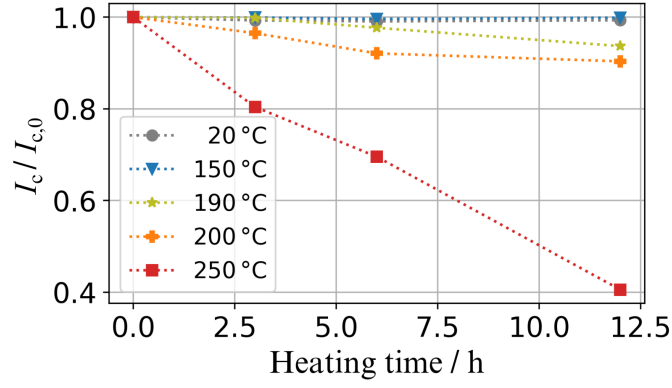
Figure 4.8.: Relative critical current over heating time for Bruker HTS tape specimens.

(a)

(b)   (c)   (d)
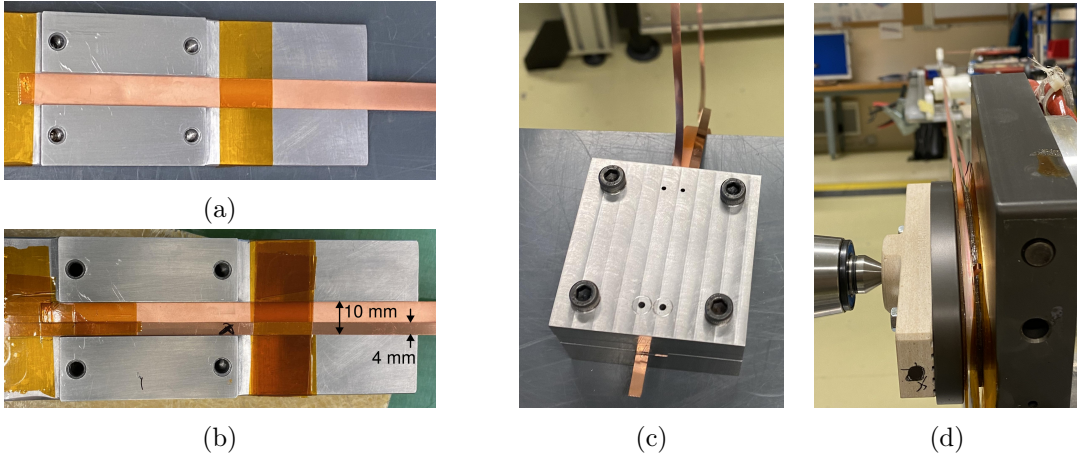
Figure 4.9.: Splicing techniques for coated ReBCO tapes. (a) The fixation of the 10 mm
             wide ReBCO tape, which connects the two sub-coils of the VR coil. (b) One
             4 mm wide tape fixed on top with soldering paste in between for splicing prepa-
             ration. (c) Pinhole punching setup right after the splicing. All manufactured
             stainless steel blocks could be heated with inserted cartridge heaters to the de-
             sired temperature. (d) VR coil winding bench with vertical heating plate and
             cartridge heaters on the right to allow splicing and winding simultaneously.

For the preparation of the VR coil manufacturing including the winding, special tooling
was required. Splicing techniques for connecting the 4 mm wide tapes of the sub-coils to
the 10 mm wide connecting tape needed to be developed. Figures 4.9a to 4.9c show the
designed and built setup for fixing the beginnings of the tapes, which clamps the tapes
together while applying solder paste in between them. The entire stainless steel block can
be precisely heated by a cartridge heater ($\pm 2\,°C$), which was inserted inside the lower part
of the structure. For soldering the first turns of each sub-coil along the connecting tape
on the curved side of the winding body and for fixing the last turns of the coil to their
penultimate, a rotating heating plate powered by four cartridge heaters was developed.
As seen in Figure 4.9d on the right side, this allowed to turn or even wind the coil while
heating up the entire structure.

4.4. Coil winding

This section covers the different winding techniques investigated to wind the VR and helical undulator coil. For reasons of the earlier described coil (self-)protection, a non-insulated (NI) approach is favored. In the end, a non-insulated single tape dry winding was chosen for the coil manufacturing of both geometries allowing a well-controlled winding process as well as reasonable charging times of the coils (see the sections 5.1 and 5.2 in the following chapter).

In contrast, the charging times of the fully soldered coils with non-insulated single tape wet winding would have been orders of magnitudes longer and the amount of solder in between the turns was difficult to control, although this technique would have granted a mechanically and electrically even more stable operation [132]. Other techniques under discussion were a non-insulated double tape winding with the superconducting layers face-to-face for an increased current exchange or with co-winding a metal tape (e.g. stainless steel or brass) for shorter charging times [139, 140, 141]. The first option was discarded because it would have complicated the design of the external current leads. The second option, however, is still of interest and recommended for further investigations in order to reduce the measured charging times and enable a better-controlled turn-to-turn resistance.

4.4.1. VR coil dry winding

All dry winding processes of the VR coils were performed in a vertical position. Ahead of superconducting coil winding, several tests to optimize the winding procedure took place which ended in two VR dummy coils wound from 4 mm wide and 100 µm thick copper tape. The coated ReBCO superconducting tape as well as the copper tape was spooled onto two spools with an approximate minimum diameter of 25 cm, each individually operated and controlled by a motor with a clutch to manage the winding tension. The copper winding body with iron core and poles was mounted on a rotating heating plate as shown in Figure 4.10a. A counter support fixed the other side of the winding body's axis. The motor and power supply for heating are not shown in the sketch.

The first two VR coils (#1 and #2) were manufactured by winding two NI sub-coils simultaneously in the same direction with 4 mm wide and 100 µm thick Bruker HTS tape. For VR coil #3, 4 mm wide and 45 µm thick SuperPower tape was used. The superconducting side faced towards the copper winding body, i.e. inwards keeping the ReBCO under compression, to provide the mechanically most stable orientation for all VR coils (cf. section 4.2).

Figure 4.10b shows steps of the winding procedure which started with fixing a 10 mm wide and 95 µm thick coated ReBCO superconducting tape from ShanghaiSCT with a stainless steel pin to the winding body. Only here, for the so-called "connecting tape", the superconducting layer faced outwards to enable the best possible electrical connection between the superconducting tapes, thus reducing the local heat load of the individual sub-coils. The first turns of each sub-coil were soldered for 5 min at 185 °C with Sn62Pb36Ag2 solder paste to the connecting tape along the curved side of the D-shaped winding body. VR coil #1 was wound with a regulated and monitored tension of 30 N, VR coils #2 and #3 with 25 N. For VR coil #1 and #2, 51 turns were wound resulting in a $4 \times 5\,\text{mm}^2$ conductor cross-section. With the thinner tape utilized for VR coil #3, more turns were anticipated. The winding process was stopped at 102 turns, thus exactly double the previous amount of turns, ending in a conductor cross-section of $4 \times 4.6\,\text{mm}^2$. The last turn of each sub-coil was soldered with 97In3Ag solder paste to their penultimate turn along the curved side of the D-shaped winding body by heating the VR coil to 155 °C for 5 min. A rotating heating plate, installed on the winding machine, was used for soldering the first

(a)   (b)
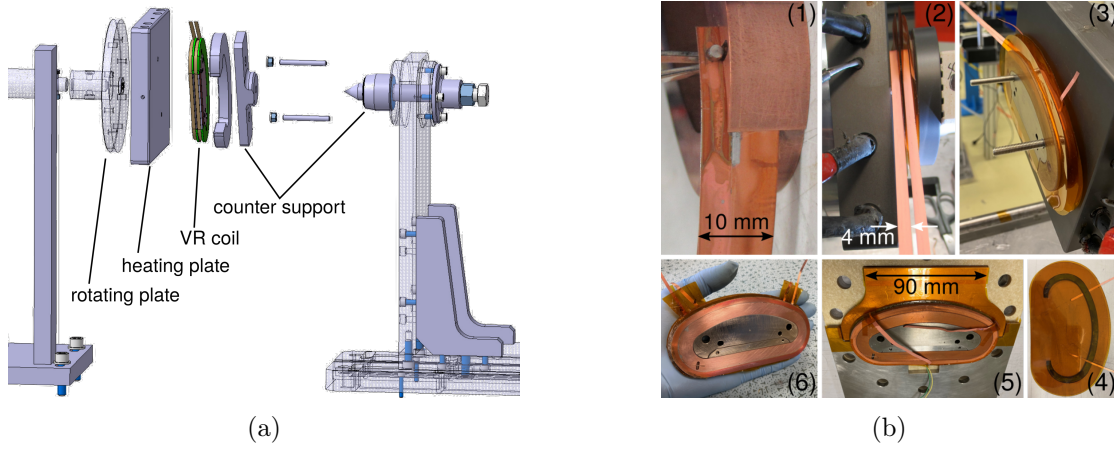
Figure 4.10.: (a) VR coil winding sketch without two tape spools, motors, and clutches.
(b) Winding collage of different steps clockwise: (1) A pin fixes the tape to
the copper body, (2) two ReBCO tapes are wound at once for the VR coil, (3)
VR coil on the winding bench and visible voltage taps, (4) center insulation
with included voltage taps, (5) VR coil and its copper current lead placement.
(6) VR coil after winding. Pictures reproduced and adapted from [113]
.
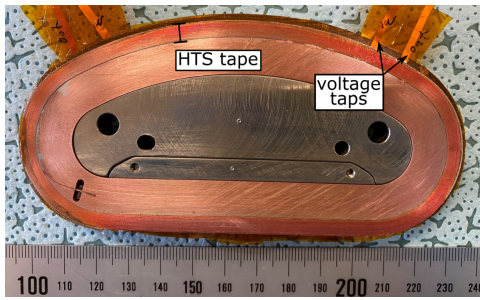
Figure 4.11.: Completed VR coil #3 and volt-
age taps right after its winding.
Scale in millimeters. Graphic
reproduced from [114].
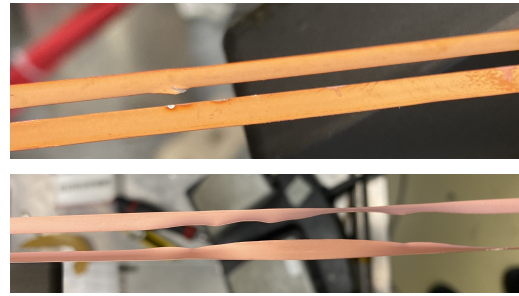
Figure 4.12.: Likely damaged coated
ReBCO superconducting
tape sections during the
winding of VR coil #1.

and the last turn of the coil, respectively, as described in the previous section. 25 µm thin
copper voltage taps were placed in between the four joint connections. Both sub-coils were
covered on their sides of the tape stack with 50 µm thick Kapton® sheets. The completed
VR coil #3 is presented exemplary in Figure 4.11.

The winding process was not always perfect and straightforward, as planned. Unexpected
movement of the insulating Kapton® forced to wind back at rare intervals. This happened
primarily during the winding of VR coil #1 and resulted twice in an impact on the super-
conducting tape when the tape got caught under the Kapton® sheet. Figure 4.12 shows
the visible mechanical influence on the tapes which most likely also resulted in damage to
the ReBCO layer, thus the superconducting properties. This may be seen when comparing
the test results of the three manufactured VR coils in the following chapter's section 5.1.

Manufacturing quality assurance   After completing the manufacturing of the VR coils
and before proceeding to the first powering tests in liquid nitrogen, the dimensions of the
coils were measured with a coordinate measuring machine called FaroArm® [142]. Five
sections of the coils were inspected as shown as an example for VR coil #2 in Figure 4.13.
In contrast to VR coil #3, the outermost layer of VR coils #1 and #2 shows a concave

(a) Faro 0.

(b)

(c)

(d)

(e)
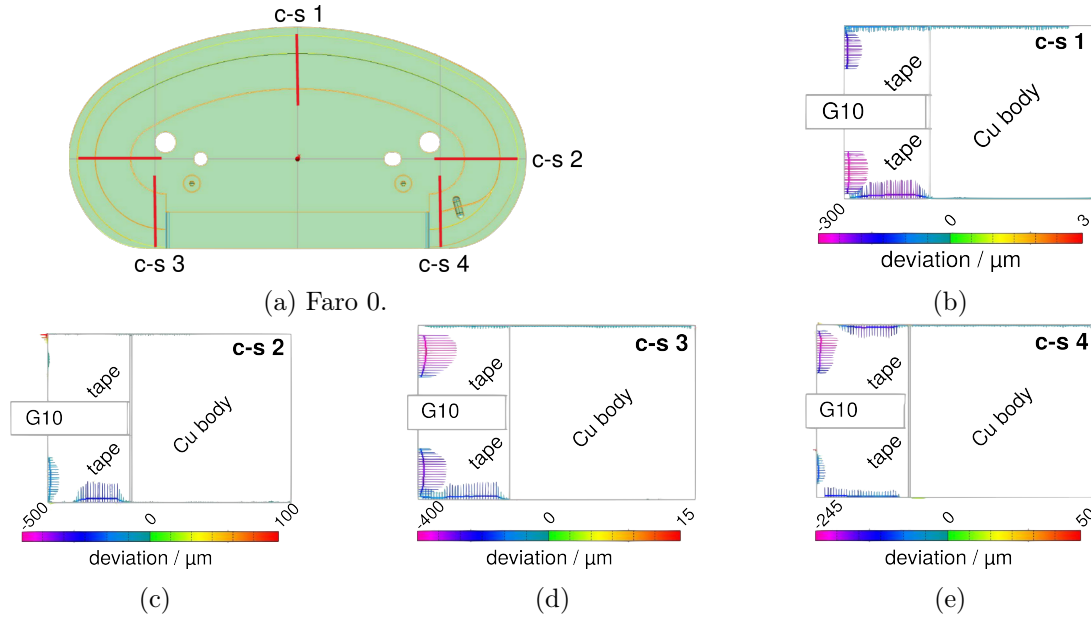
Figure 4.13.: Dimension measurements of VR coil #2 by means of a FaroArm®. (a) shows
the measured positions relative to the coil's geometry. (b) to (e) show the
measured deviations for each position, respectively. Due to the slightly con-
cave tape, the majority of deviations are negative.

profile that originates from the Bruker HTS tape's curved shape (cf. section 2.3.2). The
tape width may vary according to the supplier by 5%, implying a width of $4\,\mathrm{mm} \pm 0.2\,\mathrm{mm}$.
In this background, the exterior sides of the tape stacks are found to be within acceptable
tolerances. Single points reveal maximum deviations of around $250\,\mu\mathrm{m}$ or smaller at cross-
sections 1 and 2. However, the more important cross-sections 3 and 4 in the region of the
magnetic poles show a well-aligned tape stack for the given tolerance. These investigations
prove that the VR coil manufacturing process is able to be performed with the requested
quality.

4.4.2. VR coil wet winding

The possibility of a wet winding process was investigated, as it may provide an electrically
and mechanically very stable coil. Here, wet winding names the process of applying solder
paste during the winding process. The soldering process can then be performed during or
after the winding process, in vertical as well as horizontal orientation. In these trials, $4\,\mu\mathrm{m}$
wide and $100\,\mu\mathrm{m}$ thick copper tape was used together with Sn62Pb36Ag2 solder paste
for soldering at $185\,^\circ\mathrm{C}$. As for the dry winding, the copper tape was spooled onto two
spools with an approximate minimum diameter of $25\,\mathrm{cm}$, each individually operated and
controlled by a motor with a clutch to control the winding tension.
The solder paste was applied on top of the two tapes to be wound simultaneously by using
a spraying device with a solder paste filled cartridge. Air pressure extruded the solder
paste on the moving copper tape before it was wound on the winding body. The process
was investigated for soldering after and during the winding process. Different steps are
presented in Figure 4.14. In the straight sections of the D-shaped winding body, it was
difficult to keep the tension of the tapes, thus having no gap between the turns. All in all,
soldering after the winding turned out to be challenging but manageable for the designed
VR coil: after heating up, the liquid solder paste released space in between the turns which
emerged in a loss of winding tension. As a consequence, the entire coil was tightened by
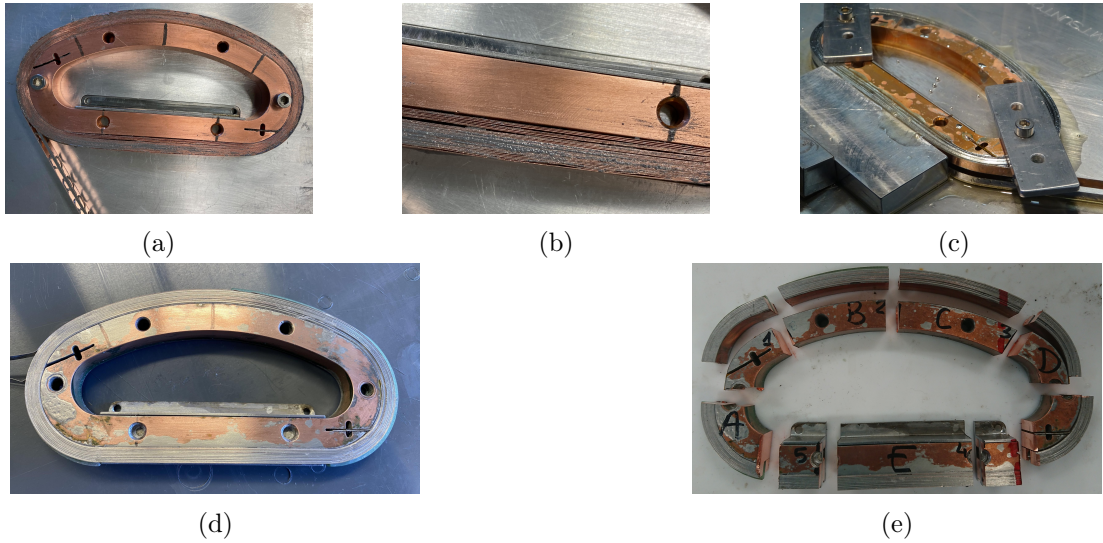
Figure 4.14.: Wet winding trial of a VR coil with separated processes of winding and heat-
ing. (a) and (b) display the horizontal winding process with solder paste. (c)
shows the heating and soldering process. (d) The resulting VR coil without
the iron body. (e) This VR coil was cut to investigate the inter-turn soldering.

the applied 30 N of winding tension which might harm the superconductor. For a second
approach, the winding body was heated to the mentioned 185 °C during the entire winding
process. The spare liquid solder accumulated in the form of a bubble where the tape met
the winding body and had to be removed occasionally.

For all wet winding trials, a vertical winding orientation delivered a better distribution of
the solder in between the turns than a horizontal position. A fully soldered dummy VR
coil wound with copper tape was cut into sample pieces for further investigations of the
cross-sections as seen in Figure 4.15. These samples were investigated under an optical as
well as a scanning electron microscope (SEM). The alignment of the tape stack as well as
the uniformity of the solder layer thickness was inspected and is displayed in Figure 4.15.
With the best efforts, the solder layers still revealed a rather large spread with thicknesses
from 7 µm to almost 30 µm, thus not the uniformity which was aimed for.

The process may be improved significantly by pre-tinning the tape before winding to define
the exact amount of solder per tape meter to be used. However, the large charging times
of a fully soldered coil were not superior to undulator magnets and further improvements
would have exceeded the scope of this work. On these grounds, a wet winding process was
neglected for the final superconducting VR coil manufacturing.

4.4.3. Helical coil dry winding

As presented in the previous chapter, the helical undulator consists of a bifilar helix with
a winding pitch of 13 mm representing the undulator period. The helical design was intro-
duced in detail in the preceding chapters' sections 2.1.2 and 3.5.

The entire coil is planned to be wound from one single piece length of superconducting tape,
or rather two single piece lengths in parallel for a two-tape stack. For both, the winding
tests and the superconducting demonstrator winding, the winding body was a 3D-printed
polymer that did not tolerate temperatures above 200 °C. Consequently, a non-insulated
dry winding process was chosen. Two cable types were investigated: single tape and a stack
of two tapes with a face-to-back superconductor orientation. The superconductor faced the
winding body for both configurations, keeping the ReBCO layer under compression. Tests

(a) (b) (c)

(d) (e) (f)
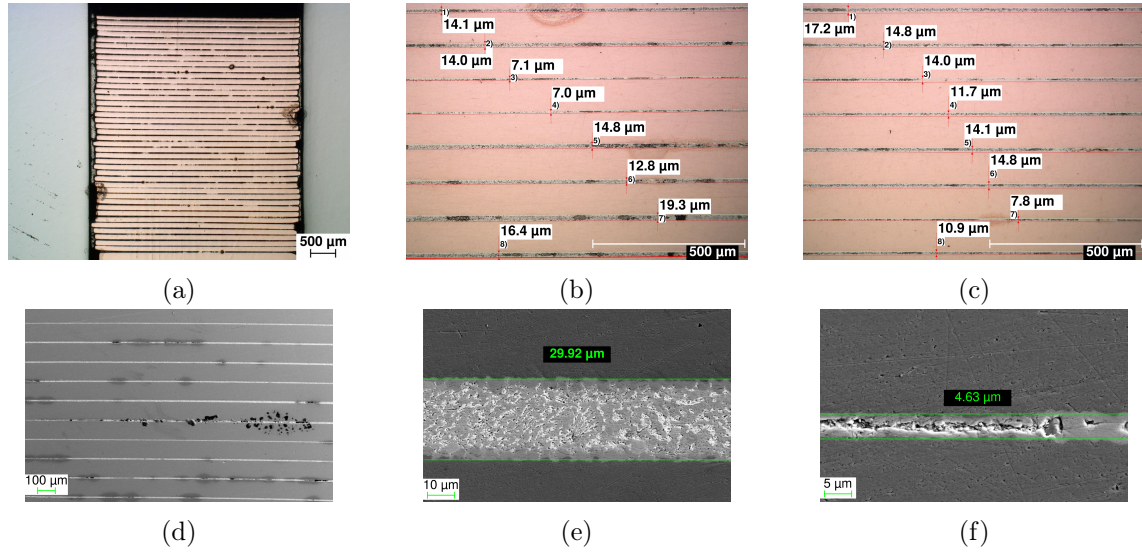
Figure 4.15.: (a) to (c) present optical microscopy images, (d) to (f) SEM images of a fully-soldered VR coil's cross-sections, as seen in Figure 4.14. Measured thicknesses of soldering layers are marked with a respective scale.
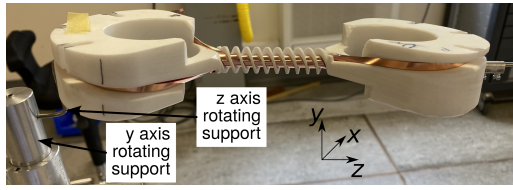
Figure 4.16.: Helical winding setup with rotating axes, as an example for the chosen coil-end design. The winding body is mounted with a rod through the beam pipe.

were performed with 4 mm wide and 100 µm thick copper and stainless steel tape. For the demonstrator coil winding a 4 mm wide and 50 µm thick coated ReBCO superconducting tape was used. Figure 4.16 shows the winding setup of the preferred return option with the two rotating axes to realize the winding. Similar to the above-described procedures, the tapes were spooled onto spools with an approximate minimum diameter of 10 cm, individually operated and controlled by motors with a clutch to manage the winding tension. A constant winding tension of 5.5 N was applied to each tape for both design options. Compared to the up to 30 N used for the VR coil winding, this relatively low value resulted from the required tape flexibility during the winding procedure for the rather sensitive tape. Here, the winding angle equals the escaping arc ζ, introduced in equation (2.30). Consequently, the winding angle had to be adjusted for changing winding diameter, thus for every turn, to keep the winding pitch constant as sketched in Figure 4.17a. Here, the angles ζ_{in} and ζ_{out} represent more inner and more outer turns, respectively. Additionally, the winding former had to be turned over to align the tape along the two returning spools. The result at the end of the helix is sketched in Figure 4.17b where the beginning and the end of the helical winding formed a fan-like structure, making the return of the tape a challenge.

For option 1, housing the return spools next to the beam axis, the beginning of the tape was clamped to the winding body. This was different for option 2 with the return spools above and under the beam axis, where the tape was soldered for shorter than 2 min at 185 °C using Sn62Pb36Ag2 solder paste to a copper terminal, located outside the helical structure in a return spool. The two designed and experimentally wound options to return the tape are presented in more detail in the following.

4.4.3.1. Tape return options

To deal with the different exit angles, two different return options have been developed. For the first option with the three returning spools on the side, the winding could be performed as planned for the full tape stack. This is shown in Figure 4.18a where stainless steel tape was used for demonstrating the winding. However, it was challenging to mechanically stabilize the tape between the helical winding body and the returning spools, and space for current leads was limited in this design. Further investigation would have been needed to find a proper shape, most likely to be produced with a 3D printing process, to fill the gap and provide room for current leads at the same time.

To fulfill these requirements, the second winding body was designed with two returning spools next to the beam pipe. Here, the tape could be wound always being in contact with a solid surface, thus mechanically stabilized. This test winding can be seen in Figure 4.18b and 4.18c with copper and stainless steel tape. The conductor tape stack was well aligned. Simply the regions, where the tape exited the helical winding body showed some minor gaps. Spacers and clamps during and after the winding process could further improve the quality in these zones. For the helical undulator demonstrator, six turns were wound with a stack of two superconducting tapes in a face-to-back superconductor orientation, resulting in twelve turns. As 120 turns were the aimed number of turns to fill the winding groove, the demonstrator represents exactly 10% of the complete superconducting coil dimension. The helical undulator demonstrator after winding and before the installation of the outer copper terminal can be seen in Figure 4.19. The outermost turn was clamped to an outer copper piece with a 100 μm thick and 4 mm wide indium sheet to cover potential gaps. Additionally, a stack of two superconducting tapes connected the final turn with a soldered connection to the outer side of the closing copper terminal. Here, the process of soldering was once more performed for shorter than 2 min at 185 °C using Sn62Pb36Ag2 solder paste.
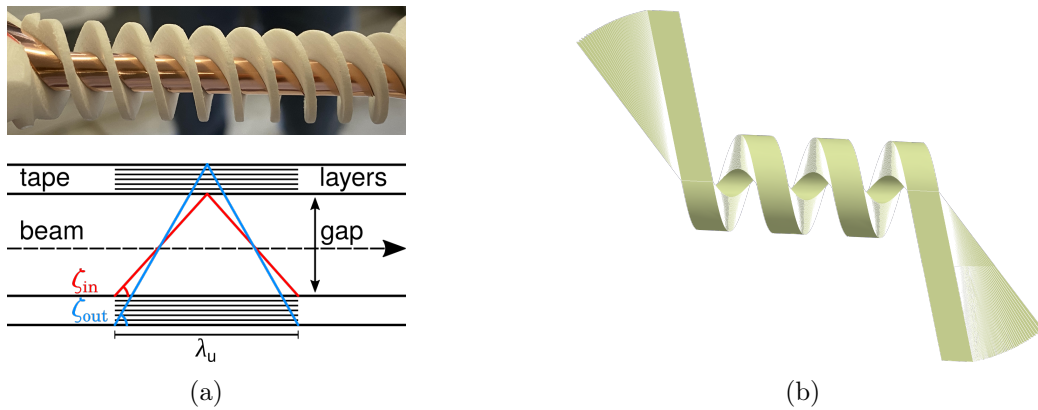
Figure 4.17.: Helical tape winding for multiple layers and constant pitch. (a) Higher layers must have a different winding angle $\zeta_{\mathrm{out}} > \zeta_{\mathrm{in}}$ to keep the pitch constant, which results in a fan at the end. (b) Fan of tapes for three helical undulator periods.
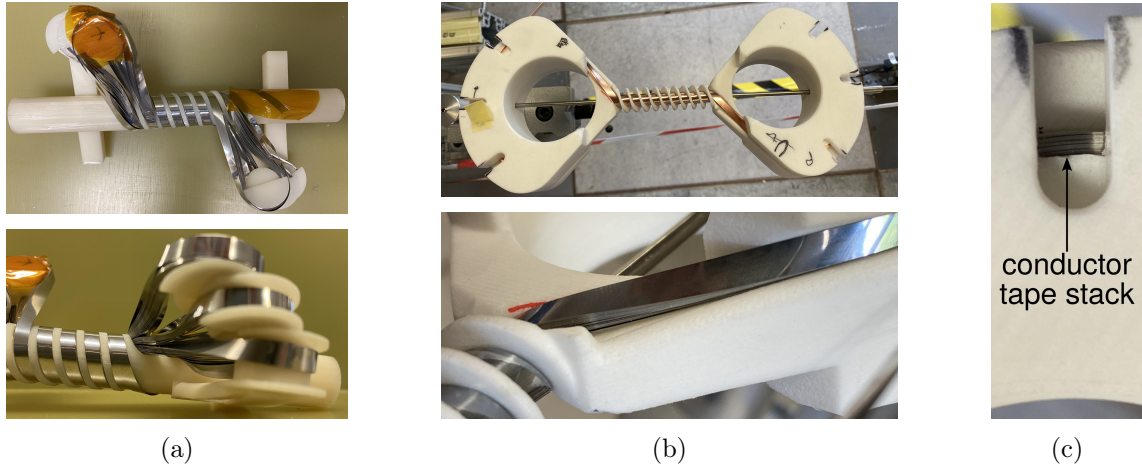
Figure 4.18.: Winding trials with 100 μm thick stainless steel and copper tape for the helical undulator option 1 and 2. (a) Top view of option 1 and a close-up of the returning spools. (b) Top view of option 2 and a close-up of the transition from the helical to the solenoidal shape. (c) Tape stack at the center of a returning spool.
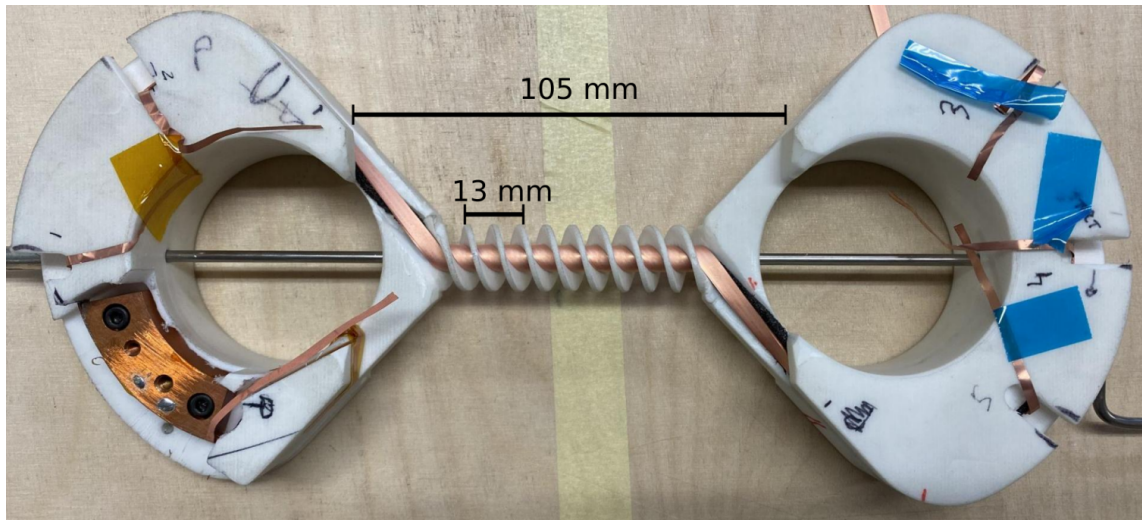
Figure 4.19.: The helical undulator demonstrator as short model of five 13 mm long periods after winding twelve turns. One copper terminal can be seen on the left. Voltage taps for each turn are sticking out of the return spools.

5. Coated *Re*BCO tape-based undulator coils: experimental results and analyses

All experimental results, analyses, and descriptions of the *Re*BCO tape-based undulator coils' powering tests performed within the scope of this work are presented hereinafter. This covers first, three one-period vertical racetrack (VR) coils and second, a helical undulator demonstrator short model. All coils were powered at 77 K, in liquid nitrogen bath cryostats. Two VR one-period coils were additionally powered at 4.2 K. Experiments were performed at CERN and/or KIT having uncertainties within the plotted line or marker thickness, if not stated differently. Substantial parts of the sub-chapter 5.1 have already been published [113, 114, 143].

5.1. Vertical racetrack undulator: one-period coil

This section is dedicated to the vertical racetrack (VR) coils' powering tests and magnetic field measurements. All three manufactured VR coils were built and first tested at CERN in liquid nitrogen (LN$_2$) at 77 K. VR coil #2 and #3 were selected for powering tests and measurements at 4.2 K in liquid helium (LHe) at KIT. The mainly investigated and presented parameters below were the same for all three VR coils:

- the coils' behavior was first tested up to the region of its predicted critical current I_c by means of current ramps,

- charging and discharging of the coils was checked via voltage decays enforced by current step functions in the fully superconducting regime,

- smaller current steps were used to explore the limits of the NI coil design up to, around and above I_c as well as to measure the transverse resistance R_{tr} at 77 K.

An electric field criterion of $1\,\mu V/cm$ along the length of the outermost turn ($\approx 30\,cm$), was used to determine the threshold value of $30\,\mu V$ for defining I_c of a coil. This was derived from simulations, determining the point of the highest absolute field value on the outermost turn of a coil, close to the central iron pole. The minimum value of both sub-coils (s-c) equaled I_c of the comprising VR coil: $I_c = \min(I_{c,s\text{-}c1}, I_{c,s\text{-}c2})$. Due to this definition, there may be deviations to the calculated critical current values described in the preceding chapter 3, which was derived for a single tape's I_c. Table 5.1 summarizes the key parameters of all performed powering tests for which each VR coil was placed in the same supporting structure, introduced in the following subsection. The Hall sensors' values had an accuracy of 0.2%. As the voltage taps are located in the first and last turns of each sub-coil, they are directly in the current's path entering and exiting the superconducting coils, thus must be corrected for ohmic resistance, leaving the inductive resistance. VR coil #1, #2 and #3 may be referred to as VRc1, VRc2 and VRc3 in the following.

Table 5.1.: Measured parameters of the VR undulator coils with $I_{\text{sim}}(\text{VRc1, 2}) = 30\,\text{A}$ at 77 K and 828 A at 4.2 K and $I_{\text{sim}}(\text{VRc3}) = 40\,\text{A}$ at 77 K and 400 A at 4.2 K.

Sub-coil	VR coil #1		VR coil #2		VR coil #3	
	1	2	1	2	1[*]	2
77 K (LN$_2$)						
I_c (A)	40	30	39	35	47	41
$B_0(I_\text{sim})$ (mT)	129	16	135	18	275	24
R_tr (µΩ)	58	48	29	19	400	58
τ (s)	26	42	32	46	4	90
R_t2t (µΩ)	1.14	0.94	0.57	0.37	3.92	0.57
4.2 K (LHe)						
I_c (A)	n/a	n/a	930	930	500	420
$B_0(I_\text{sim})$ (T)	n/a	n/a	1.40	0.23	1.26	0.23
τ (s)	n/a	n/a	76	74	5	121

[*] damaged *Re*BCO layer suspected.

5.1.1. Measurement setups

In order to deal with the Lorentz forces during the powering tests, each VR coil was mounted in a stainless steel supporting structure, which was insulated by G10 and Kapton®. Two copper leads were pressed on the curved side of the D-shaped coils to guide the current in and out. A 50 µm thin indium foil was placed between the copper lead and the VR coil's outermost turn to increase the electrical contact. Four M8 bolts on the top plate applied a contact pressure of around 5 MPa. To compensate for pressure loss due to thermal shrinkage, two spring washers were used for each bolt. The insulation of the supporting structure was tested after its mounting for 30 s with up to 1 kV at room temperature. Values above 2 TΩ confirmed the insulating quality of the mock-up assembly.

All VR coils were monitored via six voltage taps (Vtaps) during the powering tests: two on the innermost turns, two at the outermost turns, and two at the copper current leads. Voltages across the single sub-coils would trigger a quench detection above a certain threshold, meaning shutting down the current, thus dumping the energy in the NI coils. Two Hall sensors were placed below the two iron poles at a fixed distance of $d = 3.5\,\text{mm}$ (compare Figure 5.1). For the first test runs, two additional temperature sensors PT1000 were placed next to the outermost turns. The cooling power of liquid nitrogen, however, did not allow for measuring significant data, hence the two PT1000s were removed. Later, the temperature sensors were not used again for the measurements in liquid helium due to a lack of space.

A sketch of the supporting structure cross-section is shown together with the setup for powering tests in LN$_2$ at CERN in Figure 5.2. Current cables were fixed with screws to the copper leads of the VR coil. All data were acquired with a sample rate around 1 Hz while the quench detector was set to 3 mV. The mock-up was placed in an open bucket cryostat where the LN$_2$ was filled in from the top.

The measurement setup for powering tests in LHe at KIT is shown in Figure 5.3. Here, the mock-up was fixed on a G10 plate attached to an insert which was mounted inside the closed cryostat vessel for the powering tests. The external current leads were fixed through the insert and ended with Nb-Ti wires which were soldered to copper plates. A 50 µm thick indium foil was clamped in between these copper plates and the copper leads of the VR coil to increase the electrical connection. Signals were detected with a 10 Hz sample rate while the quench detector was first set to 1 mV and later switched to 4 mV.

(a) Adapted from [114]. (b)
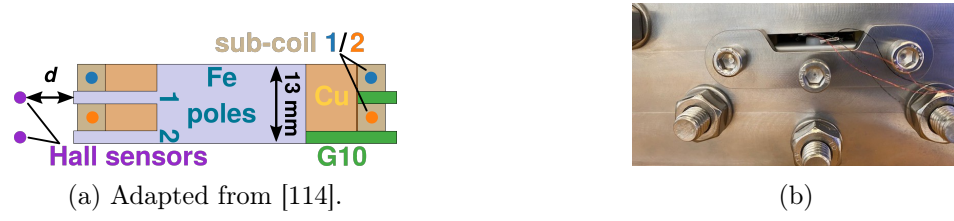
Figure 5.1.: (a) Cross-section sketch of the VR coil measurement setup with the winding body, iron core and poles, sub-coil 1 and 2. Measurement distance $d = 3.5\,\mathrm{mm}$. (b) Close-up of two fixed Hall sensors installed in the VR coil supporting structure. The fine cables were fixed to the stainless steel plate for protection and stable conditions.

(a) VR supporting structure.

(b) LN$_2$ cryostat.

(c) LN$_2$ setup.

(d) VR supporting structure setup.
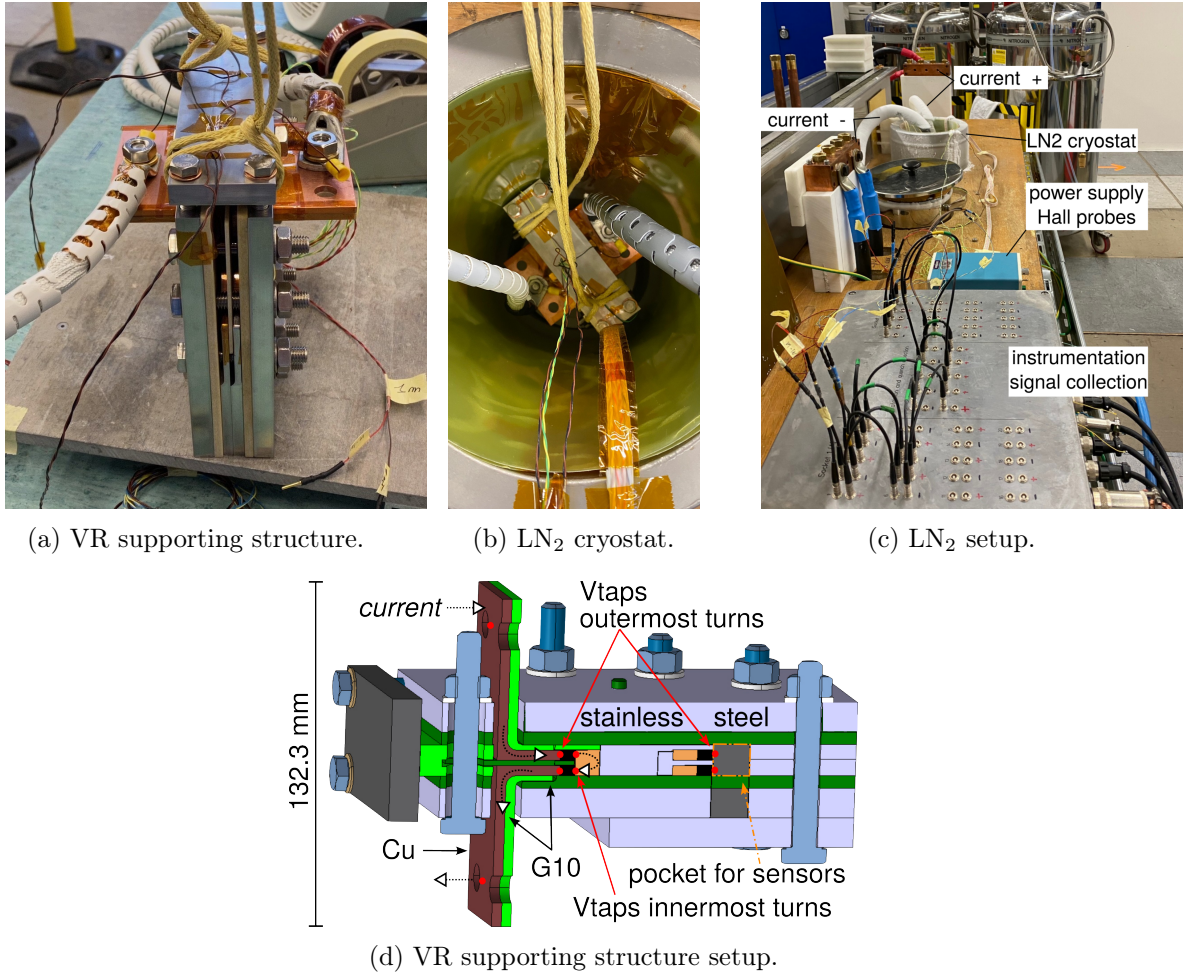
Figure 5.2.: Measurement setup in CERN's building 288 for powering tests of VR coils in liquid nitrogen (LN$_2$) with a supporting structure based on stainless steel.

(a) LHe setup and cabling.   (b) Indium foil contact.
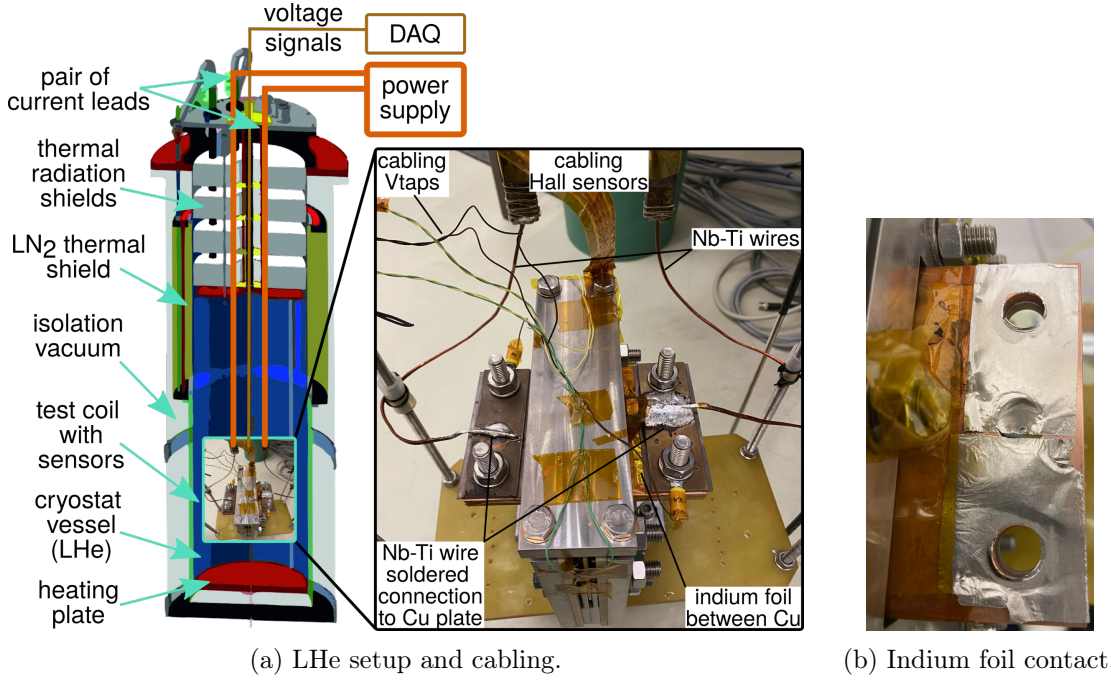
Figure 5.3.: Measurement setup CASPER I at KIT for powering tests of VR coils in liquid
            helium (LHe). 50 µm thick indium foil was placed between the clamped copper
            pieces to increase the quality of the electrical contact.

5.1.2. Powering at 77 K (in LN₂)

Multiple thermal and electrical cycles were performed for each VR coil to ensure the va-
lidity of the measured data. Additionally, a total amount of three powering test sessions,
including multiple test runs, were performed for each VR coil, the first two within ap-
proximately two weeks, and a third about three months later to investigate a possible
degradation of the performance, which was not seen. However, only the very first powering
tests occasionally showed voltage spikes and different transversal resistances which most
likely resulted from moving superconductors.

First signal checks after the cool down to 77 K were carried out with slow current ramps
of 0.05 A/s up to a maximum current value of 30 A. Second current ramps increased the
speed to 0.5 A/s and aimed at current plateaus of 10 A, 20 A, 30 A and 35 A, displayed in
Figure 5.4. As shown in the previous chapter, a different I_c per sub-coil was expected due
to the asymmetric shape of the VR coil and its iron poles which implies an asymmetric
magnetic field distribution on the conductor (cf. subsection 3.1.2). A voltage rise over
the NI sub-coils is expected when the current is ramped up: first of all, the majority of
the current will enter the coil transversely and also has to overcome the inductance before
being able to settle in the superconducting path and therefore letting the voltage decay.
However, ramping up the current further, hence reaching the local I_c, will demand the
current to flow partially in the copper matrix of the coated superconductor and/or even
bypass this zone in a transverse direction. Consequently, an elevated voltage plateau after
a decay time can be measured. As defined above, once this constant voltage reached 30 µV
the sub-coil's I_c was found. All three VR coils showed similar voltage signals. I_c values
of 30 A, 35 A and 41 A were noted for VR coil #1, #2 and #3, respectively. These values
were to be checked by means of small current steps in one of the next subsections.
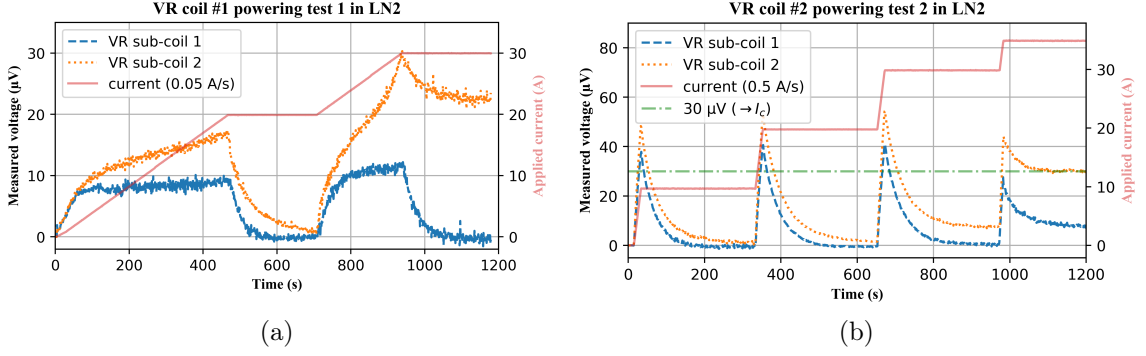
Figure 5.4.: Powering tests with currents ramps and plateaus showing voltage responses across the sub-coils of VR coil #1 (a) and #2 (b). Plots reproduced from [114].

5.1.2.1. Effective time constants

The introduced voltage decay time from above can be used to investigate the undulator VR coil's charging and discharging time. An effective time constant τ was introduced to describe the time the current needs to settle in the superconducting spiral. The voltage over a resistance R can be described for the given number of turns with the resistive transverse current path I_{tr} and the superconducting current path I_{sc}, as derived from the previous chapter's Figure 3.27 [132, 113]:

$$U = (I_{\mathrm{SC}} - I_{\mathrm{R}}) \cdot R + L \cdot \frac{\mathrm{d}I_{\mathrm{sc}}}{\mathrm{d}t} \ . \tag{5.1}$$

The current can be further described by a differential equation when $U \to 0\,\mathrm{V}$, of which the solution is known:

$$\frac{\mathrm{d}I_{\mathrm{sc}}}{\mathrm{d}t} = (I_{\mathrm{R}} - I_{\mathrm{SC}}) \cdot \frac{R}{L} \quad \Rightarrow \quad I(t) = I \cdot \mathrm{e}^{-t/\tau} \ . \tag{5.2}$$

Analog to the current, a simple exponential decay can approximately describe the voltage:

$$U(t) \approx \mathrm{a} \cdot \mathrm{e}^{-t/\tau} \qquad \text{with } \tau = L/R \ , \tag{5.3}$$

coil inductance L and constant a. After a waiting time of $5 \times \tau$, the voltage was considered to be decayed. To make sure that the coil is in a fully superconductive state, a current step plateau value of $10\,\mathrm{A}$ was chosen and kept for $300\,\mathrm{s}$. This was followed by a step to a $0.5\,\mathrm{A}$ plateau, held for another $300\,\mathrm{s}$, back to $10\,\mathrm{A}$ for $300\,\mathrm{s}$ and so on or finally down to $0\,\mathrm{A}$.

Figure 5.5 displays the recorded voltage responses for all three VR coils. Exponential fits were used to extract the individual values of τ. The expected characteristics were observed for VR coil #1 and #2, where similar τ_i of $\tau_{1,\mathrm{s\text{-}c1}}(77\,\mathrm{K}) = 26\,\mathrm{s}$, $\tau_{1,\mathrm{s\text{-}c2}}(77\,\mathrm{K}) = 42\,\mathrm{s}$ and $\tau_{2,\mathrm{s\text{-}c1}}(77\,\mathrm{K}) = 32\,\mathrm{s}$, $\tau_{2,\mathrm{s\text{-}c2}}(77\,\mathrm{K}) = 46\,\mathrm{s}$ have been measured. Although these were tests at $77\,\mathrm{K}$, further improvements of the coil's turn-to-turn resistance are needed in order to align both sub-coils' values and to guarantee a uniform ramp of an undulator magnet with a total field integral of zero. More tests at $4.2\,\mathrm{K}$ had to show if the deviations between the two sub-coils still remain and are presented in the following subsection including suggestions for improvements.

With double the number of turns, VR coil #3 was expected to show longer decay times. Its sub-coil 2 showed $\tau_{3,\mathrm{s\text{-}c2}}(77\,\mathrm{K}) = 90\,\mathrm{s}$, thus was well in agreement with the expectation. However, sub-coil 1 in VR coil #3 showed a different behavior of a drastically fast decay $(\tau_{3,\mathrm{s\text{-}c1}}(77\,\mathrm{K}) = 4\,\mathrm{s})$ with a change of voltage sign followed by a slow voltage increase. As
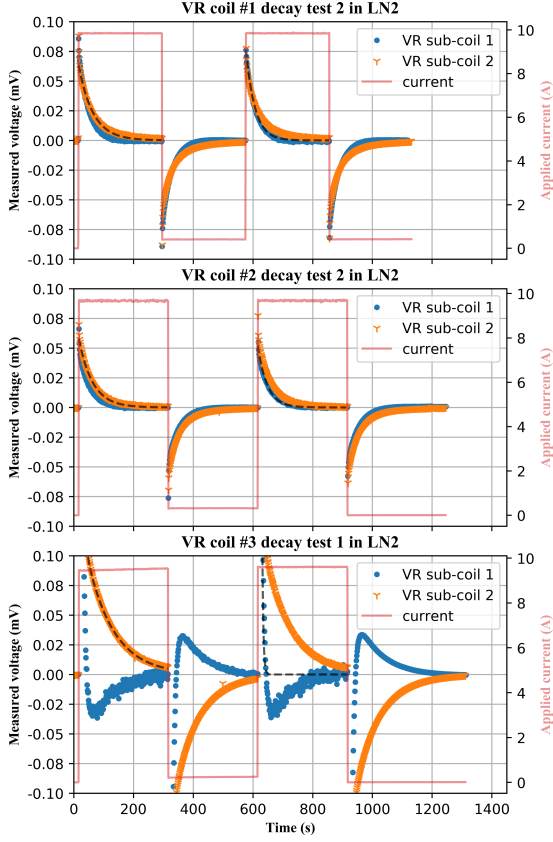
Figure 5.5.: Current step functions to 10 A and the measured voltage decays of VR coil #1 (top), #2 (center) and #3 (bottom), respectively. Exponential fits are indicated by black dashed lines. Plots reproduced from [114].

a simple exponential decay is not capable of describing this behavior, the τ value has to be regarded with suspicion. The fast decay during charging and rise during discharging is a hint at potential damage in the superconducting Re*BCO* layer which would force the current to (dis-)charge transversely and therefore bypass the superconducting spiral. Additionally, both sub-coils are connected in series in the NI VR coil design, thus having a mutual influence on the individual (dis-)charging characteristic – especially when one behaves differently. As a consequence, the slower decaying absolute voltage of sub-coil 2 dragged/pushed current out of or into sub-coil 1. The reason for the higher noise level as noticed for the measured data points of sub-coil 1 during charging is unknown. Further investigations have to reveal the exact type and position as well as possible factors of the assumed defect.

5.1.2.2. Current steps and overflow

A current step function of 2 A and 300 s voltage decay time was used to power all three VR coils progressively up to 112 A. Two Hall sensors tracked the magnetic field below the iron (Fe) poles at a distance of $d = 3.5\,\mathrm{mm}$. The B-field and decayed voltage values are plotted together with the sub-coils' I_c values in Figure 5.6.

All three VR coils showed a qualitative similar performance and the expected behavior, except for VR coil #3's sub-coil 1. I_c values of the individual sub-coils followed the simulated predictions with values noted in Table 5.1. Sub-coil 1 of VR coils #1 and #2 became resistive around 40 A and 39 A, respectively whereas 47 A were found for VR coil #3. The found difference of 30 A compared to 35 A for sub-coil 2 in VR coil #1 and #2 is not fully understood and may be caused by local damage of the superconducting layer during the winding process. Up to the I_c region, an increase of the B-field below the Fe poles 1 and 2 could be seen. As a consequence of being the central iron pole in the VR coil, the absolute

value of Fe pole 1 is significantly higher than that of Fe pole 2. Respective B-field values B_0 of 129 mT, 135 mT and 275 mT were measured below Fe poles 1 in VRc1, 2 and 3 as well as 16 mT, 18 mT and 24 mT below Fe pole 2.

Stepping the current further beyond I_c showed more and more resistive sub-coils and stabilizing B-fields for VR coil #1 and #2. Turn after turn reached its local critical current when the current was stepped up, forcing the V-I-curve to converge to Ohm's law, thus representing the transverse resistance R_{tr} across a sub-coil. This was mainly influenced by the surface resistances between the turns. Values of 58 µΩ and 48 µΩ were detected for VR coil #1, but 29 µΩ and 19 µΩ for VR coil #2. In VR coil #3, R_{tr} was found to be 400 µΩ and 58 µΩ.

Consequently, irregularities during the winding process and different turn-to-turn resistances influence the slope of the linear increase of voltage. The different winding tensions of 30 N and 25 N between VR coil #1 and #2, #3 might most likely be one possible cause. However, the main factor for VR coil #3 was the double amount of turns compared to the other two coils. But this can only explain the reasonably higher value of sub-coil 2. As seen in the previous subsection, VRc3's sub-coil 1 already showed signs of a strong resistive characteristic which was now confirmed with a magnitude larger R_{tr}, explaining the observed fast voltage decay. With the values of R_{tr}, a calculation of the turn-to-turn resistance $R_{t2t,i}$ at 77 K becomes possible by dividing through the number of turns for each sub-coil. The results can be found in Table 5.1 and are with the exception of VRc3's sub-coil 1 in the range of 1 µΩ or smaller. Last but not least, the observed B-field of VRc3's Fe poles does not show a stabilization after having reached I_c making harmed ReBCO sections far away from the Fe poles a suspected root cause with enforced current sharing between turns.

As a result, only VR coil #1 and #2 were studied regarding τ during this current step procedure to further investigate the critical current of single turns. Figure 5.7 shows τ over the applied current step for each sub-coil with the marked I_c of the respective VR coil. In theory, when an HTS coil reached I_c and turn after turn is filled with current, τ should decrease due to the limited amount of remaining turns to be charged. Both sub-coils 1 clearly showed this trend with a drop after their respective I_c around 40 A. On the contrary, sub-coils 2 had more variation in their voltage decay times before also showing a global decaying trend of τ. Within a NI coil, current sharing is always possible which might be a prominent cause of this noticed variation. Therefore, an NI approach with higher turn-to-turn resistance, such as metal insulation, would most likely stabilize the decay times up to I_c. Other possible causes of the varying time constants may be the powering cycle and the series connection of both sub-coils which might influence one coil more than the other due to minor irregularities. This evaluation turned out to be a very interesting way of understanding I_c in a NI HTS coil design but will need further investigations, also for different geometries, and a better statistical background to be more accurate.
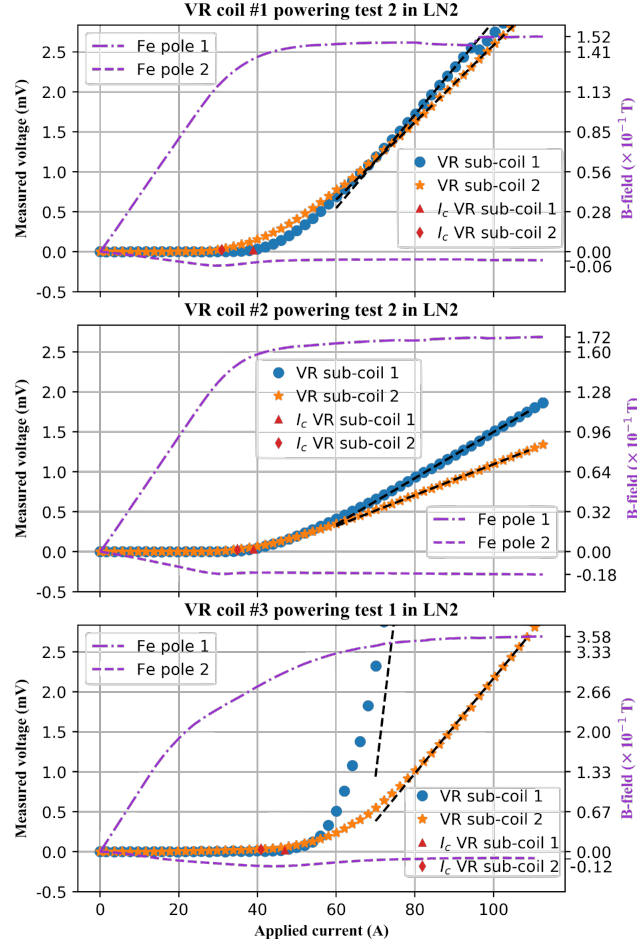
Figure 5.6.: Current step functions with 2 A steps and 300 s latency. Measured decayed
            voltage and B-field responses of VR coil #1 (top), #2 (center), and #3 (bot-
            tom) are plotted, respectively. Linear fits of the transverse resistance are indi-
            cated by black dashed lines. Plots reproduced from [114].
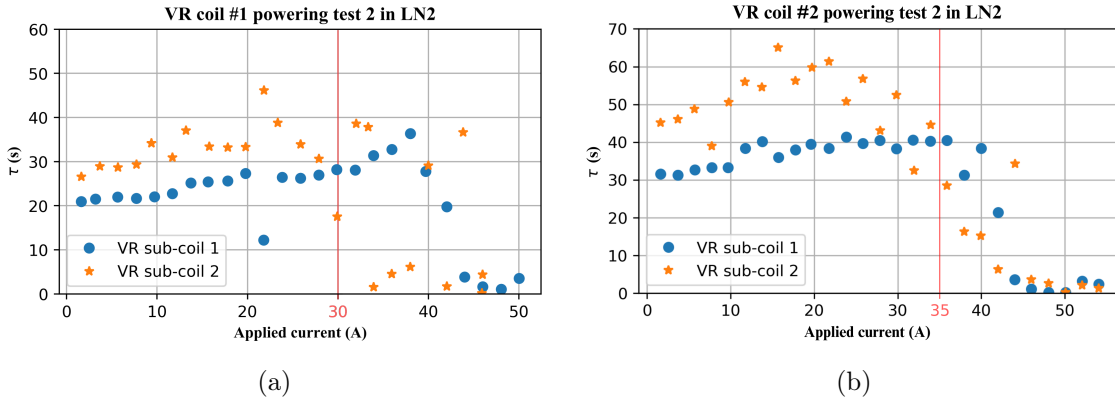
Figure 5.7.: Individual effective time constants τ for applied current steps of 2 A in VR
            coil #1 (a) and #2 (b), where I_c of sub-coils 2 are marked in red. In theory,
            τ should start decreasing when a sub-coil reached its I_c. Sub-coils 1 show a
            clear drop in τ, while sub-coils 2 show a tendency. The variation in τ can be
            explained by the NI winding, allowing free current redistribution.
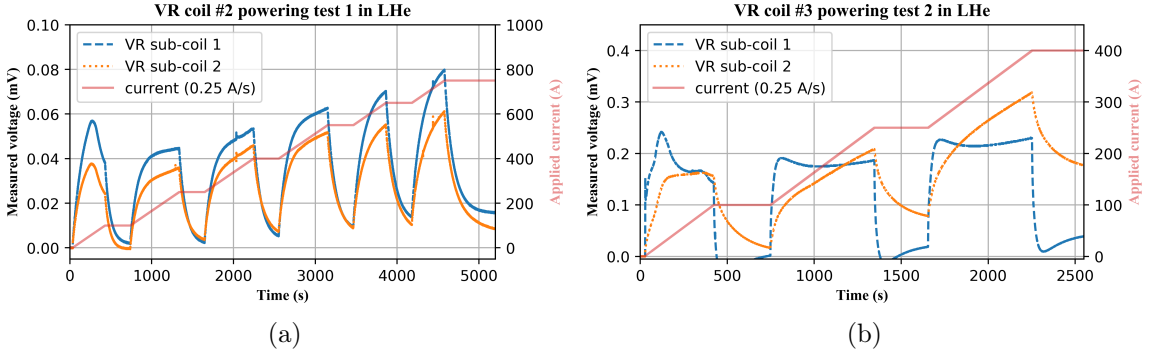
Figure 5.8.: Powering tests and voltage responses of VR coil #2 (a) and #3 (b). The current was ramped to plateaus to see the voltage responses of each sub-coil. Note that the values were not corrected according to the voltage taps' resistance.

5.1.3. Powering at $4.2\,$K (in LHe)

Multiple electrical cycles were performed for each VR coil to ensure the validity of the measured data. The only two unusual powering runs can be found in appendix E. Due to a limited amount of measurement time, only two out of three VR coils were chosen to be tested at $4.2\,$K. With VR coils #2 and #3, two VR coils with different types of coated ReBCO superconducting tapes, thus different amounts of turns were investigated. The various types of powering tests followed the ones performed at $77\,$K, presented in the previous subsection, to validate the qualitative performance.

First signal checks were performed to validate the coils' and voltage taps' connections. As shown in Figure 5.8, the current was ramped with $0.25\,$A/s to plateaus to observe the voltage across the individual sub-coils. VR coil #2 showed the expected response for current plateaus of $100\,$A, $250\,$A, $400\,$A, $550\,$A, $650\,$A and $750\,$A. The sub-coils of VR coil #3 were powered to $100\,$A, $250\,$A and $400\,$A while showing the earlier detected higher resistivity already after the first plateau. Both were powered up until a clear drift in the decayed voltage was visible, thus reaching the region of I_c.

5.1.3.1. Current ramping and magnetic field response

In order to investigate the B-field response of the VR coils at $4.2\,$K, the current was driven up with $0.25\,$A/s to different plateau values as before. A long ramp was used to bring the current in the operation region, thus close to the expected I_c. Shorter ramps followed to explore the region around and above I_c. The voltages of the sub-coils of both VR coils and their B-field responses in a $3.5\,$mm distance of the Fe poles are plotted in Figure 5.9.

The voltage was expected to rise with increasing current as observed earlier and explained above for these NI VR coils. For both VR coils, the B-field acted in accordance with the increasing current and was in excellent agreement with the predicted simulated values (cf. subsection 3.1.2). Saturation of the iron core was seen at approximately $200\,$A and $100\,$A for VR coil #2 and #3, respectively. Operating currents of $828\,$A in VR coil #2 and $400\,$A in VR coil #3 generated magnetic fields of $1.40\,$T and $1.26\,$T. After driving down the current, the field below Fe pole 1 was observed to still have a finite small value, thus implying the presence of persistent currents in the superconductor.

The measured voltage across VRc2's sub-coils showed symmetrical behavior in the same order of magnitude with a peak value of around $0.1\,$mV. After the last current ramp to $975\,$A, a faster voltage decay for sub-coils could be observed, hinting at an I_c saturation of multiple turns. Sub-coils of VRcoil #3 showed a similar behavior at first. However, the voltage over sub-coil 1 increased stronger than across sub-coil 2, beginning from currents
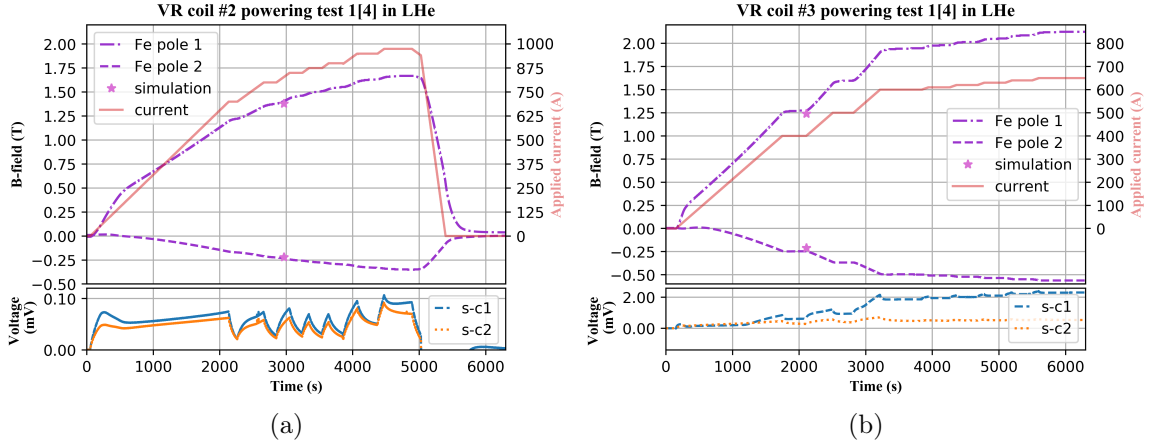
Figure 5.9.: Powering tests and voltage responses of VR coil #2 (a) and #3 (b). The current was ramped to plateaus to see the voltage and the B-field responses. Simulated B-field values for operating currents are marked with purple stars. Reproduced from [143].

higher than $400\,A$ until a four times larger voltage of around $2\,mV$ was observed across VRc3's sub-coil 1 at $600\,A$. As already discussed earlier for the powering tests at $77\,K$, this increased resistance was most likely induced by locally damaged superconducting zones, probably caused during the winding process, forcing the current to flow transversely. Nevertheless, VR coil #3 performed interestingly well with observed B-fields in the expected ranges. As a consequence, the damage is most likely not located closely around the Fe poles. Further investigations, e.g. unwinding and testing sections of the superconductor will most likely be needed to analyze the root cause.

5.1.3.2. Effective time constants

The above analyzed powering tests at $77\,K$ introduced an effective time constant τ to describe the undulator VR coil's charging and discharging time, thus the needed time for the current to settle in the superconducting path. As seen earlier, the decaying voltage can be described by an exponential decay. However, at $4.2\,K$, the coils' turn-to-turn resistance decreases further due to the changing material properties, making a double exponential decay necessary to describe the voltage more accurately, as explained in [132]. In fact, one more term will be added to equation (5.3):

$$U(t) \approx \mathrm{a} \cdot \mathrm{e}^{-t/\tau_{\mathrm{ini}}} + \mathrm{b} \cdot \mathrm{e}^{-t/\tau_{\mathrm{avg}}} \qquad , \tag{5.4}$$

with constants a and b. τ_{ini} and τ_{avg} correlate with the initial and average effective time constants of the NI VR coils. Here, the ramping time of a coil is mainly defined by $\tau_{\mathrm{avg}} \equiv \tau$. To ensure a fully superconductive state for both coils, a current step plateau value of $200\,A$ was chosen and sustained for about $350\,s$ for VRc2. For VRc3 with double the amount of turns, the plateau was kept steady for $1000\,s$. This was followed by a step to a $0\,A$ plateau, sustained for the same respective times, back to $200\,A$ and so on or finally down to $0\,A$. Figure 5.10 plots the observed voltage responses of VR coil #2 and #3 for one step as an example. The individual values of τ were extracted by means of exponential fits. From the powering tests at $77\,K$ expected characteristics were observed for VR coil #2, where two similar τ_i of $\tau_{2,\mathrm{s\text{-}c1}}(4.2\,K) = 76\,s$, $\tau_{2,\mathrm{s\text{-}c2}}(4.2\,K) = 74\,s$ have been measured. As earlier stated, VR coil #3 was expected to show longer decay times due to having double the number of turns. Its sub-coil 2 confirmed that expectation with $\tau_{3,\mathrm{s\text{-}c2}}(4.2\,K) = 121\,s$. Again, sub-coil 1 in VR coil #3 showed a different behavior of a drastically fast decay
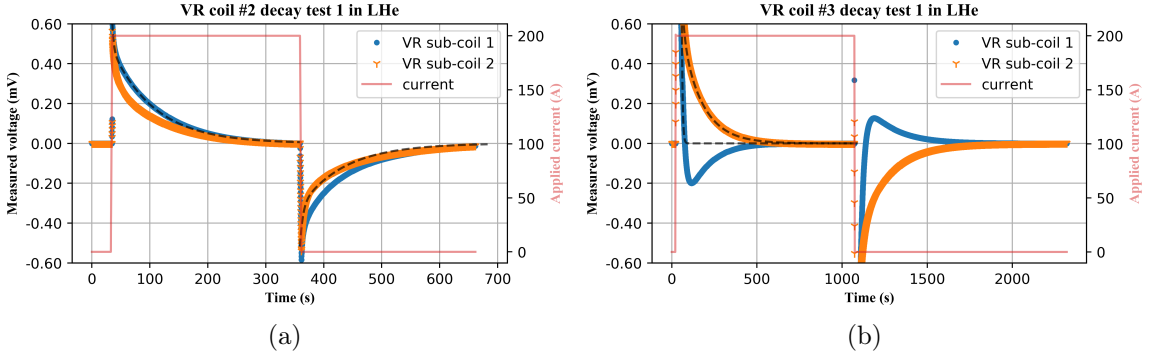
Figure 5.10.: Current step functions to 200 A and the measured voltage decays of (a) VR coil #2 and (b) VR coil #3. Exponential fits are indicated by black dashed lines. Reproduced from [143].

with $\tau_{3,\text{s-c1}}(4.2\,\text{K}) = 5\,\text{s}$ and a change of voltage sign followed by an increase in voltage to zero. As discussed earlier, this τ value has to be regarded with care, since a simple exponential decay is not capable of describing this behavior correctly. The change of sign can be explained as already understood before.

The conformity of the charging times is particularly critical for undulators in a synchrotron, where the insertion device might be switched on or rather charged simultaneously to an already running beam. Here, devastating effects on the beam stability could be induced by a non-zero field integral. Consequently, although being already comparable, the time constants of VR coil #2 should undergo further optimization trying to align both values. This could be done e.g. by implementing a well-controlled turn-to-turn resistance or even by the use of partial insulation. The above-described current ramping showed what B-field level the VR coils could reach and how the B-field increased. To investigate the time constants in more detail and explore the B-field variation in the region of operation, the current was driven up with a ramp rate of 0.25 A/s to 750 A and 400 A, for VR coil #2 and #3, respectively. The variation of the B-field was then monitored at the central Fe pole 1 for more than 600 s, as displayed in Figure 5.11. Magnetic field changes ΔB were analyzed after $5 \times \tau$, with τ being defined as the greater of the two measured values per VR coil. ΔB of 0.23 mT were observed for VR coil #2 and 0.05 mT for VR coil #3 over a 15 s long detection time. These variations meant a relative B-field change of 0.018 % and 0.004 %, respectively, with an equivalent detuning of the hypothetical undulator. The difference in value can be well explained when looking at the voltage across the investigated sub-coils, where a faster settling time was caused by higher resistances: voltage peak values of VR coil #3 were about four times higher than the ones of VR coil #2.

Nevertheless, the two investigated VR coils appear to stabilize faster than other, earlier NI coil approaches (compare [28]). The same group demonstrated as well the expected influence of partial insulation to maintain the undulator field after 200 s, observing a ΔB of 2 mT over 45 s, yet losing partially the advantage of a self-protective coil. Having a well-controlled turn-to-turn resistance will certainly make the charging time faster, however, will need further investigation in more detail. Metal insulation or rather a separation between turns, e.g. made of stainless steel or brass, may be a promising approach, maintaining the self-protective characteristics of a NI coil design. Such approaches have already been successfully studied for high-field HTS solenoids [139, 140, 141].
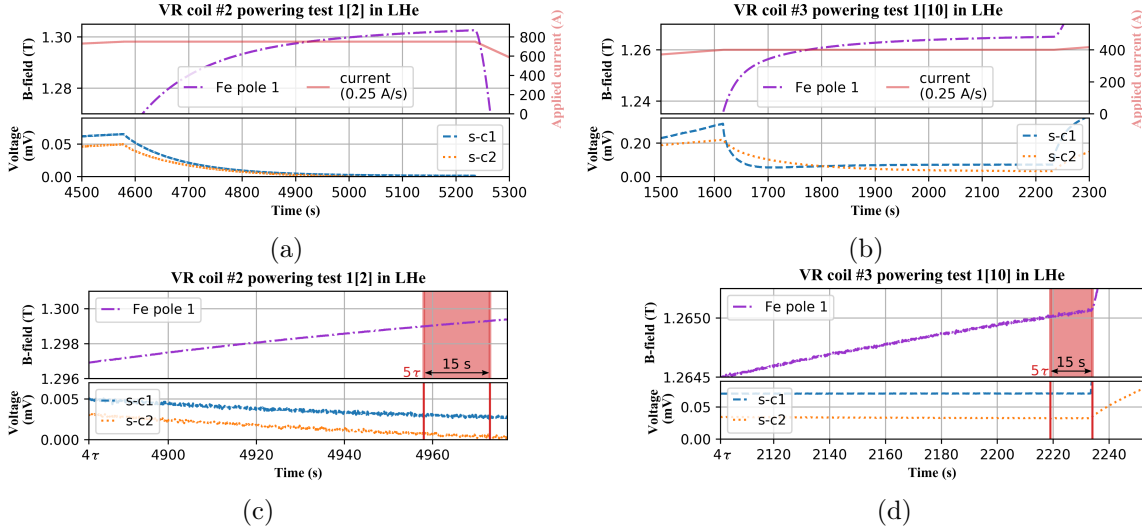
Figure 5.11.: Measured B-fields over time, $3.5\,\mathrm{mm}$ below the respective Fe pole 1 of VR coil #2 (a) and #3 (b) with the voltage across the individual sub-coils (s-c) after a $0.25\,\mathrm{A/s}$ current ramping rate. Reproduced from [143]. (c) and (d) display the investigated time interval for determining ΔB around 5τ.

5.1.3.3. Current steps and overflow

To detect the VR coils' I_c, both were powered step-by-step until a sub-coil's voltage fell back to an asymptotic voltage plateau of greater or equal to $30\,\mathrm{\mu V}$ after a decaying time t_d. For VR coil #2, the current was incremented with steps of $40\,\mathrm{A}$ and $t_\mathrm{d} = 300\,\mathrm{s}$ in between steps, whereas VR coil #3 had steps of $20\,\mathrm{A}$.

The decayed voltage can be seen in Figure 5.12 for the applied current and the corresponding signals of the Hall sensors. Up to an I_c of $930\,\mathrm{A}$, VR coil #2 showed a stable performance for both its sub-coils. With the geometry of the Bruker HTS tape, this equals to a J_e of $2.3\,\mathrm{kA/mm^2}$, creating a B-field $B_0 = 1.6\,\mathrm{T}$ below the central Fe pole 1. The iron core saturation could be seen around $200\,\mathrm{A}$. After I_c, a clear rise in voltage was detected for both sub-coils of VRc2. A similar performance was observed for VRc3's sub-coil 2, which revealed an I_c of $420\,\mathrm{A}$ with stable low voltage. The curved data points of sub-coil 1 together with the spotted voltage spikes in previous power runs once more strengthen the assumption of potential local damage in the superconducting layer. The variation in the decayed voltage of sub-coil 1 was most likely caused by a significant transverse current flow on different routes, leading to various decay speeds, thus voltages after t_d. Nevertheless, an I_c of $500\,\mathrm{A}$ was detected for sub-coil 1. The clear linear increase of the magnetic field even beyond the critical current hints additionally at a local defect, rather than having reached the coil's absolute critical current.

As already mentioned, the current needs more time to settle in the superconducting path with double the number of turns for VR coil #3 compared to #2. Consequently, t_d should have been longer than the waited $300\,\mathrm{s}$. In hindsight, the measured I_c would have been more representative for VR coil #3 with a t_d of $600\,\mathrm{s}$. The relatively low increase of voltage for sub-coil 2 and the further strongly increasing B-field revealed a potential higher I_c for a longer voltage decay time. Yet, a B-field B_0 of $1.3\,\mathrm{T}$ could be measured below the central Fe pole 1 for an I_c of $420\,\mathrm{A}$, corresponding to a J_e of $2.3\,\mathrm{kA/mm^2}$ with the geometry of the utilized Superpower tape. Furthermore, $B_0 = 1.6\,\mathrm{T}$ would be the result of $500\,\mathrm{A}$, or rather $J_\mathrm{e} = 2.7\,\mathrm{kA/mm^2}$.
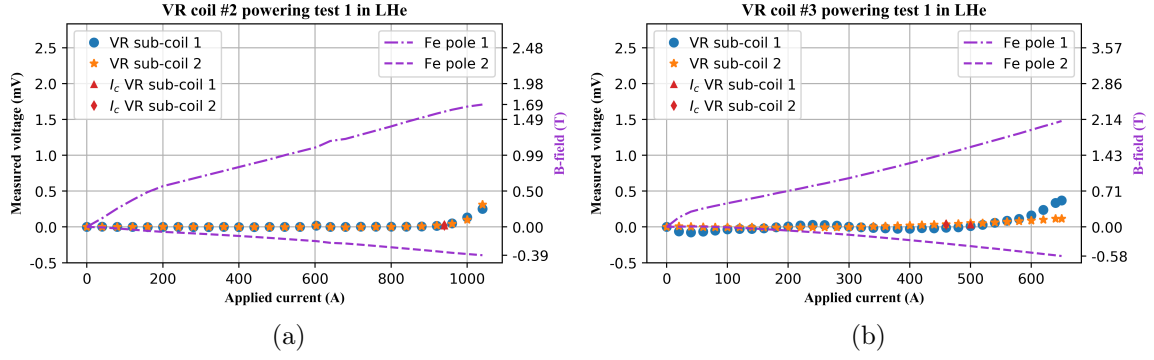
Figure 5.12.: Current step functions for VR coil #2 and #3 with 40 A steps (a) and 20 A steps (b), respectively. Measured decayed voltage and B-field responses after 300 s latency are plotted, respectively. Reproduced from [143].

The quenching behavior of VR coil #3 should be investigated in an ultimate powering test. This was performed with current ramps until the voltage started slowly increasing while keeping the current constant on a plateau as plotted in Figure 5.13. To enforce a steep voltage slope, more than 650 A were needed until sub-coil 1 triggered the voltage threshold of 4 mV inducing a rapid current ramp down after 0.5 s due to which the B-field decreased accordingly. The strongly evaporating Helium and the high resistance clearly prove a quench event which happened at roughly 130% of I_c – a value most likely never to be reached in ordinary undulator operation.

VR coil #3 was cooled down after this incident and could be powered as before this event without any visible degradation in B-field performance, proving the stability of this NI coil design. However, clear signs of burned areas on both, the HTS coil and the insulating material were seen after opening the mock-up as captured in Figure 5.14. In the quench event, the current was forced through the normal conducting materials of the coated superconducting tape causing heat. With 140 °C as the upper operating temperature of G10, the burned marks on the G10 together with the coil performance after this event led to a potential temperature between 140 °C and approximately 200 °C, leaving the superconductor still operational. The quench clearly started in the region where the copper leads end touching the VR coil. As there is no way for the current to escape, this seems consistent since the outer copper support did not surround the entire coil.

(a)   (b)
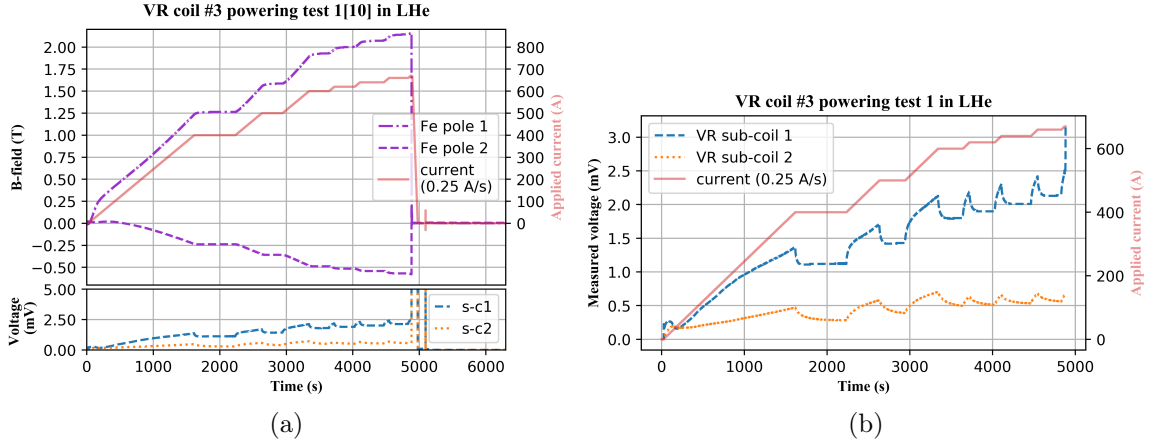
Figure 5.13.: Powering test and voltage responses of VR coil #3 for a powering run forcing a quench. (a) All the data including current steps and ramps, B-field response, and the voltage across the two sub-coils (s-c). Reproduced from [143]. (b) A close-up of the voltages across sub-coil 1 and 2. The current was driven to plateaus to see the voltage responses of each sub-coil. The ramping was stopped after a runaway of the voltage was detected.

(a)   (b)
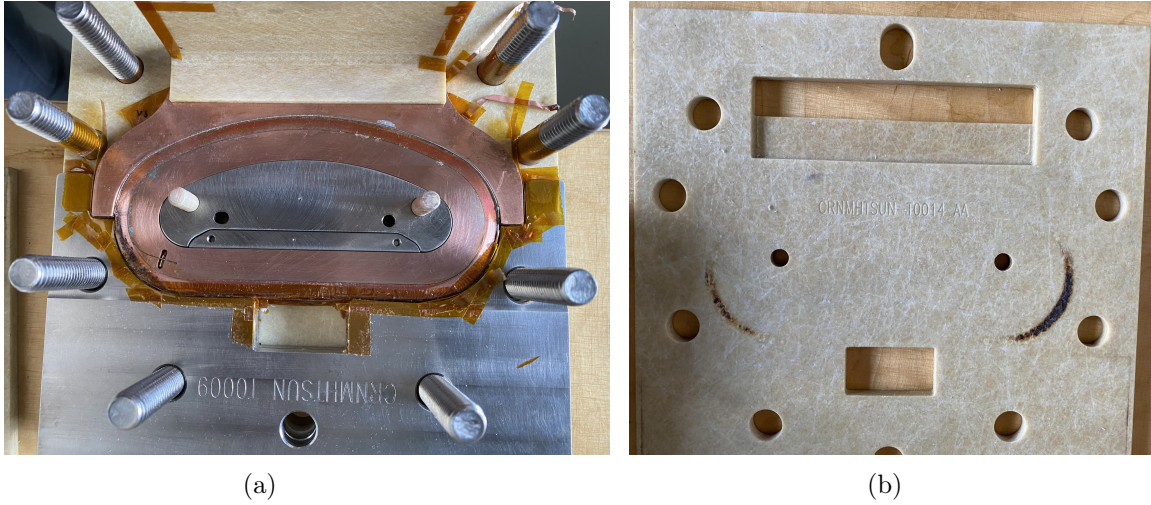
Figure 5.14.: The mock-up opening after the quench event. (a) VR coil #3 inside its supporting structure, (b) Branded G10 insulation plate which can withstand temperatures up to 140 °C. The current was forced through normal conducting zones next to the end of the copper lead.

5.2. Helical undulator demonstrator: short model

This section covers the experimental studies of the helical undulator demonstrator, which was wound as a short model with five periods. The demonstrator represents 10% of the full superconductor length, thus 12 turns instead of 120. However, the innermost turns of this type of helical coil see the highest magnetic flux density according to calculations (cf. Figure 3.13b) and have to undergo the smallest bending radii (≥ 2.5 mm), which makes their realization the most challenging for the full-size magnet. Therefore, powering tests at 77 K were performed in liquid nitrogen at CERN to show the proof of principle by matching the calculated critical operating currents to the tested ones. The following points were covered in this investigation:

- the coils' behavior was first tested up to the region of its predicted critical current I_c by means of current ramps,

- current ramps were further used to explore the limits of the NI coil design up to, around, and above I_c as well as to measure the transverse resistance R_tr at 77 K.

- charging and discharging of the coils was checked via voltage decays enforced by current step functions in the fully superconducting regime.

Magnetic measurements could not be realized within the work of this thesis, as developing a movable measurement setup to be operated in LN$_2$ along the length of the 4 mm wide aperture would have needed a significant additional amount of time and further investigations. An electric field criterion of $1\,\mu\mathrm{V/cm}$ along the length of the innermost turn (≈ 73.5 cm), was used to determine the threshold value of $73.5\,\mu\mathrm{V}$ for defining I_c of the helical demonstrator coil. This was derived from simulations, determining the point of the highest absolute field value on the innermost turn of this coil.

5.2.1. Measurement setup

To bring the current into and out of the superconducting coil, two copper leads were pressed on top of the inner and outer copper terminals with a $50\,\mu\mathrm{m}$ thin indium sheet in between to increase the contact. Each was clamped by an M3 and M4 bolt and supported by spring washers, to compensate for pressure loss due to thermal shrinkage. As both current leads were located close to each other, i.e. between 1.4 mm and 2 cm due to the reduced number of turns, they are insulated by four layers of $50\,\mu\mathrm{m}$ thin Kapton® sheet, and an additional 5 mm thick G10 plate, where possible.
The helical undulator demonstrator was monitored via seven voltage taps (Vtaps) during the powering tests: one voltage tap on each turn's inner tape plus an additional on the in-going current's copper lead. As all voltage taps but one are located directly on the superconductor and with distance to the copper terminals, only an inductive resistance can be seen during current changes. Voltages across the individual turns or across the coil would trigger a quench detection above a certain threshold, meaning shutting down the current, thus dumping the energy in the non-insulated helical undulator demonstrator coil. The test station and cryostat setups were similar to the one presented earlier in Figure 5.2c. The helical undulator demonstrator was placed in an open vat cryostat where the LN$_2$ was filled in from the top. Current cables were fixed with screws to the copper leads of the helical coil. All data were acquired with a sample rate around 5 Hz while the quench detector was set to 1 mV. The setup for powering tests in LN$_2$ at CERN is shown in Figure 5.15.

104
5. *Coated ReBCO tape-based undulator coils:*
experimental results and analyses

(a)   (b)
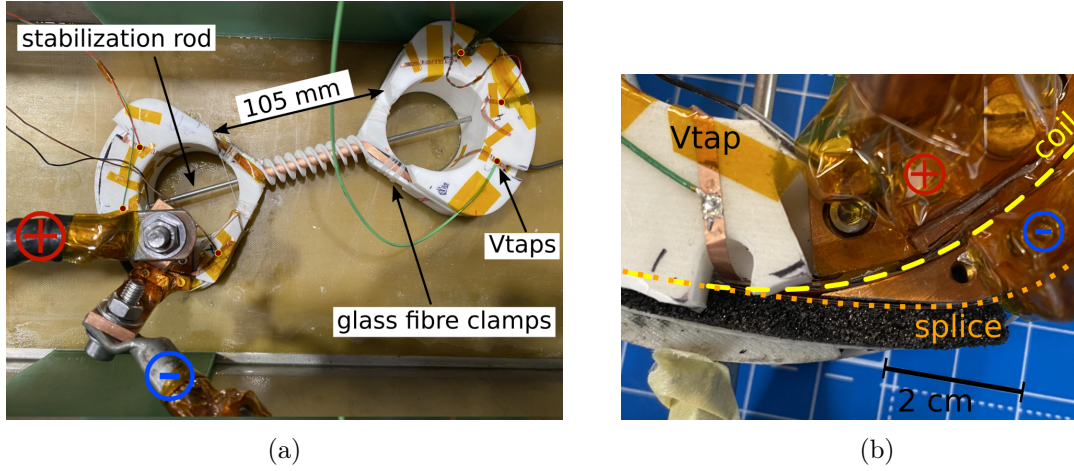
Figure 5.15.: Helical undulator measurement setup inside a LN_2 bath cryostat. (a) All
cables are voltage taps for individual turns. A non-magnetic stainless steel
(316LN) rod was placed inside the beam pipe, to stabilize the coil mechani-
cally. Glass fiber cords were used to fix the tape stack at critical locations.
(b) The yellow dashed line sketches the superconducting coil path in the re-
gion of the current leads. The dotted orange line represents the additional
soldered connection from the outermost turn to the copper terminal, realized
with a two-tape stack.

5.2.2. Powering at 77 K (in LN_2)

Multiple thermal cycles and electrical powering test runs were performed over two weeks
to ensure the validity of the measured data. Additional powering runs of interest can be
found in appendix D.2. Similar to the investigated VR coils, the very first powering tests
occasionally showed voltage spikes far away from the critical current region, which most
likely resulted from moving superconductors. First signal checks after the cool down to 77 K
were carried out with current ramps of 0.25 A/s up to a maximum current value of 30 A
and verified the correct operation. A voltage rise over the helical undulator demonstrator is
expected when the current is ramped or stepped up for the same reasons as presented earlier
for the VR coils: first of all, the majority of the current will enter the coil transversely and
also has to overcome the inductance before being able to settle in the superconducting path
and therefore letting the voltage decay. This behavior can be seen in both investigations
presented in the following subsections.

5.2.2.1. Effective time constants

The introduced effective time constant τ from the VR coil investigations was used to inves-
tigate the helical undulator demonstrator's charging and discharging time by monitoring
the voltage decay (compare equation 5.3). To make sure that the coil is in a fully super-
conductive state, a current step plateau value of 10 A was chosen and kept for 60 s. This
was followed by a step to a 0.5 A plateau, held for another 60 s, back to 10 A for 60 s and
so on or finally down to 0 A.
Figure 5.16 displays the monitored voltage responses over the helical undulator demonstra-
tor. Exponential fits were used to extract τ. Even if there are only 12 out of 120 turns,
a clear decay of voltage can be seen as the current needs time to settle in the supercon-
ducting coil. Multiple powering tests with the described step function show a $\tau_{\text{Hel}} = 4.7$ s.
Taking the earlier results for the VR coils #2 and #3 having different amounts of turns
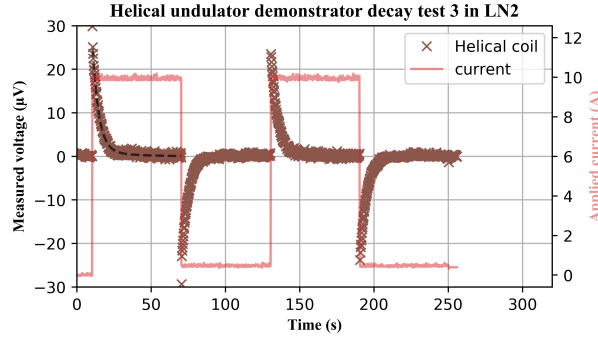
Figure 5.16.: Current step function to 10 A and the measured voltage decays of the helical undulator demonstrator at 77 K. The exponential fit is indicated by a black dashed line.

into account, the following estimation may be drawn: doubling the amount of turns approximately results in a doubling of the (dis-)charging time. Applying this approximated scaling law yields an effective time constant of $10 \times \tau_{\mathrm{Hel}} = 47\,\mathrm{s}$ for a full-size helical undulator short model. After a waiting time of $5 \times \tau$, the voltage is considered to be fully decayed. However, scaling the decaying time up to a full-size helical undulator short model may not be completely straightforward and also depends on other technical factors such as the stable winding tension, thus the overall turn-to-turn resistance. Consequently, more tests for a full-size short model and at $4.2\,\mathrm{K}$ need to be performed in order to produce more significant charging times data for a *Re*BCO tape-based helical undulator. Furthermore, multiple short models have to be built and tested to ensure the reproducibility of this performance.

5.2.2.2. Current ramps to critical current and beyond

As already mentioned, a voltage rise over the helical undulator demonstrator is expected when the current is ramped up, due to the current overcoming the coil's inductance before being able to settle in the superconducting path and therefore letting the voltage decay. However, driving up the current further, hence reaching the local I_{c}, will demand the current to flow partially in the copper matrix of the coated superconductor and/or even bypass this zone in a transverse direction. Consequently, an elevated voltage plateau after a decay time can be measured. As defined above, once this constant voltage reaches $73.5\,\mathrm{\mu V}$ the demonstrator's I_{c} is found. Figure 5.17 presents the powering of the helical undulator demonstrator up to and beyond its I_{c}. Although voltage taps monitored each individual turn, solely the voltage signal across the entire demonstrator and turn 2 is plotted as an example to ensure readability. Here, the current was driven with $0.5\,\mathrm{A/s}$ up to $100\,\mathrm{A}$, $120\,\mathrm{A}$, $140\,\mathrm{A}$, $150\,\mathrm{A}$, and $160\,\mathrm{A}$ with a resting time at each plateau of $60\,\mathrm{s}$. A first clear increase in voltage was seen for the ramp to $150\,\mathrm{A}$ in turn 2. Multiple powering runs revealed an I_{c} value of $150\,\mathrm{A}$ for this demonstrator coil, wound with a non-insulated two-tape stack cable.

Driving the current further up to $160\,\mathrm{A}$, representing $106.7\%\ I_{\mathrm{c}}$, directly caused a voltage runaway. However, the overall voltage stayed at a constant-high value of roughly $612\,\mathrm{\mu V}$ for keeping the current constant again and could be driven down together with ramping down the current. This relatively high-voltage plateau can be interpreted as transverse current trespassing, implying a transverse resistance $R_{\mathrm{tr}} = U/I \approx 3.8\,\mathrm{\mu\Omega}$ for this helical undulator demonstrator short model. Scaling this value up to a full-size helical undulator short model as seen above for the time constants, yields $10 \times R_{\mathrm{tr}} = 38\,\mathrm{\mu\Omega}$. However, this value will most likely be an overestimate, as a full-size version of this helical undulator
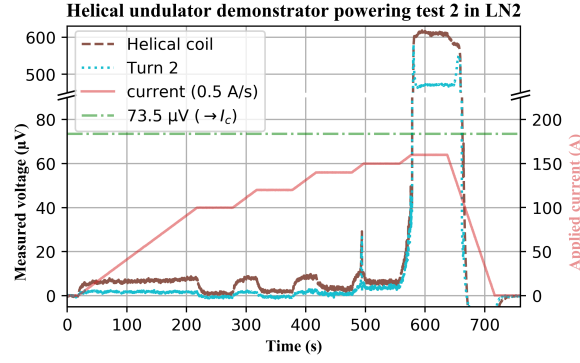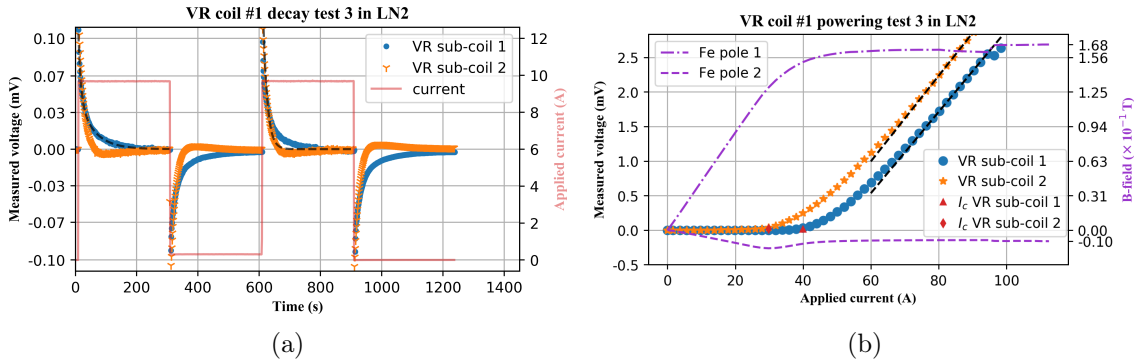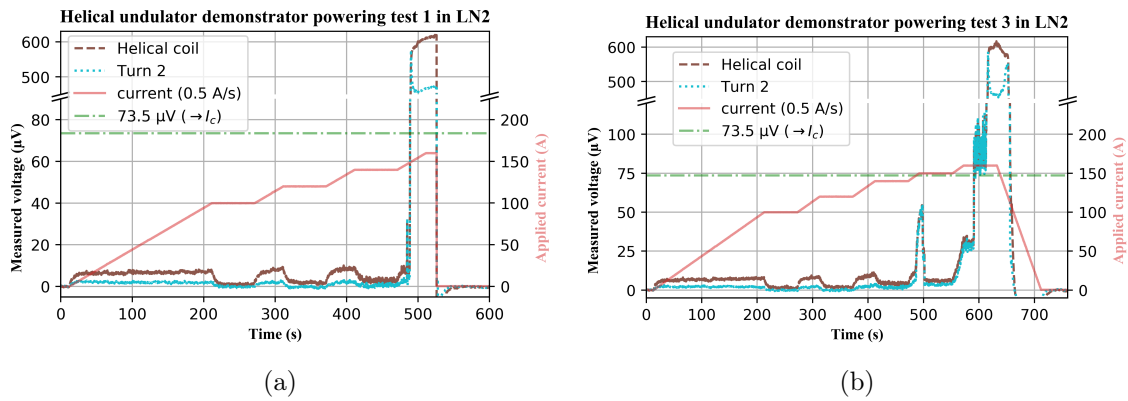
Figure 5.17.: Powering test and voltage responses of the helical undulator demonstrator at 77 K. The current was driven to plateaus to see the voltage responses of each turn as well as across the entire coil. The ramping was stopped after a clear voltage plateau was detected.

magnet will have larger copper terminals, thus providing a greater area for the current to flow transverse.

The helical undulator exercised in this demonstrator did not show any showstopper so far for further exploration toward a full-size helical undulator short model. It is worth noticing that the experimentally found I_c value agrees with the calculated prediction, yielding confidence regarding this extremely compact and novel *Re*BCO-based undulator design. Nevertheless, magnetic field measurements should be performed to further cross-check its performance.

6. Conclusion

6.1. Achievements

The application of high-temperature superconductors (HTS) in the form of coated ReBCO superconducting tapes to undulator magnets for compact free-electron lasers was investigated in this thesis. Advanced high-field short-period undulators of the three most common coil geometries (vertical and horizontal racetracks as well as a helical undulator) were analyzed. Methods for the manufacturing of such optimized coils and operational results were presented, including the following main achievements:

- The parameter space was investigated to determine an ideal operating range where the application of ReBCO is significantly superior to the current Nb-Ti technology and in which modular coil models for all three geometries were designed, optimized, and evaluated.

- An advanced design of a vertical racetrack (VR) coil and the very first design[1] of a helical undulator wound with HTS tape were both derived and assessed. Manufacturing techniques and processes were developed and major technical challenges were identified and solved.

- Important characteristics of coated ReBCO superconducting tapes for coil manufacturing were analyzed by bending and heating experiments as well as critical current measurements in self-field and external field at 77 K.

- Three VR coils were built as no-insulation (NI) coils and tested at 77 K and 4.2 K. At low temperatures, safe operations at high engineering current densities of $2.3\,\mathrm{kA/mm^2}$ and $3.6\,\mathrm{kA/mm^2}$ generated magnetic fields of up to 1.5 T and 2 T at 3.5 mm distance from the magnetic iron poles, respectively. Additionally, operations beyond the coil's critical current with no detected degradation were achieved, proving the aimed stability of the copper-stabilized NI coil design.

- The very first HTS helical undulator demonstrator[1] was built from coated ReBCO superconducting tape as a five-period short model and successfully tested at 77 K.

In conclusion, the potential and value of the HTS ReBCO for superconducting undulators have been demonstrated successfully as well as the feasibility to build and operate such designs with modular coils. These ReBCO-based NI undulator coils can produce up to 70% higher magnetic flux density amplitudes at 4.2 K compared to the state-of-the-art superconducting undulator magnets made of Nb-Ti. However, a few more steps are needed to mature this technology for the application. Mastering the quench protection for HTS coils as well as the screening currents after ramp up and down are the main concerns. The presented NI approach demonstrated already impressively how HTS coils can be protected.

---

[1] To the author's knowledge.

Yet, this comes with current redistribution which may be an issue for the field quality. Overall, significantly outperforming the state-of-the-art superconducting undulators and a potential operation at higher temperatures with the indirect effect of saving energy, thus cost, makes the investigated advanced HTS undulator coils a very attractive option for the next generation of compact synchrotron light sources.

6.2. Prospects

As presented above, many challenges were overcome, and all questions from chapter 1 were answered, which resulted in substantial achievements in the field of compact high-field undulators. However, not all aspects of the design, manufacturing, and operation of HTS undulator magnets could be handled in the scope and time frame of this thesis. Some had to be disregarded because the technology needs to mature further, others because they exceed the scope or due to limited funding. With his having noted, future work should address the following aspects:

- The observed effective time constants at $4.2\,\mathrm{K}$ of $90\,\mathrm{s}$ and $120\,\mathrm{s}$ may be reasonable for steady-state operation, yet need to become shorter to enable fast charging tunable undulators. Potential improvements concerning the used cable may be done, e.g. applying a multiple-tape stack with two or more tapes as cable to lower the coil's inductance or co-winding a metal tape for increasing the turn-to-turn resistance.

- One VR sub-coils showed an alarming high resistance (VR coil #3, sub-coil 1). The likeliest origin is damage or defect in the ReBCO layer, which might have been caused during the winding process. Unwinding the VR coil might help to find the source of this high resistance and its location, and may give information on how to prevent such incidents in the future.

- As a logical next step, a short vertical racetrack model undulator should be built, to demonstrate the feasibility of NI coils, also in terms of stress and strain. The modularity has to be proven experimentally in order to easily realize an extension of the overall length of the magnet. Here, especially the connection between the modular VR coils needs to be evaluated by building at least a five-period short model.

- On-axis magnetic field measurements of the helical undulator demonstrator should be performed to validate the simulations, completing the proof of principle of this very compact design.

- The horizontal coil design should be further investigated, as it provides a preferred tape orientation, thus great potential. Here, the coil ends have to be redesigned for short periods as the tape's bending radius is a critical limit.

- The influence of potential eddy currents has to be investigated for the field quality, especially after ramping the magnet, as no fully transposed cables were used. Notably, coated ReBCO superconductors may not evenly distribute the current during ramp-up since the applied current first flows along the tape edges due to shielding effects, causing screening currents, and thus counter fields [144].

- For the presented coils, beam-dynamics studies should be performed after having measured a magnetic flux density field map of the helical undulator and of a VR undulator short model to evaluate the field quality and its margins. This may also include further investigation of the influence of synchrotron radiation on the magnet's heat load.

HTS, including *Re*BCO-based superconductors, are still undergoing further developments and enhancements for applications in terms of critical current densities, e.g. thinner substrates, advanced pinning methods, and optimized cable geometries [79, 145]. Consequently, further future improvements may be expected. Further, HTS makes a new field of operating temperatures above $4\,\mathrm{K}$ or very high current densities, thus magnetic fields, accessible not only for superconducting undulators but for electromagnets and general power applications, such as fusion power. Therefore, more relaxed cryogenic requirements and cooling cost reductions become feasible, facilitating the future application of superconducting undulators. The anticipated higher demand for HTS will further lower the market price and thus increase the availability and application of HTS, such as *Re*BCO.

Appendices

A. Supplementary fundamentals

A.1. Calculation methods for magnetic field amplitudes.

In subsection 2.1.2, the following integrals of the components $B_{x,0}$ and $B_{y,0}$ can be treated consistently with equation 2.34:

$$B_{x,0} = \frac{\mu_0 I}{4\pi} \oint \frac{(\mathrm{d}\vec{r}\,' \times \vec{s})|_x}{s^3} = \frac{\mu_0 I}{4\pi} \oint \frac{s_z \mathrm{d}r'_y - s_y \mathrm{d}r'_z}{s^3}$$

$$= \frac{\mu_0 I}{4\pi} \int_{\phi_1}^{\phi_2} \frac{R^2 \tan(\zeta) \cdot (\sin(\phi) - \phi \cos(\phi))}{s^3} \mathrm{d}\phi \; , \tag{6.1}$$

$$B_{y,0} = \frac{\mu_0 I}{4\pi} \oint \frac{(\mathrm{d}\vec{r}\,' \times \vec{s})|_y}{s^3} = \frac{\mu_0 I}{4\pi} \oint \frac{s_x \mathrm{d}r'_z - s_z \mathrm{d}r'_x}{s^3}$$

$$= \frac{\mu_0 I}{4\pi} \int_{\phi_1}^{\phi_2} \frac{-R^2 \tan(\zeta) \cdot (\cos(\phi) + \phi \sin(\phi))}{s^3} \mathrm{d}\phi \; . \tag{6.2}$$

B. Critical current density scaling laws

The following subsections list the describing functions of the treated and investigated superconductors' critical current density functions. The according parameters, utilized in this thesis are listed in the provided tables.

B.1. *Re*BCO

The J_c description of coated *Re*BCO conductors is considered to be limited by the interaction between individual flux lines and pinning centers and is mainly based on the description of a CERN internal report and a Ph.D. thesis by J. Fleiter [115, 146]. The following base function was implemented for fitting the critical surface as a function of magnetic flux density B, temperature T, and field orientation angle ι:

$$J_c(B,T,\iota) = \min\big(J_{c,ab}(B,T), J_{c,c}(B,T)\big) + \frac{\max\big(0, J_{c,ab}(B,T) - J_{c,c}(B,T)\big)}{1 + \left(\frac{\iota - \iota_{max}}{g(B,T)}\right)^{\nu}} \ . \quad (6.3)$$

Here, ι_{max} is the angle at which the critical current reached its maximum across all measured field orientations. Therefore, this formula is valid for $\iota \in [\iota_{max}, \iota_{max} + \pi/2]$, which is commonly $\iota \in [\pi/2, \pi]$. Further, $J_{c,ab}$ and $J_{c,c}$ are the critical current densities for external fields in parallel and perpendicular orientation, where ι_{max} is typically correlated with $J_{c,ab}$. The min- and max-functions are necessary to prevent irregularities for $J_{c,ab}(B,T) < J_{c,c}(B,T)$, which might happen at high temperatures [69]. Finally, ν is a unitless exponent and the anisotropy is described by the function g:

$$g(B,T) = g_0 + g_1 B e^{-g_2 e^{g_3 T}} \ , \quad (6.4)$$

where g_0, g_1, g_2, g_3 are fitting parameters. Further, the respective critical current densities are defined as

$$J_{c,ab} = \frac{\alpha_{ab}}{B} \cdot b_{ab}^{p_{ab}} (1 - b_{ab})^{q_{ab}} \cdot \Big((1 - t^{n_1})^{n_2} + a(1 - t^n) \Big)^{\gamma_{ab}} \quad (6.5)$$

$$J_{c,c} = \frac{\alpha_c}{B} \cdot b_c^{p_c} (1 - b_c)^{q_c} \cdot (1 - t^n)^{\gamma_c} \ , \quad (6.6)$$

with the reduced magnetic fields b_{ab} and b_c, the reduced temperature $t = T/T_{c0}$ with the maximum critical temperature T_{c0} for $B = 0\,\mathrm{T}$, the normalization constants α_{ab} and α_c and the reduced field dependence parameters p_{ab} and p_c as well as q_{ab} and q_c. The reduced temperature dependence is described by γ_{ab} and γ_c and varies between perpendicular and parallel field orientations due to the nature of pinning centers' intrinsic difference. The reduced fields in the respective field orientations are given as

$$b_{ab} = \frac{B}{B_{i,ab}} \ , \quad \text{with} \quad B_{i,ab} = B_{i0,ab}\Big((1 - t^{n_1})^{n_2} + a(1 - t^n) \Big)$$

$$b_c = \frac{B}{B_{i,c}} \ , \quad \text{with} \quad B_{i,c} = B_{i0,c}(1 - t^n) \ ,$$

where the the maximum irreversibility fields are described by $B_{i0,ab}$ and $B_{i0,c}$ at $T = 0\,\mathrm{K}$, and n, n_1, n_2 represent fitting parameters. However, $n = 1$ is a common assumption in order to decouple the two critical current densities $J_{c,ab}(B,T)$ and $J_{c,c}(B,T)$.
The total critical current density J_c can further be transformed into the current carrying capacity of the tape superconductor:

$$I_c = \bar{J}_{cpw} \cdot d = J_c \cdot dw \cdot \hat{s}, \quad (6.7)$$

Table B.1.: Fitting parameters with units for describing the used SuperPower HTS tape.

Parameter	$\iota_{\max}$	a	ν	α_{ab}	α_{c}	γ_{ab}	γ_{c}	$B_{i0,ab}$	$B_{i0,c}$	T_{c0}
Unit	-	-	-	AT/mm^2	AT/mm^2	-	-	T	T	K
Value	$\pi/2$	0.1	1.85	68.3×10^6	1.86×10^6	1.63	2.44	250	140	93

Parameter	g_0	g_1	g_2	g_3	n	n_1	n_2	p_{ab}	p_c	q_{ab}	q_c	d	w
Unit	-	-	1/T	1/T	-	-	-	-	-	-	-	mm	mm
Value	0.03	0.025	0.06	0.058	1	1.4	4.45	1	0.5	5	2.5	2	4

where $\bar{J}_{cpw}$ is the critical current density per unit width, d the thickness of the superconducting *Re*BCO layer, w the width of the tape superconductor, and $\hat{s}$ a scaling factor ($\hat{s} = 5.875$ for SuperPower).

Equation (6.3) is still valid for describing Bruker HTS tape, but its J-subfunctions have to be slightly adapted respectively [116]. The respective critical current densities are redefined as

$$J_{c,ab} = J_{c0,ab} \cdot e^{-\left(\frac{T}{T_{ab}^*}\right)^{n_1}} \cdot \left(\frac{B}{B_{ab}^*} + p\right)^{q\frac{T}{T_{ab}^*}+m_1} \tag{6.8}$$

$$J_{c,c} = J_{c0,c} \cdot e^{-\left(\frac{T}{T_c^*}\right)^{n}_2} \cdot e^{-\left(\frac{B}{B_c^*}\right)^{m_2}}, \tag{6.9}$$

where the fitting parameters are $J_{c0,ab}$, $J_{c0,c}$, B_{ab}^*, B_{ab}^*, T_{ab}^*, T_c^*, m_1, m_2, n_1, n_2, p, and q. The values can be found in Table B.2.

Table B.2.: Fitting parameters with units for describing the used Bruker HTS tape.

Parameter	$\iota_{\max}$	$J_{c0,ab}$	$J_{c0,c}$	B_{ab}^*	B_{ab}^*	T_{ab}^*	T_c^*	d	w
Unit	-	A/mm^2	A/mm^2	T	T	K	K	mm	mm
Value	$\pi/2$	4.401×10^5	8.034×10^{12}	1	1	43.27	30.34	2	4

Parameter	g_0	g_1	g_2	g_3	m_1	m_2	n_1	n_2	p	q
Unit	-	-	1/T	1/T	-	-	-	-	-	-
Value	0.03	0.025	0.06	0.058	-0.177	0.2983	2.207	1.511	0.7698	-0.01107

B.2. Nb$_3$Sn

The critical current density for Nb$_3$Sn was described by using Summers' fit [147], depending generally also on the strain ϵ:

$$J_\text{c}(B,T,\epsilon) = \frac{C_{\text{Nb}_3\text{Sn}}(\epsilon)}{\sqrt{B}}\left(1 - \frac{B}{B_{\text{c2}}(T,\epsilon)}\right)^2\left(1 - \left(\frac{T}{T_{\text{c0}}(\epsilon)}\right)^2\right)^2,\tag{6.10}$$

with the upper critical flux density $B_{\text{c2}}(T,\epsilon)$ and the critical temperature $T_{\text{c0}}(\epsilon)$ at $B = 0\,\text{T}$, and fitting parameter $C_{\text{Nb}_3\text{Sn}}$. They can be further described as

$$B_{\text{c2}}(T,\epsilon) = B_{\text{c20}}\left(1 - \left(\frac{T}{T_{\text{c0}}(\epsilon)}\right)^2\right)\left(1 - 0.31\left(\frac{T}{T_{\text{c0}}(\epsilon)}\right)^2\left(1 - 1.77\ln\left(\frac{T}{T_{\text{c0}}(\epsilon)}\right)\right)\right),\tag{6.11}$$

$$T_{\text{c0}}(\epsilon) = T_{\text{c0m}}\sqrt[3]{1 - \alpha|\epsilon|^{1.7}},\tag{6.12}$$

$$C_{\text{Nb}_3\text{Sn}}(\epsilon) = C_{\text{Nb}_3\text{Sn},0}\sqrt{1 - \alpha|\epsilon|^{1.7}},\tag{6.13}$$

with the critical temperature $T_{\text{c0}}(\epsilon) =$ at $B = 0\,\text{T}$ and $\epsilon = 0$.
However, equation (6.10) was simplified and used as follows in this thesis:

$$J_\text{c}(B,T) = \mathcal{J}\frac{C_{\text{Nb}_3\text{Sn},0}}{\sqrt{B}}\left(1 - \frac{B}{B_{\text{c2}}}\right)^2\left(1 - \left(\frac{4.2\,\text{K}}{T_{\text{c0}}(\epsilon)}\right)^2\right)^2.\tag{6.14}$$

Table B.3.: Fitting parameters with units for describing the superconductor Nb$_3$Sn, adapted from [112].

Parameter	$C_{\text{Nb}_3\text{Sn},0}$	B_{c20}	T_{c0}	$\mathcal{J}$	$\alpha \leq 0$	$\alpha \geq 0$
Unit	$\sqrt{\text{T}}\,\text{A}/\text{mm}^2$	T	K	-	-	-
Value	11030	24.92	18	0.74048	900	1250

B.3. Nb-Ti

The critical current density for Nb-Ti was described by using Lubell's[148] and Bottura's fit [149]:

$$J_{\text{c}}(B,T) = J_{\text{c,ref}} \cdot \frac{C_{\text{Nb-Ti}}}{B} \left(\frac{B}{B_{\text{c2}}(T)}\right)^{\alpha} \left(1 - \frac{B}{B_{\text{c2}}(T)}\right)^{\beta} \left(1 - \left(\frac{T}{T_{\text{c0}}}\right)^{1.7}\right)^{\gamma}, \qquad (6.15)$$

with $J_{\text{c,ref}}$ being the critical current density at $4.2\,\text{K}$ in $5\,\text{T}$ and where $B_{\text{c2}}(T)$ is the critical magnetic flux density at the operating temperature T, given as

$$B_{\text{c2}}(T) = B_{\text{c20}} \left(1 - \left(\frac{T}{T_{\text{c0}}}\right)^{1.7}\right). \qquad (6.16)$$

Here, B_{c20} is the upper critical magnetic flux density at $T = 0\,\text{K}$. Fitting parameters are α, β, γ, and $C_{\text{Nb-Ti}}$. The used values are given in Table B.4 and were adapted from [150].

Table B.4.: Fitting parameters with units for describing the superconductor Nb-Ti.

Parameter	α	β	γ	$C_{\text{Nb-Ti}}$	B_{c20}	T_{c0}	$J_{\text{c,ref}}$
Unit	-	-	-	T	T	K	A/mm^2
Value	0.63	0.98	2.32	31.4	14.4	9.2	837

C. Technical drawings: VR coil

The ideal design had to be transferred into real parts with mechanical margins for manufacturing and assembly. Therefore and to ensure a VR coil with period length $\lambda_u \leq 13$ mm, ideal values had to be adapted. All drawings were prepared by CERN services and have been anonymized.
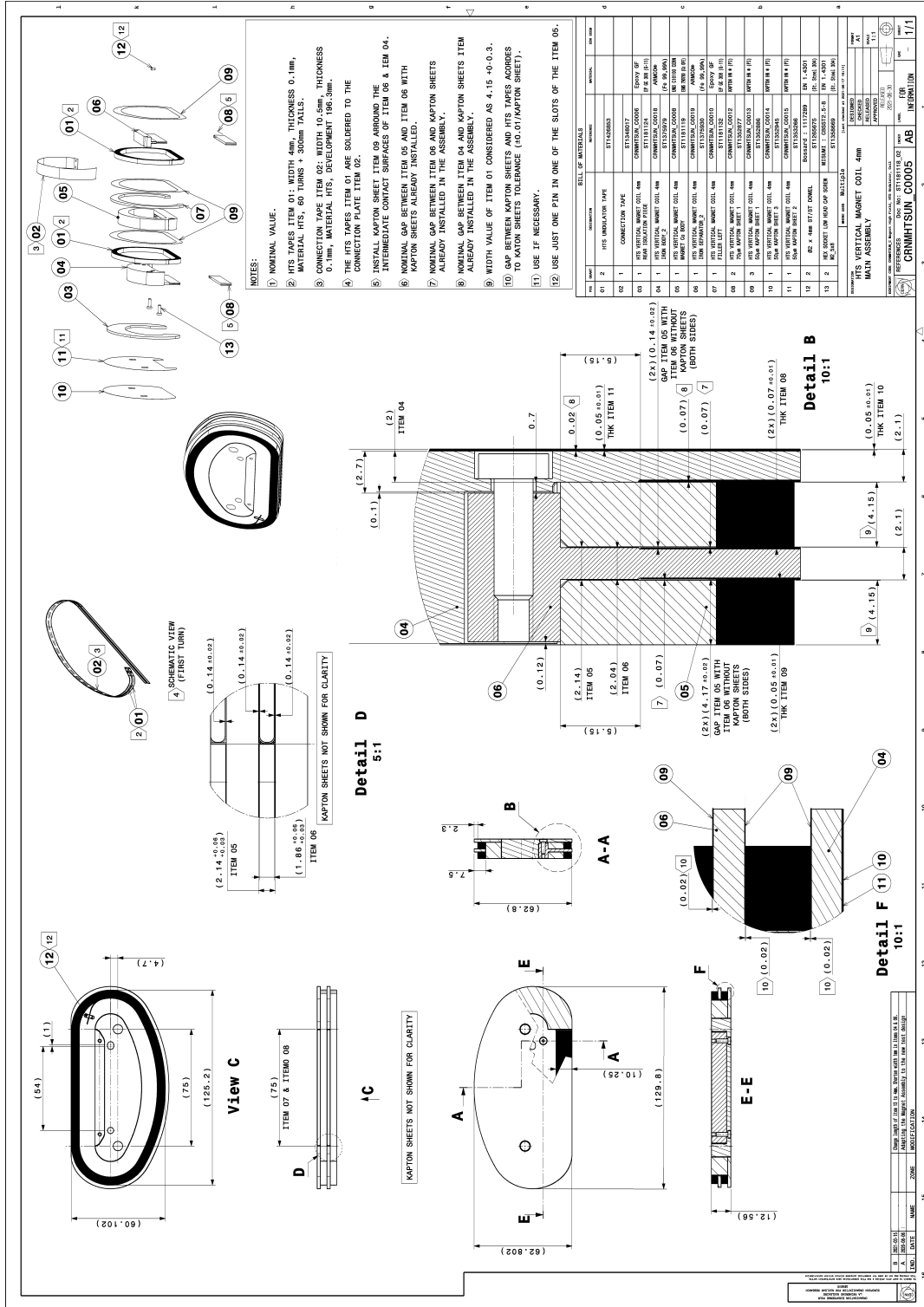
Figure C.1.: Technical overview of the VR coil.

Figure C.2.: Technical overview of the VR coil's copper winding body.

Figure C.3.: Technical overview of the VR coil's iron core body with pole 2.

Figure C.4.: Technical overview of the VR coil's iron pole 1 body.

Figure C.5.: Technical overview of the VR coil's backside G-11 insulation plate.
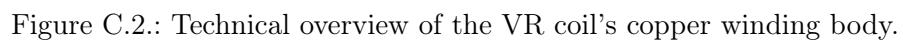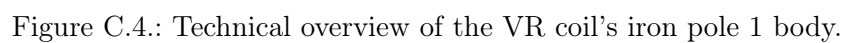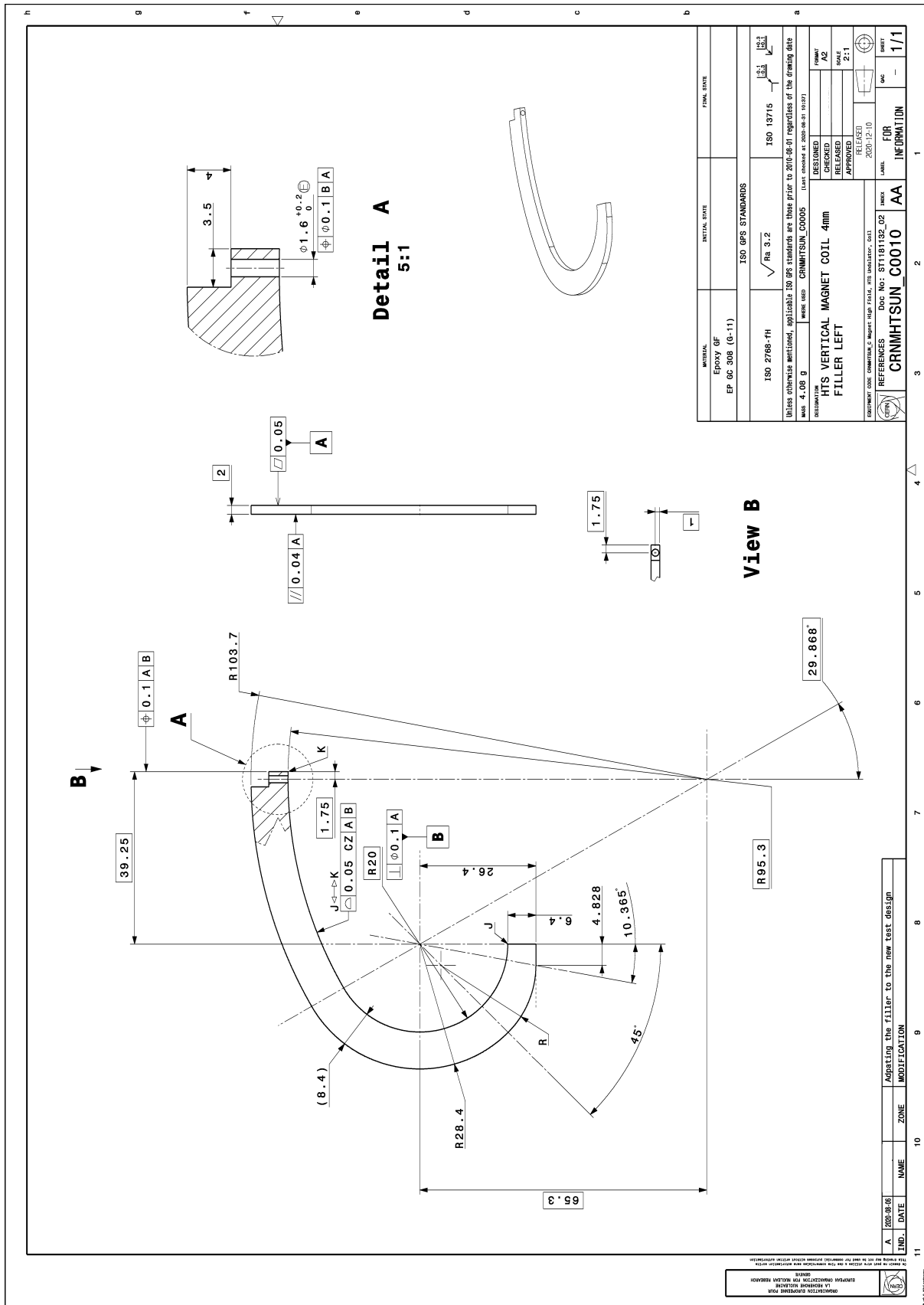
Figure C.7.: Technical overview of the VR coil's G-11 central sub-coil insulation (2/2).

C.1. VR coil support

Figure C.8.: Technical overview of the VR coil support.

Figure C.9.: Technical overview of the VR coil's copper lead.

Figure C.10.: Technical overview of the VR coil's lower support (1/2).
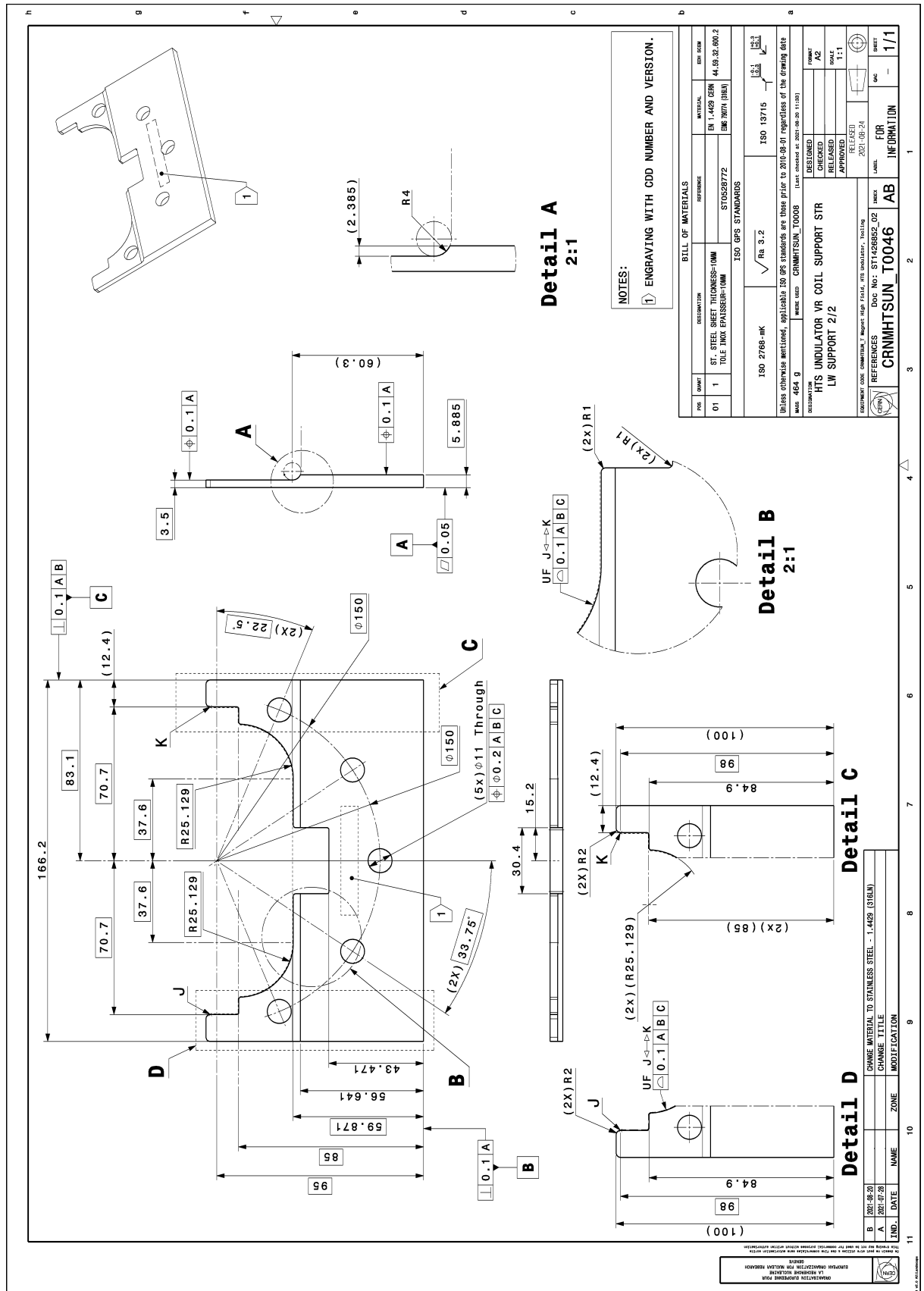
Figure C.11.: Technical overview of the VR coil's lower support (2/2).
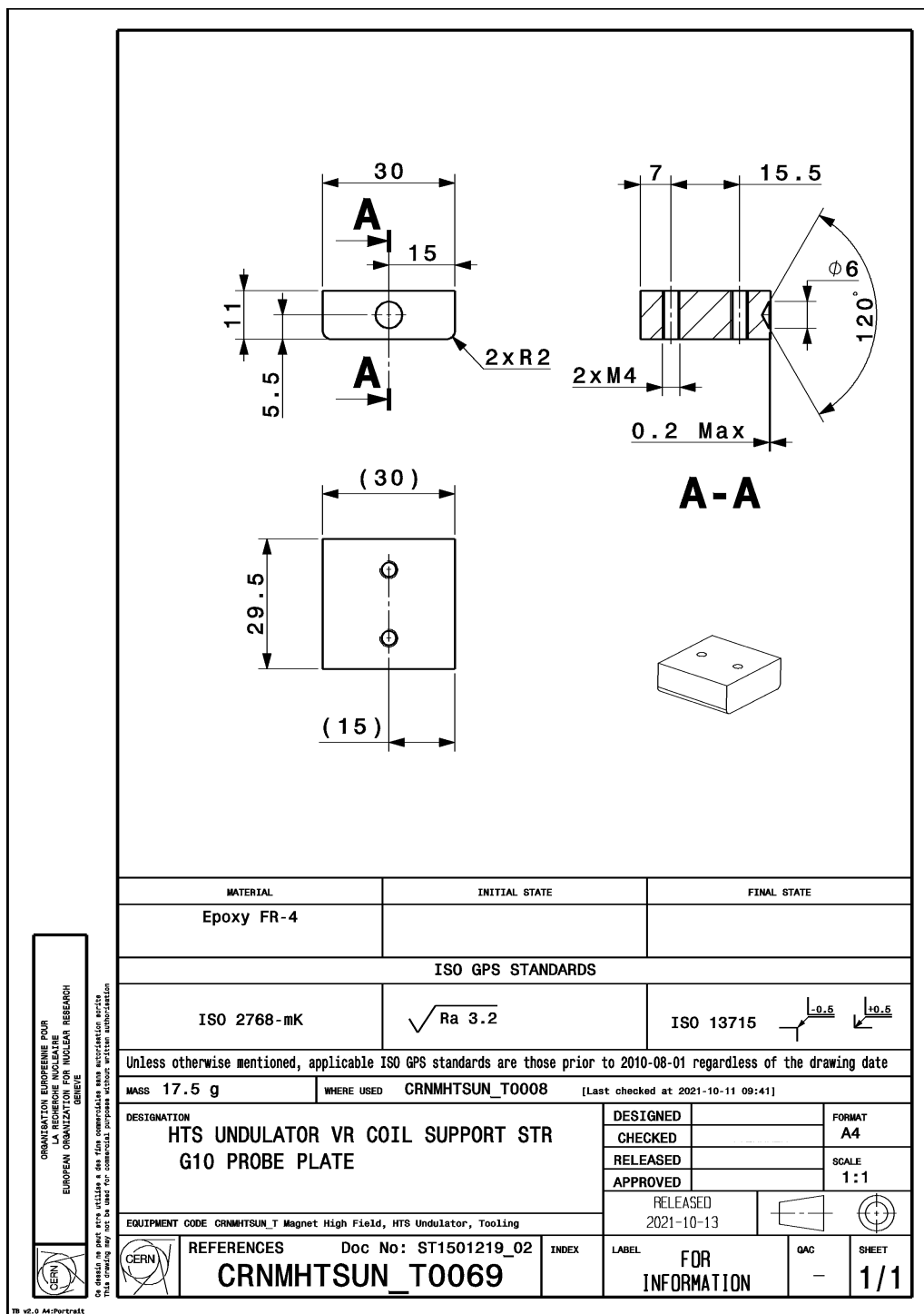
Figure C.12.: Technical overview of the VR coil's measurement block.

Figure C.13.: Technical overview of the VR coil's measurement block cover.

D. Additional powering test results at 77 K

D.1. VR coils

Subsection 5.1.2 presents the measurement results of the built VR coils at 77 K, in LN_2. As stated earlier, all powering test runs were performed multiple times to verify the VR coils' performance. The two presented test runs in Figure D.14 represent the only extraordinary behavior.

During the third and last powering test of VR coil #1, a different time constant τ was observed in sub-coil 2, compared to the previous runs, while sub-coil 1 stayed unchanged. As seen in Figure D.14a, the time constant of sub-coil 2 is observed as $\tau_{1,\text{s-c2}} = 14\,\text{s}$, thus was reduced by 28 s. This was also confirmed by the current step function, ramping the current to 112 A by steps of 2 A. Here, the transverse resistance of sub-coil 2 measures $R_{\text{tr}} = 62\,\mu\Omega$, thus increased by 14 μΩ. Additionally, an increase by up to 10% in the B-field and its saturation value can be seen. However, the critical current values stayed intact.

At present, the origin of this change is unknown and needs further investigation. As the same supporting structure was used for all VR coils, the coils had to be mounted and unmounted. Therefore, sub-coil 2 might has been harmed during this process which resulted in increased turn-to-turn resistance.

(a)   (b)

Figure D.14.: Powering test and voltage responses of the helical undulator demonstrator at 77 K. The current was driven to plateaus to see the voltage responses of each turn as well as across the entire coil. The ramping was stopped after a clear voltage plateau was detected.

D.2. Helical undulator demonstrator

Figure D.15 presents two powering tests of the helical undulator demonstrator up to and beyond its I_c. Although voltage taps monitored each individual turn, solely the voltage signal across the entire demonstrator and turn 2 is plotted as an example to ensure readability. Here, the current was driven with $0.5\,\text{A/s}$ up to $100\,\text{A}$, $120\,\text{A}$, $140\,\text{A}$, $150\,\text{A}$, and $160\,\text{A}$ with a resting time at each plateau of $60\,\text{s}$. A first clear increase in voltage was seen for the ramp to $150\,\text{A}$ in turn 2. Also, voltage spikes appeared here more commonly. Driving the current further up to $160\,\text{A}$, representing 106.7% I_c, directly caused a voltage runaway. However, the overall voltage stayed at a constant-high value of roughly $600\,\mu\text{V}$ for keeping the current constant again. The voltage over turn 2 influenced the overall voltage by the majority.

(a)   (b)

Figure D.15.: Powering test and voltage responses of the helical undulator demonstrator at $77\,\text{K}$. The current was driven to plateaus to see the voltage responses of each turn as well as across the entire coil. The ramping was stopped after a clear voltage plateau was detected.

E. Additional powering test results at 4.2 K

Subsection 5.1.3 presents the measurement results of the built VR coils at 4.2 K, in LHe. As stated earlier, all test runs were performed multiple times to verify the VR coils' performance. The two presented runs in Figure E.16 represent the only extraordinary behaviors. The magnetic field build-up in VR coil #2 showed abnormal behavior in its second powering test run at 4.2 K (cf. Figure E.16a). The B-field below Fe pole 2 first rises before changing signs, hinting on current sharing. However, this cannot be detected in the voltage signal. Further investigations have to reveal the cause of this measurement, which is not fully understood, yet. The field below Fe pole 1 behaves normally and in the same way as for the other powering test runs.
Figure E.16b presents the first voltage runaway in VR coil #3 during the powering tests at 4.2 K due to the resistive sub-coil 1 showing voltage plateaus above 2.5 mV. Interestingly, the voltage across sub-coil 1 stayed around 2 mV for the following powering tests, for unknown reasons. The field below the iron poles behaves in the same way as for the other powering test runs, without any notable degradation.

Figure E.17 shows the raw data of a current step function measurement. The single decays are represented by their decayed value in Figure 5.12. A resistive, linear slope can be seen for every single decay, caused by the voltage taps. Sub-coil 1 shows a fast voltage decay as noted for the measurement of the effective time constants, most likely caused by defects in the superconductor. For sub-coil 2, a 300 s voltage decay time may be too short, as the voltage was not able to fully decay. On the right end, a voltage runaway in sub-coil 1 forced the stop of the powering test. Here, sub-coil 2 was an order of magnitude below this sub-coil 1's voltage.
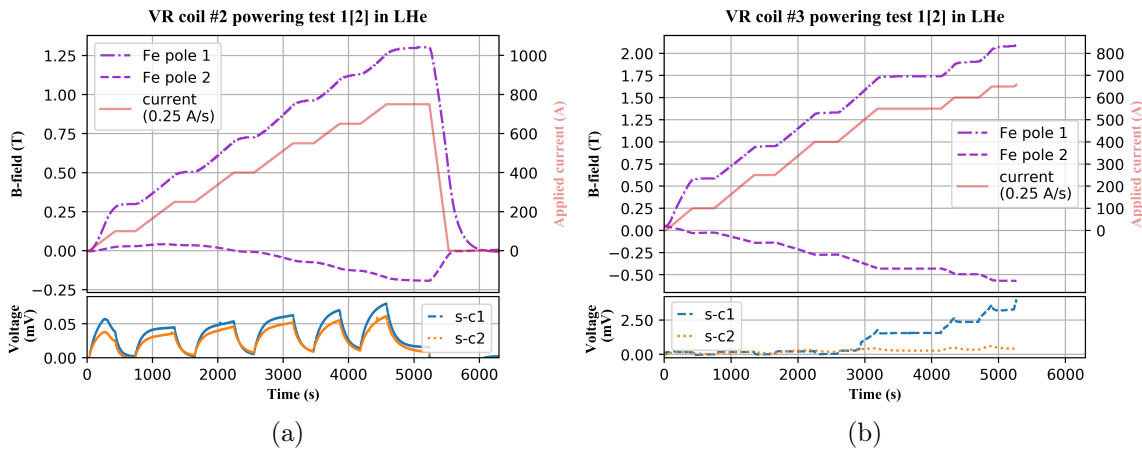
Figure E.16.: Powering tests and voltage responses of VR coil #2 (a) and #3 (b). The current was ramped to plateaus to see the voltage and the B-field responses.
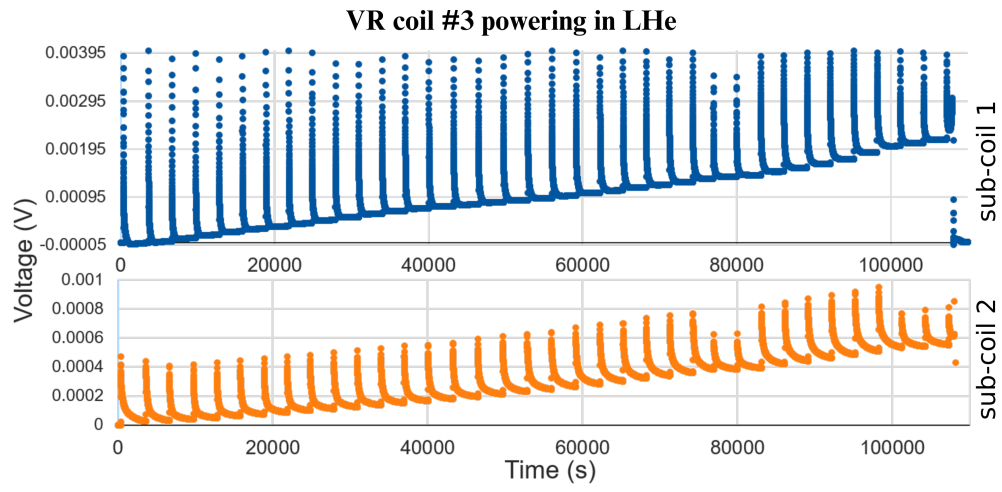
Figure E.17.: Raw data plot of VR coil #3 during the current step function with steps of 40 A and 300 s voltage decay time.

Publications and contributions

Articles

- "**High-temperature superconducting undulator prototype coils for compact free-electron lasers**", S. C. Richter *et al.*, in *IEEE Transactions on Applied Superconductivity*, vol. 33, no. 5, August 2023,
  as invited contribution presented at the *ASC'22*, Honolulu, HI, USA, October 2022,
  `doi:10.1109/TASC.2023.3242625`.

- "**Status and powering test results of HTS undulator coils at 77 K for compact FEL designs**", S. C. Richter *et al.*, in *Journal of Physics: Conference Series*, vol. 2420, no. 1, January 2023,
  also presented at the *IPAC'22*, Bangkok, Thailand, June 2022,
  `doi:10.1088/1742-6596/2420/1/012019`.

- "**Progress on HTS Undulator Prototype Coils for Compact FEL Designs**", S. C. Richter *et al.*, in *IEEE Transactions on Applied Superconductivity*, vol. 32, no. 4, June 2022,
  also presented at the *EUCAS'21*, Moscow, Russia, September 2021,
  `doi:10.1109/TASC.2022.3150288`.

Conference contributions and proceedings

- "**Powering test results of HTS undulator prototype coils for compact FELs at 4.2 K**", S. C. Richter *et al.*, invited talk presented at the *ASC'22*, Honolulu, HI, USA, October 2022, 2LOr1C-01.

- "**Status of a Prototype HTS Helical Undulator Coil for Compact FELs**", S. C. Richter *et al.*, poster presented at the *IPAC'22*, Bangkok, Thailand, June 2022.
  `doi:10.13140/RG.2.2.28578.91844`.

- "**Bending Radius Limits of Different Coated REBCO Conductor Tapes - An Experimental Investigation with Regard to HTS Undulators**", S. C. Richter *et al.*, in *Proc. IPAC'21*, Campinas, SP, Brazil, May 2021,
  `doi:10.18429/JACoW-IPAC2021-THPAB042`.

- "**High-temperature superconducting undulator designs for compact free electron lasers, CLIC and FCC-ee**", S. C. Richter *et al.*, presented at the *ASC'20* (virtual), USA, October/November 2020, Wk1LPo1F-01.

- "**High-temperature superconducting undulators for compact free-electron lasers**", S. C. Richter *et al.*, several talks presented at the *DPG Spring Meetings* from 2019 to 2023.

Co-authored papers

- "**Undulators and Light Production with the XLS-CompactLight Design Study**", F. Nguyen *et al.*, in *Moscow Univ. Phys.*, vol. 77, 2022,
  `doi:10.3103/S0027134922020710`.

- "**Development of a Transfer Line for LPA-Generated Electron Bunches to a Compact Storage Ring**", B. Haerer *et al.*, in *Proc. IPAC'22*, Bangkok, Thailand, June 2022,
  `doi:10.18429/JACoW-IPAC2022-THPOPT059`.

- "**Magnetic Characterization of a Superconducting Transverse Gradient Undulator for Compact Laser Wakefield Accelerator-Driven FELs**", K. Damminsek *et al.*, in *Proc. IPAC'22*, Bangkok, Thailand, June 2022,
  `doi:10.18429/JACoW-IPAC2022-WEPOST034`.

- "**Effective Time Constants at 4.2 to 70 K in ReBCO Pancake Coils With Different Inter-Turn Resistances**", T. H. Nes *et al.*, in *IEEE Transactions on Applied Superconductivity*, vol. 32, no. 4, June 2022,
  `doi:10.1109/TASC.2022.3148968`.

- "**XLS - D2.3: Conceptual Design Report**", G. D'Auria *et al.*, on *Zenodo* and within the CompactLight Project (`www.compactlight.eu/`), December 2021, `doi:10.5281/zenodo.6375644`.

- "**Development of an Automated High Temperature Superconductor Coil Winding Machine at CERN**", H. Reymond *et al.*, in *Proc. ICALEPCS'21*, Shanghai, China, Oct. 2021,
  `doi:10.18429/JACoW-ICALEPCS2021-TUPV034`.

- "**Operational Experience and Characterization of a Superconducting Transverse Gradient Undulator for Compact Laser Wakefield Accelerator-Driven FEL**", K. Damminsek *et al.*, in *Proc. IPAC'21*, Campinas, SP, Brazil, May 2021,
  `doi:10.18429/JACoW-IPAC2021-THPAB126`.

- "**XLS - D5.1: Technologies for the CompactLight Undulator**", F. Nguyen *et al.*, on *Zenodo* and within the CompactLight Project (`www.compactlight.eu/`), June 2019,
  `doi:10.5281/zenodo.5024409`.

- "**Proposed Beam Test of a Transverse Gradient Undulator at the SINBAD Facility at DESY**", F. J. Jafarinia *et al.*, in *Proc. IPAC'19*, Melbourne, Australia, May 2019,
  `doi:10.18429/JACoW-IPAC2019-THPGW015`.

Acknowledgments

Performing the research for this thesis and beyond was an exciting expedition. I learned a lot about physics but also about myself and life.

The work presented in this thesis was mainly performed in the Magnet Group (TE/MSC) at CERN, Geneva, CH, always in close collaboration with the Karlsruhe Institute of Technology (KIT), Karlsruhe, DE, serving as my home university. Further, this work contributed to the research activities of the CompactLight Project (XLS) and the Compact Linear Collider Study (CLIC).

On this expedition, I met many brilliant and inspiring people who helped me grow, supported my work as well as improved it further. Consequently, I would like to thank all who made this thesis possible, added value, and thus assisted me in becoming a researcher.

First of all, I sincerely thank my university supervisor Prof. Anke-Susanne Müller from KIT's Institute for Beam Physics and Technology (IBPT) for the opportunity to work on this very interesting subject over the last few years, for giving constructive feedback, and for further supporting me to follow up my research at KIT, after my time at CERN ended. Investigating high-temperature superconductors (HTS) for their application to undulator magnets offers interesting questions, challenges, and opportunities in accelerator physics, whereto I got excellent access.

In addition, I want to thank Prof. Bernhard Holzapfel from KIT's Institute for Technical Physics (ITEP) for his kind acceptance to review my thesis and for providing valuable feedback.

Next, I want to express my great gratitude to Axel Bernhard, group leader at KIT's Laboratory for Applications of Synchrotron Radiation (LAS), who was my additional supervisor from KIT. Our regular fruitful discussions and informal chats paired with his guidance, thoughtful advice, and continuous support were determinants in keeping me focused and motivated, especially during challenging times.

Likewise, I would like to express my deepest appreciation to Amalia Ballarino, section leader of Superconductors and Devices (TE/MSC-SCD), who took over my supervision at CERN in 2021 with great enthusiasm and strongly supported the vast majority of the experimental parts presented in this thesis. I thank her cordially for her valuable suggestions, expert advice, and our regular scientific discussions. Her continuous support, even beyond my time at CERN, was determinant in realizing the very first helical undulator demonstrator, wound from HTS tape.

Furthermore, I do not want to miss dedicating my warm thanks to Daniel Schörling who started my supervision at CERN and ensured me an excellent start in the Magnet Group's Superconducting Magnet Technology section (TE/MSC-SMT). He always provided me with competent advice, especially from an engineering point of view, as well as supported this thesis with enthusiasm, and questioned my approaches constructively.

Also thanks to Gijs de Rijk, former section leader of (TE/MSC-MDT, now: -SMT), for his continuous encouragement and support from the very first day I arrived at CERN.

Performing research is accompanied by a certain exchange of people, knowledge transfer, and new approaches. During my time at CERN, I was happy to share the office with great minds. I would like to thank my long-term office colleague Thomas Nes, but also Jaakko Murtomäki and Jeroen van Nugteren, not only for many fruitful discussions, inspiring ideas, and mutual support but as well for countless fun times in- and outside the office, ensuring amazing work-life-science balance!

The technicians and draftsmen in the SMT and SCD section as well as in CERN's design office helped me realize all presented undulator coils with many technical discussions, technical drawings, and endless efforts to find optimum solutions for the various issues during the manufacturing process. Their support in the workshop was crucial for preparing the experimental basis for the measurements. Therefore, I want to express my thanks representatively to Robin Betemps, Nicolas Bourcey, Sébastien Clement, Pedro Martin Vazquez, François-Olivier Pincot, Dylan Standen, and special thanks to Carlos Fernandes and Jacky Mazet.

Further, I would like to thank my colleagues Christian Barth, Piotr Koziol, and Gilles Lenoir for supporting the powering tests in LN_2 at CERN as well as Nicole Glamann, Andreas Grau, David Saez de Jauregui, and Bennet Krasch for supporting the powering tests in LHe at KIT. Thanks to their assistance, collecting data became an easy harvest and fun, no matter how long it took.

With the support of Antje Drechsler, Bernd Ringsdorf, and Sonja Schlachter from KIT's ITEP, I performed bending tests of *Re*BCO tapes in LN_2 in a very lightweight and elegant way. Thank you for this successful and pragmatic collaboration within KIT.

Also, my regular contact with the LAS group at KIT was an important constant link to my home university, always resulting in good discussions, and making the transition from CERN back to KIT easy. Representatively, I would like to thank Kantaphon Damminsek, Samira Fatehi, Julian Gethmann, Maisui Ning, and Robert Rossmanith.

Due to the worldwide COVID-19 pandemic, I had to build the very first dummy test coils of the helical undulator in my family's garage; this is only one of the countless ways I received assistance from home. Thus, I finally want to express my heartfelt gratitude to my family - the best backing and motivation I could have wished for in the background. Especially the everlasting and unconditional support, patience, understanding, and encouragement of my parents during my studies were of priceless value.

<div align="right">Vielen herzlichen Dank!</div>

Karlsruhe, April 2023

SPONSORED BY THE

Federal Ministry
of Education
and Research

KSETA

CERN

....
                    (**Sebastian C. Richter**)

Für Margarete Wilhelm.

List of Figures

List of Tables

Bibliography

[1] G. E. Brown and N. C. Sturchio, "An Overview of Synchrotron Radiation Applications to Low Temperature Geochemistry and Environmental Science," *Reviews in Mineralogy and Geochemistry*, vol. 49, pp. 1–115, jan 2002.

[2] M. Kozak, W. M. Kwiatek, and B. Kowalski, "12th International School and Symposium on Synchrotron Radiation in Natural Sciences (ISSRNS 2014)," *Nuclear Instruments and Methods in Physics Research Section B: Beam Interactions with Materials and Atoms*, vol. 364, pp. 1–3, dec 2015.

[3] T. van de Kamp, A. H. Schwermann, T. dos Santos Rolo, P. D. Lösel, T. Engler, W. Etter, T. Faragó, J. Göttlicher, V. Heuveline, A. Kopmann, B. Mähler, T. Mörs, J. Odar, J. Rust, N. Tan Jerome, M. Vogelgesang, T. Baumbach, and L. Krogmann, "Parasitoid biology preserved in mineralized fossils," *Nature Communications*, vol. 9, p. 3325, aug 2018.

[4] A. Di Cicco, G. Giuli, and A. Trapananti, *Synchrotron Radiation Science and Applications*. Springer Proceedings in Physics, 2021.

[5] D. Paterson and D. Howard, "Synchrotron Radiation in Art and Archaeology," *Synchrotron Radiation News*, vol. 32, pp. 2–2, nov 2019.

[6] S. Di Mitri, A. Aksoy, A. Bernhard, C. Cortés, H. M., J. Clarke, G. D'Auria, D. Dunning, M. Ferrario, A. Latina, E. Marin, F. Nguyen, T. Schmidt, N. Thompson, and W. Wuensch, "XLS – D2.2: FEL design with accelerator and undulator requirements (Version v1)," tech. rep., CompactLight (XLS), 2021.

[7] A. Liénard, "Champ électrique et Magnétique," *L'éclairage électrique*, vol. 16, no. 27-29, pp. 5–14, 53–59, 106– 112., 1898.

[8] F. R. Elder, A. M. Gurewitsch, R. V. Langmuir, and H. C. Pollock, "Radiation from Electrons in a Synchrotron," *Physical Review*, vol. 71, pp. 829–830, jun 1947.

[9] A. Bernhard, "Beschleunigerphysik II: Synchrotronstrahlungsquellen," 2015. Lecture script.

[10] D. H. Bilderback, P. Elleaume, and E. Weckert, "Review of third and next generation synchrotron light sources," *Journal of Physics B: Atomic, Molecular and Optical Physics*, vol. 38, pp. S773–S797, may 2005.

[11] D. M. Mills, J. R. Helliwell, Å. Kvick, T. Ohta, I. A. Robinson, and A. Authier, "Report of the Working Group on Synchrotron Radiation Nomenclature – brightness, spectral brightness or brilliance?," *Journal of Synchrotron Radiation*, vol. 12, pp. 385–385, may 2005.

[12] F. Nguyen, A. Aksoy, A. Bernhard, M. Calvi, J. A. Clarke, H. M. C. Cortés, A. W. Cross, G. Dattoli, D. Dunning, R. Geometrante, J. Gethmann, S. Hellmann, M. Kokole, J. Marcos, Z. Nergiz, F. Perez, A. Petralia, S. C. Richter, T. Schmidt,

D. Schoerling, N. Thompson, K. Zhang, L. Zhang, and D. Zhu, "XLS Deliverable D5 .1 - Technologies for the CompactLight undulator," Tech. Rep. June, CompactLight (XLS), 2019.

[13] J. A. Clarke, *The Science and Technology of Undulators and Wigglers*. Oxford University Press, jul 2004.

[14] H. Motz, W. Thon, and R. N. Whitehurst, "Experiments on Radiation by Fast Electron Beams," *Journal of Applied Physics*, vol. 24, pp. 826–833, jul 1953.

[15] L. R. Elias, W. M. Fairbank, J. M. J. Madey, H. A. Schwettman, and T. I. Smith, "Observation of Stimulated Emission of Radiation by Relativistic Electrons in a Spatially Periodic Transverse Magnetic Field," *Physical Review Letters*, vol. 36, pp. 717–720, mar 1976.

[16] M. Berndt, W. Brunk, R. Cronin, D. Jensen, R. Johnson, A. King, J. Spencer, T. Taylor, and H. Winick, "Initial Operation of SSRL Wiggler in SPEAR," *IEEE Transactions on Nuclear Science*, vol. 26, pp. 3812–3815, jun 1979.

[17] T. Hezel, B. Krevet, H. O. Moser, J. A. Rossmanith, R. Rossmanith, and T. Schneider, "A superconductive undulator with a period length of 3.8 mm," *Journal of Synchrotron Radiation*, vol. 5, pp. 448–450, may 1998.

[18] C. Boffo, T. Gerhard, M. Turenne, W. Walter, S. Casalbuoni, A. Cecilia, S. Gerstl, A. Grau, T. Holubek, C. Meuter, D. Saez De Jauregui, and R. Voutta, "Performance of SCU15: The New Conduction-Cooled Superconducting Undulator for ANKA," *IEEE Transactions on Applied Superconductivity*, vol. 26, no. 4, pp. 1–4, 2016.

[19] S. Casalbuoni, S. Bauer, E. Blomley, N. Glamann, A. Grau, T. Holubek, E. Huttel, D. Saez de Jauregui, C. Boffo, T. A. Gerhard, M. Turenne, and W. Walter, "Performance of a full length scale superconducting undulator with 20 mm period length at the KIT synchrotron," in *Proceedings of 9th Intenational Particle Accelerator Conference*, (Vancouver, BC, Canada), JACoW Publishing, 2018.

[20] Y. Ivanyushenkov, K. Harkay, M. Abliz, L. Boon, M. Borland, D. Capatina, J. Collins, G. Decker, R. Dejus, J. Dooling, C. Doose, L. Emery, J. Fuerst, J. Gagliano, Q. Hasse, M. Jaski, M. Kasa, S. H. Kim, R. Kustom, J. C. Lang, J. Liu, E. Moog, D. Robinson, V. Sajaev, K. Schroeder, N. Sereno, Y. Shiroyanagi, D. Skiadopoulos, M. Smith, X. Sun, E. Trakhtenberg, I. Vasserman, A. Vella, A. Xiao, J. Xu, A. Zholents, E. Gluskin, V. Lev, N. Mezentsev, V. Syrovatin, V. Tsukanov, A. Makarov, J. Pfotenhauer, and D. Potratz, "Development and operating experience of a short-period superconducting undulator at the Advanced Photon Source," *Physical Review Special Topics - Accelerators and Beams*, vol. 18, p. 040703, apr 2015.

[21] D. J. Scott, J. A. Clarke, D. E. Baynham, V. Bayliss, T. Bradshaw, G. Burton, A. Brummitt, S. Carr, A. Lintern, J. Rochford, O. Taylor, and Y. Ivanyushenkov, "Demonstration of a High-Field Short-Period Superconducting Helical Undulator Suitable for Future TeV-Scale Linear Collider Positron Sources," *Physical Review Letters*, vol. 107, p. 174803, oct 2011.

[22] M. Kasa, M. Borland, L. Emery, J. Fuerst, K. C. Harkay, Q. Hasse, Y. Ivanyushenkov, W. Jansma, I. Kesgin, V. Sajaev, Y. Shiroyanagi, Y. P. Sun, and E. Gluskin, "Development and operating experience of a 1.2-m long helical superconducting undulator at the Argonne Advanced Photon Source," *Physical Review Accelerators and Beams*, vol. 23, p. 050701, may 2020.

[23] A. Bernhard, A. Bragin, S. Casalbuoni, P. Ferracin, L. G. Fajardo, S. Gerstl, J. Gethmann, A. Grau, E. Huttel, S. Khrushchev, N. Mezentsev, A.-s. Muller, Y. Papaphilippou, D. S. D. Jauregui, D. Schoerling, V. Shkaruba, N. Smale, V. Tsukanov,

K. Zolotarev, A. Bernhard, J. Gethmann, S. Casalbuoni, S. Gerstl, A. W. Grau, E. Huttel, A. Mueller, D. S. D. Jauregui, N. J. Smale, A. V. Bragin, S. V. Khrushchev, N. A. Mezentsev, V. A. Shkaruba, V. M. Tsukanov, and K. V. Zolotarev, "A CLIC Damping Wiggler Prototype at ANKA : Comissioning and Preparations for a Beam Dynamics Experimental Program," in *Proc. of International Particle Accelerator Conference (IPAC'16), Busan, Korea, May 8-13, 2016*, no. May 2016, (Busan), pp. 2412—-2415, JACoW, 2016.

[24] I. Kesgin, M. Kasa, S. MacDonald, Y. Ivanyushenkov, E. Barzi, D. Turrioni, D. Arbelaez, Q. Hasse, A. V. Zlobin, S. Prestemon, and E. Gluskin, "Fabrication and Testing of 18-mm-Period, 0.5-m-Long Nb_3Sn Superconducting Undulator," *IEEE Transactions on Applied Superconductivity*, vol. 31, pp. 1–5, aug 2021.

[25] M. Majoros, M. Sumption, M. Susner, S. Bhartiya, S. Bohnenstiehl, E. Collings, M. Tomsic, M. Rindfleisch, J. Phillips, D. Lyons, and J. Yue, "A Model Superconducting Helical Undulator Wound Using a Wind and React MgB_2 Multifilamentary Wire," *IEEE Transactions on Applied Superconductivity*, vol. 19, pp. 1376–1379, jun 2009.

[26] S. C. Richter, "HTS undulator development," tech. rep., at the CLIC Workshop 2019 at CERN, Geneva, 2019.

[27] C. Boffo and T. Gerhard, "High-temperature superconductor magnet system," 2012. Patent WO 2012/013205, Germany, 2012.

[28] I. Kesgin, M. Kasa, Y. Ivanyushenkov, and U. Welp, "High-temperature superconducting undulator magnets," *Superconductor Science and Technology*, vol. 30, no. 4, pp. 1–6, 2017.

[29] T. Holubek, S. Casalbuoni, S. Gerstl, N. Glamann, A. Grau, C. Meuter, D. S. de Jauregui, R. Nast, and W. Goldacker, "A novel concept of high temperature superconducting undulator," *Superconductor Science and Technology*, vol. 30, p. 115002, nov 2017.

[30] A. Will, T. A. Arndt, E. Bründermann, N. Glamann, A. W. Grau, B. Krasch, Müller A.-S., R. Nast, D. de Jauregui, D. Astapovych, H. De Gersem, and E. Gjonaj, "Design and Fabrication Concepts of a Compact Undulator with Laser-Structured 2G-HTS Tapes," in *12th International Particle Accelerator Conference : virtual edition, May 24th-28th, 2021, Brazil : proceedings volume / IPAC2021. Ed.: R. Picoreti*, pp. 3851–3854, JACoW Publishing, 2021.

[31] M. Calvi, M. D. Ainslie, A. Dennis, J. H. Durrell, S. Hellmann, C. Kittel, D. A. Moseley, T. Schmidt, Y. Shi, and K. Zhang, "A GdBCO bulk staggered array undulator," *Superconductor Science and Technology*, vol. 33, p. 014004, jan 2020.

[32] K. Zhang, A. Pirotta, X. Liang, S. Hellmann, M. Bartkowiak, T. Schmidt, A. Dennis, M. Ainslie, J. Durrell, and M. Calvi, "Record field in a 10 mm-period bulk high-temperature superconducting undulator," *Superconductor Science and Technology*, vol. 36, p. 05LT01, may 2023.

[33] S. Dassault Systems, "Opera 2020." `https://www.3ds.com/de/produkte-und-services/simulia/produkte/opera/`, 2020.

[34] J. D. Jackson, *Classical electrodynamics*. New York: Wiley, 2nd ed., 1975.

[35] K. J. Binns, P. J. Lawrenson, and C. W. Trowbridge, *The analytical and numerical solution of electric and magnetic fields*. Chichester [u.a.]: Wiley, 1992.

[36] S. Russenschuck, *Field Computation for Accelerator Magnets*. Wiley VCH Verlag, 2010.

[37] H. Wiedemann, *Particle Accelerator Physics*. Graduate Texts in Physics, Cham: Springer International Publishing, 2015.

[38] B. international des poids et mesures, "Resolution 1 of the 26th CGPM. On the revision of the International System of Units (SI)," in *Proceedings of the 26th CGPM*, p. 472, Bureau international des poids et mesures, 2018.

[39] D. Alferov, Y. A. Bashmakov, and E. Bessonov, "Generation of circularly polarized electromagnetic radiation," *Sov. Phys. Tech. Phys.*, vol. 21, no. 11, p. 1408, 1976.

[40] S. Y. Park, J. M. Baird, R. A. Smith, and J. L. Hirshfield, "Exact magnetic field of a helical wiggler," *Journal of Applied Physics*, vol. 53, pp. 1320–1325, mar 1982.

[41] D. F. Alferov, Y. A. Bashmakov, and P. A. Cherenkov, "Radiation from relativistic electrons in a magnetic undulator," *Soviet Physics Uspekhi*, vol. 32, pp. 200–227, mar 1989.

[42] J. Fajans, "End effects of a bifilar magnetic wiggler," *Journal of Applied Physics*, vol. 55, pp. 43–50, jan 1984.

[43] W. R. Smythe, *Static and dynamic electricity*. International series in pure and applied physics, New York: McGraw-Hill, 3. ed. ed., 1968.

[44] B. M. Kincaid, "A short-period helical wiggler as an improved source of synchrotron radiation," *Journal of Applied Physics*, vol. 48, pp. 2684–2691, jul 1977.

[45] S. H. Kim, "Magnetic Field Analysis of Helical Undulators," *APS Internal Report*, vol. ANL/APS/LS, pp. 1–12, 2012.

[46] S. Kurz and S. Russenschuck, "The application of the BEM-FEM coupling method for the accurate calculation of fields in superconducting magnets," *Electrical Engineering (Archiv fur Elektrotechnik)*, vol. 82, pp. 1–10, sep 1999.

[47] S. Kurz, J. Fetzer, and W. M. Rucker, "Coupled BEM-FEM methods for 3D field calculations with iron saturation," in *Proc. of the 1st International Roxie Users Meeting and Workshop*, (Geneva), pp. 47–59, 1998.

[48] W. Colson, A. Renieri, and C. Pellegrini, *Laser Handbook, Volume 6: Free Electron Lasers*. North-Holland, 1990.

[49] A. Hofmann, *The Physics of Synchrotron Radiation*. Cambridge University Press, may 2004.

[50] P. Schmüser, M. Dohlus, and J. Rossbach, *Ultraviolet and Soft X-Ray Free-Electron Lasers*, vol. 229 of *Springer Tracts in Modern Physics*. Berlin, Heidelberg: Springer Berlin Heidelberg, 2009.

[51] S. Krinsky, "An undulator for the 700 MeV VUV-ring of the National Synchrotron Light Source," *Nuclear Instruments and Methods*, vol. 172, pp. 73–76, may 1980.

[52] Z. Huang, Y. Ding, and C. B. Schroeder, "Compact X-ray Free-Electron Laser from a Laser-Plasma Accelerator Using a Transverse-Gradient Undulator," *Physical Review Letters*, vol. 109, p. 204801, nov 2012.

[53] H. Kamerlingh Onnes, "Sur les Résistances Électriques," *Communications from the Physical Laboratory of the University of Leiden*, vol. 29, pp. 1–11, 1911.

[54] J. Eisenstein, "Superconducting Elements," *Reviews of Modern Physics*, vol. 26, pp. 277–291, jul 1954.

[55] P. J. Lee, *Engineering superconductivity*. New York: Wiley-Interscience, 2001.

[56] W. Buckel and R. Kleiner, *Superconductivity: Fundamentals and Applications*. Wiley VCH Verlag, 2nd, revis ed., 2004.

[57] B. T. Matthias, T. H. Geballe, S. Geller, and E. Corenzwit, "Superconductivity of Nb$_3$Sn," *Physical Review*, vol. 95, pp. 1435–1435, sep 1954.

[58] J. Nagamatsu, N. Nakagawa, T. Muranaka, Y. Zenitani, and J. Akimitsu, "Superconductivity at 39 K in magnesium diboride," *Nature*, vol. 410, pp. 63–64, mar 2001.

[59] T. Ishida, K. Okuda, A. I. Rykov, S. Tajima, and I. Terasaki, "In-plane anisotropy of vortex-lattice melting in large YBa$_2$Cu$_3$O$_7$," *Physical Review B*, vol. 58, pp. 5222–5225, sep 1998.

[60] Y. Ando, G. S. Boebinger, A. Passner, L. F. Schneemeyer, T. Kimura, M. Okuya, S. Watauchi, J. Shimoyama, K. Kishio, K. Tamasaku, N. Ichikawa, and S. Uchida, "Resistive upper critical fields and irreversibility lines of optimally doped high-T$_c$ cuprates," *Physical Review B*, vol. 60, pp. 12475–12479, nov 1999.

[61] C. Kittel, *Introduction to solid state physics*. Hoboken, NJ: Wiley, 8. ed. ed., 2005.

[62] M. N. Wilson, *Superconducting Magnets*. Oxford University Press, 1987.

[63] P. Seidel, *Applied Superconductivity*. Weinheim, Germany: Wiley-VCH Verlag GmbH & Co. KGaA, jan 2015.

[64] W. Meissner and R. Ochsenfeld, "Ein neuer Effekt bei Eintritt der Supraleitfähigkeit," *Die Naturwissenschaften*, vol. 21, pp. 787–788, nov 1933.

[65] M. P. A. Fisher, "Vortex-glass superconductivity: A possible new phase in bulk high-T$_c$ oxides," *Physical Review Letters*, vol. 62, pp. 1415–1418, mar 1989.

[66] M. Iio, M. Yoshida, T. Nakamoto, T. Ogitsu, M. Sugano, K. Suzuki, and A. Idesaki, "Investigation of Irradiation Effect on REBCO Coated Conductors for Future Radiation-Resistant Magnet Applications," *IEEE Transactions on Applied Superconductivity*, vol. 32, pp. 1–5, sep 2022.

[67] C. Barth, G. Mondonico, and C. Senatore, "Electro-mechanical properties of REBCO coated conductors from various industrial manufacturers at 77 K, self-field and 4.2 K, 19 T," *Superconductor Science and Technology*, vol. 28, no. 4, 2015.

[68] J. W. Ekin, *Experimental Techniques for Low-Temperature Measurements*. Oxford University Press, 2006.

[69] J. van Nugteren, *High temperature superconductor accelerator magnets*. PhD thesis, University of Twente, 2016.

[70] P. J. Lee, "Comparisons of superconductor critical current densities.." `https://nationalmaglab.org/magnet-development/applied-superconductivity-center/plots`, 2018.

[71] H. Müller and T. Schneider, "Heat treatment of Nb$_3$Sn conductors," *Cryogenics*, vol. 48, pp. 323–330, jul 2008.

[72] A. Abada and E. al., "FCC-hh: The Hadron Collider," *The European Physical Journal Special Topics*, vol. 228, pp. 755–1107, jul 2019.

[73] A. Ballarino, "Prospects for the use of HTS in high field magnets for future accelerator facilities," *5th International Particle Accelerator Conference, Dresden, Germany, 15 - 20 Jun 2014*, p. pp.974, 2014.

[74] A. Golovashkin, O. Ivanenko, Y. Kudasov, K. Mitsen, A. Pavlovsky, V. Platonov, and O. Tatsenko, "Low temperature direct measurements of H$_{c2}$ in HTSC using megagauss magnetic fields," *Physica C: Superconductivity*, vol. 185-189, pp. 1859–1860, dec 1991.

[75] D. C. Larbalestier, J. Jiang, U. P. Trociewitz, F. Kametani, C. Scheuerlein, M. Dalban-Canassy, M. Matras, P. Chen, N. C. Craig, P. J. Lee, and E. E. Hellstrom, "Isotropic round-wire multifilament cuprate superconductor for generation of magnetic fields above 30 T," *Nature Materials*, vol. 13, pp. 375–381, apr 2014.

[76] M. K. Wu, J. R. Ashburn, C. J. Torng, P. H. Hor, R. L. Meng, L. Gao, Z. J. Huang, Y. Q. Wang, and C. W. Chu, "Superconductivity at 93 K in a new mixed-phase Y-Ba-Cu-O compound system at ambient pressure," *Physical Review Letters*, vol. 58, pp. 908–910, mar 1987.

[77] C. Senatore, C. Barth, M. Bonura, M. Kulich, and G. Mondonico, "Field and temperature scaling of the critical current density in commercial REBCO coated conductors," *Superconductor Science and Technology*, vol. 29, no. 1, 2016.

[78] M. Cyrot and D. Pavuna, *Introduction to Superconductivity and High-Tc Materials*. World Scientific, jul 1992.

[79] A. Molodyk, S. Samoilenkov, A. Markelov, P. Degtyarenko, S. Lee, V. Petrykin, M. Gaifullin, A. Mankevich, A. Vavilov, B. Sorbom, J. Cheng, S. Garberg, L. Kesler, Z. Hartwig, S. Gavrilkin, A. Tsvetkov, T. Okada, S. Awaji, D. Abraimov, A. Francis, G. Bradford, D. Larbalestier, C. Senatore, M. Bonura, A. E. Pantoja, S. C. Wimbush, N. M. Strickland, and A. Vasiliev, "Development and large volume production of extremely high current density YBa$_2$Cu$_3$O$_7$ superconducting wires for fusion," *Scientific Reports*, vol. 11, dec 2021.

[80] S. C. Wimbush and N. M. Strickland, "A Public Database of High-Temperature Superconductor Critical Current Data," *IEEE Transactions on Applied Superconductivity*, vol. 27, pp. 1–5, jun 2017.

[81] M. Takayasu, L. Chiesa, L. Bromberg, and J. V. Minervini, "HTS twisted stacked-tape cable conductor," *Superconductor Science and Technology*, vol. 25, p. 014011, jan 2012.

[82] G. De Marzi, G. Celentano, A. Augieri, M. Marchetti, and A. Vannozzi, "Experimental and numerical studies on current distribution in stacks of HTS tapes for cable-in-conduit-conductors," *Superconductor Science and Technology*, vol. 34, p. 035016, mar 2021.

[83] L. Roebel, "Electrical conductor," 1915. US Patent 1,144,252.

[84] W. Goldacker, A. Frank, R. Heller, S. I. Schlachter, B. Ringsdorf, K.-P. Weiss, C. Schmidt, and S. Schuller, "ROEBEL Assembled Coated Conductors (RACC): Preparation, Properties and Progress," *IEEE Transactions on Applied Superconductivity*, vol. 17, pp. 3398–3401, jun 2007.

[85] J. Fleiter, A. Ballarino, L. Bottura, W. Goldacker, and A. Kario, "Characterization of Roebel Cables for Potential Use in High-Field Magnets," *IEEE Transactions on Applied Superconductivity*, vol. 25, pp. 1–4, jun 2015.

[86] D. C. van der Laan, "YBa$_2$Cu$_3$O$_{7-\delta}$ coated conductor cabling fr low ac-loss and high-field magnet applications," *Superconductor Science and Technology*, vol. 22, p. 065013, jun 2009.

[87] J. D. Weiss, T. Mulder, H. J. ten Kate, and D. C. van der Laan, "Introduction of CORC® wires: highly flexible, round high-temperature superconducting wires for magnet and power transmission applications," *Superconductor Science and Technology*, vol. 30, p. 014002, jan 2017.

[88] J. D. Weiss, D. C. van der Laan, D. Hazelton, A. Knoll, G. Carota, D. Abraimov, A. Francis, M. A. Small, G. Bradford, and J. Jaroszynski, "Introduction of the next generation of CORC® wires with engineering current density exceeding 650 A mm^{-2} at 12 T based on SuperPower's ReBCO tapes containing substrates of 25 μm thickness," *Superconductor Science and Technology*, vol. 33, p. 044001, apr 2020.

[89] L. Rossi, "The LHC main dipoles and quadrupoles toward series production," *IEEE Transactions on Appiled Superconductivity*, vol. 13, pp. 1221–1228, jun 2003.

[90] G. Brittles and R. Bateman, "Stability and quench - dynamic behaviour of Tokamak Energy REBCO QA coils," in *Talks at WAMHTS, Budapest*, 2019.

[91] S. Hahn, K. Kim, K. Kim, X. Hu, T. Painter, I. Dixon, S. Kim, K. R. Bhattarai, S. Noguchi, J. Jaroszynski, and D. C. Larbalestier, "45.5-tesla direct-current magnetic field generated with a high-temperature superconducting magnet," *Nature*, vol. 570, pp. 496–499, jun 2019.

[92] M. Marchevsky, "Quench Detection and Protection for High-Temperature Superconductor Accelerator Magnets," *Instruments*, vol. 5, p. 27, aug 2021.

[93] A. Akbar, N. Riva, Z. Yang, L. Thevenaz, and B. Dutoit, "Fast Hotspot Detection in SFCLs by Exploiting Strain Response in Optical Fiber Sensing," *IEEE Transactions on Applied Superconductivity*, vol. 31, pp. 1–5, aug 2021.

[94] M. Marchevsky, G. Ambrosio, M. Lamm, M. A. Tartaglia, and M. L. Lopes, "Localization of Quenches and Mechanical Disturbances in the Mu2e Transport Solenoid Prototype Using Acoustic Emission Technique," *IEEE Transactions on Applied Superconductivity*, vol. 26, pp. 1–5, jun 2016.

[95] M. Marchevsky, E. Hershkovitz, X. Wang, S. A. Gourlay, and S. Prestemon, "Quench Detection for High-Temperature Superconductor Conductors Using Acoustic Thermometry," *IEEE Transactions on Applied Superconductivity*, vol. 28, pp. 1–5, jun 2018.

[96] M. Marchevsky, A. R. Hafalia, D. Cheng, S. Prestemon, G. Sabbi, H. Bajas, and G. Chlachidze, "Axial-Field Magnetic Quench Antenna for the Superconducting Accelerator Magnets," *IEEE Transactions on Applied Superconductivity*, vol. 25, pp. 1–5, jun 2015.

[97] S. Hasegawa, S. Ito, G. Nishijima, and H. Hashizume, "Quench Detection Performance of Low-Temperature Superconducting Quench Detectors for REBCO Tape in Magnetic Fields," *IEEE Transactions on Applied Superconductivity*, vol. 31, pp. 1–5, aug 2021.

[98] S. Song, J. Lee, W. S. Lee, H. Jin, J. Lee, Y. J. Hwang, and T. K. Ko, "Quench Detection Method for HTS Coils Using Electromagnetically Coupled Coils," *IEEE Transactions on Applied Superconductivity*, vol. 25, pp. 1–4, jun 2015.

[99] J. Pfotenhauer, F. Kessler, and M. Hilal, "Voltage detection and magnet protection," *IEEE Transactions on Applied Superconductivity*, vol. 3, pp. 273–276, mar 1993.

[100] R. Denz, E. de Matteis, A. Siemko, and J. Steckert, "Next Generation of Quench Detection Systems for the High-Luminosity Upgrade of the LHC," *IEEE Transactions on Applied Superconductivity*, vol. 27, pp. 1–4, jun 2017.

[101] F. Rodriguez-Mateos and F. Sonnemann, "Quench heater studies for the LHC magnets," in *PACS2001. Proceedings of the 2001 Particle Accelerator Conference (Cat. No.01CH37268)*, vol. 5, pp. 3451–3453, IEEE, 2001.

[102] E. Ravaioli, *CLIQ. A new quench protection technology for superconducting magnets.* PhD thesis, Twente University, 2015.

[103] M. Mentink and T. Salmi, "Quench absorption coils: a quench protection concept for high-field superconducting accelerator magnets," *Superconductor Science and Technology*, vol. 30, p. 064002, jun 2017.

[104] J. S. Murtomaki, J. van Nugteren, G. Kirby, G. de Rijk, L. Rossi, and A. Stenvall, "ICED–Inductively Coupled Energy Dissipater for Future High-Field Accelerator Magnets," *IEEE Transactions on Applied Superconductivity*, vol. 28, pp. 1–15, dec 2018.

[105] J. van Nugteren, J. Murtomaki, J. Ruuskanen, G. Kirby, P. Hagen, G. de Rijk, H. T. Kate, L. Bottura, and L. Rossi, "A Fast Quench Protection System for High-Temperature Superconducting Magnets," *IEEE Transactions on Applied Superconductivity*, vol. 29, pp. 1–8, jan 2019.

[106] S. Hahn, D. K. Park, J. Bascunan, and Y. Iwasa, "HTS Pancake Coils Without Turn-to-Turn Insulation," *IEEE Transactions on Applied Superconductivity*, vol. 21, pp. 1592–1595, jun 2011.

[107] S. Hahn, Y. Kim, D. Keun Park, K. Kim, J. P. Voccio, J. Bascuñán, and Y. Iwasa, "No-insulation multi-width winding technique for high temperature superconducting magnet," *Applied Physics Letters*, vol. 103, p. 173511, oct 2013.

[108] S. Hahn, K. Kim, K. Kim, H. Lee, and Y. Iwasa, "Current Status of and Challenges for No-Insulation HTS Winding Technique," *TEION KOGAKU (Journal of Cryogenics and Superconductivity Society of Japan)*, vol. 53, no. 1, pp. 2–9, 2018.

[109] W. V. D. R. Maccaferri, M. Facchini, R. Jung, D. Tommasini, "The 5 T Superconducting Undulator for the LHC Synchrotron Radiation Profile Monitor," in *Proceedings of EPAC 2004, Lucerne, Switzerland*, pp. 1630–1632, 2004.

[110] J. van Nugteren, M. Dhallé, S. Wessel, E. Krooshoop, A. Nijhuis, and H. ten Kate, "Measurement and Analysis of Normal Zone Propagation in a ReBCO Coated Conductor at Temperatures Below 50K," *Physics Procedia*, vol. 67, pp. 945–951, 2015.

[111] M. Bonura and C. Senatore, "An equation for the quench propagation velocity valid for high field magnet use of REBCO coated conductors," *Applied Physics Letters*, vol. 108, p. 242602, jun 2016.

[112] D. Schoerling, *Superconducting wiggler magnets for beam-emittance damping rings.* PhD thesis, T.U. Bergakademie Freiberg, 2012.

[113] S. C. Richter, A. Ballarino, D. Schoerling, T. H. Nes, A. Bernhard, and A.-S. Müller, "Progress on HTS Undulator Prototype Coils for Compact FEL Designs," *IEEE Transactions on Applied Superconductivity*, vol. 32, no. 4, pp. 2–6, 2022.

[114] S. C. Richter, A. Ballarino, T. H. Nes, D. Schoerling, A. Bernhard, and A.-S. Müller, "Status and powering test results of HTS undulator coils at 77 K for compact FEL designs," *Journal of Physics: Conference Series*, vol. 2420, p. 012019, jan 2023.

[115] J. Fleiter and A. Ballarino, "Parametrization of the critical surface of REBCO conductors from Fujikura," tech. rep., CERN, 2014.

[116] M. Danial and J. Van Nugteren, "Parameterization of the critical surface of REBCO conductors from Bruker," tech. rep., CERN, 2017.

[117] T. H. Nes and S. C. Richter, "Fitting relations for HTS superconductors," tech. rep., CERN, 2020.

[118] X. Xu, "A review and prospects for Nb_3Sn superconductor development," *Superconductor Science and Technology*, vol. 30, p. 093001, sep 2017.

[119] R. Gupta, M. Anerella, J. Cozzolino, J. Escallier, G. Ganetis, M. Harrison, and P. Wanderer, "Next generation IR magnets for hadron colliders," *IEEE Transactions on Applied Superconductivity*, vol. 13, no. 2 II, pp. 1351–1354, 2003.

[120] T. H. Nes, G. Kirby, G. De Rijk, M. Canale, L. Gentini, J. Van Nugteren, A. Kario, and H. H. Ten Kate, "Design of a Cloverleaf-Racetrack Dipole Demonstrator Magnet with Dual ReBCO Conductor," *IEEE Transactions on Applied Superconductivity*, vol. 32, no. 6, pp. 1–5, 2022.

[121] R. Gupta, M. Anerella, P. Kovach, J. Schmalzle, S. Kahn, J. Kolonko, D. Larson, R. Scanlan, R. Weggel, E. Willen, A. Zeller, and S. Member, "Proof-of-Principle Design of a High-Field Overpass / Underpass Nb_3Sn Dipole," *IEEE Transactions on Applied Superconductivity*, vol. 32, no. 6, pp. 10–14, 2022.

[122] Vacuumschmelze GmbH & Co. KG. `https://vacuumschmelze.de/produkte/Weich-magnetische-Werkstoffe-und-Stanzteile/49-Kobalt-Eisen---VACOFLUX-und-VACODUR`, 2022. accessed: 2022/10/18.

[123] B. L. Rhodes, S. Legvold, and F. H. Spedding, "Magnetic Properties of Holmium and Thulium Metals," *Physical Review*, vol. 109, pp. 1547–1550, mar 1958.

[124] A. Inc., "Ansys, workbench (v. 2020 r2)." `https://www.ansys.com/`, 2020.

[125] J. S. Murtomaki, J. van Nugteren, G. Kirby, L. Rossi, J. Ruuskanen, and A. Stenvall, "Mechanical Effects of the Nonuniform Current Distribution on HTS Coils for Accelerators Wound With REBCO Roebel Cable," *IEEE Transactions on Applied Superconductivity*, vol. 27, pp. 1–5, jun 2017.

[126] J. S. Murtomaki, J. Van Nugteren, A. Stenvall, G. Kirby, and L. Rossi, "3-D mechanical modeling of 20 T HTS clover leaf end coils - Good practices and lessons learned," *IEEE Transactions on Applied Superconductivity*, vol. 29, no. 5, 2019.

[127] K. Ilin, K. A. Yagotintsev, C. Zhou, P. Gao, J. Kosse, S. J. Otten, W. A. J. Wessel, T. J. Haugan, D. C. van der Laan, and A. Nijhuis, "Experiments and FE modeling of stress–strain state in ReBCO tape under tensile, torsional and transverse load," *Superconductor Science and Technology*, vol. 28, p. 055006, may 2015.

[128] K. Zhang and M. Calvi, "Review and prospects of world-wide superconducting undulator development for synchrotrons and FELs," *Superconductor Science and Technology*, vol. 35, p. 093001, sep 2022.

[129] R. P. Walker, "Phase errors and their effect on undulator radiation properties," *Physical Review Special Topics - Accelerators and Beams*, vol. 16, p. 010704, jan 2013.

[130] R. P. Walker, "Interference effects in undulator and wiggler radiation sources," *Nuclear Instruments and Methods in Physics Research Section A: Accelerators, Spectrometers, Detectors and Associated Equipment*, vol. 335, pp. 328–337, oct 1993.

[131] J. Fleiter and A. Ballarino, "In-Field Electrical Resistance at 4.2 K of REBCO Splices," *IEEE Transactions on Applied Superconductivity*, vol. 27, no. 4, pp. 1–5, 2017.

[132] T. H. Nes, G. De Rijk, G. Kirby, F. O. Pincot, J. Liberadzka-Porret, C. Petrone, S. C. Richter, J. Van Nugteren, A. Kario, and H. H. Ten Kate, "Effective Time Constants at 4.2 to 70 K in ReBCO Pancake Coils with Different Inter-Turn Resistances," *IEEE Transactions on Applied Superconductivity*, vol. 32, no. 4, 2022.

[133] M. Majoros, M. D. Sumption, M. A. Susner, C. Kovacs, E. W. Collings, X. Peng, D. Doll, M. Tomsic, and D. Lyons, "A model superconducting helical undulator fabricated using a small filament, tube-type, multifilamentary Nb$_3$Sn wire," *Superconductor Science and Technology*, vol. 25, no. 11, 2012.

[134] S. C. Richter, D. Schoerling, S. S. I Schlachter, B. Ringsdorf, A. Drechsler, A. Bernhard, and A.-S. -S Müller, "Bending Radius Limits of Different Coated REBCO Conductor Tapes - An Experimental Investigation with Regard to HTS Undulators," *Proceedings of IPAC2021*, pp. 3837–3840, 2021.

[135] S. Otten, A. Kario, A. Kling, and W. Goldacker, "Bending properties of different REBCO coated conductor tapes and Roebel cables at T = 77 K," *Superconductor Science and Technology*, vol. 29, no. 12, 2016.

[136] W. Goldacker, "Bending strain investigations on BSCCO(2223) tapes at 77 K applying a new bending technique," in *AIP Conference Proceedings*, vol. 614, pp. 469–476, 2003.

[137] M. Takayasu, L. Chiesa, D. L. Harris, A. Allegritti, and J. V. Minervini, "Pure bending strains of Nb$_3$Sn wires," *Superconductor Science and Technology*, vol. 24, no. 4, 2011.

[138] H.-S. Shin, A. Nisay, M. Dedicatoria, and K. Sim, "Establishment of an easy Ic measurement method of HTS superconducting tapes using clipped voltage taps," *Progress in Superconductivity and Cryogenics*, vol. 16, pp. 29–32, jun 2014.

[139] S. B. Kim, T. Kaneko, H. Kajikawa, J. H. Joo, J. M. Jo, Y. J. Han, and H. S. Jeong, "The transient stability of HTS coils with and without the insulation and with the insulation being replaced by brass tape," *IEEE Transactions on Applied Superconductivity*, vol. 23, no. 3, pp. 47–50, 2013.

[140] T. Lecrevisse and Y. Iwasa, "A (RE)BCO Pancake Winding With Metal-as-Insulation," *IEEE Transactions on Applied Superconductivity*, vol. 26, pp. 1–5, apr 2016.

[141] P. Fazilleau, B. Borgnic, X. Chaud, F. Debray, T. Lécrevisse, and J. B. Song, "Metal-as-insulation sub-scale prototype tests under a high background magnetic field," *Superconductor Science and Technology*, vol. 31, no. 9, 2018.

[142] FARO Europe GmbH. `www.faro.com`, 2022. accessed: 2022/10/19.

[143] S. C. Richter, A. Ballarino, A. Bernhard, A. W. Grau, D. Saez de Jauregui, and A.-S. Müller, "High-temperature superconducting undulator prototype coils for compact free-electron lasers," *IEEE Transactions on Applied Superconductivity*, pp. 1–7, 2023.

[144] L. Bortot, M. Mentink, C. Petrone, J. Van Nugteren, G. Kirby, M. Pentella, A. Verweij, and S. Schöps, "Numerical analysis of the screening current-induced magnetic field in the HTS insert dipole magnet Feather-M2.1-2," *Superconductor Science and Technology*, vol. 33, p. 125008, dec 2020.

[145] M. Paidpilli and V. Selvamanickam, "Development of RE-Ba-Cu-O superconductors in the U.S. for ultra-high field magnets," *Superconductor Science and Technology*, vol. 35, p. 043001, apr 2022.

[146] J. Fleiter, *Study of the Implementation of High Temperature Superconductors in Accelerator Magnets. Étude de l'implémentation de supraconducteurs à haute température critique dans les aimants d'accélérateur.* PhD thesis, L'Université de Grenoble, 2013.

[147] L. Summers, M. Guinan, J. Miller, and P. Hahn, "A model for the prediction of Nb$_3$Sn critical current as a function of field, temperature, strain, and radiation damage," *IEEE Transactions on Magnetics*, vol. 27, pp. 2041–2044, mar 1991.

[148] M. Lubell, "Empirical scaling formulas for critical current and critical field for commercial NbTi," *IEEE Transactions on Magnetics*, vol. 19, pp. 754–757, may 1983.

[149] L. Bottura, "A practical fit for the critical surface of NbTi," *IEEE Transactions on Appiled Superconductivity*, vol. 10, pp. 1054–1057, mar 2000.

[150] A. Devred, *Practical Low-Temperature Superconductors for Electromagnets.* CERN Yellow Reports: Monographs, Geneva: CERN, 2004.